# Magnetic X-ray Reflectivity

Dissertation der Fakultät für Physik
der
Ludwig-Maximilians-Universität München

vorgelegt von Dieter Lott

aus München

München, den 14. Mai 2001

1. Gutachter:   Prof. Dr. J. Peisl
2. Gutachter:   Prof. Dr. K. Stierstadt

Tag der mündlichen Prüfung: 12.7.2001

# Thesis Outline

The scope of the thesis is to demonstrate the feasibility to examine magnetization profiles of thin films and multilayer systems via magnetic soft and hard x-ray reflectivity. The focus here is on 3d transition metals, which are used mainly for development of numerous noval magnetic devices, that are both technologically and scientifically interesting. Complementary to Neutron diffraction, which is the standard tool for the examination of magnetic structures in matter, magnetic x-ray diffraction permits to study small samples and exhibits better $Q_z$-resolution due its small and only slightly divergent beam. The biggest advantage is its element specificity, which enables one to probe different magnetic sites separately. The method of magnetic x-ray reflectivity combines the strong magnetic circular dichroism (MCD) effect, significantly enhancing the magnetic sensitivity of x-rays, with the technique of conventional specular reflectivity, a well established tool for the structural studies of the chemical makeup of thin films and artificial multilayer systems. The theory of resonant magnetic scattering within dipole approximation combined with the specular reflectivity condition suggests that the strongest effects are in the lower incident angle regime using circularly polarized x-rays. By using soft and hard x-rays structures on a scale of a few to several hundreds of Å are probed, which is the dimensions of the thicknesses of the layers of most thin film and multilayers systems.

In order to retrieve quantitative information from the measured magnetic reflectivity curves, an approach for visible light magneto-optical effects based on known dielectric tensors of the sample has been adopted and applied for soft and hard x-ray resonant scattering. Sample absorption and polarization changes in the sample are accounted for. Besides the structural composition, the thickness of the individual layers and the index of refraction, also the magnetic spin configuration can be chosen with arbitrary moment direction and magnitude by modifying the off-diagonal terms in the dielectric tensor. The magnetic optical constants, which determine the magnitude of the magnetic moments, are experimentally determined via MCD absorption measurements and then retrieving the real part through the Kramers-Kronig transformation of the measured imaginary part. This is shown in this work for several 3d

transition metals and edges. The simulations are sensitive to a variety of different spin configurations: spiral spin structures, magnetic dead layers and of collinear alignment.

Experimentally the magnetic reflectivity of 3d transition metals has to distinguish between the two available possible absorbtion edges, L and K, lying in different x-ray regions. The L-edges are situated in the soft x-ray region and exhibit large enhancements of the magnetic cross section, while the K-edges lie in the hard x-ray regime and show much smaller effects. In spite of this handicap, the latter can be important due to the much larger penetration depth and better $Q_z$-resolution. The X13 beamline at the NSLS at Brookhaven National Laboratory consisting of two branches for soft and hard-x ray operations, respectively, uses an elliptical polarized wiggler (EPW), which produces circularly polarized x-rays in the orbit plane and allows fast switching between left and right circular polarization. Lock-in detection is used to improve the signal-to-noise ratio at the soft x-ray branch and single photon detection at the hard x-ray branch to measure the magnetic signal. The EPW and the experimental setup was commissioned to demonstrate the feasibility of magnetic x-ray experiments. Especially at the hard x-ray beamline branch the small magnetic effects, less than 0.1% of the charge scattering, were possible to detect. In order to satisfy the need for high flux the CMC-CAT beamline at the APS in Argonne was used for magnetic hard x-ray reflectivity, providing an undulator beamline where the high flux of linear polarized photons was converted into circular polarization via a diamond phase plate, delivering much higher flux and better circular polarization.

The sample used to demonstrate the feasibility of the method of magnetic reflectivity consists of two multilayer structures of Fe/Cr on top of each other, where the iron spins of the upper are ferromagnetically and of the lower antiferromagnetically coupled, representing an exchange bias system. The sample was characterized with conventional x-ray reflectivity and MOKE measurements in order to accurately determine the structural composition and magnetic configuration (hysteresis loops), respectively. Magnetic reflectivity experiments on the L-edges at the X13A beamline showed strong magnetic effects, which could be clearly identified as ferromagnetic and antiferromagnetic Bragg peak contributions and simulation confirmed the collinear alignment and full magnetization of the iron spins throughout the iron layers. Energy- and magnetic field dependent measurements complete the picture. By tuning the x-ray energy

to the chromium L-edge, a signal 20 times weaker compared with iron, demonstrates that the weak magnetic moment in the chromium layers could be detected. Especially the AFM contribution shows strong effects which could be qualitatively and quantitatively evaluated. Simulation show clearly that the magnetic moment is concentrated at the interfaces and could be approximated to a magnetic layer with an effective thickness of about 0.5 Å assuming a step function in the magnetization profile.

Soft x-ray data usually suffer from strong absorption and the limited $Q_z$-range and resolution and therefore the use of hard x-rays seems desirable to probe the whole sample. Magnetic hard x-ray reflectivity measurements on the Fe/Cr double multilayer carried out at the CMC beamline by switching the magnetic field on the sample show clear magnetic Bragg reflection at the ferromagnetic structural peaks. They are very well reproduced by simulations and thus confirm the collinear alignment of the iron spins. In order to probe the AFM spin configuration the helicity of the photon beam has to be switched with constant magnetic field. In spite of complications in the reflectivity spectra it was possible to extract the relative orientation of the AFM to FM spin configuration in the two multilayers.

In summary the work showed for the example of an Fe/Cr double multilayer that magnetic soft and hard x-ray reflectivity can be applied to retrieve information about the magnetization profile of thin magnetic films and multilayer, and can compliment polarized neutron scattering.

# Content

# 1. Introduction

The familiar power of a magnet - its power of attracting iron - has been known since the time of Thales. The name magnet is derived from the town Magnesia (now Manisa) in Asia Minor, in whose neighborhood a naturally magnetic material was found. This mineral, known as magnetite or lodestone, contains considerable quantities of oxides of iron and was used as a crude compass before artificial magnets were employed for that purpose.

Nowadays magnetism is embodied in everybody's life. Magnets made from a variety of elements and alloys can be found in many forms, e.g. by using only the attractive force to hold doors or windows or in more sophisticated forms in devices with electromagnetic controls, electric motors, relays and electromagnetic switches. In computer technology the advances in the development of magnetic devices has led to faster and therefore better computers. Especially, the quality of read and write heads of hard discs made of thin magnetic multilayer films determine the present limit of the speed with which single bits can be read and processed. As in most areas of technological progress, the goal is to go to smaller and smaller sizes, reaching a point where devices are constructed on scales on the order of atoms. Terms like nanoscience or nanotechnology are used today in many scientific and technological areas to describe a very important new field, in which companies and research institutions have combined their efforts.

Beside the pure technological aspects, there are also a wide variety of scientifically interesting discoveries made in the last decades since the interest in magnetic materials has been revitalized. Novel magnetic phenomena like giant or colossal magneto resistance (GMR, CMR) effects, exchange bias, interlayer coupling behavior or spin valves do not only show a big potential in the technological sector, but also help to provide a better understanding of the magnetic properties in solid state matter and magnetic interactions. Magnetism originating from single atoms seems to be pretty well understood in terms of the quantum mechanical treatment, but by forming solids and especially in combination with other, magnetic as well as nonmagnetic materials, many noval behaviors have been discovered and need to be understood. In order to probe magnetism, a wide variety of tools can be employed as e.g. magnetic force microscope (MFM), magneto optical Kerr effect (MOKE) or superconducting quantum interference device (SQUID), but for a long time only neutron scattering with its large

magnetic cross section was able to examine the magnetic structure of thin films and multilayer on a nanometer scale and in a nondestructive way, even if the magnetic layer is buried. In the last ten years another technique, resonant magnetic x-ray scattering, was developed to provide not only an alternative tool to polarized neutron scattering, but also provide additional and complementary results.

In this study magnetic x-ray reflectivity will be discussed, where the interest is focussed on the determination of magnetization profiles along the surface normal of thin magnetic films and multilayers. The interest is focussed on systems with 3d transition metals, which represent the most important magnetic materials for technological applications.

The work is structured in the following way. First the method of magnetic reflectivity will be discussed. In particular, x-ray magnetic circular dichroism, which enhances the sensitivity to the magnetism of the thin films and multilayer systems, will be illustrated. After a short overview of the magnetism in 3d transition metals and a discussion of the magnetic scattering amplitude in the geometry of specular reflectivity, an optical approach to calculate the charge as well as the magnetic reflectivity will be introduced in the third chapter. This approach allows the simulation of the magnetic reflectivity profiles of thin layers and multilayer films and the determination of the magnetization profiles. The same chapter provides a method to determine the optical constants at absorption edges, where the tabulated values are not sufficiently accurate. In the fourth chapter the experimental setups used for the measurements will be described. In particular, it will be focussed on the need for circular polarization and detection of the magnetic signal. With all these ingredients, a multilayer system containing ferromagnetic and antiferromagnetic configurations as well as exhibiting interlayer coupling and exchange bias behavior will be examined. The method of magnetic reflectivity will be demonstrated in both, the soft and hard x-ray regions, showing the feasibility to extract essential information from the reflectivity spectra. Finally the results will be compared with the measurements on the same sample via polarized neutron reflectivity carried out by others, and illustrates the similarities and differences of both techniques, particularly showing the complimentary results derived from x-ray measurements. Finally, an outlook of the future development and applications of magnetic x-ray reflectivity will be given.

# 2. Method of Magnetic X-ray Reflectivity

In 1954 Gell-Mann and Goldhaber predicted relativistic spin-dependent corrections to the classical Thomson term in the photon scattering cross section from electrons [1]. The sensitivity of photons to magnetization densities was already known since Zeeman [2], who described the polarization phenomena for visible light induced by applying a magnetic field. But for a long time it was still difficult to observe the polarization effects of x-rays due to the fact that the index of refraction is very close to unity in this region of the electromagnetic spectrum. Nevertheless, Platzman and Tzoar [3] pointed out in 1970 that x-rays as an electromagnetic wave could be useful for the determination of magnetic structures. Unfortunately, the intensities from pure magnetic scattering were expected to be very small. Blume calculated the magnetic intensity for the non-resonant case and estimated the ratio between the pure magnetic and the charge cross sections to be [6]:

$$\frac{\boldsymbol{S}_{magnetic}}{\boldsymbol{S}_{charge}} \approx \left(\frac{\hbar \boldsymbol{w}}{mc^2}\right)^2 \frac{N_m^2}{N^2} \langle S \rangle^2 \frac{f_m^2}{f^2}, \tag{2.1}$$

where $\hbar\omega$ is the photon energy, m the mass of the electron and c the speed of light. $N_{(m)}$ denotes the number of (magnetic) electrons per atom and $f_{(m)}$ the (magnetic) form factors. $\langle S \rangle$ is the expectation value of the spin operator, which is unity at low temperatures and approaches zero at the Curie temperature. In the case of iron and a photon energy of 10 keV, a ratio of about $4 \cdot 10^{-6} \langle S \rangle$ can be expected, which made magnetic x-ray experiments extremely difficult for a long time. Nevertheless, de Bergevin and Brunel showed with their pioneering experiments in the early seventies and eighties [4,5] the feasibility of magnetic x-ray scattering experiments. In their first experiment in 1972 [4], using a standard x-ray tube, they detected the weak (1/2, 1/2, 1/2) and (3/2, 3/2, 3/2) magnetic reflections in the cubic antiferromagnet NiO and proved the magnetic nature by showing how the magnetic peak vanishes when the temperature reached the Néel point. The ratio of the magnetic and charge scattering cross sections was found at about $5 \cdot 10^{-8}$ and agreed well with the calculations.

However, instead of the pure magnetic intensity, it is possible to use the interference term between charge and magnetic scattering to increase the magnetic sensitivity and extract the magnetization properties. This interference term occurs only if the polarization factors are

complex, i.e. in using circular polarized light, or if the structure is noncentrosymmetric. Furthermore, while these first experiments were still carried out on standard x-ray tubes and made the detection of these weak signals very difficult, the availability of synchrotron radiation in the early eighties provided a new x-rays source with dramatically increased brightness and flux. Additionally, the tunability of the photon energy and its polarization properties opened the gate for a surge of magnetic scattering experiments. In a precursor to the following numerous magnetic scattering experiments and motivated by the unique properties of synchrotron radiation, Blume et al. worked out a detailed treatment of the non-resonant case [6] and later expended this theory also to the resonant case [7]. Besides magnetic scattering, synchrotron radiation facilities were also used to carry out absorption experiments in order to study the local magnetic properties of magnetized materials, i.e.: magnetic dichroism [8] or spin dependent absorption [9]. It is important to note that the absorption and scattering process represent two aspects of the same physical interaction and are very closely connected through the optical theorem, which states that absorption is governed by the imaginary part of the forward scattering amplitude. Gisela Schütz et al. [8] measured the difference between two magnetization states in an iron foil in a magnetic circular dichroism absorption experiment and discovered a significant increase by tuning the energy to the K-absorption edge of iron. The close connection of imaginary and real part of the scattering amplitude indicated the possibility of an significant increase in magnetic intensity in scattering experiments by tuning the energy to an absorption edge of the magnetic site. Namikawa et al. [10] discovered a small effect at the K-edge of nickel. Gibbs and coworkers [11] confirmed the expectations by measuring a large increase at the $L_3$ absorption edge in holmium. The enhancement of the magnetic scattering intensity at the absorption edges was soon explained by Hannon et al. [12] using an atomic picture.

This rest of the chapter is organized as follows: a short overview of Resonant Magnetic X-ray Scattering (XRES) in an atomic picture is given, followed by a more detailed explanation of Magnetic Circular Dichroism (MCD), a spectroscopic tool taking advantage of the large enhancements achieved by tuning the photon energy to an absorption edge of the magnetic site. The chapter concludes with the discussion of the magnetic scattering amplitude in the geometry of specular reflectivity and shows that the combination of the MCD effect and the interface sensitive specular reflectivity is well suited to probe magnetic structures of thin films and multilayer systems.

## 2.1 Magnetic x-ray scattering on a magnetic ion

The total coherent elastic scattering amplitude from a magnetic ion is given by [12]:

$$f = f_0 + f' + i f'' + f_{non-res}^{mag} , \tag{2.2}$$

where $f_0 \propto Z r_0$ is the Thomson charge scattering amplitude with the number of electrons Z and the classical electron radius $r_0$. $f_{non-res}^{mag}$ is the non-resonant magnetic amplitude and can be expressed by

$$f_{non-res}^{mag} = i\, r_0 (\hbar \omega / mc^2) f_D [\tfrac{1}{2} \vec{L}(\vec{Q}) \cdot \vec{A} + \vec{S}(\vec{Q}) \cdot \vec{B}] . \tag{2.3}$$

$\vec{L}(\vec{Q})$ and $\vec{S}(\vec{Q})$ are the Fourier transforms of the orbital momentum and spin densities, respectively, and are multiplied by polarization vectors $\vec{A}$ and $\vec{B}$ given by the geometry of the experiment.

$\vec{A}$ and $\vec{B}$ can be calculated with $\vec{A} = 2(1 - \hat{k} \cdot \hat{k}')(\hat{e}' \times \hat{e}) - (\hat{k} \times \hat{e})(\hat{k} \cdot \hat{e}') + (\hat{k}' \times \hat{e})(\hat{k}' \cdot \hat{e}')$ and $\vec{B} = (\hat{e}' \times \hat{e}) + (\hat{k}' \times \hat{e}')(\hat{k}' \cdot \hat{e}) - (\hat{k} \times \hat{e})(\hat{k} \cdot \hat{e}') - (\hat{k}' \times \hat{e}')(\hat{k} \cdot \hat{e})$. $\hat{k}$ and $\hat{k}'$ are the incident and scattered wave vectors, and $\hat{\varepsilon}$ and $\hat{e}'$ are the incident and scattered polarization vectors, respectively. $\vec{Q} = \vec{k}' - \vec{k}$ is the wave-vector transfer and $f_D$ the Debye-Waller factor. It should be noted that $\vec{A}$ and $\vec{B}$ are formally different. Therefore spin and orbital momentum contribute differently to the non-resonant magnetic scattering amplitude $f_{non-res}^{mag}$ and can be experimentally distinguished. A more detailed description of the non-resonant magnetic scattering can be found in [6, 13]. The resonant process enters the scattering amplitude by its dispersive and absorptive parts, $f'$ and $f''$, respectively, and can lead to large enhancements in the magnetic scattering amplitude if the photon energy is tuned to an absorption edge of a magnetic site. Here, it should be noted that magnetic scattering is mainly due to *electric* multipole transitions. The sensitivity to the spin polarization of bands, which are responsible for the magnetism of a single site arises from the Pauli exclusion principle, which only allows transitions to

unoccupied orbitals, and the exchange induced splitting of the orbitals. The main contribution stems from the electric dipole and quadrupole terms, which, if allowed, dominate the resonant magnetic cross section and will be exclusively considered here.

The resonant contribution to the coherent scattering amplitude for the electric $2^L$-pole resonance (EL) in a magnetic ion derived by Hannon et al. [12] is given by

$$f_{EL}^e(\omega) = \frac{4\pi}{|k|} f_D \sum_{M=-L}^{L} \left[ \hat{\varepsilon}'^* \cdot \vec{Y}_{LM}^{(e)}(\hat{k}') \vec{Y}_{LM}^{(e)*}(\hat{k}) \cdot \hat{\varepsilon} \right] F_{LM}^{(e)}(\omega) \,, \tag{2.4a}$$

where $\vec{Y}_{LM}^{(e)}(\hat{k})$ are the vector spherical harmonics. The dimensionless transition matrix element $F_{LM}^{(e)}(w)$ determines the strength of the resonance and can be calculated with

$$F_{LM}^{(e)}(\omega) = \sum_{\alpha,\eta} \frac{P_\alpha P_\alpha(\eta) \; \Gamma_x(\alpha M \eta; EL)/\Gamma(\eta)}{\chi(\alpha,\eta) - i} \,, \tag{2.4b}$$

where $\alpha$ and $\eta$ are the initial ground and the excited states of the ion, respectively. $P_\alpha$ and $P_\alpha(\eta)$ are the probabilities that the ion is in the initial state $\alpha$ and of the transition from $\alpha$ to a final state $\eta$, respectively, which are determined by the overlap integrals between the two states $\alpha$ and $\eta$. $\Gamma_x/\Gamma$ is the ratio of the partial line width for EL radiative decay from $\eta$ to $\alpha$ to the total line width $\Gamma$ for the excited state $\eta$ determined by all deexcitations of $\eta$ due to both radiative and non-radiative processes. $c(a,h) = (E_h - E_a - \hbar w)/(\Gamma/2)$ gives the deviation in energy from the resonance in units of the half width of the resonance and makes $F_{LM}^{(e)}$ strongly energy dependent.

## Electric dipole transition (E1)

Electric dipole transitions usually contribute the strongest to the magnetic scattering cross section. At such a transition with L = 1 and magnetic quantum number change of M = 0, ± 1, the vector spherical harmonics can be written [12]:

$$[\hat{\varepsilon}' \cdot \vec{Y}_{1\pm1}(\hat{k}')\vec{Y}_{1\pm1}^{*}(\hat{k}) \cdot \hat{\varepsilon}] = (3/16\pi)[\hat{\varepsilon}' \cdot \hat{\varepsilon} \mp i\,(\hat{\varepsilon}' \times \hat{\varepsilon}) \cdot \hat{z}_n - (\hat{\varepsilon}' \cdot \hat{z}_n)(\hat{\varepsilon} \cdot \hat{z}_n)] \qquad (2.5)$$

and

$$[\hat{\varepsilon}' \cdot \vec{Y}_{10}(\hat{k}')\vec{Y}_{10}^{*}(\hat{k}) \cdot \hat{\varepsilon}] = (3/8\pi)[(\hat{\varepsilon}' \cdot \hat{z}_n)(\hat{\varepsilon} \cdot \hat{z}_n)] \qquad (2.6)$$

with $\hat{z}_n$ the unit vector of the magnetic moment of the nth ion. Substituting (2.5) and (2.6) in equation (2.4) leads to the resonant magnetic scattering amplitude for dipole transitions:

$$f_{nE1}^{XRES} = [(\hat{\varepsilon}' \cdot \hat{\varepsilon})\,F^{(0)} - i\,(\hat{\varepsilon}' \times \hat{\varepsilon}) \cdot \hat{z}_n\,F^{(1)} + (\hat{\varepsilon}' \cdot \hat{z}_n)(\hat{\varepsilon} \cdot \hat{z}_n)\,F^{(2)}]\,, \qquad (2.7)$$

with

$$F^{(0)} = (3/4k)\,[F_{11} + F_{1-1}]\,, \qquad (2.8a)$$

$$F^{(1)} = (3/4k)\,[F_{11} - F_{1-1}]\,, \qquad (2.8b)$$

$$F^{(2)} = (3/4k)\,[2F_{10} - F_{11} - F_{1-1}]\,. \qquad (2.8c)$$

The first term of (2.7) is independent of the direction of the magnetic moment $\hat{z}_n$ and can be thought of as a correction to the charge scattering which is not sensitive to the sample magnetization. This term is often called the anomalous scattering contribution, arising from tuning the photon energy to an absorption edge. The polarization dependence $(\hat{\varepsilon}' \cdot \hat{\varepsilon})$ is the same as the non-resonant charge scattering, e.g. Thomson term from (2.2) and is only finite for the $\sigma \rightarrow \sigma'$ ($\hat{\varepsilon} = \hat{\varepsilon}_\sigma$, $\hat{\varepsilon}' = \hat{\varepsilon}'_\sigma$) and $\pi \rightarrow \pi'$ ($\hat{\varepsilon} = \hat{\varepsilon}_\pi$, $\hat{\varepsilon}' = \hat{\varepsilon}'_\pi$) channels, where $\sigma$ and $\pi$ correspond to polarization perpendicular and parallel to the scattering plane, respectively. The second term is linear in $\hat{z}_n$ and shows a polarization dependence of $(\hat{\varepsilon}' \times \hat{\varepsilon})$. Therefore, contrary to the first term, the polarization can be rotated upon scattering depending on the scattering geometry. Figure 2.1 shows three basic magnetization states, where the scattering plane is in the $x_1$-$x_3$

plane. Arrows indicate the longitudinal, transverse and polar magnetization direction. In the longitudinal and polar cases, the second term of the resonant magnetic scattering amplitude leads to $\sigma \rightarrow \pi'$ and to $\pi \rightarrow \sigma'$ scattering contributions, while in the transverse case the polarization of the incident light remains unrotated and shows $\pi \rightarrow \pi'$ scattering. It should be noted that the magnetic scattering occurs at the same reciprocal lattice points as non-resonant magnetic scattering, which is also linear in $\hat{z}_n$.

The polarization dependence of the third term is more complicated than the previous terms. Since $\hat{z}_n$ appears twice, the term is quadratic in the magnetization direction, which gives rise to zero and second harmonic magnetic satellites. For the three basic magnetization directions, no rotation of the polarization state of the incident light occurs. The longitudinal and polar case produce only $\pi \rightarrow \pi'$ scattering, while in the transverse magnetization state $\sigma \rightarrow \sigma'$ can be observed. It should be noted that second harmonic magnetic satellites are only due to the resonant process and cannot be observed in the non-resonant limit.
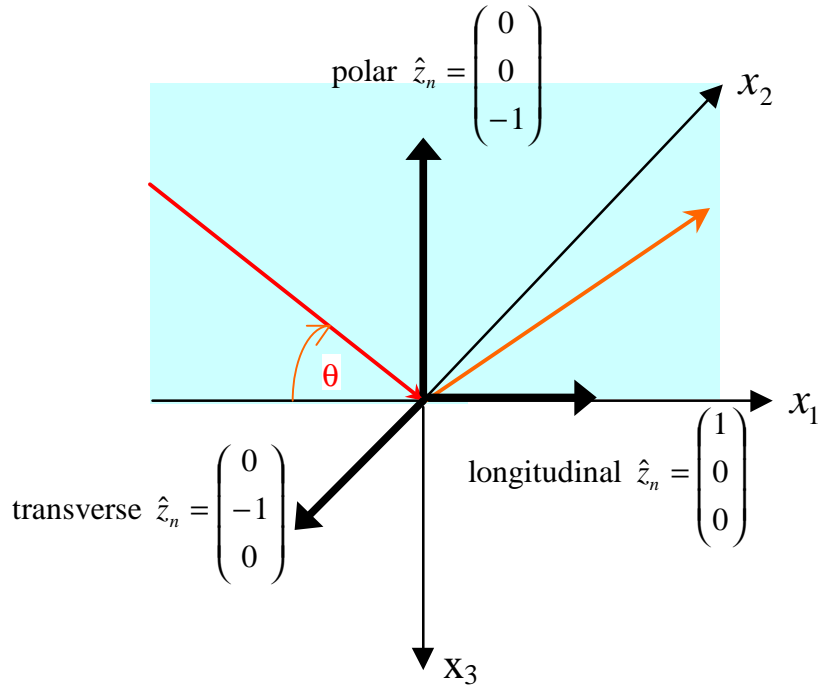


**Figure 2.1** *Coordination system showing the longitudinal, transverse and polar magnetization case (thick arrows). The scattering plane is in the $x_1$-$x_3$ plane with the thick dashed arrows indicating the scattering process.*

## Electric quadrupole transition (E2)

The next lowest electric multipole transition is the electric quadrupole transition. The expansion of the vector spherical harmonics in the L = 2 case lead to 13 distinct terms of four orders in the magnetic moment [12]:

$$\textit{order 0}: \ (\hat{k}' \cdot \hat{k})\,(\hat{e}' \cdot \hat{e})\,F_{E2}^{(0)} \tag{2.9a}$$

$$\textit{order 1}: \quad -i\,[(\hat{k}' \cdot \hat{k})\,(\hat{e}' \times \hat{e}) \cdot \hat{z}_n + (\hat{e}' \cdot \hat{e})\,(\hat{k}' \times \hat{k}) \cdot \hat{z}_n\,]\,F_{E2}^{(1)} \tag{2.9b}$$

$$
\begin{aligned}
&\quad [(\hat{k}' \cdot \hat{k})(\hat{e}' \cdot \hat{z}_n)(\hat{e} \cdot \hat{z}_n) + (\hat{e}' \cdot \hat{e})(\hat{k}' \cdot \hat{z}_n)(\hat{k} \cdot \hat{z}_n)](F_{E2}^{(2)} - F_{E2}^{(0)})\\
\textit{order 2}: &+ [(\hat{e}' \cdot \hat{k})(\hat{k}' \cdot \hat{z}_n)(\hat{e} \cdot \hat{z}_n) + (\hat{k}' \cdot \hat{e})(\hat{e}' \cdot \hat{z}_n)(\hat{k} \cdot \hat{z}_n)]F_{E2}^{(2)}\\
&- [(\hat{k}' \times \hat{k}) \cdot \hat{z}_n(\hat{e}' \times \hat{e}) \cdot \hat{z}_n]F_{E2}^{(0)}
\end{aligned} \tag{2.9c}
$$

$$
\begin{aligned}
\textit{order 3}: \ &-i\,[(\hat{k}' \cdot \hat{z}_n)\,(\hat{k} \cdot \hat{z}_n)(\hat{e}' \times \hat{e}) \cdot \hat{z}_n + (\hat{e}' \cdot \hat{z}_n)\,(\hat{e} \cdot \hat{z}_n)\,(\hat{k}' \times \hat{k}) \cdot \hat{z}_n\,](F_{E2}^{(3)} - F_{E2}^{(1)})\\
&-i\,[(\hat{e}' \cdot \hat{z}_n)(\hat{k} \cdot \hat{z}_n)(\hat{k}' \times \hat{e}) \cdot \hat{z}_n + (\hat{k}' \cdot \hat{z}_n)(\hat{e} \cdot \hat{z}_n)(\hat{e}' \times \hat{k}) \cdot \hat{z}_n\,]\,F_{E2}^{(3)}
\end{aligned} \tag{2.9d}
$$

$$\textit{order 4}: \quad [(\hat{k}' \cdot \hat{z}_n)(\hat{k} \cdot \hat{z}_n)(\hat{e}' \cdot \hat{z}_n)\,(\hat{e} \cdot \hat{z}_n)\,F_{E2}^{(4)} \tag{2.9e}$$

where

$$F_{E2}^{(0)} = (5/4k)[F_{22} + F_{2-2}] \tag{2.10a}$$

$$F_{E2}^{(1)} = (5/4k)[F_{22} - F_{2-2}] \tag{2.10b}$$

$$F_{E2}^{(2)} = (5/4k)[F_{21} + F_{2-1}] \tag{2.10c}$$

$$F_{E2}^{(3)} = (5/4k)[F_{22} - F_{2-1}] \tag{2.10d}$$

$$F_{E2}^{(4)} = (5/4k)[F_{22} + F_{2-2} - 4F_{21} - 4F_{2-1} + 6F_{20}]. \tag{2.10e}$$

Scattering from such a process is in general weaker than from the electric dipole transitions, but can also lead to significant signals. Contrary to the first order electric dipole harmonic which only has the $\pi \to \pi'$, $\pi \to \sigma'$ and $\sigma \to \pi'$ channels, E2 allows also the $\sigma \to \sigma'$ channel to contribute to the magnetic signal and can lead to the observation of additional harmonics

around magnetic reflections. Especially in incommensurate antiferromagnets each order can give rise to separate magnetic satellites. As an example, Gibbs et al. [11] observed in their first resonant magnetic x-ray scattering experiment at the $L_3$ -edge of Ho third and fourth order magnetic satellites, which showed strong $\sigma \rightarrow \sigma'$ magnetic scattering, and therefore clearly indicates quadrupole origin. The quadrupole transition also contributes to the first and second order satellites, but the dominant dipole contribution defines the scattering picture. More detailed calculations and descriptions can be found elsewhere [11,12,14].

Simultaneously with the development of theoretical pictures to explain resonant magnetic x-ray scattering and experiments, a related technique, magnetic circular dichroism (MCD), also became more popular for the determination of local magnetic properties in magnetic materials. This spectroscopic tool generally used in the absorption geometry shows the magnetic sensitivity of circularly polarized x-rays to magnetic material and can be exploited in other geometries to probe magnetism. Furthermore, it is used for the determination of magnetic scattering amplitudes for a wide variety of magnetic sites as illustrated in Chapter 3.

# 2.2 Magnetic Circular Dichroism (MCD)

Magnetic circular dichroism is basically a phenomenon which occurs when the magnetization state of a material causes a difference in the absorption between left and right circularly polarized light. The polarization dependent attenuation coefficient therefore yields information about the magnetic state of the absorber.

In a simplified picture, the MCD effect can be described as a two step process, illustrated in figure 2.3. First a circularly polarized photon creates and spin polarizes a photoelectron from a core level. The resulting photoelectron spin is governed by the helicity of the absorbed photon. In the second step the spin polarized photoelectron is excited into an unoccupied valence state and the transition rate depends strongly on the number of available final states with the spin parallel to the spin of the photoelectron. Due to the magnetization of the system the spin polarized density of states is different for both polarization states and therefore the transition probability for spin up and spin down photoelectrons is also different, which results in a difference in the absorption of left and right circularly polarized photons.
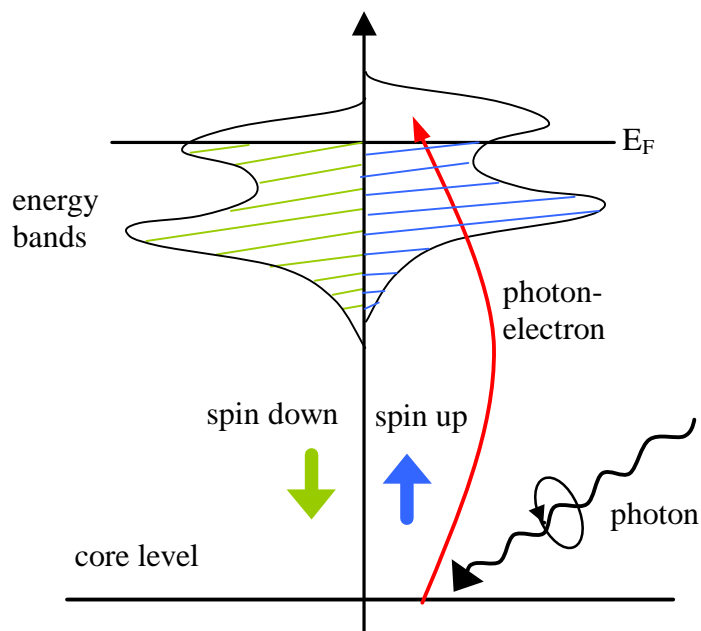


**Figure 2.3** *Two-step picture of spin-dependent photoabsorption. A circularly polarized photon is absorbed by spin polarizing a photoelectron, which is lifted into an unoccupied spin polarized valance band.*

Applying Fermi's Golden Rule for this two step scenario the absorption coefficients can be written as

$$\mu_\uparrow \propto p_{\uparrow\uparrow}\,\rho_\uparrow(E) + p_{\uparrow\downarrow}\,\rho_\downarrow(E) \qquad (2.11)$$

for incident right circularly polarized light ($\uparrow$) and

$$\mu_\downarrow \propto p_{\downarrow\uparrow}\,\rho_\uparrow(E) + p_{\downarrow\downarrow}\,\rho_\downarrow(E) \qquad (2.12)$$

for incident left circularly polarized light ($\downarrow$). $\rho_{\uparrow(\downarrow)}$ is the unoccupied spin density of the state for up (down) electrons and p the relative weights for spin up and down photoelectron polarization by absorbing right or left circularly polarized photons, respectively. The first arrow in p indicates the helicity of the incident photon beam and the second the spin polarization of the excited photoelectron. The proportional factors for both equations (2.11) and (2.12) are the same. Symmetry arguments allow one to make some further simplifications. By changing the helicity of the incident x-rays, the sign of the photoelectron polarization changes, but the magnitude remains the same. Therefore the value of the transition depends only on the relative orientation between photon helicity and magnetization direction, leading to following definitions:

$$p_{\uparrow\uparrow} = p_{\downarrow\downarrow} := p_p \qquad (2.13a)$$

and

$$p_{\uparrow\downarrow} = p_{\downarrow\uparrow} := p_a, \qquad (2.13b)$$

where $p_p$ and $p_a$ are the weights for the helicity of the photon beam parallel and antiparallel to the spin polarized photoelectron, respectively. Measuring the asymmetry ratio of both absorption coefficients by taking the difference divided by the sum leads to following equation:

$$\frac{\Delta\mu(E)}{\mu(E)} = \frac{\mu_\uparrow(E)-\mu_\downarrow(E)}{\mu_\uparrow(E)+\mu_\downarrow(E)} = \left(\frac{p_p - p_a}{p_p + p_a}\right)\cdot\left(\frac{\rho_\uparrow(E)-\rho_\downarrow(E)}{\rho_\uparrow(E)+\rho_\downarrow(E)}\right) = P_e\cdot\frac{\rho_s(E)}{\rho_{0,s}(E)}, \quad (2.14)$$

where

$$\rho_s(E) = \rho_\uparrow(E) - \rho_\downarrow(E) \tag{2.15}$$

is the spin polarized density of the states and

$$P_e = \left( \frac{p_p - p_a}{p_p + p_a} \right) \tag{2.16}$$

the polarization of the photoelectrons. In this picture, the photoelectron polarization is assumed to be independent of the incident energy.

As already mentioned before, absorption and scattering are very closely related through the optical theorem. This relation is not only valid for the charge part, but can be also extended to the magnetic part. The optical theorem for absorption coefficient can be written as

$$\mu(E) \propto \text{Im} f(E, \theta = 0^o). \tag{2.17}$$

In the case of magnetic dichroism, where the energy is close to an absorption edge, the resonant magnetic scattering amplitude is dominant. Considering the electric dipole transitions (E1) and neglecting all magnetic higher order terms, leads to the following expression:

$$\mu_{MXD}(E) \propto \text{Im} f_{nE1}^{XRES}(E) \approx \text{Im}[[(\hat{\varepsilon}' \cdot \hat{\varepsilon}) F^{(0)} - i(\hat{\varepsilon}' \times \hat{\varepsilon}) \cdot \hat{z}_n F^{(1)}] \tag{2.18}$$

In an absorption experiment the polarization vector for incident and scattered beam as well as the wave propagation vector remain the same, $\hat{\varepsilon} = \hat{\varepsilon}'$ and $\hat{k} = \hat{k}'$, respectively. By decomposing the polarization vector into its perpendicular components (see figure 2.1 with $\theta = 0°$),

$$\hat{\varepsilon} = \hat{\varepsilon}' = \begin{pmatrix} 0 \\ \varepsilon_\perp \\ \varepsilon_\parallel \end{pmatrix}, \tag{2.19}$$

the scalar and vector product of the first and second term in (2.18) can be easily found as

$$\hat{\varepsilon}' \cdot \hat{\varepsilon} = \hat{\varepsilon}^* \cdot \hat{\varepsilon} = \hat{\varepsilon}_\perp^2 + \hat{\varepsilon}_{||}^2 = 1, \tag{2.20}$$

and

$$\hat{e}' \times \hat{e} = \hat{e}^* \times \hat{e} = (e_\perp^* e_{||} - e_{||}^* e_\perp) \cdot \hat{u}_3 = i\,P_c\,\hat{k}, \tag{2.21}$$

respectively, where the * indicates the complex conjugate and $P_c$ is the Stokes parameter which determines the mean value of the photon helicity or the degree of circular polarization. The scalar product is completely independent of the photon polarization while the vector product is only non zero if the components of the polarization vectors of the incident light, $\varepsilon_\perp$ and $\varepsilon_{||}$, are out of phase and the beam possesses net circular polarization ($P_c \neq 0$). The absorption coefficient can be now written as

$$\boldsymbol{m} \propto \mathrm{Im}\,(F^{(0)} - \hat{k}\cdot\hat{z}\,P_c\,F^{(1)}) \tag{2.22}$$

or expressed as

$$\boldsymbol{m} = \boldsymbol{m}_0 + \boldsymbol{m}_c\,P_c\cos\boldsymbol{j}, \tag{2.23}$$

where $\mu_0$ and $\mu_c$ are the polarization independent and spin dependent absorption coefficients, respectively, and $\varphi$ the angle between the sample magnetization $\hat{z}$ and the beam direction $\hat{k}$. With the calculations above two important observations are made. The spin dependent absorption coefficient $\mu_c$ stems from the second term considered in (2.18) and this term is therefore exclusively responsible for the MCD-effect. Second, the MCD effect scales with the degree of circular polarization $P_c$ and with the cosine of the angle $\varphi$, which is maximum if beam and magnetization directions are identical.

In order to separate the magnetic signal from the spin independent part, the difference of the absorption coefficient for both helicities has to be taken. This leads to an asymmetry ratio for the absorption coefficient of

$$\frac{\Delta \boldsymbol{m}}{\boldsymbol{m}} = \frac{\boldsymbol{m}_c}{\boldsymbol{m}_0} \cdot P_c \, \cos \boldsymbol{j} \ . \tag{2.24}$$

Under the assumption of 100% circularly polarized light ($P_c = \pm 1$) and parallel alignment between photon helicity and the applied magnetic field ($\varphi = 0°$), the equation can be simplified and compared to the earlier result in (2.14) for the asymmetry ratio derived earlier from the two step model. It leads to the following expression

$$\frac{\mu_c}{\mu_0} = P_e \cdot \frac{\rho_s}{\rho_0} , \tag{2.25}$$

which illustrates the connection between the spin dependent absorption coefficient $\mu_c$ and the spin polarized density of states $\rho_s$.

Generally, it has to be noted that the magnetism of real magnetic systems arises from both spin and orbital momentum. In a classic picture, the negatively charged electron orbits around a positively charged nucleus leading to an orbital magnetic momentum. At the same time the electron possesses a magnetic moment itself due to its spin, which interacts with the orbital momentum. This is described by the spin-orbit coupling term. Even though the spin-orbit coupling can be illustrated in a classical model, it is a relativistic effect and needs relativistic quantum mechanical calculations to derive the resulting consequences. One important effect results in the splitting of the states with the same orbital momentum $m_l$ in pairs, where the spin momentum $m_s$ is parallel and antiparallel to the orbital momentum, respectively. As an example, the p core states in a magnetic material are energetically split into a $p_{1/2}$ and $p_{3/2}$ level. Using the dipole selection rule, a photoelectron from one of these levels can be excited into a d-band ($l = l+1$) or s-band ($l = l -1$). The latter turns out to be much weaker than the first case and will be neglected here [15]. Now, the photoelectron polarization can be estimated for a $p_{1/2} \rightarrow d$ ($L_2$ edge) and $p_{3/2} \rightarrow d$ transition ($L_3$ edge). Figure 2.4 shows the $L_2$ edge transition when a right circularly polarized photon gets absorbed ($\Delta m_l = +1$). The boxes denote the individual configuration for the initial $p_{1/2}$ and final d states and the arrows indicate allowed transitions. To the left of each box in the initial state is the squared Glebsch-Gordan coefficient, which
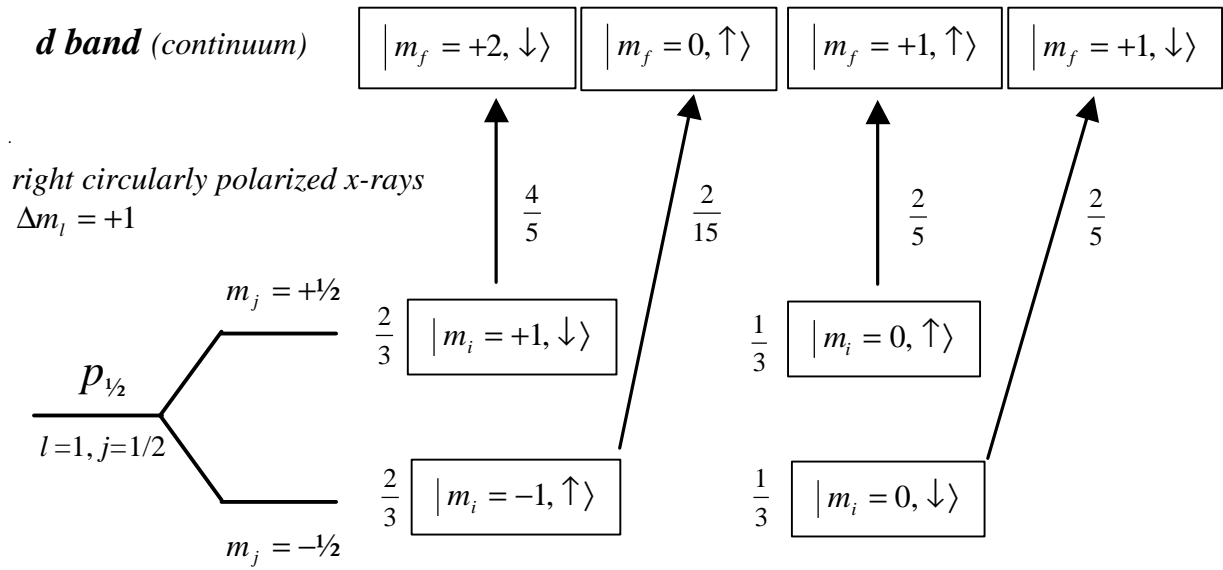
**Figure 2.4** *Transition from a $p_{1/2}$ core level to an unoccupied d band above the Fermi energy by absorbing a right circularly polarized photon ($\boldsymbol{D}m_l = +1$). All possible configuration are shown in boxes with $|m_l, m_s\rangle$ indicating the orbital and spin momentum. The weight of each initial configuration is left to the boxes and the transition rates are denoted next to each arrow.*

gives the weight for each configuration. The relative strength of each transition from the p to the d state by absorbing a right circularly polarized photon can be calculated with [16]

$$P_{transition} = \frac{[(l+1)+(m_l+1)]\,[(l+1)+m_l]}{[2(l+1)+1]\,[2(l+1)-1]} \tag{2.26}$$

and are indicated right to each arrow. The parallel and antiparallel transition probabilities in (2.16) can be now estimated with

$$p_p \propto \frac{2}{3}\cdot\frac{2}{15}+\frac{1}{3}\cdot\frac{2}{5}=\frac{2}{9} \tag{2.27}$$

and

$$p_a \propto \frac{2}{3}\cdot\frac{4}{5}+\frac{1}{3}\cdot\frac{2}{5}=\frac{2}{3}. \tag{2.28}$$

Using equation (2.16), now the photoelectron polarization can be calculated and results in

$$P_e(p_{1/2}) = -\frac{1}{2} \tag{2.29}$$

for the $L_2$ transition. The same procedure can be applied to the $p_{3/2}$ core level exciting a photoelectron to a d-state, describing the $L_3$ edge transition, and leads to a photoelectron polarization of

$$P_e(p_{3/2}) = +\frac{1}{4}. \tag{2.30}$$

Experimentally, the opposite sign expected for the photoelectron polarization of both split p states is reflected in the opposite sign in the measured asymmetry ratio. Furthermore, another observation can be made by looking at this example. In the absence of spin orbit coupling the two p-states would not be split energetically. Since the $p_{3/2}$ state possesses twice as many electrons as the $p_{1/2}$ state, the net photoelectron polarization would cancel out to zero and therefore no spin-dependent polarization would be observed. This is in contrast with the observed MCD signal at the K-edges of 3d transition metals, where the initial s state ($l=0$) is not spin-orbit split. The simplified picture assumes that the MCD process can be completely separated into two independent steps, the polarization of a core electron through the circularly polarized photon and the capturing of the excited photoelectron in an empty final state of the atom, respectively. But in real systems the photoelectron polarization cannot be referred only to the polarization of the initial core level and treated independently of the final state. In the case of spin-orbit splitting in the final state, the photoelectron polarization shows also a finite value for unsplit core levels like the s state. Nevertheless, the whole consideration above indicates that the spin-orbit splitting of the initial states has the biggest influence and leads to much larger MCD effects.

# Sum rules

The success of magnetic circular dichroism as a spectroscopic tool is not only due to its element and site specificity but also to the ability to separate the spin and orbit contributions to the total magnetic moment via powerful theoretical sum rules developed in the early nineties by Thole and Carra [17,18]. The sum rules are based on the single ion approximation and relate the optical cross section to the average orbital and spin moments of the conduction band ground states. Analyzing the total magnetic moment by separating the orbital and spin momentum of each element can provide a much better understanding of the macroscopic magnetic properties of many technological and scientifically interesting multilayer systems, containing several different magnetic components.

Two important magneto-optical sum rules have been derived, which yield element specific orbital and spin magnetic moments from x-ray absorption spectroscopy (XAS) and its associated MCD measurements. For example, in the case of 2p core level, the $L_2$ ($p_{1/2}$ state) and $L_3$ ($p_{3/2}$ state) transitions have to be taken into account, leading to following expression for the sum rules [19- 21]:

$$m_l \cong -\frac{4 \int\limits_{L_2+L_3} \boldsymbol{m}_c \, d\boldsymbol{w}}{3 \int\limits_{L_2+L_3} (\boldsymbol{m}_\uparrow + \boldsymbol{m}_\downarrow) \, d\boldsymbol{w}} \cdot N_d \qquad (2.31)$$

and

$$m_s \cong -\frac{6 \int\limits_{L_3} \mu_c \, d\omega - 4 \int\limits_{L_2+L_3} \mu_c \, d\omega}{\int\limits_{L_2+L_3} (\mu_\uparrow + \mu_\downarrow) \, d\omega} \cdot N_d \cdot \left(1 + \frac{7\langle T_z \rangle}{2\langle S_z \rangle}\right)^{-1}, \qquad (2.32)$$

where $m_l$ and $m_s$ are the orbital and spin moments given in units of $\mu_B$ per atom and $\mu_{\uparrow(\downarrow)}$ is the absorption coefficient for right ($\uparrow$) and left ($\downarrow$) circularly polarized x-rays. $\mu_c$ describes the different absorption coefficient between right and left circularly polarized light and $N_d$ denotes for the number of valence holes. $\langle T_z \rangle$ is the magnetic dipole term and $\langle S_z \rangle$ equal to half of $m_s$ in Hartree atomic units [20, 21]. $L_2$ and $L_3$ indicate the integration range. From the experimental

point of view it is important that the measured sum spectra are corrected for the $L_2$ and $L_3$ edge jumps resulting from the p $\rightarrow$ s transition, which is not included in the sum rule formulas. This background can usually be easily removed by a step function, assuming a constant density of s orbital states [19, 21, 22].
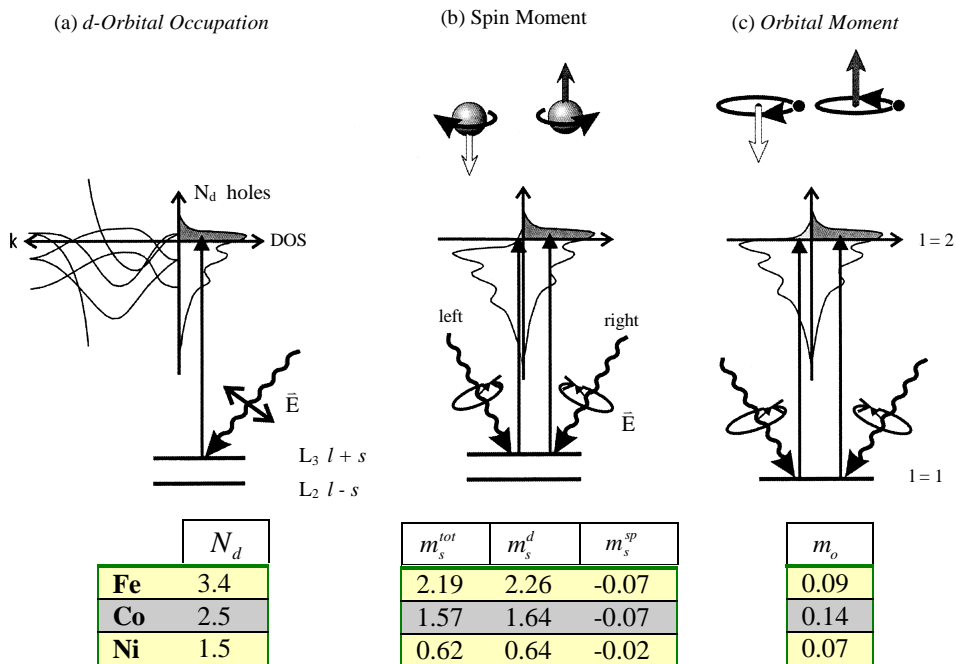
The sum rules have been tested by band structure calculations [23, 24] and have been experimentally verified for bulk iron and cobalt samples [21]. It should be noted that while orbital momentum is directly linked to the dichroism intensity, the determination of the spin momentum requires an additional factor, the magnetic dipole term $\langle T_z \rangle$. First principle theoretical calculations performed by Wu et al. [23, 24] showed that the magnetic dipole term $\langle T_z \rangle$ is very weak for bulk samples with cubic symmetry and can therefore be omitted to simplify the evaluation. In the case of bulk bcc iron and hcp cobalt, ratios of $\langle T_z \rangle / \langle S_z \rangle$ are found of -0.38% and -0.26% [21], respectively, and can be therefore neglected in the evaluation of the sum rules. However, in ultrathin films and surfaces, the approximation of cubic symmetry is not longer valid and the magnetic dipole term $\langle T_z \rangle$ becomes sizeable. Neglecting of $\langle T_z \rangle$ can result in errors of up to 50% as demonstrated at a nickel (001) surface [24, 41] and lead to misinterpretation. Stöhr et al. [25] suggested a modification of the sum rules presented above to overcome this restriction and allow the determination of the spin and magnetic dipole contributions to the spin sum rule separately. They proposed to measure an angular average of MCD intensities in an external magnetic field, orientated along the Cartesian axis. The magnetic field has to be sufficiently strong to saturate the sample along all directions. This angle averaging spin rule basically enables one also to study anisotropic magnetic properties of ultra thin films and interfaces.

## 3d transition metals

In this work the interest is focussed on 3d transition metals, which represent one of the most scientifically and technologically important groups for magnetism. The magnetic properties of 3d transition metals are primarily determined by their d valence electrons. Figure 2.5 shows the d occupation number and the spin and orbital moments for the 3d transition metals iron, cobalt and nickel. The tabulated values were calculated by Eriksson and Söderlind et al. using the linear muffin-tin orbitals (LMTO) technique [28, 29]. From iron to cobalt the Fermi level $E_F$ moves towards the top of the d band, resulting in a decreasing number of d-holes, $N_{3d}$. Figure 2.5 (b) shows the splitting of the spin-up and spin-down subbands due to the exchange interaction. In a simple model, e.g. the Stoner model for ferromagnetism, the spin magnetic moment $m_s$ can be simply assumed as the difference between the number of spin-up and spin-down electrons in Bohr magnetons $\mu_B$ :

$$m_s = (N^\uparrow - N^\downarrow)\mu_B . \tag{2.33}$$

The values in table (b) show that the spin momentum originates almost completely from the d shells, while the combined 4s and 4p shell contribution is less than 5% [26, 27].



| | $N_d$ |
|---|---|
| **Fe** | 3.4 |
| **Co** | 2.5 |
| **Ni** | 1.5 |

| | $m_s^{tot}$ | $m_s^d$ | $m_s^{sp}$ |
|---|---|---|---|
| | 2.19 | 2.26 | -0.07 |
| | 1.57 | 1.64 | -0.07 |
| | 0.62 | 0.64 | -0.02 |

| | $m_o$ |
|---|---|
| | 0.09 |
| | 0.14 |
| | 0.07 |

**Figure 2.5** *Origin of the d-shell occupation (a), spin moment (b), and orbital moment (c) in a ferromagnetic transition metal. The tabulated values for iron, cobalt and nickel are from calculation of Eriksson et al. and Söderlind et al. [28, 29], figure partly from [26. 27].*

The orbital moment arises from the difference in the number of holes with $m_l = +1, +2$ and $m_l = -1, -2$ , and its value is proportional to the size of the spin-orbit interaction. In the 3d transition metals the spin-orbit interaction is only on the order of a few meV and therefore very much smaller than the exchange interaction, which is typically in the range of eV. Thus, the orbital moment is significantly smaller than the spin moment as also seen in the table (c) for the individual values of the orbital magnetic moment for iron, cobalt and nickel.

The 3d states, mainly responsible for the magnetic moment in the 3d transition metals, are best probed in x-ray absorption experiment by exciting a 2p electron into the unoccupied 3d bands above the Fermi level. This $2p \rightarrow 3d$ transition leading to the $L_2$ and $L_3$ edges in the absorption spectra requires for the 3d transition metals an energy of several hundred eV, which is on the hard end of the soft x-ray region. Due to the spin-orbit splitting and large exchange splitting of the d bands, significant effects in the order of a few (nickel) to several tens of percent (cobalt, iron) are observable in the magnetic asymmetry ratio in the MCD and magnetic scattering spectra [20, 30-32]. Furthermore, as already discussed earlier, due to the large signal, the magnetic sum rules can be easily applied at the $L_{2,3}$ transitions of 3d transition metals to separate the small orbital and larger spin magnetic moment, which render these transition ideal for testing the validity of the sum rules [20].

However, the first MCD experiment was carried out at the K-edge of iron [8] in the hard x-ray region (7112 eV). Here in the dipole approximation, the excited photoelectron undergoes a transition from the 1s ground state to the 4p conduction bands, while a quadrupole transition from $1s \rightarrow 3d$ is expected to be about two orders of magnitudes smaller with respect to the dipole part [33]. Therefore the dichroic spectrum is mainly proportional to the p-projected spin polarized density of empty states above the Fermi energy, which contributes less than 5% to the total magnetic moment of the 3d transition metal site (see figure 2.5). Since the initial 1s level is not split, the photoelectron polarization $P_e$ mainly arises from the weak spin-orbit coupling in the final p-states and thus leads to small dichroic signals on the order of the size of $P_e$. For iron the upper limit for $P_e$ was estimated to 0.8% [16, 34] and therefore the expected dichroic signal $\mu_c/\mu_0$ is even smaller. Calculations using the simple atomic model illustrated in this chapter reproduce most of the important features observed in the dichroic spectrum, but in order to get quantitative information fully relativistic spin polarized calculations have to be applied [33]. For all K-edge transitions of 3d transition metals, which take place in the hard x-ray region

(7112 eV, 7709 eV and 8333 eV for the iron, cobalt and nickel K-edges), the effect is about two orders of magnitude smaller than observed at the $L_{2,3}$ absorption edge due to above discussed missing spin-orbit splitting of the core level and the small spin polarization of the excited 4p final state. Nevertheless, the MCD effect in the hard x-ray regime could be observed for all three important 3d transition metals, iron, cobalt and nickel, and are widely used to examine the magnetic properties of all kinds of different magnetic systems, like multilayers or alloys containing 3d transition metals in both x-ray regions.

# Related effects

MCD is the most used technique in x-ray spectroscopy to examine the magnetic properties of matter. The circular polarization of the x-rays connect the charge and the magnetic contributions and lead to sizeable signals, yielding information about a large variety of magnetic systems. However, next to the MCD signal, other techniques can be used to extract similar and sometimes complementary information, using effects which are related to the MCD effect. Two of them, the magnetic linear dichroism (MLD) and the Faraday effect are discussed below.

## Magnetic Linear Dichroism (MLD)

In the discussion of the MCD effect it was shown how local magnetization states in matter are probed by using circularly polarized x-rays, but also linearly polarized photons can influence the absorption states of magnetic materials. A few remarks should illustrate the possibilities and differences to MCD. The technique of probing magnetic material with linear polarization instead of circularly polarized light is called magnetic linear dichroism (MLD). Analogous to the treatment of the magnetic circular dichroism, the magnetic absorption coefficient which is proportional to the imaginary part of the magnetic scattering amplitude is examined. As already pointed out in the discussion of the MCD effect the second term in (2.7), which is responsible for magnetic sensitivity of MCD, vanishes in the case of linear polarized light due to the zero net polarization $P_c$. Therefore the third term of the forward scattering amplitude in (2.5) has to be taken into account, which exhibits a squared scalar product of magnetization direction and

polarization vector and which was neglected in the discussion about the MCD. Thus, the absorption coefficient for MLD in dipole approximation in the given absorption geometry with $\hat{\epsilon} = \hat{\epsilon}'$ and $\vec{k} = \vec{k}'$ can be written as

$$\boldsymbol{m}_{MLD} \propto \text{Im}\left[(\hat{\boldsymbol{e}} \cdot \hat{\boldsymbol{e}}) F^{(0)} - i (\hat{\boldsymbol{e}} \cdot \hat{z}_n)^2 F^{(2)}\right], \tag{2.34}$$

As in the case for circular polarization the first term is simply one and analogous to (2.32) the absorption coefficient for linearly polarized light in the dipole approximation can be written as

$$\mu_{MLD} = \mu_0 + (\hat{\epsilon} \cdot \hat{z}_n)^2 \Delta\mu_l, \tag{2.35}$$

where $\mu_0$ is the magnetization independent term and $\Delta\mu_l$ the MLD-dependent part. By using the geometry pictured in figure 2.6 the whole equation can be expressed with the angles $\varphi$ and $\gamma$ for the projection from $\hat{z}_n$ to $\hat{\epsilon}$:

$$\mu_{MLD} = \mu_0 + \Delta\mu_l \sin^2\varphi \cos^2\gamma. \tag{2.36}$$

In order to experimentally prove the magnetic origin of a MLD-signal the projection of the linear polarization of the incident x-rays to the spin orientations in the sample has to be rotated without turning the sample. In general this can be realized by applying perpendicular magnetization directions to the sample, which is often difficult because of magneto-crystalline anisotropy, or by changing between the σ and π polarization of the incident x-rays, which is on the other hand
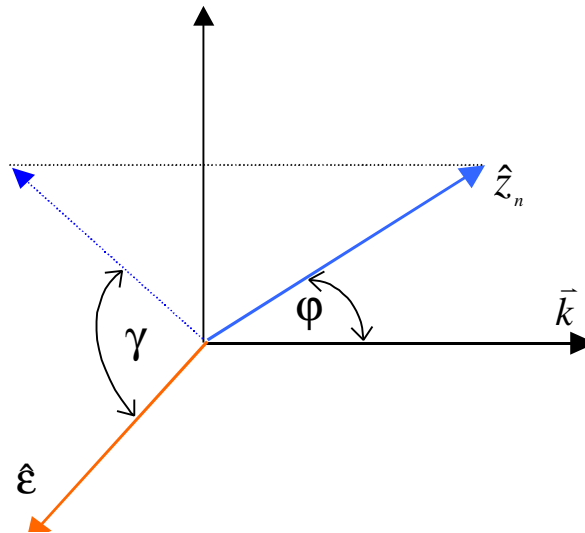


**Figure 2.6** *coordinate system defining the angle between the polarization vector* $\hat{\epsilon}$ *and wave propagation vector* $\vec{k}$

technically difficult. Contrary to the MCD effect, which is linear in the local magnetic moment, MLD probes the square of the magnetic moment of the ions. Therefore, while MCD shows in general huge effects on ferromagnetic samples, but is cancelled out for antiferromagnetic contributions due the vanishing net magnetization, MLD probes ferromagnetic and antiferromagnetic contributions equally. Strong magnetic linear dichroism has been predicted at the M-absorption edges in magnetic rare earth materials [35] and later at the $L_{2,3}$ edges of 3d transition metals [36], which was verified by van der Laan et al. measuring the terbium $M_{4,5}$ edges in terbium iron garnet [37] and by Kuiper et al. applying MLD at the Fe $L_{2,3}$ edge of antiferromagnetic $Fe_2O_3$ (hematite) [38]. In recent years, MLD studies were also connected with other techniques. For example, MLD can be combined with photoelectron emission microscopy (PEEM), which opens up the possibility of imaging the antiferromagnetic domain structure of a surface or interface [39, 40], similar to MCD-PEEM spectroscopy of ferromagnets [41]. As an example, Stoehr et al. could resolve a clear antiferromagnetic contrast at a NiO (100) thin film grown on a MgO (100) substrate and permitted the analysis of the different temperature dependence of defect regions [39]. Combining both MCD and MLD with PEEM allows the study of samples with both ferromagnetic and antiferromagnetic components separately and understand their interference, which is of technological and scientific interest presently.

Nevertheless, it should be noted that most studies of magnetic dichroism are done with circularly polarized light due to high interest in samples with ferromagnetic net magnetization, which in general exhibit much larger MCD than MLD effects.

## Faraday effect

A completely different approach for analyzing the magnetic responses of magnetic dichroic systems can be taken by exposing it with plane polarized photons. A plane wave can be thought of a superposition of two - left and right, respectively - circularly polarized waves with equal magnitude. A magnetized sample exhibiting dichroism absorbs one component of the circularly polarized waves more than the other and the final beam becomes slightly elliptically polarized (with a net circular polarization $P_c$), and the plane of linear polarization is rotated by an angle $\phi$. The latter effect is also known as the Faraday effect or Faraday rotation and was extended by Siddons et al. to x-rays [42]. The index of refraction N is defined as

$$N = 1 - \delta + i\beta, \tag{2.37}$$

where $\delta$ and $\beta$ are the dispersive and absorptive correction terms, respectively. Both are slightly altered by small amounts $\Delta\delta$ and $\Delta\beta$ for magnetic materials depending on whether right ($\uparrow$) or left ($\downarrow$) circularly polarized photons are used and lead to a modified index of refraction of

$$N_{\uparrow(\downarrow)} = 1 - (\delta \pm \Delta\delta) + i(\beta \pm \Delta\beta). \tag{2.38}$$

Assuming a superposition of left and right circularly polarized waves with equal magnitudes by taking into account the modified index of refraction in (2.37) leads to the following relationships for the degree of circular polarization $P_2$ and the Faraday rotation $\phi$, respectively [16]:

$$P_2 \propto -k\,d\,\Delta\beta \tag{2.39}$$

and

$$\phi \propto 2k\,d\,\Delta\delta, \tag{2.40}$$

where k is the absolute value of the wave propagation vector $\bar{k}$ and d the thickness of the magnetized sample. It is important to notice that the dispersive correction $\Delta\delta$ is directly related to the real part of the scattering amplitude. Therefore, while MCD in absorption measurements probes the imaginary part of the scattering amplitude, the Faraday effect allows the direct measurement of the real part. On the other hand due to the connection of real and imaginary part of the scattering amplitude via the Kramers-Kronig relation, only one of them has to be measured, Faraday effect or MCD absorption, respectively, and the other can be calculated. Kortright et al. measured the Faraday rotation of linear polarized soft x-rays across the Fe $L_{2,3}$ edges from a magnetized Fe/Cr multilayer [43]. Comparison with MCD data taken on the same sample showed very good agreement with the Kramers-Kronig analysis of the measurement and proved that close connection between both techniques.

## 2.3 Scattering geometry for magnetic reflectivity

In the previous section the concept of magnetic dichroism was illustrated to show how the magnetic sensitivity of x-rays can be significantly enhanced by tuning the x-ray energy to an absorption edge of a magnetic site. MCD, MLD and the Faraday effect were described in absorption geometry, in which the x-rays penetrate the sample and the absorbed intensity or polarization rotation yields information about the electronic and magnetic properties of the particular magnetic site.

In order to investigate magnetic structure on the atomic scale with x-rays, not only the magnetic sensitivity of the photons is needed but also a technique which is able to detect spatial changes of the magnetization. Gibbs et al. showed in their work on holmium how the technique of resonant x-ray scattering with linearly polarized x-rays can be used to probe the magnetic satellites of Bragg peaks of the atomic structure. A fifty-fold enhancement of the magnetic signal was observed by tuning the incident photon energy near the $L_3$-edge of holmium [11, 44]. Below $T_N = 132K$ magnetic moments develop in the basal plane of the hexagonal crystal structure of holmium, and the magnetic structure can be approximately seen as a spiral arrangement along the c-axis of the structure with the moments ferromagnetically aligned in the basal planes. The magnetic satellite reflections are located at $\pm\ \tau$ around every Bragg reflection and parallel to the c-direction, where $\tau$ is related to the pitch size of the helix structure. Polarization analysis showed that both dipole (2p $\rightarrow$ 5d) and quadrupole (2p$\rightarrow$ 4f) transitions contribute to the satellite intensities. Not much later, Isaacs et al. [45] discovered an even bigger effect at the (0,0,5/2) magnetic Bragg peak in antiferromagnetic UAs, an actinide compound, at the M-edges, where the dipole transition excites the core electron directly to the unpaired 5f electron states. At the $M_4$ edge the magnetic Bragg peak was enhanced by six orders of magnitude. These pioneering experiments were followed by studies of various magnetic material by probing magnetic satellites near Bragg reflections to gain insight to the magnetic structures. The research was focussed on rare earth and actinides materials with antiferromagnetic order due to the large magnetic enhancements at the L- and M-edges of these materials. Moreover the antiferromagnetic order separated the magnetic reflection from the charge Bragg peak and made the detection easier. Ferromagnetic materials on the other hand were still hard to explore with this technique due to the superposition of the weak magnetic

signal and the very strong charge signal. Furthermore, in order to detect Bragg reflections usually large momentum transfers are required, which can only be achieved by using hard x-rays. For 3d transition metals, which represent one of the important groups of ferromagnetic materials, only the very weak enhancement at the K-edges could be used.

This work focusses on thin film and multilayer systems containing layers of 3d transition metals. These systems consist of artificially layered structures, where the thickness of each layer is on the order of a few to tens of nanometers. 3d transition metals possess ferromagnetic properties and, as pointed out in the previous section, ferromagnetism is best probed with circularly polarized x-rays. A technique to examine these artificial thin films and multilayer systems is conventional x-ray reflectivity at low angles. Here, the reflected intensity is measured as a function of the incident angle which is equal to the exit angle in the specular condition.

The intensity variation and features in the reflectivity pattern yield information about the layer thickness, density variations and interface quality. For hard x-rays, the dimensions of the artificial layered structures are probed at angles significantly smaller than 10°. That makes it possible to take advantage also from soft x-ray resonances, where the wavelength, and therefore the angular region probing the same reciprocal space, is usually increased by one order of magnitude and allows one to cover at least the first part of the reflectivity curve seen in the hard x-ray regime.

 Combining MCD and conventional specular x-ray reflectivity enables one in principle to observe the magnetic depth profile of thin films and multilayer systems. Instead of unpolarized or linearly polarized x-rays, circularly polarized x-rays are used to record the magnetic and charge reflectivity spectra. By switching the helicity of the incident photons while keeping the magnetization at the sample constant, the intensity with the magnetization parallel and antiparallel to the photon spin are measured. If a net ferromagnetic magnetization exists, the two intensities differ, and the difference can be related to the magnetic reflectivity, while the sum represents the charge scattering. It is important to mention that in general also the magnetization of the sample can be reversed instead of flipping the helicity of the x-ray beam to measure the same result. Both methods are in principle equivalent.

In addition to the features in the reflectivity curve originating from the structural composition of the system, the resonant magnetic scattering amplitude exhibits also additional angular dependence due to the polarization cross terms as can be seen in (2.7). Hill and McMorrow

reformulate the dipole operator in (2.7) by choosing polarization states as a basis, which are either parallel ($\pi$) or perpendicular ($\sigma$) to the scattering plane [14]. The scattering geometry of specular reflectivity with the polarization dependent vectors are illustrated in figure 2.7. Writing the dipole operator in form of a 2 x 2 matrix with $\sigma \rightarrow \sigma'$ channel in the top left, $\pi \rightarrow \pi'$ in the bottom right and the mixed polarization states $\sigma \rightarrow \pi'$ and $\pi \rightarrow \sigma'$ in the top right and bottom left position, respectively, leads to the following matrix presentation of the resonant dipole scattering amplitude:

$$
\begin{aligned}
f_{nE1}^{XRES} = F^{(0)} & \begin{pmatrix} 1 & 0 \\ 0 & \cos 2q \end{pmatrix} - i F^{(1)} \begin{pmatrix} 0 & z_1 \cos q + z_3 \sin q \\ z_3 \sin q - z_1 \cos q & -z_2 \sin 2q \end{pmatrix} \\
& + F^{(2)} \begin{pmatrix} z_2^2 & -z_2(z_1 \sin q - z_3 \cos q) \\ z_2(z_1 \sin q + z_3 \cos q) & -\cos^2 q\,(z_1^2 \tan^2 q + z_3^2) \end{pmatrix},
\end{aligned}
\tag{2.41}
$$

where $\theta$ is the incident and scattered angle and $z_i$ the components of the magnetic moment along the unit axis $\hat{u}_i$ seen in figure 2.7 with $i = 1, 2, 3$.
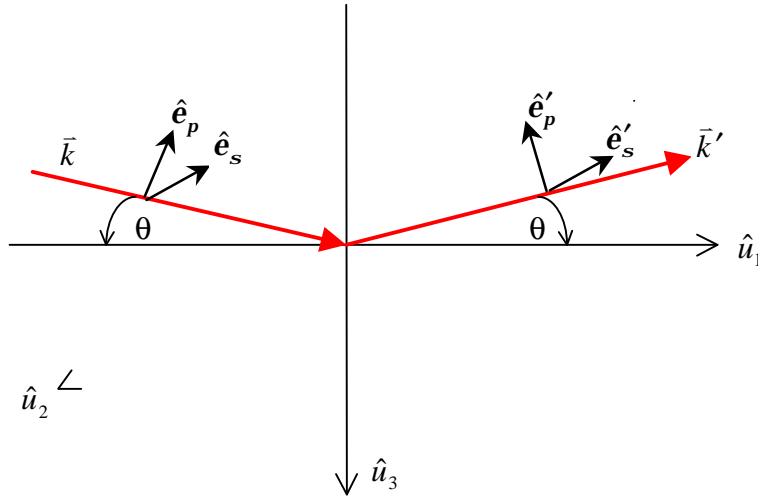


**Figure 2.7** *Coordination system of reflectivity geometry with indicated polarization dependencies with scattering angle $q$.*

Equation (2.41) can now be used to examine the angular dependence of the magnetic scattering amplitude of a single magnetic ion in specular reflectivity. In order to exploit the MCD effect in the calculations the $\pi$ and $\sigma$ components have to be connected with a 90° phase relation to take the circular polarization of the photons into account. The magnetic signal is expressed as the difference between the intensities of left and right circularly polarized light scattered by a single magnetic ion, where the magnetic intensity is the complex product of the corresponding magnetic scattering amplitude

$$I_{E1}^{XRES} \propto f_{E1}^{XRES^*} \cdot f_{E1}^{XRES}. \tag{2.42}$$

Using the base $(e_s, e_p)$, the polarization vector for right ($\uparrow$) and left ($\downarrow$) circularly polarized light can be expressed as

$$e_\uparrow = \begin{pmatrix} 1 \\ -i \end{pmatrix} e^{iwt} \tag{2.43a}$$

and

$$\varepsilon_\downarrow = \begin{pmatrix} 1 \\ i \end{pmatrix} e^{i\omega t}, \tag{2.43b}$$

respectively, where $\omega$ is the frequency of the light. Now the difference between the intensities for right and left circularly polarized light scattered from a single magnetic ion can be calculated, magnetized in the (1,0,0), (0,1,0) and (0,0,1) direction, respectively, leading to the following expressions, where the magnetic contributions are separated for the different mixtures of the resonance terms $F^{(0)}$, $F^{(1)}$ and $F^{(2)}$:

$$\Delta I_{E1}^{XRES}(\hat{z}_n = (1,0,0)) \propto F^{(0)}F^{(1)^*}(3\cos\theta + \cos 3\theta) + F^{(1)}F^{(2)^*}(-0.5\cos\theta + 0.5\cos 3\theta) \tag{2.44a}$$

$$\Delta I_{E1}^{XRES}(\hat{z}_n = (0,1,0)) \propto 0 \tag{2.44b}$$

$$\Delta I_{E1}^{XRES}(\hat{z} = (0,0,1)) \propto F^{(0)}F^{(1)^*}(3\sin\theta + \sin 3\theta) + F^{(1)}F^{(2)^*}(-0.5\sin\theta + 0.5\sin 3\theta) \tag{2.44c}$$

In Figure 2.8 the angular dependence for the different terms in (2.44a) and (2.44c) is plotted and it can be clearly seen that for low angles the magnetic sensitivity is maximized by magnetizing the sample in the (1,0,0) direction, while the sensitivity for magnetic moments perpendicular to the sample surface becomes important for higher angles. It should be also noted that the specular magnetic reflectivity is not sensitive at all to magnetic moments pointing perpendicular to the scattering plane ( (0,1,0)-direction) if circularly polarized light is used.
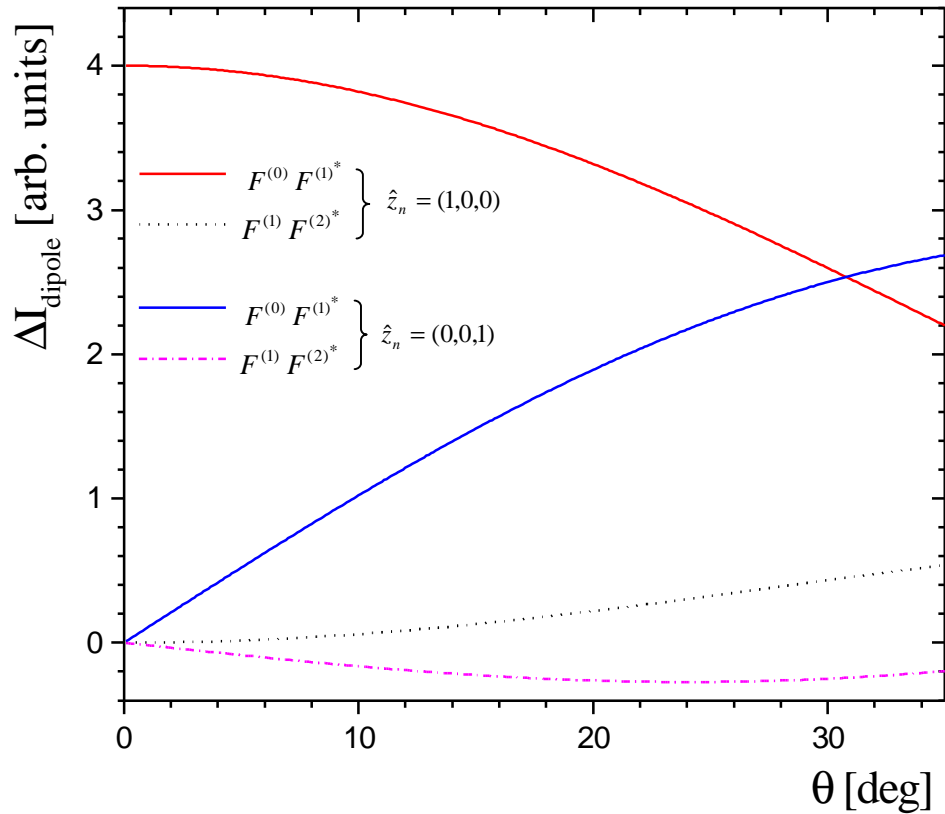


**Figure 2.8** *Difference signal of incident left and right circularly polarized intensities, scattering by a magnetic ion with magnetic moment in (1,0,0) and (0,0,1) direction. Full line and dashed line show contributions from different resonance terms.*

# 3. Simulation of Charge and Magnetic X-ray Reflectivity

Charge x-ray reflectivity is a well-established method that has been used for years to provide structural information for both condensed and soft matter samples on a microscopic scale. The reflectivity exhibits plenty of information in the oscillation or decline of the reflectivity curve. In order to receive a more quantitative analysis and accurate structural information, calculations are necessary, which can model the reflectivity curve in a precise way. This has already been done for a long time [47, 48], but with the development of computers it became more and more practicable to fit the measured reflectivity curves with the calculated curves, varying the parameters implemented in a model until the best simulation is found. Until now it is the best and most accurate way to find the structural compositions of thin film system and is used widely, e.g. where structural information on a microscopic length scale is needed without damaging the system.

This chapter describes the calculations of x-ray reflectivity curves of thin films and multilayers. X-ray reflectivity is considered here as a method for looking at structures on a scale from a few to hundreds of nanometers, which is the range of the typical thicknesses of layers in artificial systems. This kind of reflectivity is commonly known as the specular *small angle x-ray reflectivity* which originally stems from reflectivity measurements in the hard x-ray region. Here, the upper end of the length scale is only probed with grazing incident angles and has to be distinguished from the commonly used x-ray reflectivity at high angles looking at Bragg peaks and inter-atomic distances and interactions. The specular condition means that incident and reflected angle are the same and therefore the momentum transfer in the sample has only a z component $Q_z$, and therefore only density changes along the surface normal are probed (here the z-direction) and lateral fluctuations (e.g. rough interfaces) are averaged.

First the standard calculations for charge reflectivity with hard x-rays will be described, which is used for the determination of the charge density profile of all the samples examined in this work. It should be remembered that detailed information about the charge density is essential for the evaluation of the magnetic reflectivity since the magnetic signal is determined mainly

through the interference term between the charge and magnetic scattering amplitudes. Unfortunately the standard approach for the charge reflectivity uses simplifying approximations for the polarization, which make it very difficult to include the magnetic spin structure in the assumed models. Here another approach was chosen, the so called *magnetic optical approach*, which is described next. It also has its starting point from Maxwell equations, but its calculations also take into account the polarization of the photon beam and the magnetic spin configurations of the sample. In the following is a series of simulations on a simple test system which illustrate the basic features of possible charge and magnetic reflectivity curves by varying the magnetic parameters of the sample. The approach used has no restrictions as the wavelength of the light used as long as the optical constants are known. Some comments are made for the transition form hard x-rays to the soft x-ray region. The chapter is closed with a short summary and some further comments.

# 3.1 Charge Reflectivity in the hard x-ray region

The simulation of the charge reflectivity in the hard x-ray region is a very precise method to characterize the structural properties of thin films and multilayer systems on a nanometer scale. The basic formulas necessary to calculate the charge reflectivity will be outlined below. It should be referred to a wide variety of books and publications, where more exact and more detailed representation can be found, especially the originally work [49-51] as well as some very well written review articles [52-55].

Using the Fresnel formulas in the limit of very small incident angles and considering the index of refraction N is very close to 1, the following reflection and transmission coefficients, r and t, respectively, are found:

$$r = \frac{k_1 - k_0}{k_0 + k_1}, \qquad t = \frac{2k_0}{k_0 + k_1} = 1 + r \qquad (3.1)$$

with

$$k_j = \frac{2\boldsymbol{p}}{\boldsymbol{l}}\sin\boldsymbol{q}_j \quad with \quad \boldsymbol{q}_j = 2\boldsymbol{p}\sqrt{N_j^{\,2} - 1 + \sin\boldsymbol{q}} \qquad (3.2)$$

where $k_j$ is the wave vector in the medium and $\theta$ the incident angle, as shown in figure 3.1 at an interface. As already mentioned in chapter 2, the index of refraction N for x-rays in the hard x-ray region is slightly smaller than one and the difference can be split into a real and imaginary part, $\delta$ and $\beta$, respectively:

$$N = 1 - \delta + i\beta, \tag{3.3}$$

with

$$\boldsymbol{d} = \frac{N_a}{2\boldsymbol{p}} r_0 \boldsymbol{l}^2 \sum_j \frac{\boldsymbol{r}_j}{A_j} (Z_j + f_1^j) \tag{3.4}$$

and

$$\boldsymbol{b} = \frac{N_a}{2\boldsymbol{p}} r_0 \boldsymbol{l}^2 \sum_j \frac{\boldsymbol{r}_j}{A_j} (f_2^j) \tag{3.5}$$

where $\delta$ is the dispersive and $\beta$ the absorptive correction of the index of the refraction, which are typically of the order of $10^{-5}$ in the hard x-ray regime. $N_a$ is Avogadro's number, $r_0$ the classical electron radius, $\rho_j$ and $A_j$ the density and atomic weight of the $j^{th}$ element, respectively, $\lambda$ the wavelength of the x-rays and $f_1^j$ and $f_2^j$ the dispersive and absorptive correction factors of the $j^{th}$ element, respectively.
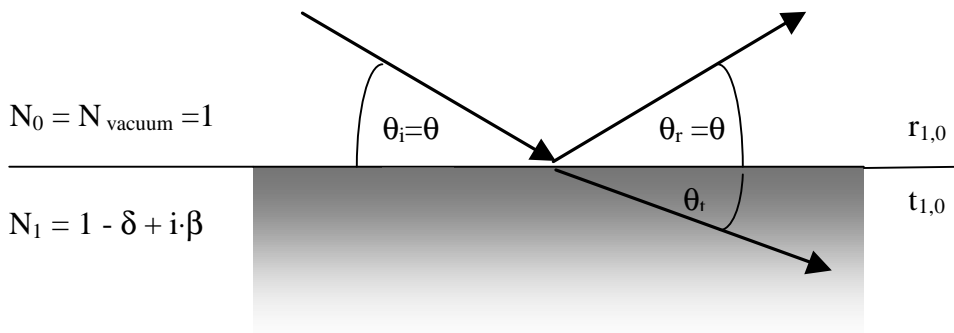


**Figure 3.1** *Reflection at a single interface. The beam in vacuum ($N_0 = 1$) enters the medium ($N_1$). One part gets reflected at the same angle $\boldsymbol{Q}$ (specular condition) with the reflection coefficient $r_{1,0}$ and the other part transmitted at the angle $\boldsymbol{Q}_t$ with the transmission coefficient $t_{1,0}$.*

In the case of two interfaces, e.g. a thin film of the thickness d on a substrate, all even multiple reflected waves at both interfaces have to be summed up (Airy-summation), which leads to the following term for the reflectivity [48]:

$$R_{2,0} = \frac{r_{2,1} + e^{-2ik_1 d}\, r_{1,0}}{1 + r_{2,1}\, e^{-2ik_1 d}\, r_{1,0}}$$
(3.6)

This procedure can be now generalized for systems with arbitrary number of interfaces:

$$R_{j+1,0} = \frac{r_{j+1,j} + e^{-2ik_j d}\, r_{j,0}}{1 + r_{j+1,j}\, e^{-2ik_j d}\, r_{j,0}}; \quad R_{1,0} := r_{1,0}$$
(3.7)

The whole iterative summation, called the Paratt-algorithm, starts from the substrate and works its way up to the top layer and enables to calculate the reflection coefficient for thin films and multilayer systems. The resulting intensity I, which is the actual measured quantity in the reflectivity experiment, is the complex product of the resulting reflection coefficient:

$$I = \left| R_{j+1,0} \right|^2.$$
(3.8)

It is important to note that by measuring I all the phase information gets lost, the so called phase problem. This leads to the problem that the back transformation of the reflectivity curve is not clearly defined. In order to solve the structure generally it is started from the other side, assuming a model and trying to fit this model to the experimental measured reflectivity curve by calculating the reflectivity curve via (3.7) and (3.8) for the whole angular range available in the experimental data. The parameters are changed until the best fit to the experimental curve is achieved.

Up to this point the calculated reflectivity curve considers only perfect, smooth interfaces. In reality even the smoothest interface exhibits roughness on the atomic scale which affects the reflectivity curve by damping the observed features and by a faster decay of the intensity with increasing angle of incidence. Vidal and Vincent have examined the effects of roughness

assuming a smeared out interface profile with a Gaussian distribution [56], which leads to the following modification for the transmission and reflection coefficients, r′ and t′, respectively:

$$r'_{j,j+1} = r_{j,j+1} \; e^{-2 k_j k_{j+1} \sigma^2} \; , \qquad t'_{j,j+1} = t_{j,j+1} \; e^{\frac{1}{2} (k_{j+1} - k_j)^2 \sigma^2} \qquad (3.9)$$

With (3.9) equation (3.7) can be generalized to

$$R'_{j+1,0} = \frac{r'_{j+1,j} + e^{-2ik_j d} \; R'_{j,0} (t'_{j+1,j} \, t'_{j-1,j} - r'_{j+1,j} \, r'_{j-1,j})}{1 + r'_{j+1,j} \; e^{-2ik_j d} \; r'_{j,0}} \qquad (3.10)$$

It should be noted that expressions for the *rough* reflection and transmission coefficient have been derived in a different way by other groups [57, 58], but lead to basically the same result as it is given by (3.9). A more detailed discussion can be found in [59].

For the evaluation of reflectivity experiments the penetration depth of the incident x-rays plays an important role. The penetration depth depends also on the reflection angle as well as on the wavelength of the incident light. In order to identify the extracted information from reflectivity profiles, it is therefore important to consider the penetration depth of the x-rays in the reflectivity geometry. This can be calculated by [60]

$$\Lambda = \frac{\lambda}{\sqrt{2\pi}} \left[ \sqrt{(\theta^2 - \theta_c^2)^2 + 4\beta^2} - (\theta^2 - \theta_c^2) \right]^{-\frac{1}{2}} , \qquad (3.11)$$

where $\theta_c \approx \sqrt{2\delta}$ is the so called critical angle for total reflection. Due the fact that the index of refraction N is in many cases, especially in the hard x-ray region, slightly less than one there is a region at low angles where the incident x-rays are totally reflected. Figure 3.2 shows the penetration depth for two different energies E = 700 eV in the soft x-rays and E = 7000 eV in the hard x-ray regime plotted as a function of the momentum transfer $Q_z$, where $Q_z$ is given by

$$Q_z = \frac{4\pi}{\lambda} \sin \theta . \qquad (3.12)$$

It can clearly be seen how the choice of the wavelength influences the penetration depth. For the same $Q_z$-value hard x-rays penetrate much further into the sample than the soft x-rays due to the much stronger absorption of the longer wavelength.
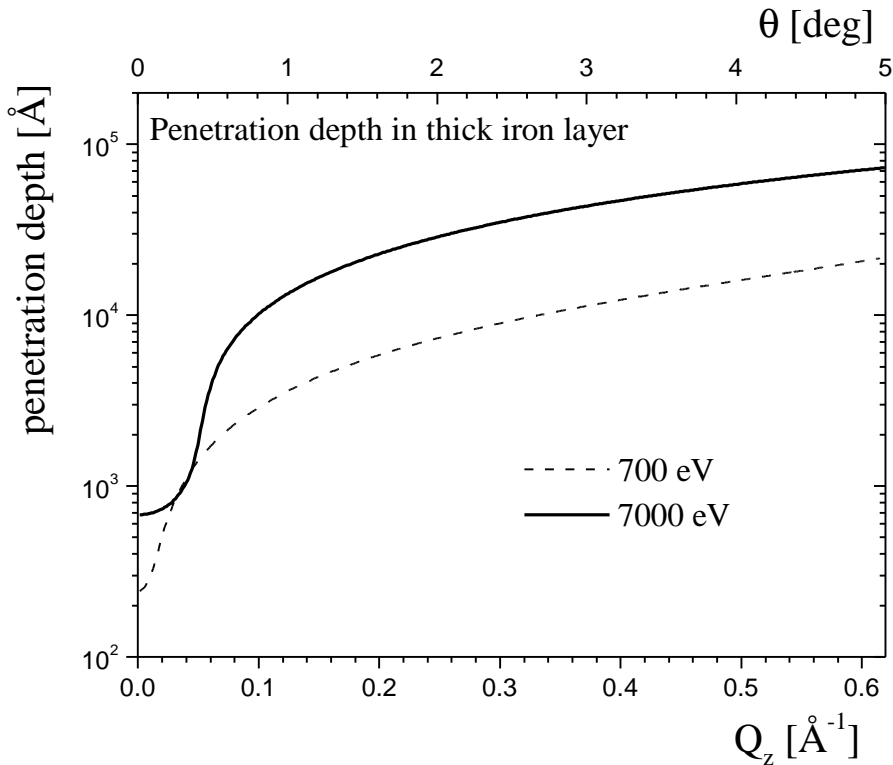


**Figure 3.2** *Penetration depth in bulk iron calculated for two different photon energies in the soft and hard x-ray region calculated with equation (3.11) along $Q_z$. Upper x-scale shows the angular region for E = 7000 eV. The soft x-ray region scales by a factor of about 10 (see equation (3.12)).*

With (3.1-3.5), (3.9) and (3.10) we have the tools to calculate reflectivity curves in the hard x-ray region (at small angles). The parameters besides the sample structure are the index of refraction N for the elements used, the wavelength $\lambda$ and for each layer a specific thickness d and roughness $\sigma$. As mentioned before, the determination of the charge density profile plays an important role in the evaluation of the magnetic reflectivity data.

# 3.2 Magnetic reflectivity calculations

The calculation of the charge reflectivity discussed in the previous paragraph neglects the polarization dependence of the scattering process, which is justified for small angles and of the very large cross section of the charge contribution. In the case of magnetic scattering these assumptions are no longer valid, e.g. the magnetic cross section is usually weak compared to the charge cross section and the change in polarization plays a crucial part in determining the magnetic properties. Therefore another approach has to be taken, which will be called the *magneto optical approach* here.

Magneto-optics is already known for more than a century [61, 62] and is widely applied today in various techniques using the so-called magneto-optical Kerr effect. The magneto-optical approach, used to calculate the reflection and transmission coefficient of magnetic and non-magnetic thin films and multilayer systems by taking into account the polarization dependence for σ- and π-polarized photons, was originally developed for angle dependent magneto-optical Kerr effect calculations with lasers [63-65]. It can be extended to the x-ray regime without significant changes.

In the approach used here, first a single boundary between two media is considered to explain the basic idea behind the calculation and to derive the necessary boundary conditions for the problem. Then the magnetic quantity will be introduced and the necessary formulas derived to solve a single interface. In the next step this calculation will be extended to multilayer systems.

## 3.2.1 Single interface between two media

Starting from Maxwells equations simple calculations show that the tangential components of the electric ($E_x$ , $E_y$) and magnetic fields ($H_x$ , $H_y$) are conserved [47]. In other words we can create a boundary-field vector $\vec{F}$ with the following relations:

$$\vec{F} = \begin{pmatrix} E_x \\ E_y \\ H_x \\ H_y \end{pmatrix} \qquad (3.13) \qquad \text{and} \qquad \vec{F}_1 = \vec{F}_2, \qquad (3.14)$$

where the indices 1 and 2 indicate two different media. The boundary-field vector $\vec{F}$ remains unchanged for light travelling from media 1 to media 2. Experimentally it is more common to describe the state of the light in a system with a basis of $\sigma$ and $\pi$ polarization photon states, the so called magneto-optical coefficient $E_\sigma$ and $E_\pi$. These magneto-optical coefficients form another vector :

$$\vec{P} = \begin{pmatrix} E_\sigma^{(i)} \\ E_\pi^{(i)} \\ E_\sigma^{(r)} \\ E_\pi^{(r)} \end{pmatrix} \qquad (3.15)$$

the suffixes (i) and (r) indicate the incident and reflected beams. In order to solve the boundary condition the connection between $\vec{F}$ and $\vec{P}$ has to be found and is called the medium boundary matrix A:

$$\vec{F} = A \vec{P} \qquad (3.16)$$

which leads in the case of a single boundary to the following relation:

$$A_1 \vec{P}_1 = A_2 \vec{P}_2 \qquad (3.17)$$

The goal now is to find the medium boundary matrix A. Once this is determined a simple vector equation is left which can be solved. Before proceeding with the determination of the medium boundary matrix A, other considerations should to be taken into account.

In a magnetic medium four different rays have to be considered. The incident $\vec{E}^{(i)}$ and reflected $\vec{E}^{(r)}$ each consist of two rays (see figure 3.3a) due to the difference in the index of refraction for each path in a magnetic medium, which can be written as:

$$n = N(1 \pm \tfrac{1}{2} Q g), \tag{3.18}$$

where $g = \cos(\vec{k}, \vec{M})$ is the cosine between the propagation vector $\vec{k}$ and the magnetization $\vec{M}$ of the medium, N the index of refraction and Q the magnetic optical constant. The components of each ray satisfy the Fresnel equation and are therefore interrelated dependent, e.g. $E_y^{(j)}$ and $E_z^{(j)}$ can be represented as a function of $E_x^{(j)}$. This relationship can best be expressed by using the D-vector in the magnetic material:

$$D_j = \sum_{j'} \varepsilon_{jj'} \cdot E_{j'} \tag{3.19}$$

where $\varepsilon_{jj'}$ is the dielectric tensor. This tensor can be derived for an arbitrary configuration of the magnetization. Choosing the configuration depicted in figure 3.3b, the components of the magnetization vector are given by the following expressions:

$$M_x = M \cos\gamma \sin\varphi \tag{3.20a}$$

$$M_y = M \sin\gamma \sin\varphi \tag{3.20b}$$

$$M_z = M \cos\varphi \tag{3.20c}$$

and lead, for a general direction of the magnetization, to the following expression of the dielectric tensor $\varepsilon$:

$$\varepsilon_{jj'} = N^2 \begin{pmatrix} 1 & i\cos\varphi\, Q & -i\sin\gamma\sin\varphi\ Q \\ -i\cos\varphi\, Q & 1 & i\cos\gamma\sin\varphi\, Q \\ i\sin\gamma\sin\varphi\ Q & -i\cos\gamma\sin\varphi\, Q & 1 \end{pmatrix} \tag{3.21}$$
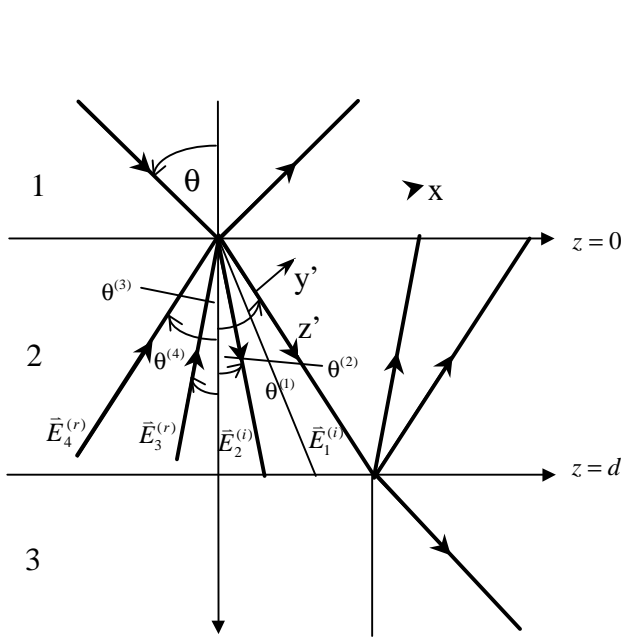
**Figure 3.3a** *The beam enters the magnetic medium and gets reflected and transmitted in four different rays (explanation in text).*
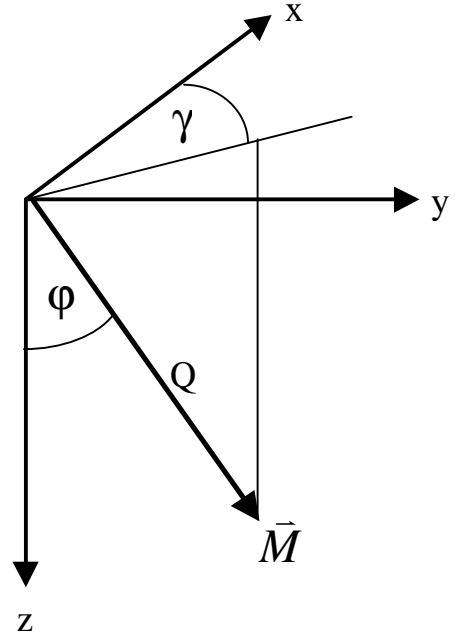
**Figure 3.3b** *Coordinates of the magnetic spin vector, described by magnitude Q and angles* ***j*** *and* ***g***

In order to construct the medium boundary matrix A for a magnetic medium the connection between the components of $E_x^{(j)}, E_y^{(j)}, E_z^{(j)}$ has to be determined. In the local coordinate system x y'z' (see fig. 3.3a), in which z' is the propagation of the D-wave in the medium, the components of the E-vector in an eigenmode are related by the equation [66]:

$$\frac{D_{y'}}{D_x} = \mp i,$$

(3.22)

where $\mp$ is due to the two circularly polarized waves.

Snell's law for the first two media in figure 3.3a gives following expression:

$$N_1 \sin \theta_1 = N_2 \sin \theta = n^{(1,2)} \sin \theta^{(1,2)} = n^{(3,4)} \sin \theta^{(3,4)},$$

(3.23)

where $\theta$ is the angle of incidence to which all other angles can be referred. From (3.21) we can find the following expressions for the direction sines and cosines of the four waves:

$$\alpha_y^{(1,2)} = \alpha_y (1 \mp \tfrac{1}{2} g_i Q),$$
(3.24a)

$$\alpha_y^{(3,4)} = \alpha_y (1 \mp \tfrac{1}{2} g_r Q),$$
(3.24b)

$$\alpha_z^{(1,2)} = \alpha_z (1 \pm \frac{\alpha_y^2}{2\alpha_z^2} g_i Q),$$
(3.24c)

$$\boldsymbol{a}_z^{(3,4)} = \boldsymbol{a}_z (1 \pm \frac{\boldsymbol{a}_y^2}{2\boldsymbol{a}_z^2} g_r Q),$$
(3.24d)

with

$$g_i = \cos\varphi\, \alpha_z + \alpha_y \sin\gamma \sin\varphi,$$
(3.25a)

$$g_r = -\cos\varphi\, \alpha_z + \alpha_y \sin\gamma \sin\varphi,$$
(3.25b)

where $\alpha_y = \sin\theta$ and $\alpha_z = \cos\theta$. By switching from the local coordinate system x y'z' to the more general x y z coordinate system, (3.17) transforms into following equations:

$$\left(\frac{D_y}{D_x}\right)_{1,2} = \mp i\alpha_z^{(1,2)},$$
(3.26a)

$$\left(\frac{D_z}{D_x}\right)_{1,2} = \pm i\alpha_y^{(1,2)},$$
(3.26b)

$$\left(\frac{D_y}{D_x}\right)_{3,4} = \pm i\alpha_z^{(3,4)},$$
(3.26c)

$$\left(\frac{D_z}{D_x}\right)_{3,4} = \pm i\alpha_y^{(3,4)}.$$
(3.26d)

Now everything necessary has been derived to find the relation between the components of the electric field vector $\vec{E}$ in a magnetic medium. (3.21) and (3.24) to (3.26) leads to the following expressions:

$$E_y^{(1,2)} = E_x^{(1,2)}\left(\mp i a_z^{(1,2)} + i a_y^{(1,2)^2}\cos j\ Q - i a_y^{(1,2)} a_z^{(1,2)}\sin g \sin j\ Q \pm a_y^{(1,2)}\cos g \sin j\ Q\right), \quad (3.27a)$$

$$E_y^{(3,4)} = E_x^{(3,4)}\left(\pm i \alpha_z^{(3,4)} + i \alpha_y^{(3,4)^2}\cos\varphi\ Q + i \alpha_y^{(3,4)}\alpha_z^{(3,4)}\sin\gamma\sin\varphi\ Q \pm \alpha_y^{(3,4)}\cos\gamma\sin\varphi\ Q\right) \quad (3.27b)$$

$$E_z^{(1,2)} = E_x^{(1,2)}\left(\pm i \alpha_y^{(1,2)} - i \alpha_z^{(1,2)^2}\sin\gamma\sin\varphi\ Q \pm \alpha_z^{(1,2)}\cos\gamma\sin\varphi\ Q + i \alpha_y^{(1,2)}\alpha_z^{(1,2)}\cos\varphi\ Q\right), \quad (3.27c)$$

$$E_z^{(3,4)} = E_x^{(3,4)}\left(\pm i \alpha_y^{(3,4)} - i \alpha_z^{(3,4)^2}\sin\gamma\sin\varphi\ Q \mp \alpha_z^{(3,4)}\cos\gamma\sin\varphi\ Q - i \alpha_y^{(3,4)}\alpha_z^{(3,4)}\cos\varphi\ Q\right), \quad (3.27d)$$

It can be shown that

$$E_x^{(1,2)} = \tfrac{1}{2}\left(E_s^{(i)} \pm i E_p^{(i)}\right), \qquad (3.28a)$$

$$E_x^{(3,4)} = \tfrac{1}{2}\left(E_s^{(r)} \pm (\pm i)E_p^{(r)}\right), \qquad (3.28b)$$

Additionally, the x, y - components of the magnetic field vector $\vec{H}$ are connected with the y and z components of the electric field vector E through the following relations:

$$H_x^{(j)} = n^{(j)}\alpha_y^{(j)} E_z^{(j)} - n^{(j)}\alpha_z^{(j)} E_y^{(j)}, \qquad (3.29a)$$

$$H_y^{(j)} = n^{(j)}\alpha_z^{(j)} E_x^{(j)} \qquad (3.29b)$$

With (3.27) - (3.29) the connection between $\vec{F}$ and $\vec{P}$ can be straightforwardly found. Doing so, the medium boundary matrix for a magnetic medium with arbitrary magnetization direction finally takes on the following form:

$$
A =
\begin{pmatrix}
1 & 0 \\[4pt]
-\dfrac{i}{2}\,\mathbf{a}_y^2\,Q\left(\dfrac{g_i}{\mathbf{a}_z}-2\cos j +2\dfrac{\mathbf{a}_z}{\mathbf{a}_y}\sin g \sin j\right) & \mathbf{a}_z +i\,\mathbf{a}_y\,\cos g \sin j\; Q \\[12pt]
\dfrac{i}{2}\,g_i\,Q\,N & -N \\[12pt]
\mathbf{a}_z\,N & \dfrac{i}{2}\,g_i\,Q\dfrac{N}{\mathbf{a}_z} \\[16pt]
1 & 0 \\[4pt]
\dfrac{i}{2}\,\alpha_y^2\,Q\left(\dfrac{g_r}{\alpha_z}+2\cos\varphi+2\dfrac{\alpha_z}{\alpha_y}\sin\gamma\sin\varphi\right) & -\alpha_z +i\,\alpha_y\,\cos\gamma\sin\varphi\; Q \\[12pt]
\dfrac{i}{2}\,g_r\,Q\,N & -N \\[12pt]
-\alpha_z\,N & -\dfrac{i}{2}\,g_r\,Q\dfrac{N}{\alpha_z}
\end{pmatrix}
\tag{3.30}
$$

In the non-magnetic case the whole medium boundary matrix A simplifies to

$$
A =
\begin{pmatrix}
1 & 0 & 1 & 0 \\
0 & \alpha_z & 0 & -\alpha_z \\
0 & -N & 0 & -N \\
\alpha_z N & 0 & -\alpha_z N & 0
\end{pmatrix}
\tag{3.31}
$$

With (3.24) and (3.25) the problem for a single boundary between two media can be solved, independent of whether they are magnetic or non-magnetic. Assuming two media with determined medium boundary matrices $A_1$ and $A_2$ (e.g. first interface in figure 3.2) equation (3.17) has to be solved. The P-matrices depend on the polarization of the incoming beam. In the case of circularly polarized light, equation (3.17) can be written as

$$A_1 \begin{pmatrix} 1 \\ \pm i \\ r_{c1} \\ r_{c2} \end{pmatrix} = A_1 \begin{pmatrix} t_{c1} \\ t_{c2} \\ 0 \\ 0 \end{pmatrix},$$

(3.32)

after dividing both P-matrices by $E_{1s}^{(i)}$ and defining following reflection and transmission coefficients,

$$r_{c1} = \frac{E_{1s}^{(r)}}{E_{1s}^{(i)}}, \qquad r_{c2} = \frac{E_{1p}^{(r)}}{E_{1s}^{(i)}}, \qquad t_{c1} = \frac{E_{2s}^{(i)}}{E_{1s}^{(i)}}, \qquad t_{c2} = \frac{E_{2p}^{(i)}}{E_{1s}^{(i)}},$$

(3.33)

the measured reflected intensity is then calculated by

$$I = \left( \frac{r_{c1} + r_{c2}}{(1+i)} \right) \cdot \left( \frac{r_{c1} + r_{c2}}{(1+i)} \right)^*$$

(3.34)

## 3.2.2 Multilayer films

So far, only a single boundary has been considered. In order to apply these formulas to systems consisting of more than two media additional considerations have to be taken care of. Here we first want to treat a system with two boundaries as it is depicted in figure 3.3a. While the beam is travelling from the boundary at $z = 0$ to the boundary $z = d$ through the medium 2, the phase of the wave changes and the amplitude gets damped due to absorption. Therefore the four components $E_x^{(j)}$ undergo the following transformation:

$$E_x^{(j)}(0) = E_x^{(j)}(z) \exp\left[ -i \frac{2\pi}{\lambda} n^{(j)} \alpha_z^{(j)} z \right],$$

(3.35)

where $\lambda$ is the wavelength of the light and z the depth into the material from the first boundary (z=0). In order to keep the calculation uniform the modification can be written in matrix form, the so called medium propagation matrix $\overline{D}$ :

$$\overline{D} = \begin{bmatrix} U & U\,\delta_i & 0 & 0 \\ -U\,\delta_i & U & 0 & 0 \\ 0 & 0 & U^{-1} & U^{-1}\,\delta_r \\ 0 & 0 & U^{-1}\,\delta_r & U^{-1} \end{bmatrix},$$

(3.36)

with

$$U = \exp\left[-i\frac{2\pi}{\lambda}N\alpha_z\,d\right],$$

(3.37)

$$\delta_i = \frac{\pi}{\lambda}N\,d\,\frac{Q}{\alpha_z}g_i,$$

(3.38)

$$\delta_r = \frac{\pi}{\lambda}N\,d\,\frac{Q}{\alpha_z}g_r,$$

(3.39)

where d is the film thickness.

It can be easily shown, that the matrix $\overline{D}$ and the vector $\vec{P}$ follow the equation:

$$\vec{P}_2(0) = \overline{D}_2(z)\,\vec{P}_2(z)$$

(3.40)

From (3.40) it is now straightforward to derive the matrix equation for such a two layer system:

$$A_1 P_1(0) = A_2 P_2(0) = A_2\overline{D}P_2(d) = A_2\overline{D}A_2^{-1}A_2 P_2(d) = A_2\overline{D}A_2^{-1}A_3 P_3(d)$$

(3.41)

This result can be generalized for multilayer films with $l$ successive layers:

$$A_i\,P_i = \prod_{m=1}^{l}(A_m\,D_m\,A_m^{-1})\,A_f\,P_f\,.$$

(3.42)

# 3.3 Determination of optical constants

With (3.30), (3.34) and (3.42) we are now in a position to calculate the charge and magnetic reflectivity of multilayer system with arbitrary magnetic configuration. Besides the incident angle and the structural setup of a multilayer system or thin film it is still necessary to determine the optical constants, the index of refraction N and the magnetic optical constant Q. At energies far above the absorption edge - typically beyond 100 eV - the values for N have been calculated theoretically by Cromer and Liberman [67-69] and are in very good agreement with the measured values. They can be found in the widely used Henke-tables [70]. However, in the vicinity of absorption edges the calculated values are not longer valid mainly due to neglected XANES and EXAFS contributions, which play an important role. One way to obtain values for N and Q in this region is to perform accurate measurements of the x-ray absorption for N and circular dichroism for Q, respectively. The paragraph below will describe the procedure of how these were determined for all the simulations calculated in this work.

The index of refraction N and the magnetic optical constant Q for an element with density $\rho$ and atomic weight A can be written as

$$N = 1 - \alpha + i\,\boldsymbol{b}\,, \tag{3.43}$$

and

$$Q = q_1 + i\,q_2\,, \tag{3.44}$$

with

$$\delta = \frac{N_a}{2\pi} r_0 \lambda^2 \frac{\rho}{A}\left(Z + f_1^{\text{charge}}\right), \tag{3.45a}$$

$$\beta = \frac{N_a}{2\pi} r_0 \lambda^2 \frac{\rho}{A}\left(f_2^{charge}\right), \tag{3.45b}$$

$$q_1 = \frac{N_a}{2\pi} r_0 \lambda^2 \frac{\rho}{A}\left(f_1^{magnetic}\right), \tag{3.45c}$$

$$q_2 = \frac{N_a}{2\pi} r_0 \lambda^2 \frac{\rho}{A}\left(f_2^{magnetic}\right), \tag{3.45d}$$

where $N_a$ is the Avogadro's constant, $r_o$ is the classical electron radius, $\lambda$ the wavelength of the light and $f_1^{charge}, f_2^{charge}, f_1^{magnetic}, f_2^{magnetic}$ the real and imaginary parts of the correction factors of the charge and magnetic scattering amplitudes, respectively. With the determination of the correction factors the optical constants N and Q can be obtained. The real and imaginary part are not independent quantities. The causality between the electric field of the light and the polarization which is generated in the medium leads to a relationship between the real and imaginary parts of the atomic scattering amplitude, which is described by the well known Kramers-Kronig relation (KK) [71]:

$$f_1^{charge\,(magnetic)}(E_0) = \frac{2}{\pi} \int_0^\infty \frac{E\ f_2^{charge\,(magnetic)}}{E_0^{\,2} - E^2}\ dE,\qquad (3.46)$$

where $E_0$ is the energy of interest and E runs over an energy range as wide as possible. In principle, in order to determine the correct correction factors via KK, all the absorption edges should be described in detail. In practice edges which are far enough away (by about more than
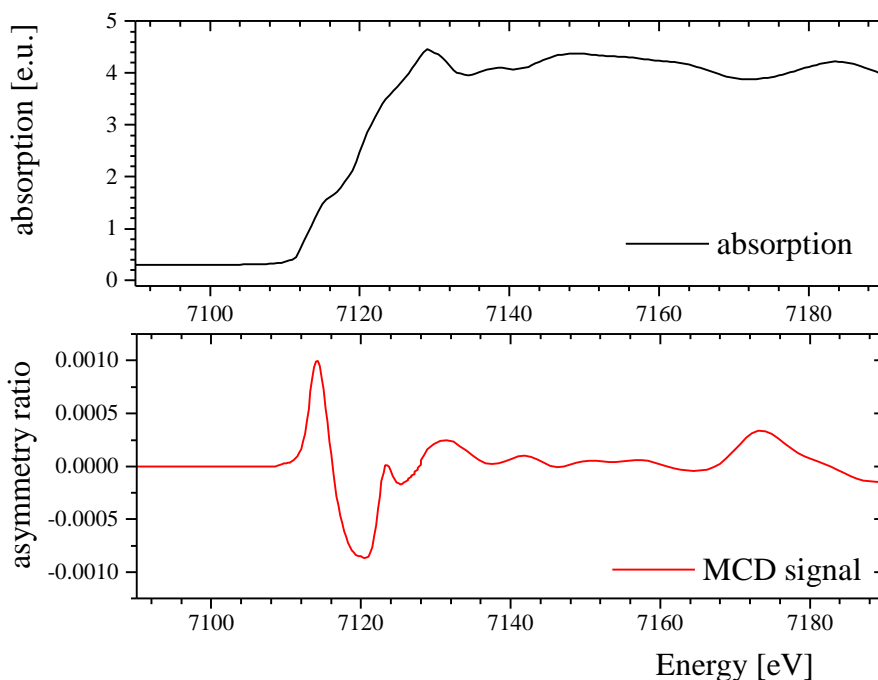


**Figure 3.4** *MCD-Absorption on an 8μm thick iron Foil at beamline X13-B. Upper plot shows absorption in electron units, lower plot the asymmetry ratio of the MCD signal measured by flipping the magnetic field at constant helicity.*

100eV) from the region of interest play only a very minor role and can therefore use the values of the Henke tables for the charge contribution and zero in the case of the magnetic correction.

To illustrate the whole procedure, the corrections at the iron K-edge are used as example. Figure 3.4 shows typical MCD data for a 8 μm thick iron foil. Description of the typical setup of an MCD experiment and information about the beamline X13B, where the experiment was carried out, can be found in Chapter 4. The top panel shows the measured charge absorption coefficient μ, connected with the imaginary part β of the index of refraction through

$$\beta = \frac{\mu \lambda}{4\pi} \tag{3.47}$$

At the same time clearly a magnetic circular dichroism signal can be detected (bottom panel), plotted here as the asymmetry ratio, the difference divided by the sum,

$$\frac{\Delta I}{2I} \approx -\frac{P_c \mu_c d}{\cos \alpha} \ , \tag{3.48}$$

where $P_c$ is the degree of circular polarization of the light, d the thickness of the foil, α the angle between the sample normal and the incident beam and $\mu_c$ the spin-dependent absorption coefficient. By knowing the degree of polarization and the effective thickness of the sample, $\mu_c$ can easily be determined. With (3.45b), (3.45d) and (3.48) the following correction factors $f_2^{charge}$ and $f_2^{magnetic}$ and the absorption coefficients μ and $\mu_c$ can be derived:

$$f_2^{charge\ (magnetic)} = \mu_{(c)} \ \frac{A}{\lambda \ \rho \ N_a \ r_0} . \tag{3.49}$$

In order to apply the Kramers-Kronig relation the energy range of both absorption spectra has to be extended over a larger range. In this case, calculated values from the Henke tables for 30 eV to 100 keV are used. Equation (3.34) was then applied to the extended $f_2^{charge}$ and $f_2^{magnetic}$ to derive their real parts $f_1^{charge}$ and $f_1^{magnetic}$. Figure 3.5 and figure 3.6 show the result for the
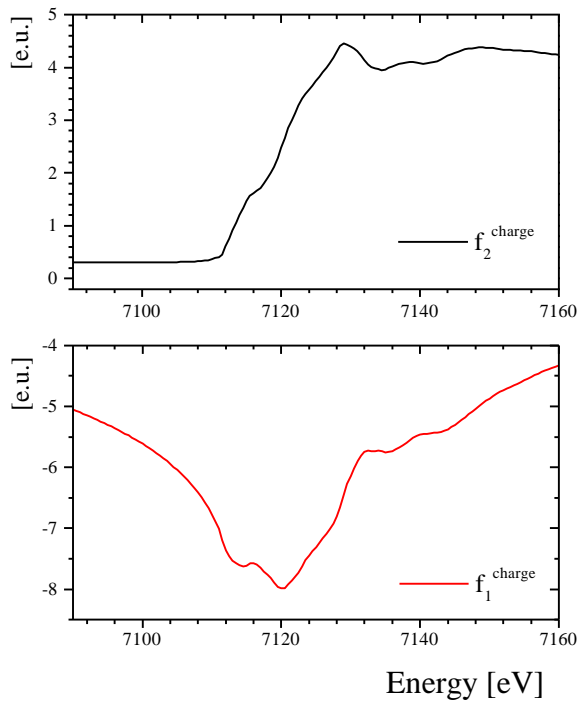
**Figure 3.5** *Charge correction factors $f_1^{charge}$ and $f_2^{charge}$ from absorption measurements on an iron foil. $f_1^{charge}$ determined via KK relation from $f_2^{charge}$.*
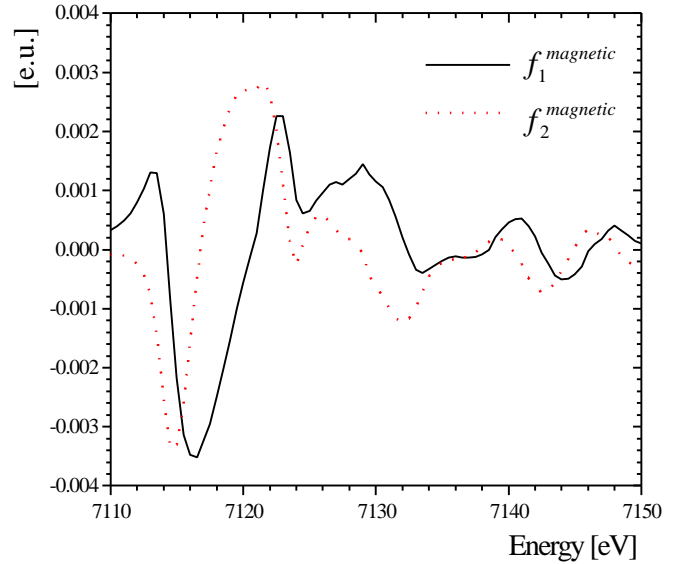
**Figure 3.6** *Magnetic correction factors $f_1^{magnetic}$ and $f_2^{magnetic}$ for iron from MCD absorption measurements. $f_1^{magnetic}$ determined via KK relation from $f_2^{magnetic}$*

region around the K-absorption edge of iron, where magnetic reflectivity experiments are carried out in the hard x-ray region when probing samples containing iron.

After determining the real parts of the correction factors of the charge and magnetic scattering amplitudes from their imaginary parts via the Kramers-Kronig relation, it is straight forward to calculate the index of refraction N and the magnetic optical constant Q, using equations (3.45a-d). Figures 3.7 and 3.8 show the single components of the correction factors of the charge index of refraction and the magnetic optical constants, respectively, for iron.

Now all the ingredients have been obtained to simulate magnetic and charge reflectivity at the K-edge of iron in any magnetic sample. Other edges in the hard and soft-x-ray region can be calculated similarly via this procedure.
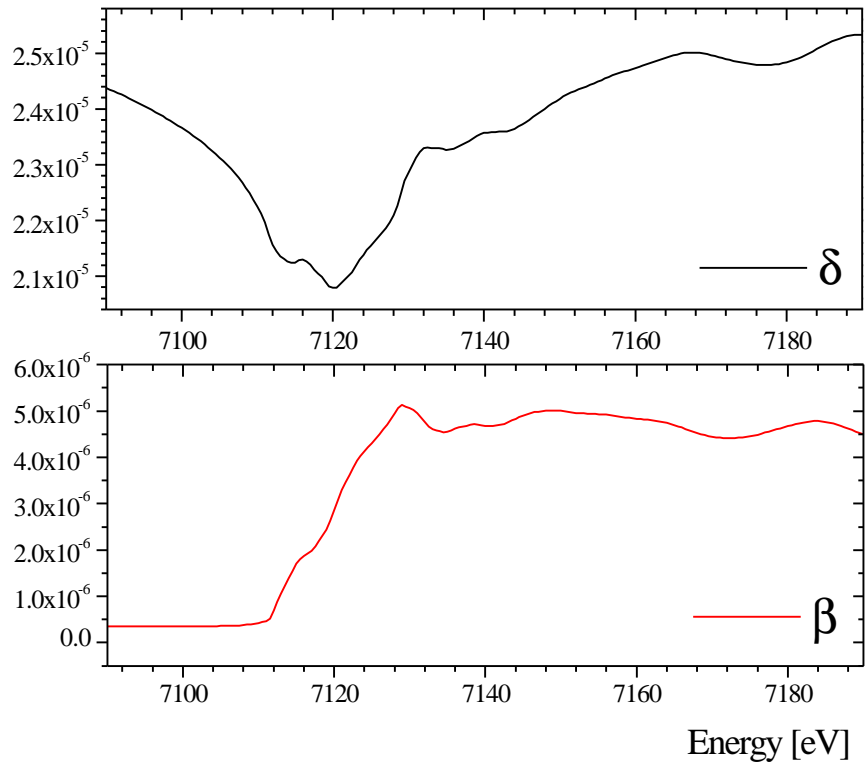
**Figure 3.7** *Real (δ) and imaginary(β) terms of the index of the refraction, N, of iron at the iron K-edge.*
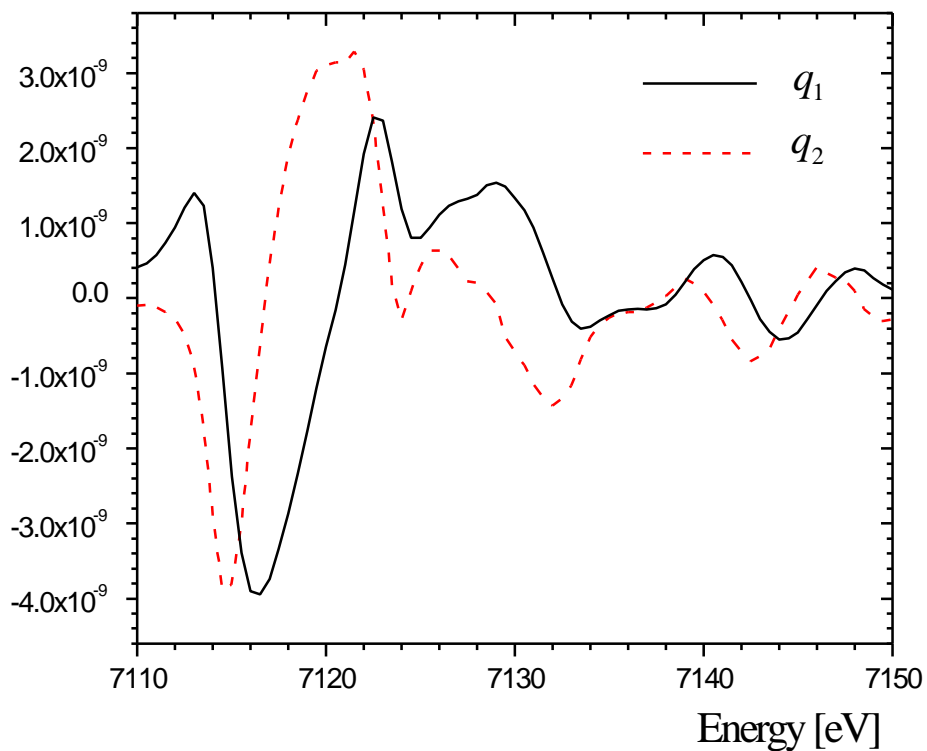


**Figure 3.8** *Real (q$_1$) and imaginary (q$_2$) part of the magnetic optical constant, Q, of iron at the iron K-edge.*

# 3.4 Simulation: Single Iron layer on Silicon

In this paragraph a simple magnetic system will be simulated in order to show how the magnetic reflectivity curve is affected by different magnetic spin configurations. A single layer of 100 Å of ferromagnetic iron on a silicon substrate (see figure 3.9) provides a simple system, in which the structural complexity is low, but still sufficient to illustrate some important different magnetic configurations. The energy chosen for these simulations lies in the hard x-ray region slightly above the iron K-edge at 7115 eV, where the magnetic optical constant has its maximum for this particular edge. The index of refraction for iron and silicon were calculated from absorption measurements as shown before and taken from tabulated values [23], respectively, and the magnetic optical constant for the ferromagnetic iron was simplified for illustrative reasons to $Q_{Fe}=(5-5i)\cdot 10^{-9}$, close to the value calculated from MCD measurements. The simulations with the optical approach calculate the reflected intensity of the left- and right circularly polarized light, respectively. By dividing the sum of both intensities by two and taking their difference the charge and the magnetic reflectivity curves can be retrieved, respectively. But it should be noted as pointed out in chapter 2, that the same result is achieved by flipping the ferromagnetic configuration and holding the polarization of the incoming light, here left or right circular polarization, constant.

## 3.4.1 Charge reflectivity

Figure 3.9 shows the calculated charge reflectivity (circles) with the magnetic optical approach method. At small angles the simulated reflectivity remains nearly constant at 1 before it starts to fall rapidly off. This region of total reflectivity is due to the fact that the index of refraction for iron (which is the top layer) is slightly smaller than 1 in the hard x-ray energy range and therefore air (N = 1) is the denser material. This leads to the condition of total reflection, where the beam gets totally reflected from the interface as long as the angle is small enough. The so

called critical angle $\theta_c$, which separates the total reflection region from the higher angle part can be easily derived, using Snell's law and the definition of the index of refraction N in (3.3):

$$\Theta_c \approx \sqrt{2\delta} \qquad (3.50)$$
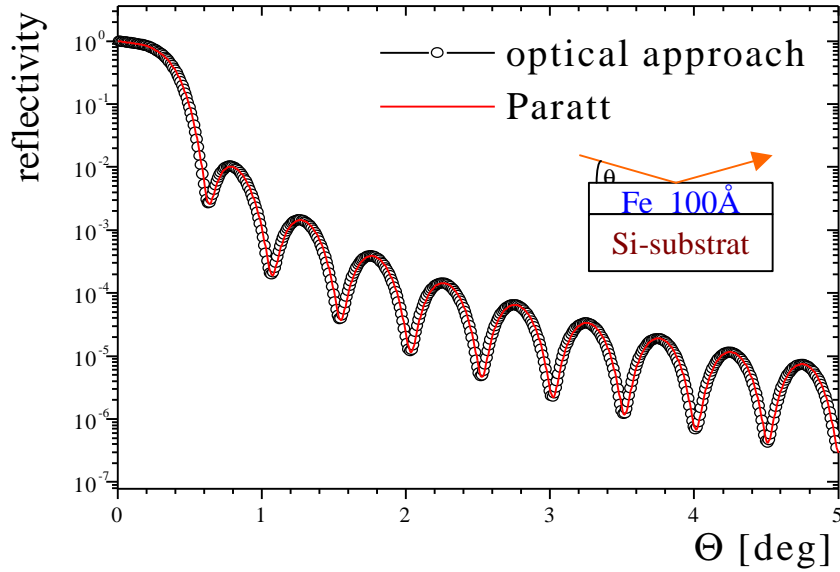


**Figure 3.9** *Charge Reflectivity of a 100Å iron on a silicon substrat calculated by proposed optical approach (circles) and compared with the Paratt algorithm (line)*

Since the deviation $\delta$ of N from 1 is very small for hard x-rays the total reflectivity regime is restricted up to $0.38^o$ as can be seen in the reflectivity curve. At higher angles the reflected intensity starts decrease with $(\sin\theta)^{-4}$, known as *Fresnel reflectivity* of a perfectly flat interface, and also exhibits oscillations with regular periodicity due to the thickness, $t_{Fe}$, of the single iron layer. The thickness of the iron layer can be extracted from the distance between the maxima (or minima) of the oscillations by applying

$$t_{Fe} = \frac{2\pi}{\Delta Q_z^n}, \qquad (3.51)$$

with

$$\Delta Q_z^n = Q_z^{n+1} - Q_z^n, \qquad (3.52)$$

and

$$Q_z^n = \frac{4\pi}{\lambda} \sin \Theta_n \; . \tag{3.53}$$

Here, $\theta_n$ is the angle of the $n^{th}$ maximum or minimum and $Q_z$ is the momentum transfer along the surface normal as already discussed in section 3.1. Even though the calculated reflectivity curve shows all the features, qualitatively and quantitatively, which are expected, a direct comparison with the Paratt algorithm, which has for decades been the standard tool to fit the charge reflectivity, gives further confidence in the validity of the simulation. The full line in figure 3.9 shows the reflectivity curve calculated by using the Paratt algorithm. It can be clearly seen that the curve exactly follows the simulated reflectivity profile calculated within the optical approach and gives further support for the simulation. After showing that the charge reflectivity can be calculated we will now proceed with the simulation of the magnetic reflectivity. Three parameters describe the magnetic configuration of the system, the magnetic optical constant $Q_{fe}$ , and the angles $\varphi$ and $\gamma$ (see fig. 3.3), which determine the amplitude and direction of the magnetic spins in the iron layer, respectively.

## 3.4.2 Collinear alignment

In the simplest configuration all the iron spins are aligned parallel to the sample surface and point in scattering plane ($\varphi = 90°$, $\gamma = 90°$) and $Q_{Fe}$ is assumed to be uniform over the whole iron layer. Figure 3.10 shows the magnetic reflectivity signal as the difference in the reflectivity of left and right circularly polarized x-rays. The signal decreases very quickly. In the inset, which magnifies the region between $\Theta = 1°$ and $\Theta = 4.5°$, oscillations with regular periodicity can be observed very similar in position and periodicity to the maxima of the charge reflectivity curve, which stem from the regular oscillatory magnetic spin profile and therefore will be called *magnetic Bragg peaks*.

54
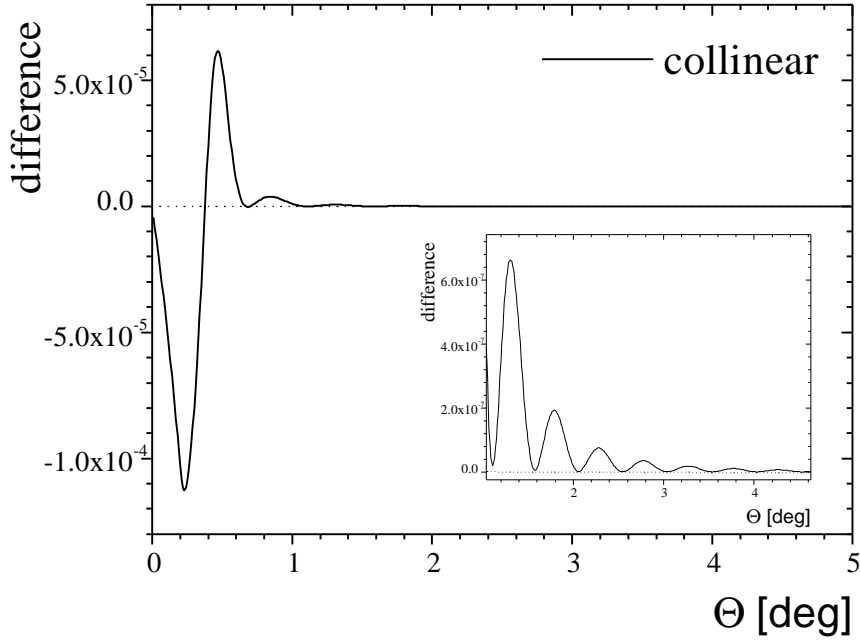


**Figure 3.10** *Magnetic reflectivity, presented as the difference between left and right circularly polarized x-rays, of 100 Å iron on silicon substrate, with iron spins collinear aligned (see text). Inset shows magnification of curve at a angle range from 1° to 4.5°.*

The rapid decrease of the intensity and the impossibility of using a logarithmic scale due to negative values make it very difficult to show the curve over a long angle range. In order to overcome that it became popular to present the magnetic reflectivity by the so called asymmetry ratio, which is the difference in reflectivity divided the sum:

$$\frac{\Delta I}{2I} = \frac{I_{\uparrow\uparrow} - I_{\uparrow\downarrow}}{I_{\uparrow\uparrow} + I_{\uparrow\downarrow}} .$$

(3.54)

Figure 3.11 shows the asymmetry ratio (dashed line) calculated simply by dividing the difference signal by the sum of the charge reflectivities. This asymmetry ratio also exhibits oscillations with regular periodicity and provides now the whole range of the magnetic reflectivity spectrum. But it should be carefully noted that the peaks in the asymmetry plot are often not of magnetic origin but produced by the minima in the charge reflectivity. In this case, the magnetic maxima lie on the rising hump of the oscillation of the asymmetry ratio. Nevertheless, this kind of plot allows usually the better determination of the magnetic profile, especially by dealing with weak magnetic signals.
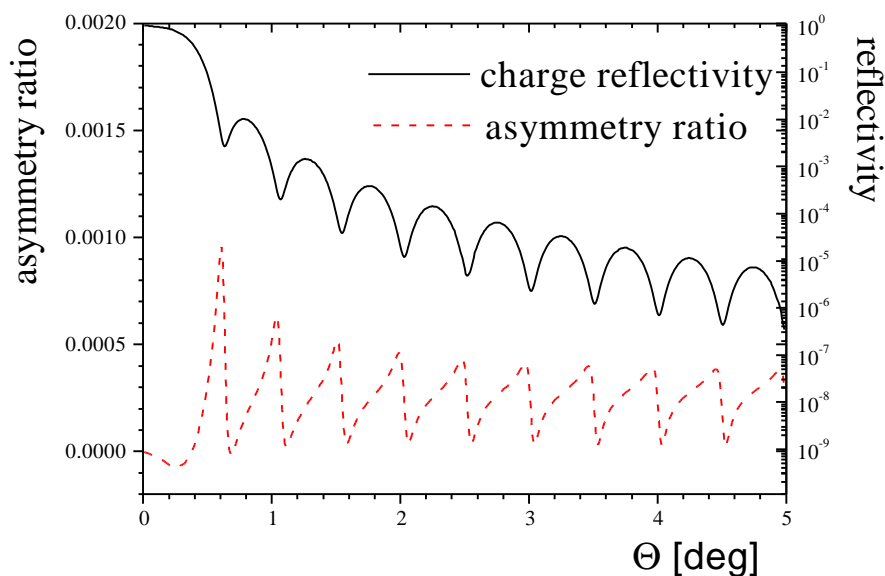
**Figure 3.11** *Magnetic reflectivity of 100Å iron on silicon substrate shown as the asymmetry ratio (dashed line) in comparison with the charge reflectivity (full line)*

## 3.4.3 Magnetic optical constant Q

Next we want to concentrate on effects of the magnetic optical constant Q, which can be considered as a measure of the scattering amplitude of the magnetic spins. As shown before,
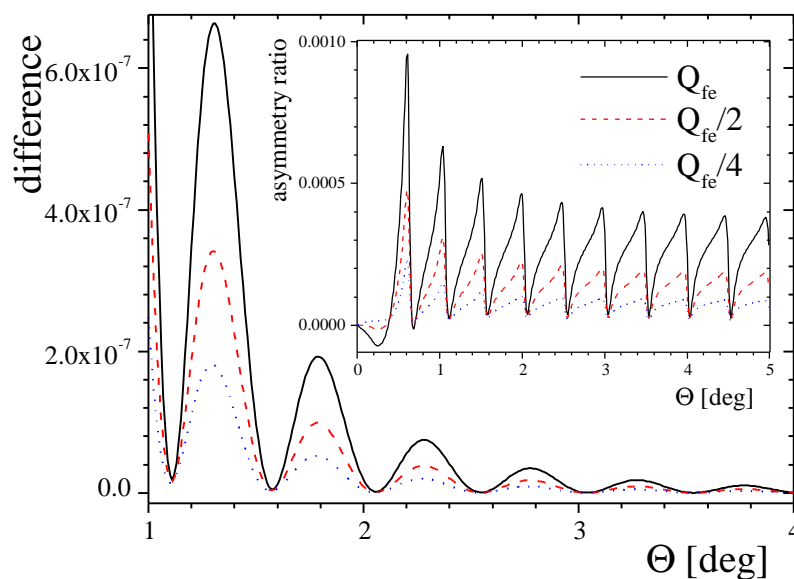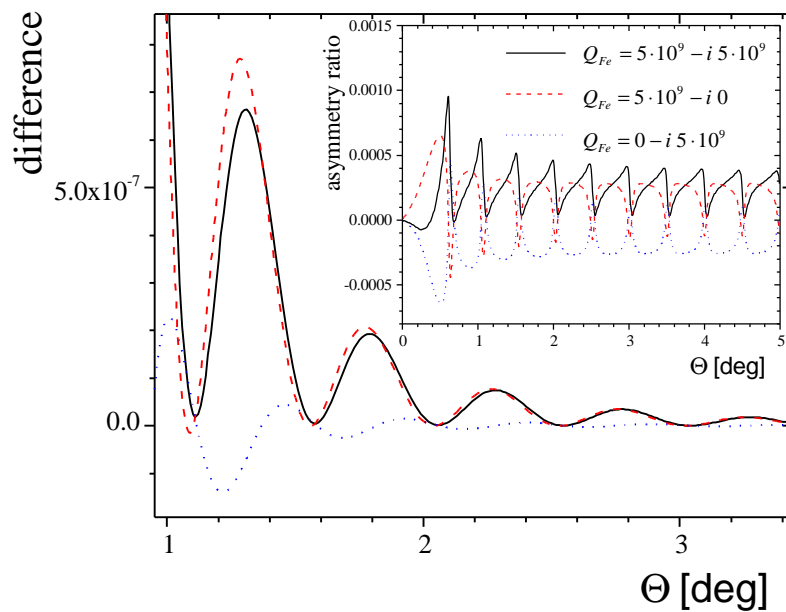


**Figure 3.12** *Magnetic reflectivity of Fe(100 Å)/Si system by varying the magnetic optical constant, difference in outer picture and asymmetry ratio in inset*

this quantity can be determined from MCD absorption experiments and is the magnetic analogue to the index of refraction N of the charge part and characterizes the magnetic contrast. In the following paragraph the effect of Q will be illustrated by simulating the difference in reflectivity and asymmetry ratios as a function of the magnetic optical constant.

Figure 3.12 shows how the magnetic signal scales linearly with the magnitude of the magnetic optical constant. The reduction of the magnetic spin amplitude directly affects the magnetic reflectivity by reducing the amplitude of the magnetic maxima, as can be seen in both the difference signal shown in figure 3.12 as well as in the asymmetry ratio in the inset.

 The magnetic optical constant has a real and an imaginary part. Figure 3.13 presents the simulated magnetic reflectivity for the two extreme cases: the dashed line presents the pure real part of  Q and the dotted line the pure imaginary part. Both curves show different maxima and behavior. It should be noted that in this simple case the sum of both intensities results in the black curve which is the same as magnetic reflectivity curve simulated with the sum of the magnetic optical constants of the extreme cases. In section 3.3 it has been pointed out that the magnetic optical constant and its ratio of imaginary and real part varies significantly with the photon energy. By choosing a different energy the shape of the magnetic reflectivity curves, i.e. the difference and asymmetry ratio, can change drastically.



**Figure 3.13** *Magnetic reflectivity of Fe(100 Å)/Si system by varying the real and imaginary magnetic of the  optical constant*
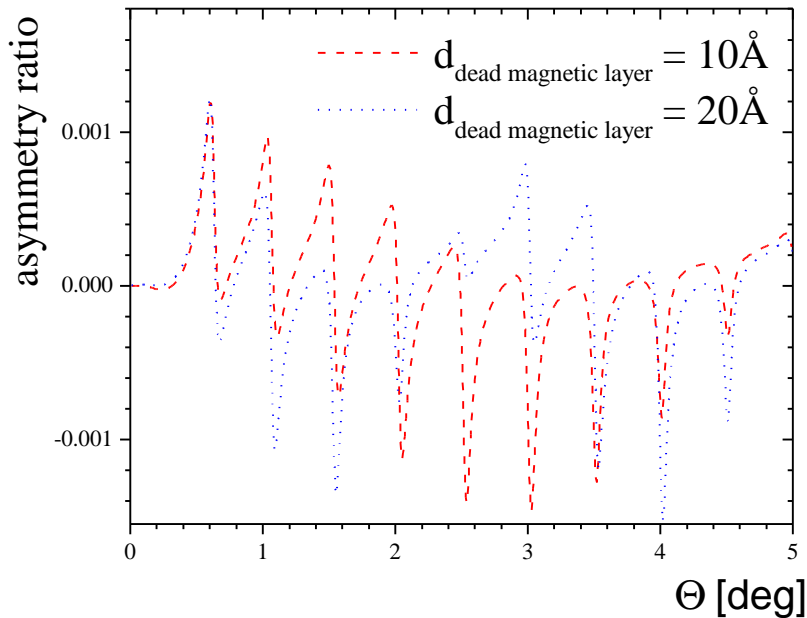
## 3.4.4 Magnetic dead layer

In many cases, a magnetically dead layer exists on the surface or at the interface of a ferromagnetic thin film and substrate and can affect the magnetic properties [72-74]. Here in our example of a 100 Å iron film on silicon the first d Å of the iron at surface are assumed to be nonmagnetic before the iron spins are again aligned collinear as in the previous example. This means that the magnetic optical constant Q in the iron layer has an abrupt change from 0 to the full value after the first d Å. Figure 3.14 shows the difference signal in a region between $\Theta = 1°$ and $\Theta = 3.1°$ for two different thicknesses d of the magnetic dead layer, 10 Å (dashed line) and 20 Å (dotted line), and for the completely magnetized iron layer (full line). The larger the magnetic dead layer the more the magnetic reflectivity deviates from it is original form, which is not only visible in the sign changes, but also in a periodicity shift of the oscillation. A clearer picture is provided in figure 3.15, where the asymmetry ratio is plotted. Here a clear oscillation in the envelope of the asymmetry ratio can be seen. Its periodicity becomes smaller as the thickness of the magnetic dead layer increases. To understand this behavior the dead
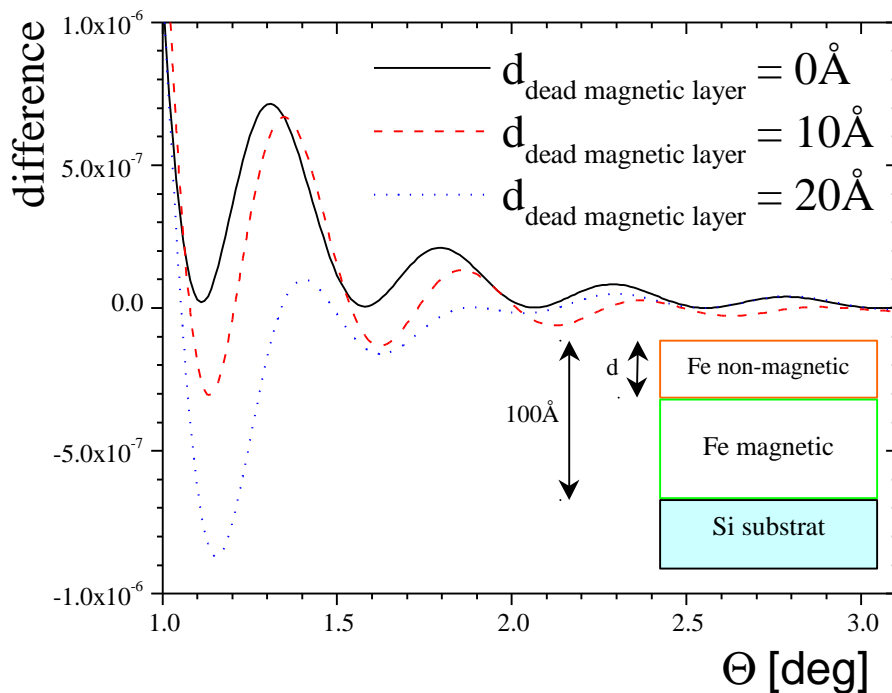


**Figure 3.14** *Simulation of the magnetic reflectivity (difference) of 100Å iron on silicon substrat with the first d Å of the top iron layer nonmagnetic.*

layer has only to be pictured as an additional modulation in the magnetization profile. Thus, by using equations (3.51) to (3.53) the periodicity of the oscillation can be exactly correlated to the thickness of the magnetic dead layer, and so the calculated $t_{fe}$ corresponds exactly to the thickness d of the magnetic dead layer. By placing the magnetic dead layer at a different positions in the sample, e.g. in the middle or at the end instead of the top part, changes the pattern of the oscillation, but not the periodicity (*not shown here*). Thus the asymmetry ratio is not only sensitive to the thickness of the magnetic dead layer but also to their position in the system.

**Figure 3.15** *Asymmetry ratio of magnetic reflectivity simulation with magnetic dead layers (for sample setup see figure 3.14).*

## 3.4.5 Spin configuration

Contrary to the charge density, which can be described in the x-ray region by the complex scalar of the index of refraction N, the magnetic spin is a vector quantity and thus possesses not only a magnitude, but also a direction. Here in the simulation the magnitude is quantified by the magnetic optical constant Q, and the direction described by the angles $\varphi$ and $\gamma$ (see figure 3.3). So far it has been shown how changes in the magnetic magnitude Q affect the magnetic
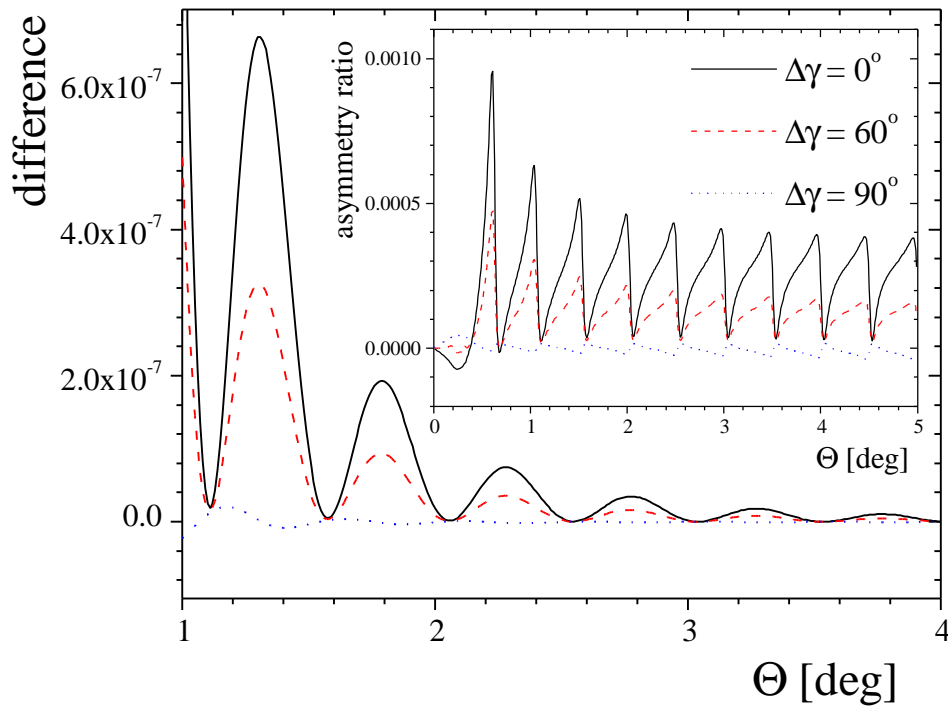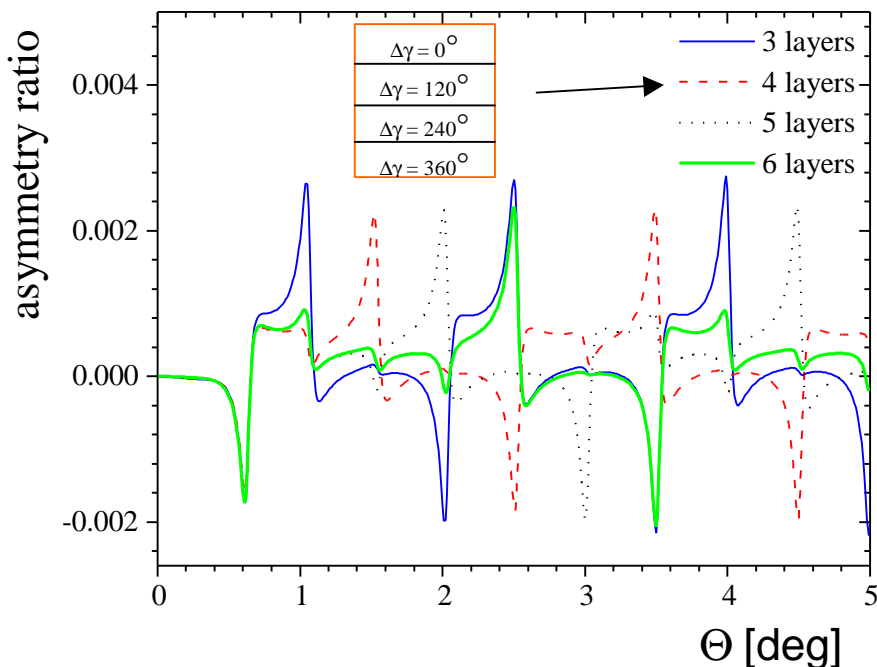
**Figure 3.16** *Simulation of magnetic reflectivity of Fe(100Å)/Si system.* **Dg** *is the deviation of the angle of the iron spin from the collinear alignment*

reflectivity curve, keeping the spin direction for all simulations collinear. In this section the direction of the spins is changed while keeping Q constant, in order to demonstrate how different spin arrangements modify the difference signal and asymmetry ratio.

In the first example we consider, all of the iron spins in our system point in the same direction with angles deviating from the scattering plane ($\Delta\gamma = 0°$). In figure 3.16 three configurations are shown, where the in-the-layer plane angle $\gamma$ was varied by $\Delta\gamma$ (see figure 3.3). The full line represents the collinear arrangement with $\Delta\gamma = 0°$ and two variations, one with $\Delta\gamma = 60°$ and one perpendicular with $\Delta\gamma = 90°$ are also shown. The difference signal decreases proportional to the projection of the spins onto the scattering plane ($\Delta\gamma = 0°$). At $\Delta\gamma = 60°$ the magnetic signal is half as big as if all spins are aligned collinear and at $\Delta\gamma = 90°$ it is nearly zero. The small remaining signal is due to the angle deviation from $\theta = 0°$ which leaves a small portion of the spin projected onto the $\Delta\gamma = 0°$ direction. This example shows one possible spin configuration in which the magnetic optical constant is reduced. It should be also noted that a similar result can be achieved by tilting the magnetic spins in the perpendicular direction (variation of $\varphi$) since the projection will result in exactly the same effective magnetic optical constant Q seen by the photon beam. To distinguish both cases one needs a different

experimental arrangement, for example by rotating the sample by 90° or using linearly polarized light to change the anisotropy in the polarization of the incident beam.

 A more complicated case is when the spin direction rotate throughout the layers. Such a spiral magnetic spin configuration exists in various materials and could be one mechanism for the magnetic coupling of magnetic multilayer [75, 76]. One possible configuration is shown in the next example. There the iron spins make a 360° in plane turn (γ) from the top to the bottom of the iron film. This turn is divided into x different layers with equal thickness and equal intervals of the angle from $\Delta\gamma = 0°$ to $\Delta\gamma = 360°$. In each layer the iron spins point in the same direction and the magnetic optical constant is again held constant over the whole iron layer. In figure 3.17 the resulting asymmetry ratios are shown for different numbers of sublayers with equal turning angles $\Delta\gamma$, e.g. as an example the inset shows angles for four sub-layers. All asymmetry ratios exhibit oscillatory behavior, but the period and the phase depend on the number of sub-divisions. Even though the oscillations are not really sinusoidal, by considering only positions of the maxima it is again possible to calculate the thickness of the sub-layers for



**Figure 3.17** *Magnetic reflectivity simulation of Fe(100Å)/Si system with 360° spiral spin configuration in x = 3,4,5,6 equally thick iron layers. Inset shows division of iron layer with its even angle contribution from the top to the bottom for x = 4.*

each configuration using equations (3.51) and (3.53). The finer the division of the iron layer the larger is the observed period of the absolute maxima in the asymmetry ratios. It should be mentioned that again the same result can be achieved if the magnetic spins are turned in perpendicular direction, by variation of φ instead of γ, as long as the projection of the spins onto the scattering plane is the same.

## 3.4.6 Soft x-rays

All the simulations shown and discussed above are calculated in the hard x-ray regime. But since this work also deals with magnetic soft x-ray reflectivity some comments should be made about how the magnetic x-ray reflectivity picture is affected by the longer wavelength. Going to the soft x-ray region means an increase in the wavelength of the beam, here at iron (from the *hard* K-edge to the *soft* L-edges) by about a factor of 10, which drastically changes the optical constants of the material. The correction factors for the charge reflectivity increase by about two magnitudes. The absorption is much stronger and therefore the soft x-ray beam gets attenuated much more quickly in the material. Comparing the optical constants for iron for the
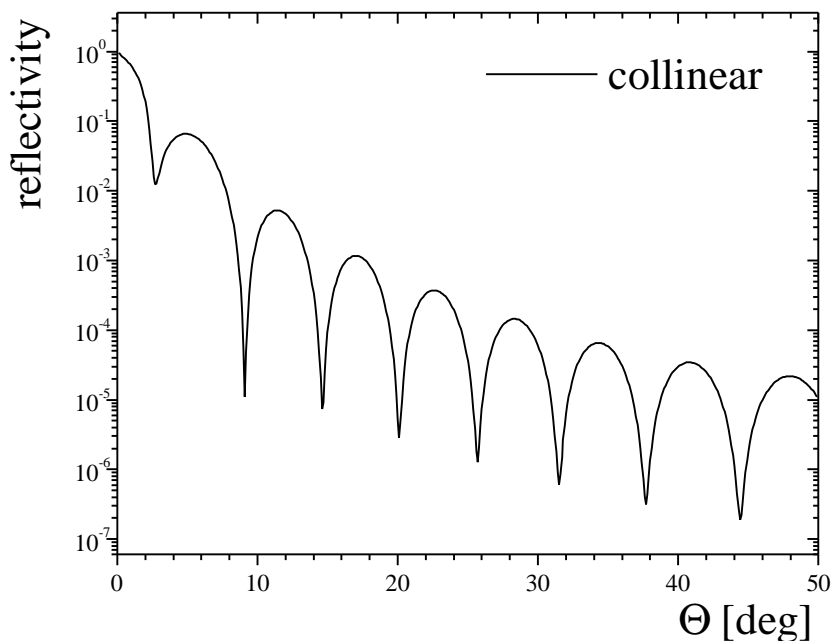


**Figure 3.18** *Charge reflectivity curve of iron (100 Å) on silicon with soft x-rays (E = 705eV). Iron spins are collinear aligned.*

K-edge to the L-edges (see figure 5.16 in chapter 5) show these differences clearly. For the 3d transition metals, which are the subject of this study, the MCD-Absorption effect is about 100 times stronger at the L-edges compared to the K-edges as already pointed out in chapter 2.2. This gives a much larger and more easily detected magnetic signal in the x-ray reflectivity. Instead of a 0.1%-effect as one can expect in the hard x-ray region, the magnetic reflectivity can be comparable in magnitude to the charge reflectivity in the soft x-ray region. Figure 3.18 shows the charge reflectivity curve for the 100 Å iron film on a silicon substrate calculated near the iron $L_3$-edge (705 eV) in the soft x-ray region. The first significant difference from the reflectivity in the hard x-ray regime is the large angle range, which is necessary to cover the same number of structural oscillations. This can be immediately understood by looking at the definition of the reciprocal momentum transfer vector along the surface normal $Q_z$ (3.12). Due to the $1/\lambda$ factor a much larger angle region has to be probed in order to reach the same $Q_z$ - value, which is the quantity, which determines the structural probing size. Also, it should be noted that the index of refraction of iron at this particular energy is slightly greater than 1. Thus no region of total reflection is observed. Otherwise the curve exhibits regular, well defined oscillations superimposed on the expected intensity similar to the hard x-ray simulation. The oscillation period is again determined by the thickness of the iron layer (3.51)-(3.53).
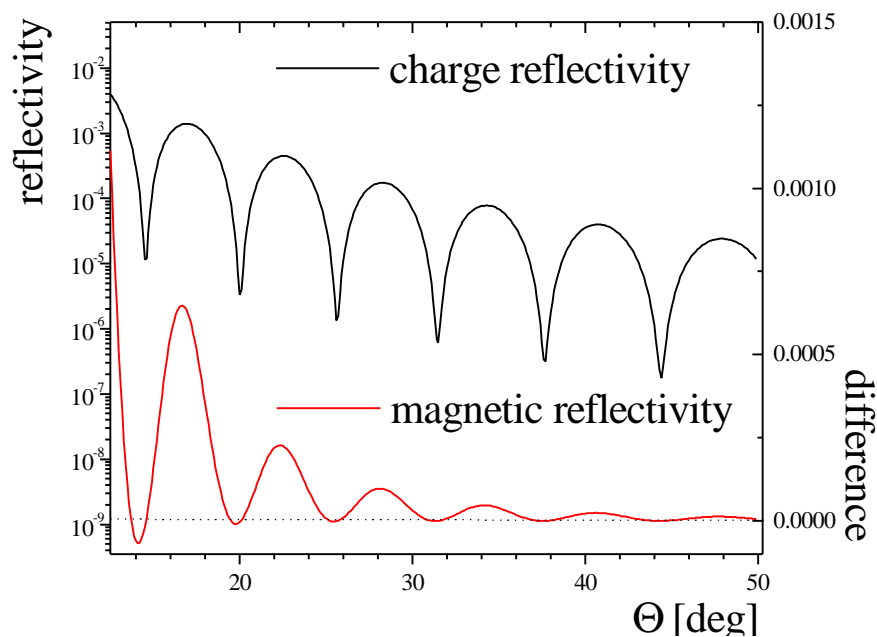


**Figure 3.19** *Charge and magnetic soft x-ray reflectivity curve of Fe(100 Å)/Si at 705 eV. Iron spins collinear aligned.*

Figure 3.19 shows the calculated difference signal (lower line) of collinear alignment of the iron spins, in which the optical constant Q for iron was determined from MCD-measurements at the L-edges of iron (see chapter 5.2). As seen in the hard x-ray region the curve exhibits magnetic oscillations, whose period exactly corresponds to the periodicity of the oscillations in the charge reflectivity curve. The small shift in position is due to the complex nature of Q and can be varied somewhat by changing the photon energy. Due to this the asymmetry ratio curve shown in figure 3.20 shows the misleading large spikes at positions of the minima in the charge reflectivity curve. The ratios for the *real* magnetic maxima can be found in the down slopes and show a 20% effect.
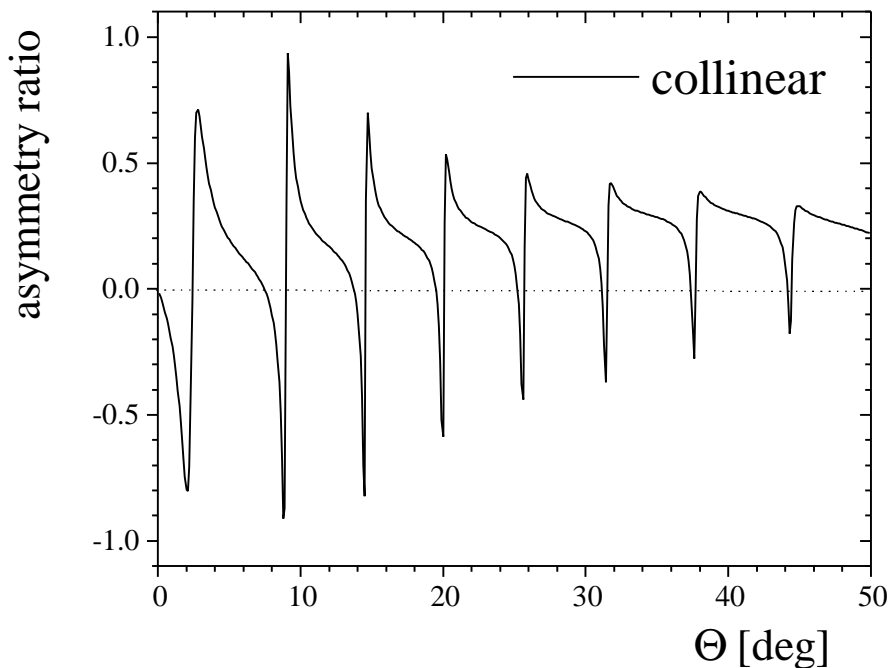


**Figure 3.20** *Asymmetry ratio of soft x-ray reflectivity on collinear aligned Fe(100 Å) on Si substrate at E = 705eV.*

Reducing the magnetic optical constant by twisting the angle, perpendicular or in the layer plane, or assuming dead layers or spiral spin configurations lead basically to the same results as shown for the hard x-ray region, even though the shape of the magnetic reflectivity curve, difference and asymmetry ratio, usually differs because of the large changes in the optical constants.

## 3.4.7 Roughness

In real magnetic thin films and multilayer systems roughness plays an important role in the determination of magnetic properties, as it can be seen for the case of exchange bias and other magnetically coupled systems. Thus it would be desirable to find a way to include roughness in the calculation and determine a kind of rms-roughness for layered systems as it has been done by Nevot Croce [57] for the charge reflectivity. Unfortunately it turns out that the calculations as shown in the previous chapter are already sufficiently complex that trying to include a kind of damping mechanism (similar to the Debye-Waller factor) for rough interfaces in the simple matrix equations has not yet been realized. Osgood et al. [77] started another approach to tackle the problem of roughness, by looking at the diffuse magnetic scattering. In the Born Approximation the magnetic resonant cross section has been derived, where correlation functions are the key parameter in describing the rough interfaces. Even then the result is dependent on initial assumptions about the interface structure. Furthermore the dominant factor in these magnetic cross sections is the interference terms between magnetic and charge contributions and it is still not clear how the magnetic and charge roughness could be clearly separated.

## 3.5 Summary

This chapter described all the calculations undertaken to simulate the charge and magnetic reflectivity curves of thin magnetic layers and multilayer systems. The first part summarized the *standard* reflectivity calculations, which deal with the charge part. Special assumptions like grazing incidence (hard x-rays) and polarization independence lead to very convenient equations, in which a root mean square roughness can be included to describe the damping of the reflected amplitudes by non-ideal (e.g. rough) interfaces. In order to simulate the magnetic reflectivity the polarization dependence cannot be neglected. Therefore a different approach has been chosen, the so-called *magnetic optical approach*, which also starts with Maxwell's equations at the interface between two media. The conservation of the tangential components of the electric and magnetic field, expressed in terms of the experimentally setup convenient $\pi$-

and σ-components of the electric field vectors, leads to the medium boundary matrix A in which an arbitrary magnetization direction of the magnetic spins has been included in the dielectric tensor of the magnetic medium. In order to extend that to multilayer systems the propagation matrix D is introduced, which handles the absorption and phase shift of the electromagnetic wave travelling through the medium. By solving the matrix equation assuming left and right circularly polarized light with fixed magnetization of the sample, equivalent to flipping the magnetic configuration and a constant helicity of the light, the charge and the magnetic reflectivity curves can be derived.

In order to determine the optical constants, especially the magnetic optical constant Q, absorption measurements have to be carried out, since theoretically calculated values for the index of refraction N are not sufficiently accurate near an absorption edge. From the imaginary part of the correction term, calculated from absorption data and extended over a wide range in energy using tabulated values, the real part can be derived via the Kramers-Kronig relation. This finally gives the index of refraction N as well as the magnetic optical constant Q. The procedure was demonstrated at the iron K-edge.

In order to illustrate the magnetic reflectivity calculations a simple system with 100Å of ferromagnetic iron on a silicon substrate was simulated within the magnetic optical approach. The charge reflectivity curve agrees very well the calculation using the standard Paratt algorithm. Different magnetic scenarios were simulated for changes in the magnetic optical constant or the configuration of the iron spins. The simulations show that all of these effects are observable in the magnetic signal, even though some can have multiple origin, as e.g. the reduction of the magnetic intensity, which require further measurements in order to fully describe the magnetic structure. Basically it should be noted that in the specular reflectivity setup only a projection of the spin onto the sample normal (z-direction) can be detected, which can lead to ambiguous interpretations of the magnetic reflectivity curve. Nevertheless, due to the absorption of the light travelling through the sample giving different weights to regions in the z-direction, it is possible to investigate complex spin configurations along the z-direction, as seen for spiral structures.

The derivation of the magnetic reflectivity simulation via the magnetic optical approach is independent of the wavelength of the light. The change of the wavelength - for example by tuning the wavelength from the hard x-ray to the soft x-ray region - can change the picture of

the charge as well as the magnetic reflectivity curves due to the large changes in the optical constants, but the behavior and features observed remain basically the same.

# 4. Experimental Beamline Stations

This chapter describes the experimental setups which were used for the magnetic x-ray reflectivity experiments in both the soft and hard x-ray region. In the previous chapters it was pointed out, that the magnetic interaction of x-rays is weak compared to the scattering from the charge contribution. The first experimental observation of magnetic scattering with x-rays was made in the early seventies [78]. Because the intensity from conventional x-ray sources were low those experiments were very difficult and extremely time consuming. But in the past two decades, the development of synchrotron radiation sources with their unique characteristics of high intensity, tunability and a high degree of polarization have had a significant impact on the field of magnetic x-ray scattering and made x-ray investigations of magnetic order routine. In this chapter the experimental arrangements, which were used for the magnetic x-ray measurements presented in this study, will be discussed. It begins with a short overview of synchrotron radiation. Then in the following two sections, the two beamlines used, the X-13 beamline at the National Synchrotron Light Source (NSLS) in Brookhaven and the undulator beamline CMC-CAT at the Advanced Photon Source (APS) in Argonne, are described. Both are insertion device beamlines which were adapted to provide intense circularly polarized x-rays, which are critical for magnetic x-ray reflectivity experiments.

# 4.1 Synchrotron Radiation (SR)

In this section the basic properties of SR are briefly illustrated. A much more detailed description and discussion about SR and their properties can be found in several review articles and text books [79-82]. From classical electrodynamics it is well known that an electron emits electromagnetic radiation when accelerated. In the non-relativistic case ($\beta = v/c << 1$) the radiation emitted from an electron moving in a circular orbit has a doughnut-like pattern with dipole characteristics and an energy on the order of neV. If the electron is accelerated up to relativistic speeds ($\beta \cong 1$) this pattern gets transformed through the Lorentz transformation and

the angular distribution of the emitted radiation seen from in laboratory frame is concentrated in a cone with the small emission angle of

$$1/\gamma = mc^2 / E \text{ [GeV]}, \tag{4.1}$$

where E is the particle energy. This radiation from relativistic electrons was first observed in 1947 by Elder et al. at the General Electric synchrotron in Schenectady, New York, and hence named synchrotron radiation [83]. While at first this radiation was more an unwanted parasitic effect, it was soon realized that it could be of great use as an intense and tunable radiation source. In fact, in the last twenty years many new accelerators and electron storage rings have been designed and constructed for the exclusively use of SR.

In order to keep the electrons in a circular orbit they have to be accelerated by dipole bending magnets (BM) which deflect them from their straight path. The bending radius R of such a BM depends on the particle energy E and the magnetic field B of the magnet with R = 3.335 E[GeV]/B[T]. Even though the whole electron storage ring is kept in ultra high vacuum (UHV), the electrons still suffer energy loss due to the emitted radiation and Coloumb interactions between each other. This results in the loss of electrons since an electron with less energy can no longer follow the prescribed path in the ring, and leads to the necessity of refilling the storage ring with electrons after a certain time, typically on the order of once or twice a day.

One of the advantages of SR is the well defined and reproducible x-ray beam. In order to achieve this, the electron beam in the storage ring has to be very well controlled. But the dipole magnets which bend the electrons on the circular orbit and therefore produce synchrotron radiation also disperse the electron beam. Therefore quadrupole and sextupole magnets have to be used to correct for the dispersion and refocus the electron beam to its original size and dispersion. The most important concept of such an arrangement of dipole, quadrupole and sextupole magnets, mounted in pairs to focus in both dimensions, is the Chasman-Green lattice which was developed for the National Synchrotron Light Source (NSLS) and is now used in most modern SR sources in the world.

A crucial feature of synchrotron sources compared to the standard x-ray sources is the broad spectrum emitted from the circulating electrons. The critical wavelength $\lambda_c$ is defined as the half power point of the spectrum. The critical wavelength is given by

$$\lambda_c = 5.59 \, R[m] \, / E^3 \, [GeV]. \tag{4.2}$$

The long wavelength limit of the synchrotron spectrum is given by the electron-orbit frequency, which is typically in the ns or μs range. The spectrum falls off rapidly for wavelength shorter than $\lambda_c$ and at $\lambda_c / 6$ has only 1% of the maximum. Often instead of the critical wavelength $\lambda_c$ the critical energy $E_c$ is used, which is given by

$$E_c = 2218 \, E^3 \, [GeV] / R[m] = 665 \, E^2 [GeV] \, B[T]. \tag{4.3}$$
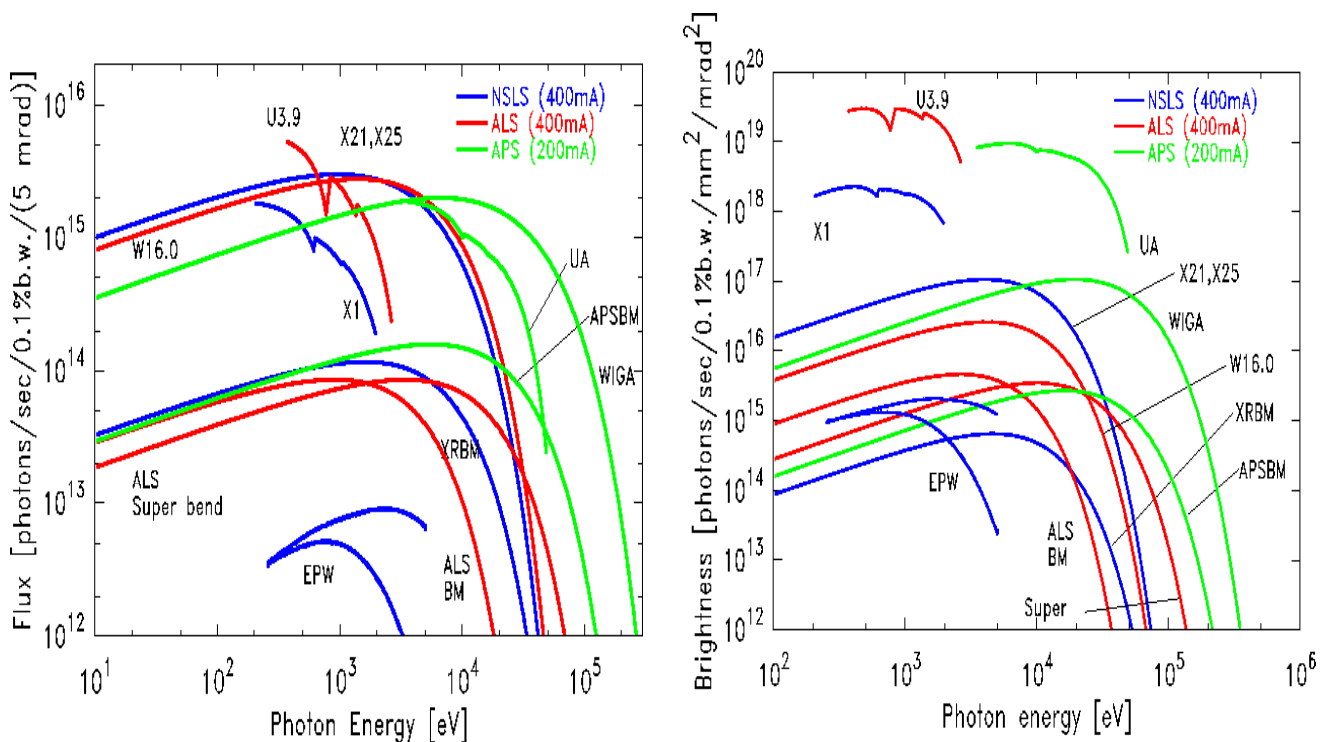


**Figure 4.1** *The total flux and brightness for several beamlines at three synchrotron sources (NSLS, ALS and APS) with different critical energies $E_c$. BM denotes the bending magnet beamlines, U, X1 and UA the undulator beamlines, W, EPW X21, X25 and WIGA wiggler beamlines at the particular x-ray rings (plot made by S.Hulbert).*

Generally the properties of different light sources can be compared in terms of the spectral flux, brightness and brilliance, with the following definitions:

**Flux**: photons emitted per second with the photon energy E and a band pass of $\Delta E/E = 0.1\%$.

**Brightness**: same as Flux normalized for an horizontal acceptance angle $\Delta\alpha = 1$ mrad$^2$.

**Brilliance**: same as Brightness normalized to a source size of 1 mm$^2$

A comparison of the total flux and brightness of several SR sources is shown in figure 4.1. The difference in their operating electron energies can be directly seen in the shift of the critical energy $E_c$. In addition to the higher photon energies the collimation of the radiation and the lifetime of the electrons in the storage ring improves with the increase in the electron energy. On the other hand, radiation protection becomes more difficult. Considering (4.3) there are two ways to shift the critical photon energy $E_c$ to higher values, minimizing the Radius R or increasing the particle energy E. The more effective way is changing the latter parameter, since the increase in the critical energy goes with the third power of E and only linear in R. Furthermore the smallest R is limited by the maximum magnetic field B of the BM technically possible, which is about 10 Tesla. It should be noted that at most storage rings the applied field at the BM is in the order of 1 Tesla or lower in order to allow a high number of experimental stations, which is proportional to the number of bends.

## Angular Polarization of Synchrotron radiation

Another important property of synchrotron radiation is the well defined angular distribution of its polarization. In the orbit plane the circulating electrons emit 100% linear polarized light, but with increasing elevation angle $\psi$ above or below the orbit plane the x-rays become more and more circularly polarized, with an accompanying decrease in intensity. Figure 4.2 shows a typical example calculated from a BM at the NSLS for a photon energy of 7112 eV. In order to receive 75% circularly polarized rays one looses about half of the intensity. Carrying out experiments using circularly polarized light from a BM is always a trade off between the gain in the degree of circular polarization $P_c$ and the loss in intensity I. Assuming Possion statistics for the measured photon distribution, the figure of merit FOM can be calculated with
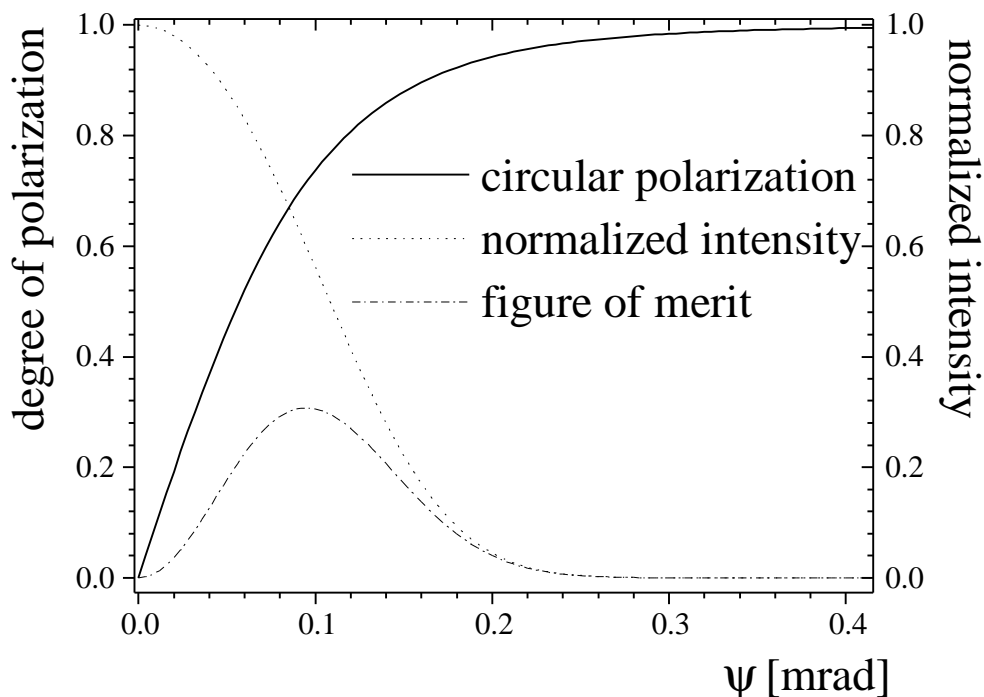
**Figure 4.2** *degree of circularly polarization $P_c$ (full line) and normalized intensity (dashed line) with elevating angle from the orbit plane ($\mathbf{y} = 0$ mrad).*

$$FOM = P_c^2 \cdot I \, , \tag{4.4}$$

and is plotted in figure 4.2. For the conditions shown here (NSLS, 2.8 GeV ring energy, photon energy of 7112 eV), the trade off between intensity loss and the degree of circular polarization, $P_c$, x-rays is optimized for an elevation angle, $\psi$, of about 0.9 mrad. The light is about 70% circularly polarized, but has suffered about 40% loss of intensity.

## Insertion devices

One of the most important features in the Chaseman-Green lattice is the inclusion of dispersion free straight sections. These straight sections are used for radio frequency (RF) cavities providing energy to the circulating electrons, for quadrupole and sextupole magnets that focus the electron beam, for the electron injection line and in particular for insertion devices (ID). These IDs consist of periodic magnetic structures, which "wiggle" the electron trajectory in the straight section of the storage ring but avoid any net deflections or displacements of the electron beam from its original orbit in order not to affect the operation at the BM. The parameter characterizing ID's is the deflection parameter K, defined as

$$K = \frac{e\,B_0\,\lambda_u}{2\pi mc}\;,\tag{4.5}$$

with $\lambda_u$ is the magnet period and $B_0$ the magnetic field at the insertion device. This K parameter describing the motion of the electron beam in an ID classifies the different devices. The maximum deflection angle of the orbit is

$$\delta = \frac{K}{\gamma}\;.\tag{4.6}$$

For $K \leq 1$ the insertion device is called *undulator*. The deflection angle $\delta$ is smaller than $1/\gamma$ and therefore the emitted photons stay in a narrow cone and can interfere with the radiation caused by the next bend of the electrons. This leads to coherent interference of the radiation of a single electron from the different magnetic periods of the ID's and instead of a continuous spectrum a line spectrum with sharp peaks are observed at the wavelengths

$$\lambda_n = \frac{\lambda_u}{2n\gamma^2}(1 + \tfrac{1}{2}K^2)\;,\tag{4.7}$$

with n = 1, 3, 5 … (only odd harmonics have a non-zero contribution to the intensity in the orbit plane). Due to the coherent interference the intensity produced from the magnetic structure of an undulator scales with $N^2$, where N is the number magnetic periods, and leads to a large increase in brightness and flux compared to that of a BM.

For insertion devices with long period lengths $\lambda_u$ of the magnetic structure or high magnetic fields $B_0$ the parameter K becomes much larger than one, $K \gg 1$ and the ID is called a *wiggler*. The radiation emitted from every magnetic pole adds incoherently and thus leads to a continuous spectrum similar to that of a bending magnet, but with a critical energy determined by the peak field in the magnetic structure of the wiggler. Within the deflection opening angle $\delta$ in (4.6) the intensity is 2N higher than from a bending magnet with the same critical energy. Leaving the orbit plane the elliptically polarized light produced from every half pole combines with the light from the next one and since they are of opposite sign the circular polarization cancels. Therefore the radiation produced by a wiggler is linearly polarized even above or below the orbit plane. However, these devices can be modified to tailor them for special applications or demands in polarization. Such an insertion device will be discussed in detail in the next section where a special multipole wiggler is installed at the X-13 beamline at the NSLS in order to produce circularly polarized x-rays in the orbit plane.
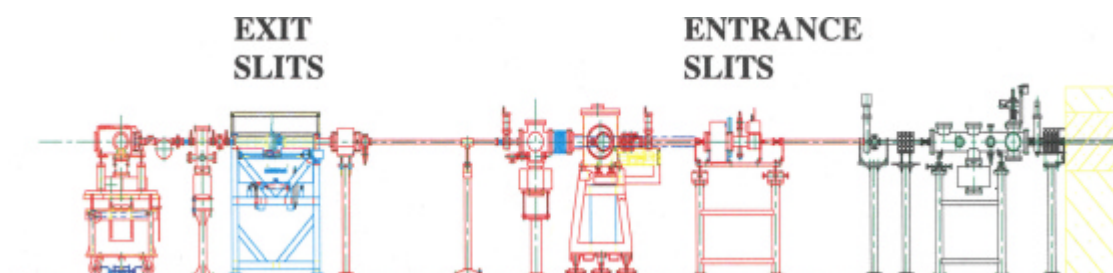
(a)
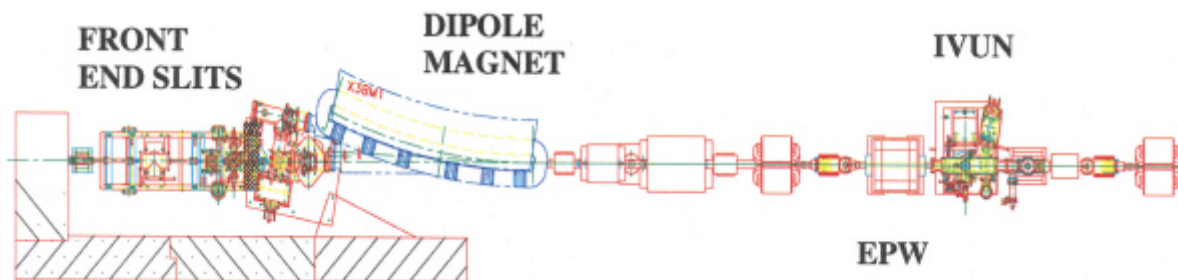


(b)
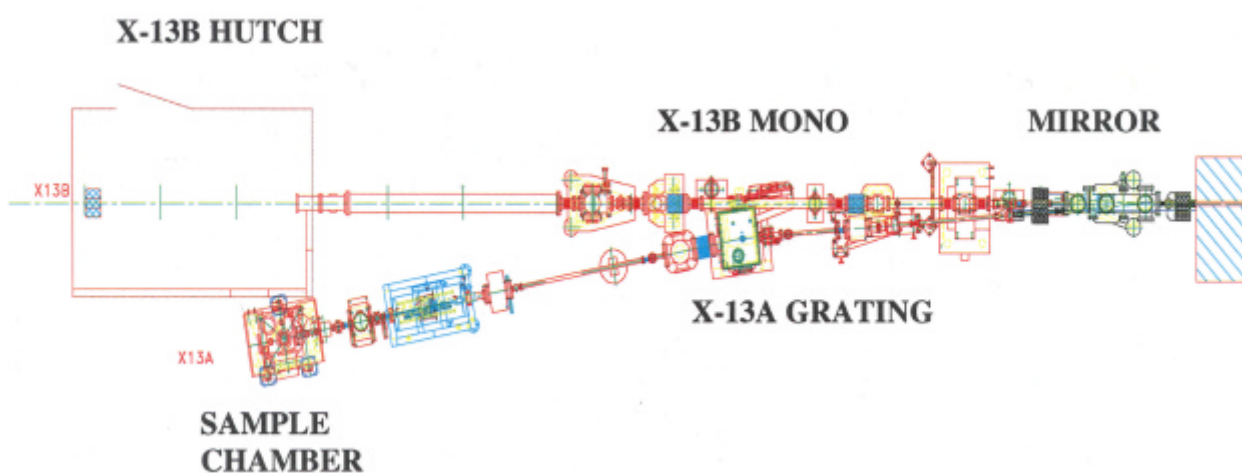


(c)



**Figure 4.3** *Experimental setup of X-13 beamline at the National Synchrotron Light Source at Brookhaven National Laboratory. (a) shows the X-13 straight section with the implemented Elliptical Polarized Wiggler (EPW). In (b) the beamline setup is depicted with both sections, the hard x-ray beamline X-13B going straight and the soft x-ray beamline, X-13A, where the x-ray beam is deflected by a small angle. (c) presents a side view of the X-13A beamline.*

# 4.2 X-13 beamline at the NSLS, BNL

X-13 is one of the eight straight sections in the x-ray ring of the National Synchrotron Light Source (NSLS) at the Brookhaven National Laboratory. 1993 the straight section was adapted to permit insertion devices to be tested, e.g. undulators with special features and a multipole wiggler. The general layout of X-13 can be seen in figure 4.3. The top panel shows the straight section of the electron storage ring for X-13 in which two insertion devices are implemented, an in-vacuum undulator  (IVUN) and an elliptically polarized wiggler (EPW). In this study only the EPW is used and the gap of the IVUN is always driven completely open in order not to affect the performance of the EPW. Two sets of front end slits are used to define the angular acceptance from the EPW and to reduce possible background radiation produced by other sources.

After the safety shutter, where the beam pipe enters the experimental floor (see figure 4.3(b)), a spherical gold-coated mirror with a radius of approximately 140 m is used to horizontally deflect the x-ray beam and makes the operation of two branches, X13A and X13B, possible. These branches, X13A and X13B, are designed for soft and hard x-rays, respectively.

## 4.2.1 The Elliptical Polarized Wiggler (EPW)

As already mentioned in 4.1 using circularly polarized light from a bending magnet suffers from a significant loss of intensity with increasing degree of circular polarization. Additionally in many experiments using circularly polarized x-rays, it is desirable to measure both helicities at the same time or at least shortly after one another, which is very difficult using a BM source. As a way to overcome this problem people have designed elliptical multipole wigglers that have switchable polarizations. The principle was proposed by Yamamoto and Kitamura [84] in 1987 and later modified by Walker and Diviacco [85]. Such an elliptical multipole wiggler device consists of two wiggler systems, where the second one is orthogonal out of phase with respect to the first one by one half pole. This magnetic arrangement forces the electron beam on a spiral-like path, thus the radiation from such a device is elliptically polarized. Furthermore the emitted x-rays from each bend add up, rather than canceling, and lead to higher intensities.

The Elliptical Polarized Wiggler (EPW) - a collaboration between Brookhaven National Laboratory (BNL), Argonne National Laboratory (ANL) and the Budker Institute of Nuclear Physics in Novosibirsk, Russia - was installed at the X-13 straight section of the NSLS in December 1994 [86, 87]. The vertical wiggler consists of an array of permanent magnets while the horizontal one was replaced by an electromagnetic wiggler that permits the modulation of the helicity of the on-axis circularly polarized radiation in time. Figure 4.4 shows the schematic view of the EPW. The vertical wiggler is a hybrid structure, consisting of Nd-Fe-B rectangular magnetic blocks and vanadium-permendur wedge poles, producing the vertical magnetic field. It has five full poles and two half strength end poles. The electromagnetic wiggler consists of six full strength poles and the end correction is provided by two $3/4$-strength and two $1/4$-strength poles. The most important parameters are listed in table 4.1.

| Parameter | Permanent Magnet | Electro-Magnet |
|---|---|---|
| Magnetic period [cm] | 16 | 16 |
| Peak field [T] | 0.8 | 0-0.2 |
| Deflection parameters K | 10 | 0-3 |
| Magnetic gap [mm] | 27 | 54 |
| Camber aperature [cm] | 2.5 | 5.0 |
| Switching frequency | 0 | 0-100 |

**Table 4.1** *Charactistics of the EPW for the permanent and electromagnetic wiggler structure [86]*

The EPW was commissioned during spring 1995 at a switching frequency of 2Hz. By utilizing trim coils and the global feedback system the orbit fluctuation produced by the electromagnetic wiggler is very much reduced. An orbit motion of less than 1.5 microns could be observed [88].
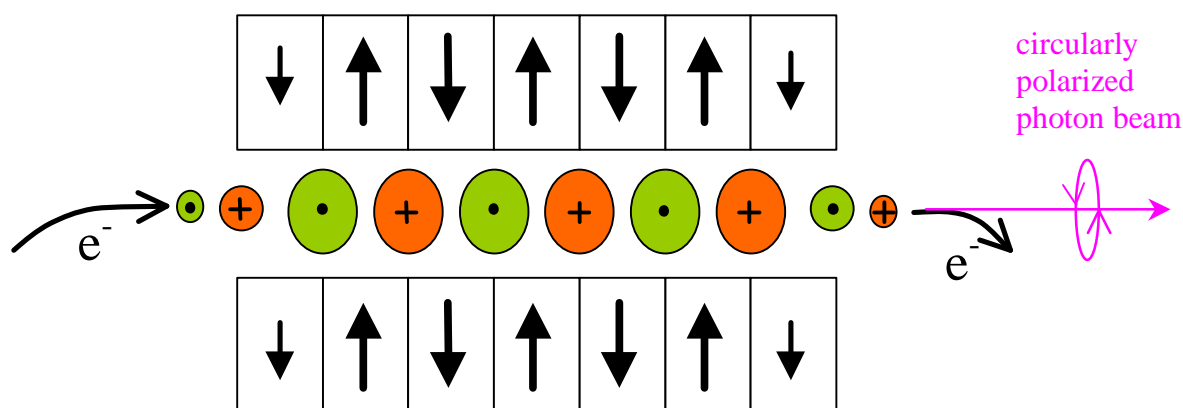
**Figure 4.4** *Schematic top view of the magnet arrangement of the EPW. Permanent magnets are shown as rectangles with arrows, electromagnet as circles with the sign indicating the magnetic field directions. More detailed explanation in text.*

One of the advantages of the EPW is its ability to switch the current driving the electromagnets of the horizontal wiggler, which results in a change in the helicity of the emitted x-ray beam from the EPW. This switching can occur with a frequency up to 100 Hz and enables the use of lock-in techniques for the signal detection. By excluding all other interfering frequencies than the modulation frequency the systematic background produced by other sources, e.g. electronic noise, vibrational noise etc, can be reduced. The lock-in technique is especially useful for weak signals sitting on top of a strong background. This is the case with the weak magnetic x-ray signal on top of the strong scattering of the x-rays from the charge distribution. However, in the scope of this work a switching frequency of 2 Hz was used. The top part of figure 4.5 shows schematically the switching of the current of the electromagnetic wiggler. The time it actually takes to switch from -400 A to +400 A is about 2 msec, which is exaggerated in the figure 4.5. It should be mentioned that a current of 400 A corresponds to an horizontal deflection parameter $K_x$ of 1.0 and was used during all the experiments in this study. The oscilloscope trace in the lower panel shows the response of an ion chamber downstream of the Si (111) channel cut monochromator. Every time the current switches and the polarization changes from left to right circular and back again, linearly polarized light sweeps through the orbit plane for a short moment and a huge spike can be seen in the trace. A set of slits between the monochromator and
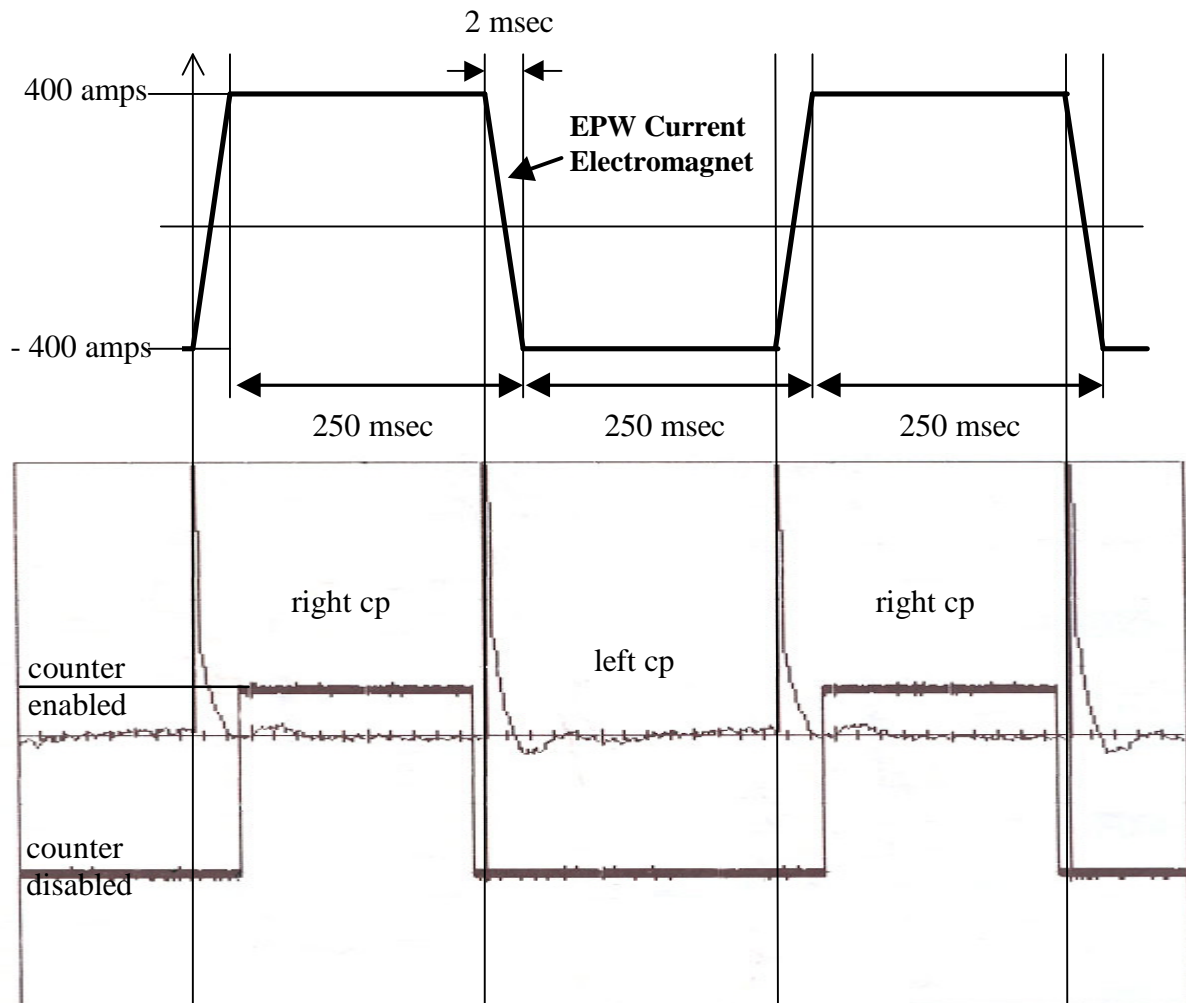
**Figure 4.5** *Top figure: Switching of the current at the electromagnets (schematically), bottom figure: response signal measured with ion chamber after monochromator. A time delay device enables counter only to certain time intervals indicated by the boxes, and therefore separates right and left circular polarization (cp).*

ion chamber, which were used to select a certain portion of the beam from the EPW, were adjusted to equalize the intensities for the left and right circular polarization. It should also be noted that about 20 msec is necessary to stabilize the circularly polarized light after the switching, compared to the 2 msec needed for the switching of the current of the electromagnet. This makes the duty cycle unfavorable at higher frequencies, especially in frequency region where there is very low background (61-100 Hz). For example, even at 25 Hz only half of the time can be actually used.
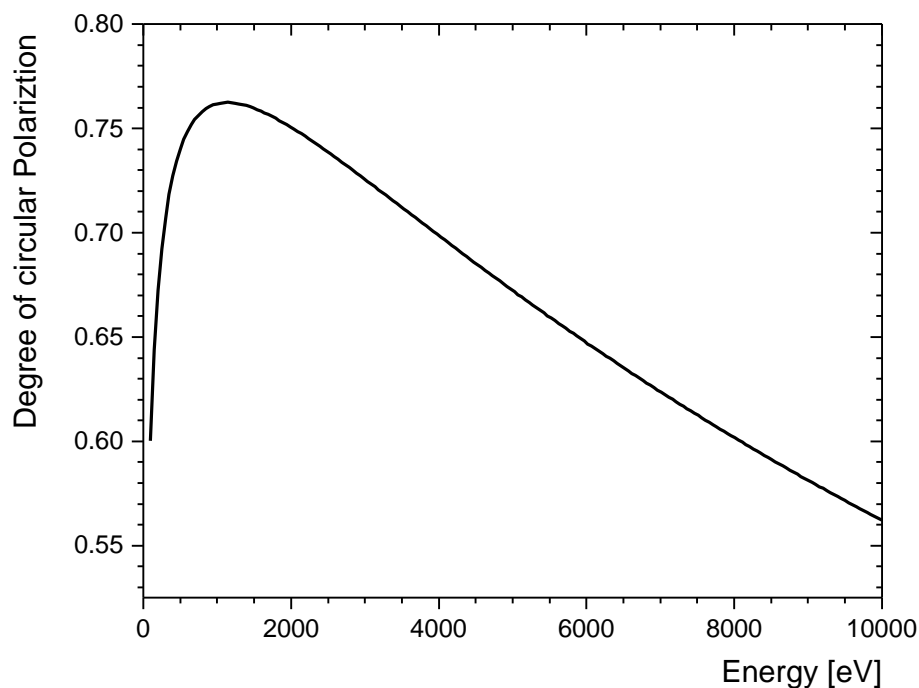
**Figure 4.6** *Calculated values for the degree of polarization for EPW settings of $K_x = 1.0$ and $K_y = 10$ [146].*

Figure 4.6 shows a calculation of the degree of circular polarization considering the deflection parameter used in the experiments performed at the X13 beamline here in the work. In the hard x-ray region a circular polarization of around 60% is expected with slow variations, while in the soft x-rays the value changes more rapidly between 60% and 76%.

## 4.2.2 Soft X-ray branch X-13 A

The X-13A beamline, schematically shown in figure 4.3 (b) and (c), is designed for soft x-ray operation. Since soft x-rays are strongly absorbed in air all optical elements and the experimental setup operates under ultra high or high vacuum conditions. As already mentioned, a gold-coated mirror is moved into the x-ray beam in order to deflect it into the X-13A beamline. This mirror accepts about 0.5 milliradians of the beam from the EPW and deflects it through an angle of 4°. At the same time the photon beam is focused horizontally on the entrance slits of the spherical grating monochromator located 4 m downstream of the mirror. The grating has a radius of 57.3 m and disperses in the horizontal plane with the exit axis displaced by 6° from the entrance slits. Two gold coated gratings with groove densities of 800 mm$^{-1}$ and 1600 mm$^{-1}$ are mounted on a vertical shaft and can be interchanged without breaking

the vacuum, allowing the monochromator to cover an energy range from 250 eV to up to 1800 eV. Since the entrance and exit directions are fixed, the focusing conditions (Rowland circle) in the dispersion (horizontal) plane for all wavelengths is only fulfilled by moving the exit slits which are mounted on a translatable platform. With every change in the wavelength the position of the exit slits have to be also changed. Between the exit slits and the sample chamber a rotating blade chopper is installed, which enables one to obscure the linearly polarized peak. Directly downstream of the chopper a gold mesh detector monitors the intensity of the incident beam. The sample chamber is schematically shown in Figure 4.7. This vacuum chamber includes a two circle goniometer for reflectivity. The sample stage can be rotated by 360° independently of the detector arm which is restricted to 90° and has a horizontal slit system in order to define the $Q_z$-resolution. The distance between sample and the slits directly in front of the detector is 23 cm and the typical detector slit size is 1.6 mm, resulting in a resolution of 0.40°. The sample can be mounted on an electromagnet, which applies a field in direction of the photon wave vector to maximize the magnetic effect. A bipolar power supply controls the magnet current and is connected through an interface to a computer to allow e.g. magnetic measurements as a function of the applied field.
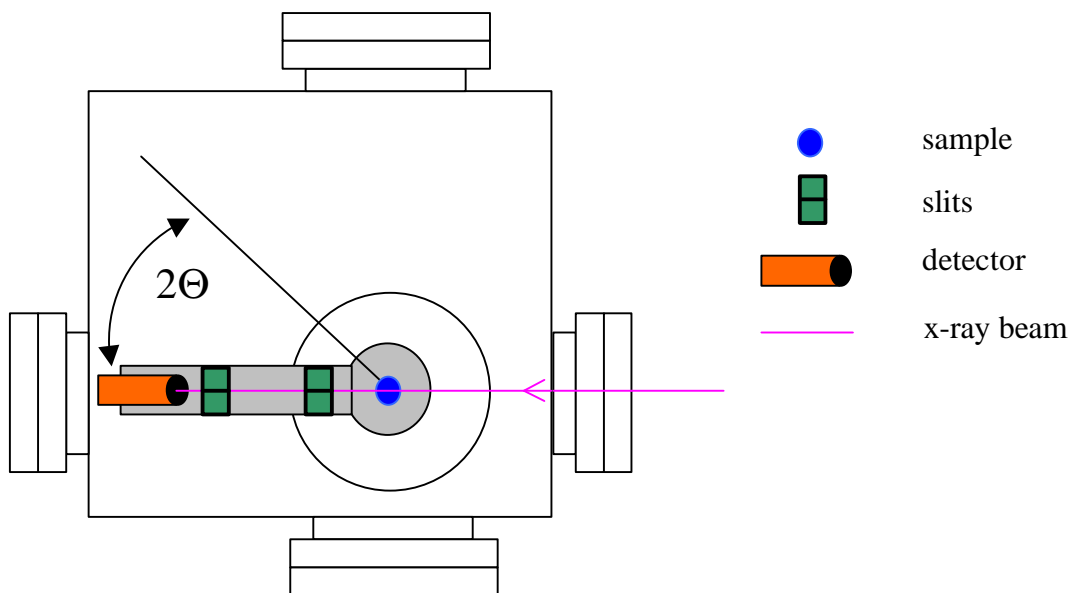


**Figure 4.7** *Top view of the sample chamber attached on X-13A beamline for reflectivity measurements. Chamber is kept under high vacuum. Important to note that diffraction plane lies in the horizontal plane.*

## Signal detection

At the X-13A branch the detection of the signals is provided by lock-in amplifiers. Basically the lock-in technique enables simultaneous detection of the difference as well as the sum of the scattered intensity from left and right circularly polarized light, which are switched with a frequency f. The recorded intensity I(t) can be divided in its Fourier components [89]:

$$I(t) = I(0) + \frac{\sqrt{2}}{\pi}(I_\uparrow - I_\downarrow)\sin(\omega t) - \frac{1}{\pi}(I_\uparrow + I_\downarrow)\cos(2\omega t) + \ ... \ , \qquad (4.8)$$

where $\omega = 2\pi f$ , $I_\uparrow$ and $I_\downarrow$ are the measured intensities from left and right circularly polarized light. By Fourier transformation of I(t) the specific components in the frequency spectra can be separated from the others and back-transformation leads ideally to a signal clear of any other
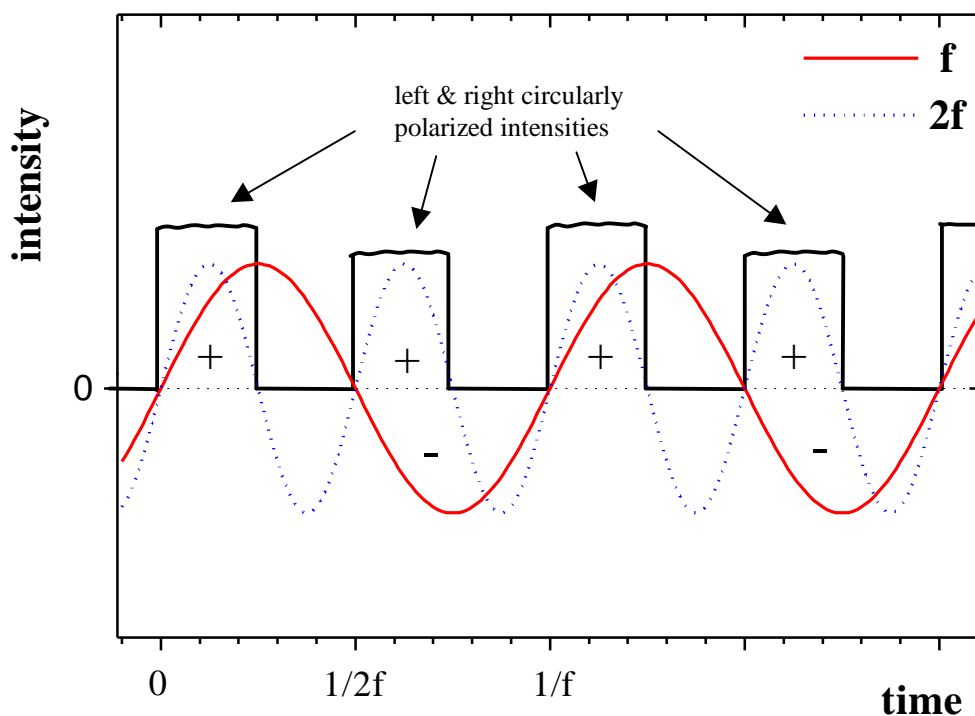


**Figure 4.8** *Detection of difference signal between left and right circularly polarized x-ray intensities using lock-in technique after modulating signal with a frequency f. Amplifier using frequency f (full line) and 2f (dashed line) detect the difference and the sum of the different helicities.*

distribution. Equation (4.8) shows that by selecting f and 2f , the difference and the sum signal of both circular polarizations can be separated.

The method of this lock-in technique is shown in a simplified picture in figure 4.8. After the spikes of linear polarized intensity (see figure 4.5) are blocked out, only the signals from the circularly polarized light remain (full square pattern in figure 4.8). The full and dashed lined sinusoidal waves with the frequency f and 2f illustrate mathematically the Fourier components for the frequency components f and 2f. By summing up the intensity using the sign for every wave indicated in figure 4.8, the detection with the wave of frequency f and 2f measure the difference and the sum of the left and right polarized intensities, respectively.

The full scheme of signal detection mechanism is shown in figure 4.9. First the chopper, running with the frequency 2f, blocks the linear spike from the EPW emitted light. A gold mesh monitors the remaining intensity and a diode detects the reflected intensity from the sample. The signals from the gold mesh and the diode are converted from current to voltage (I $\rightarrow$ V) and fed into three lock-in amplifiers. Two lock-in amplifiers (lock-in amp 2 and 3) connected to the diode and mesh signal are fed with the frequency 2f and thus provide the sum of the left and right polarized intensity of the signal I and the monitor intensity $I_0$, respectively. On the other side, lock-in amplifier 1 is also connected to diode but fed with the frequency f so that it measures the difference signal $\Delta I$. The frequency f and 2f, which are fed into the lock-in amplifiers are generated from the switching frequency of the EPW current. The switching signal is in phase in order to block the linear intensity with the chopper [89].
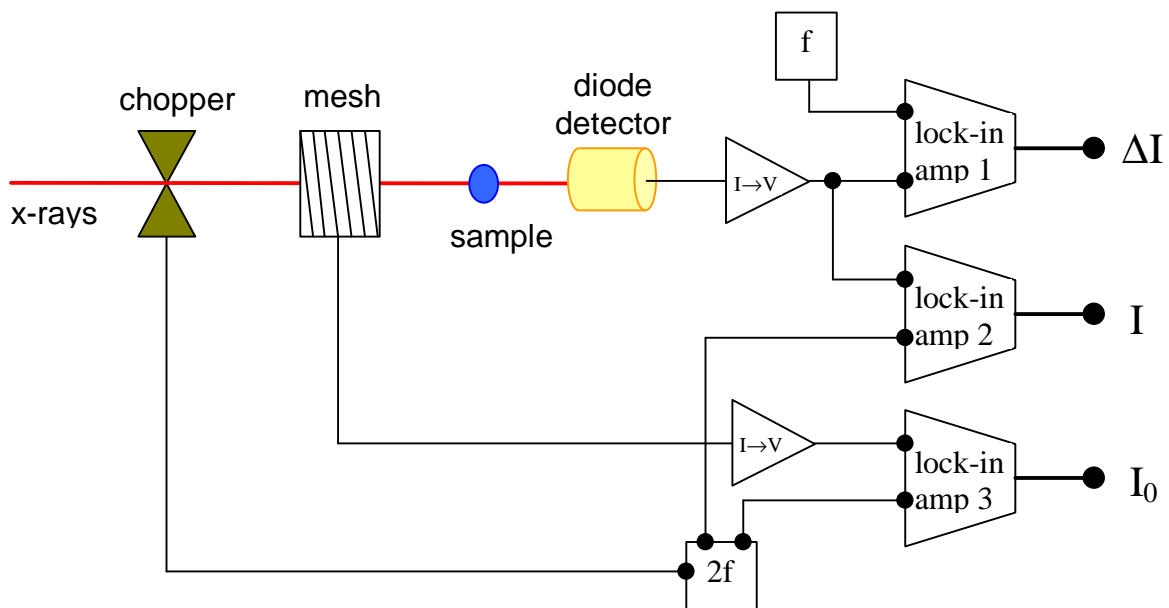


**Figure 4.9** *Schematic view of the signal detection mechanism at the soft x-ray beamline X-13A. For a more detailed description see text.*

## Flux and degree of circular polarization

The spectral intensity output of circularly polarized photons for both gratings with groove densities of 800 mm$^{-1}$ and 1600 mm$^{-1}$, respectively, is presented in figure 4.10. The intensity is detected by a diode detector with a horizontal and vertical slit size of 200 μm x 1 mm, respectively, and at x-ray current of 220 mA. The entrance slits were also set horizontally to 200 μm. From the measured current and the quantum efficiency of this particular diode the number of photons per second are calculated and plotted on a logarithmic scale in figure 4.10. Both spectra have an overlap point which is at about 720 eV close to the Fe-L-edge. Several dips can be observed in the intensity spectrum. They can be assigned to absorption edges of *light* elements like carbon, nitrogen and oxygen, which are still present in the high vacuum of the sample chamber. In this study, the grating with a groove density of 800 mm$^{-1}$ was used. At 700 eV close to the iron L-edges, about $2.8 \cdot 10^9$ circularly polarized photons can be detected for a spot size of 200 μm x 1 mm. The energy resolution was measured at the nitrogen K-edge at around 400 eV and resulted in an $\Delta E/E = 4 \cdot 10^{-4}$ for an entrance and exit horizontal slit size
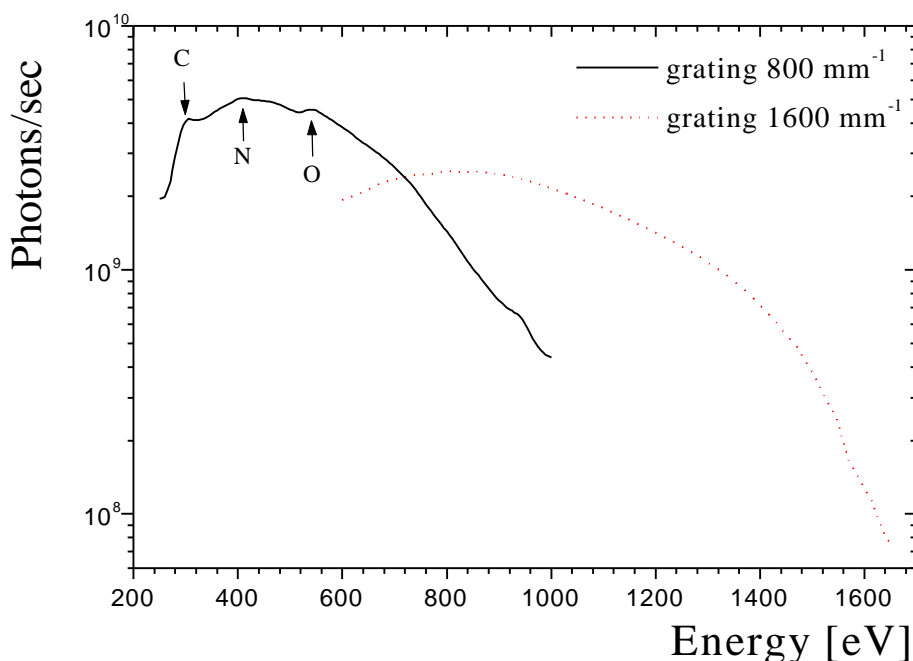


**Figure 4.10** *X-ray intensity in number of circularly polarized photons per second for both gratings with 800 mm$^{-1}$ and 1600 mm$^{-1}$ grooving densities measured by the diode detector. The slits were opened 200 **m**m (horizontal) x 1mm (vertical) at a ring beam current of 220 mA. The arrows indicate the K-absorption edges of carbon, nitrogen and oxygen, respectively.*

of 25µm, respectively [90]. In the case of a slit size of 200 µm the energy resolution is much lower. Calculated values predict $\Delta E/E$ on the order of $10^{-3}$.

The degree of circular polarization was measured by Kao et al. via MCD on a single iron film [31]. At a horizontal deflection parameter of $K_x$ of 1.0 the measured spectra corresponded only to a value of about 60% for the degree of circular polarization which is much lower than the calculated value seen in figure 4.6. This is perhaps due to variations in the field of the electromagnet caused by imperfections in both magnetic wiggler structures which would lead to a drop in the degree of circular polarization. For the calculations of the magnetic effects measured in the soft x-ray region a value of about 60% is assumed keeping in mind that the value can vary by several percent.

## Scan modes

The beamline computer controls orientation of the grating and the position of the exit slits via the serial port (RS-232). Both have to be moved simultaneously in order to track the focus point as the energy of the x-rays is changed. The $\theta$ and $2\theta$ motors controlling the sample and detector angles in the sample chamber, respectively, are connected through a GPIB-board and can be moved independently in order to allow adjustment and also offset scans, in which $\theta$ has a a small offset of $\Delta\theta$ from the $\theta/2\theta$ condition. Also the sample magnet power supply is controlled via GPIB from the computer, which can be driven from -20 A to 20 A and provides a magnetic field at the sample from -1.2 kOe to 1.2 kOe.

Basically, three main scan parameters determine the measurements, the incident photon energy, E, the angular position of sample and detector, $\theta$ and $2\theta$, respectively, and the applied magnetic field on the sample, H. In general, all three parameters can be varied at the same time, but usually two are kept constant while the change of the signal is recorded. These three basic scans are called energy, angular reflectivity and magnetization scan, in which the energy, the angular reflectivity position or the magnetic field applied at the sample is varied, respectively, while the other parameters are kept constant. The magnetization scan is usually carried out in a loop by returning to the initial magnetic field and is therefore a hysteresis loop measurement. All these scans are used and shown in more detail in chapter 5, which describes the magnetic x-ray reflectivity measurement on a Fe/Cr double multilayer sample.

## 4.2.3 X-13B: Hard X-ray Beamline

With the mirror out of the pathway, the x-rays produced by the elliptically polarized wiggler pass straight to the other branch of the beamline labeled X-13B, which is designed for hard x-ray operation. After some radiation protection lead shields and valves the first and only optical element in this branch is a channel-cut Si (111)-crystal monochromator. Before the monochromator, the vertical acceptance for the divergent wiggler beam can be selected by four different slits, which have two sizes of 2 mm and 4 mm with and without a graphite filter. The monochromator has a gap between the first and the second crystal of 0.69 cm (0.27 inches). This work has focussed on the K-edges of the 3d-transition metals, e.g. of iron, cobalt and nickel energies of 7.112, 7.709 and 8.332 keV, respectively, which leads to 13.7°, 14.8° and 16.4°, respectively, for the Bragg angle of the monochromator crystal. The accepted bandwidth is about $\Delta E/E = 10^{-4}$. The second part of channel cut crystal can be tilted slightly with respect to the first by a piezo-element motor and thus reduces third and higher harmonics of the selected wavelength.

After the monochromator tank a water-cooled beam stop is mounted to prevent any unintentional white beam operation in the event that the monochromator angle is driven to zero. In monochromatic operation a photon shutter in front of the hutch allows to open and close the beam before the beam pipe enters the hutch. Two 0.25 mm thick beryllium windows in the beam hutch are used to protect the ultra high vacuum of the beamline. These beryllium windows together absorb less than 15% of hard x-rays for photon energies above 6 keV.

### X-13B-hutch

Basically two different magnetic measurements were performed in the X-13B hutch, Magnetic Circular Dichroism Absorption (MCD) experiments and Resonant Magnetic X-ray Reflectivity. The MCD setup is shown in the upper part of figure 4.11. A slit system, consisting of horizontal and vertical slits (here in the figure only the vertical slits are shown) define the incoming x-ray beam. Typically, slits of 1 mm (vertical) x 10 mm (horizontal) were used for the MCD-absorption experiment. An ion chamber after the slits monitors the incoming intensity before the beam hits the sample. For the MCD experiment, usually a transmission foil is used, which is mounted on an electromagnet at an angle of about 45° as shown in the figure

4.11. The electromagnet used for all MCD-measurements in this study provides a maximum magnetic field of 350 Gauss. The top part of the poles have a rectangular portion removed in order to allow the beam to be exactly parallel or antiparallel to the magnetic field direction. A second ion chamber detects the transmitted beam. Finally, a lead beam stop is used to absorb the high energy x-rays for safety reasons.

The second setup used at the X-13B hutch for magnetic resonant x-ray reflectivity is shown in figure 4.11 (b). Exactly as the setup described for the MCD measurements, the beam is first defined by entrance slits and its intensity monitored by an ion chamber. A typical size of 0.5 mm for the vertical slit is chosen in order to provide better $Q_z$-resolution. Since the resolution in the other directions is unimportant for specular reflectivity experiments, the horizontal slit size is always maximized and thus depends on the sample width. The same electromagnet was used with the sample mounted flat on a sample stage. The whole magnet with sample can be tilted at the angle $\theta$ in the plane of incidence. The x-ray beam reflected from the sample at $2\theta$ passes through a collimation pipe filled with helium, on which two slit systems, both with horizontally and vertically defining blades, were mounted at the beginning and end, respectively. The first, the collimation slits, help to get rid of unwanted scattered x-rays, and reduce the effects coming from the divergence of the beam. The second, the detector slits, define the $Q_z$-resolution of the experiment with

$$\Delta Q_z = \frac{4\pi}{\lambda}\cos\theta\,\Delta\theta \tag{4.8}$$

and

$$\Delta\theta = 2\cdot\arctan\left(\frac{d}{2l}\right) \tag{4.9}$$

with d as the vertical slits size of detector slits and l as the distance between sample and detector slits. For typical values of d = 1 mm and l = 148 cm an angular resolution of $\Delta\theta \approx 0.04°$ can be achieved.

(a)



(b)
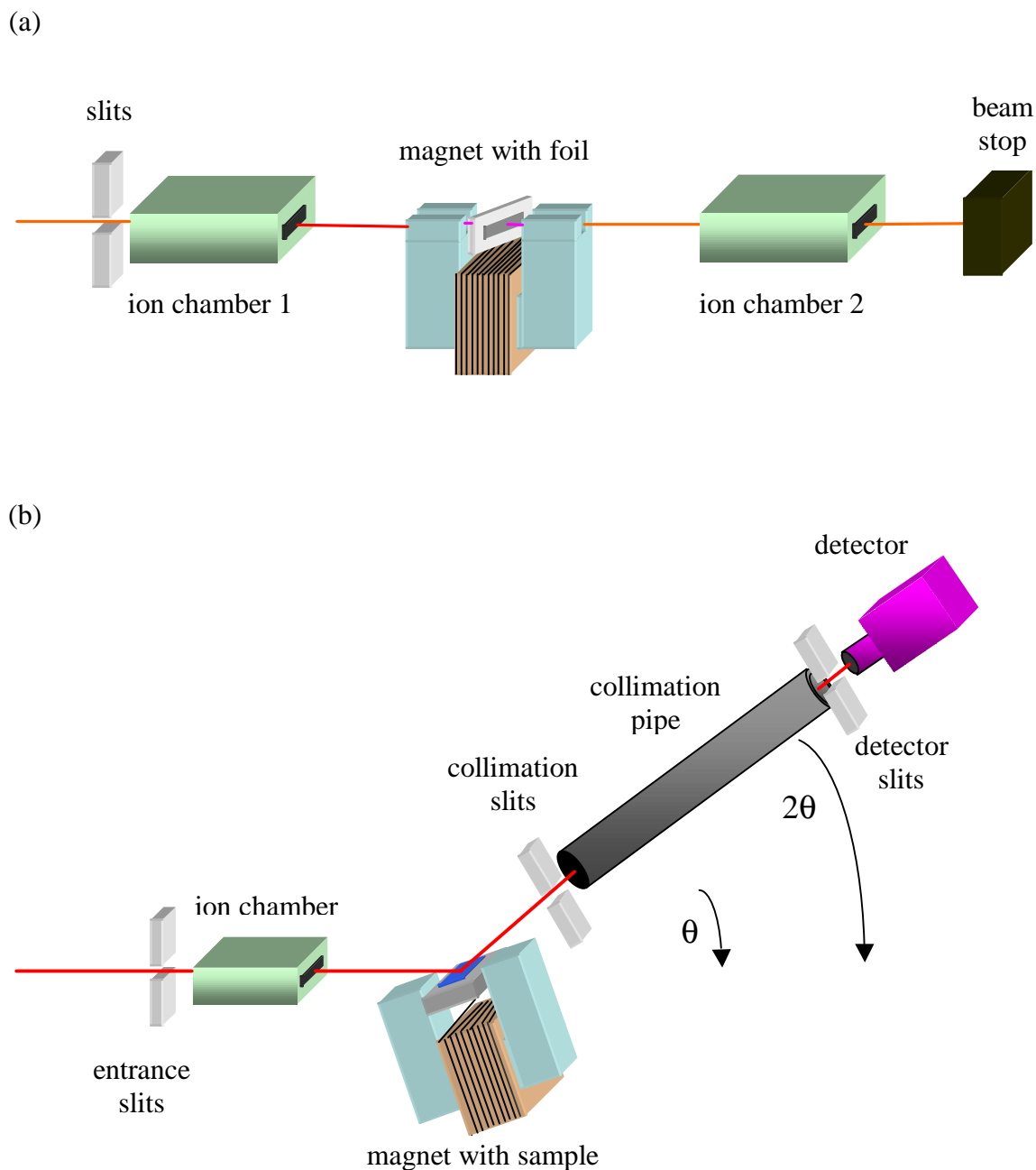


**Figure 4.11** *Experimental setups at the X-13B beamline at the NSLS, Brookhaven: (a) setup for MCD experiment, here shown on a metallic foil; ion chamber 1 is the monitor, ion chamber 2 the detector; (b) setup for specular reflectivity (charge and magnetic). The collimation pipe is filled with helium to avoid strong absorption by air. The sample is mounted on the electromagnet.*

## Signal detection

At the X-13B branch the signal is detected by using the photon counting method. As it implies, it is based on a detector which is able to count single photons. Contrary to the lock-in technique it requires counting all channels separately and calculating the sum and the difference of the single measured intensities afterwards. The detection procedure is shown schematically in 4.13. The circularly polarized components of x-rays produced by the wiggler, which is running with a switching frequency f, are separated by a time delay device into two separate channels. Triggered by the EPW switching signal, the time delay generator enables the counter for a certain time frame between the two switching pulses indicated by the boxes in figure 4.12. During the switching between left and right circularly polarized light, resulting in big spikes in the intensity, the counters are disabled. In order to separate left ($I\downarrow$) and right ($I\uparrow$) circularly polarized light, the delay generator possesses two channels which are gating the counters and are illustrated in figure 4.12 as two separate rows. Each of the channels for left and right circularly polarized light are further separated depending whether the magnetic field on the sample is aligned parallel or antiparallel to the helicity of the incoming light and split in four different channels $I\uparrow\uparrow$ , $I\uparrow\downarrow$ , $I\downarrow\uparrow$ and $I\downarrow\downarrow$ , where the first arrow indicates the helicity of the
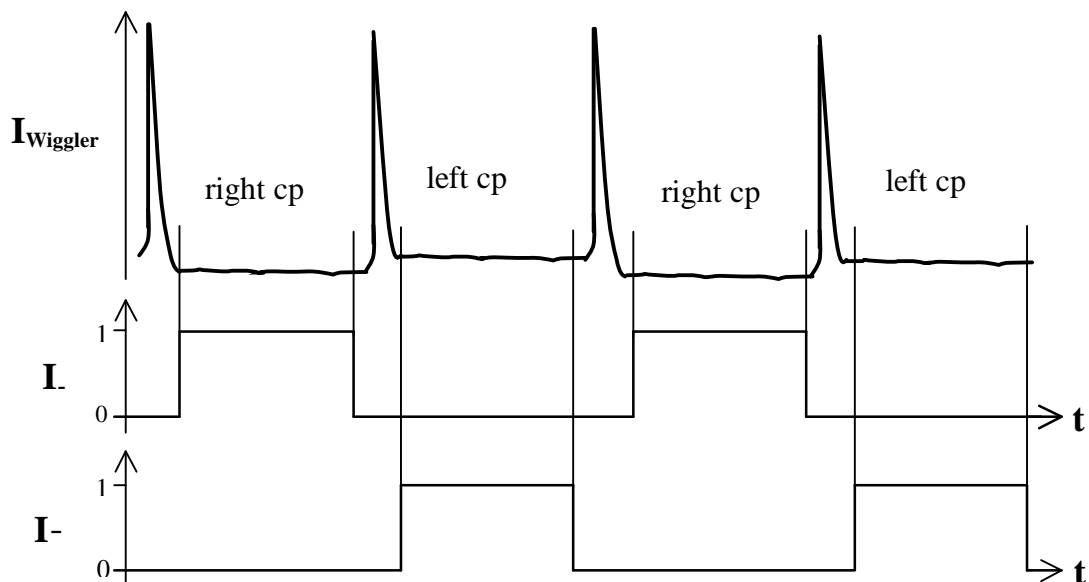


**Figure 4.12** *Incoming intensity produced by EPW is counted in two channels $I$₋ and $I$-,, respectively. Time delay unit enables counting only in certain time intervals shown as boxes above and disables counting during switching of the helicity.*
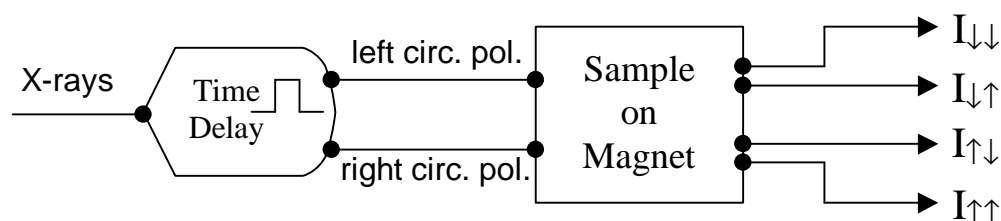
**Figure 4.13** *Scheme of the data processing at X-13B. Left and right circularly polarized x-rays get seperated by an time delay device. Additionally to the two different magnetization directions at the sample, the four distinguishable channels are counted, labeled $I_{\downarrow\downarrow}$, $I_{\downarrow\uparrow}$, $I_{\uparrow\downarrow}$ and $I_{\uparrow\uparrow}$.*

polarization and the second the magnetic field direction. All four components of the measured signal are detected separately in four different counter channels and can be then used for calculating the sum, difference and asymmetry ratios.

Typically the EPW was operated with 2 Hertz as shown in figure 4.5. In the 2 Hertz mode 200 msec of the 250 msec time interval between switching of the EPW could be used for measurements. The remaining 50 msec are lost due to the linear spike occurring at the switching and the short stabilization time after it.

In principle it is possible to look at the difference signal between left and right circularly polarized light with this method. Unfortunately it turned out that the energy of the photons from both helicities have slightly different energies, which is probably due to a small angle shift in the incident beam at the monochromator. Figure 4.14 shows an absorption experiment on a non- magnetic manganese foil at the manganese K-edge. The upper and lower plot shows the transmitted intensity (full line) and the asymmetry ratio between right and left circularly polarized x-rays (open circles), respectively. Clearly large changes of magnitude appear while the energy was tuned through the absorption edge of manganese. These features are largest when the transmitted intensity makes the biggest changes. Comparing the asymmetry ratio with the derivative of the transmitted intensity (dotted line) shows a close similarity and suggests an energy offset between helicities. In order to confirm that, the intensities for both helicities were slightly shifted by an amount of $\Delta E$ and the asymmetry ratio recalculated. The results are presented in figure 4.15, showing the different asymmetry ratio for different $\Delta E$s. The best result was achieved with $\Delta E = 8$ meV, indicating that a very small energy shift can lead to large artificial effects. The MCD-signal which is extremely small for the 3d transition metals at
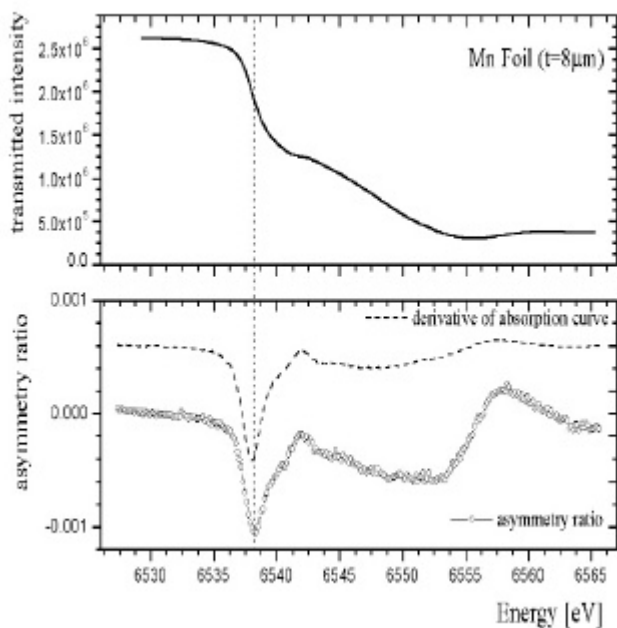
**Figure 4.14** *Absorption measurement of manganese foil (8mm) at the manganese K-edge using difference of left and right circularly polarized light of the EPW. Upper plot shows transmitted intensity and lower plot the asymmetry ratio (circles) and the derivative of the transmitted intensity (dashed line)*
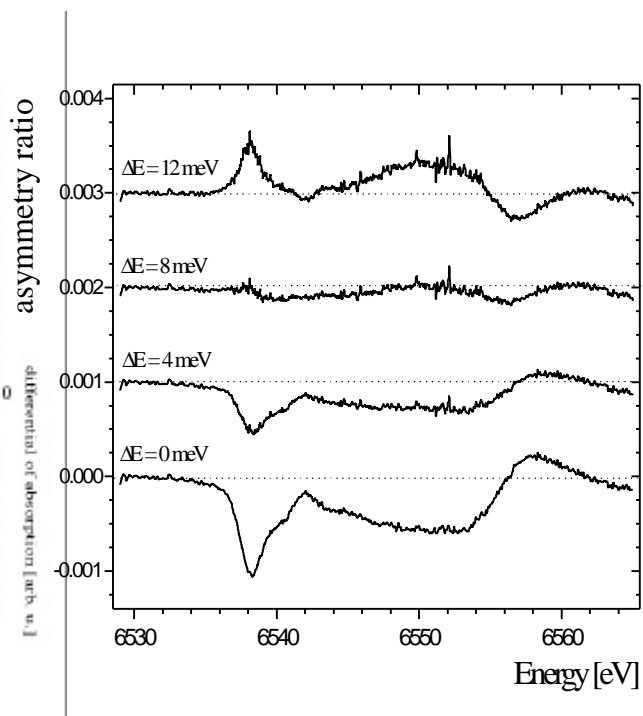
**Figure 4.15** *Asymmetry ratios of measurements at the manganese foil at the manganese K-edge (see figure 4.14). The measured intensity for left and right circularly polarized light was shifted to each other of an amount of **DE** = 0, 4, 8 and 12 meV.*

the K-edges are strongly influenced by this artifact and even by correcting of the energy shift the signal still exhibits some deviations from the expected signal as seen in figure 4.15. Moreover, since the energy shift varies with the photon energy, it is hard to transfer the result from the manganese K-edge to other edges to separate the real MCD or magnetic scattering signal from this artifact.

However, as already mentioned before, it is basically equivalent to take the difference and sum by changing the saturation magnetization of the sample with fixed helicity of the photon beam, as long as two intensities are considered which have the helicity parallel and antiparallel to the magnetic field direction, respectively. Even though the difference between the two helicity states really cannot be used, it can be very helpful to look at both helicity channels separately. They should give opposite magnetic signals and can therefore give further confirmation of the magnetic nature of the signal.

## Characterization

The two key properties of a beamline chosen for magnetic x-ray experiments involving the MCD effect are flux and the degree of circular polarization. As pointed out in the first paragraph of this chapter the figure of merit is given by formula (4.4) by assuming that the photon distribution obeys Poisson statistics. Therefore, by a gain in polarization of a factor g, only $1/g^2$ in intensity is necessary to achieve the same statistic as with the original polarization and intensity.

Figure 4.16 shows the number of photons per second measured by a diode detector at a beam spot size of 0.5 mm (vertical) x 10 mm (horizontal) in an energy range covering the K-edges of iron, cobalt and nickel. At the iron edge (7112 eV) about $4.5 \cdot 10^9$ photons per second are available. Considering the critical energy of 3.552 keV produced by the typical EPW settings, it is seen that the maximum of the curve is at around 7600 eV much higher than actually expected. This can be explained by the stronger absorption of the lower energy x-rays by air, where they have to pass through around 50 cm until they get detected by the diode. In figure 4.16 the transmission coefficient for the x-rays through 50 cm of air is plotted, which is approximately the air path between the x-rays leaving the beam pipe and the diode which
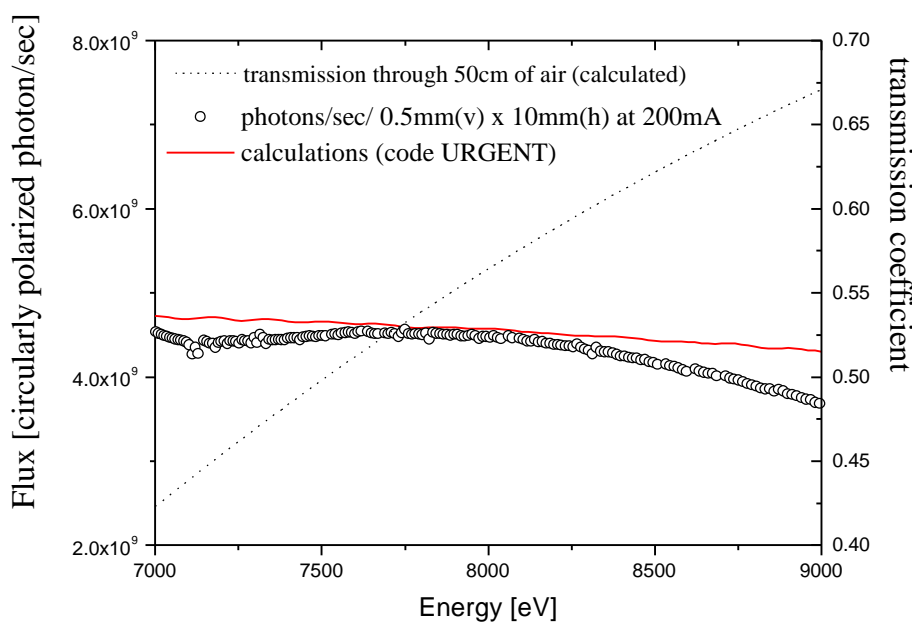


**Figure 4.16 N***umber of elliptical polarized photons per second detected in a spot size of 0.5 mm (vertical) x 10 mm (horizontal) at a ring current of 200 mA. Full line shows calculated (code URGENT) flux for the EPW with deflection parameter $K_x=1.0$ and $K_y=12.0$ in consideration of the air absorption (dotted line)*

detected the flux. It clearly shows the much stronger absorption of lower energy photons. Calculations of the flux of the EPW for the deflection parameter $K_x = 1.0$ and $K_y = 10.0$ [92] used in the experiments and including the absorption of the air path in the experiment shows very good agreement with the measured spectrum.

## Degree of polarization

In order to determine the degree of circular polarization of the EPW in the hard x-ray region a MCD-experiment was carried out. Since the spin-dependent absorption coefficient for iron is already known from various experimental studies [8, 34, 93], it can be used to characterize the degree of circular polarization.

Light transmitted through a material of thickness t and absorption coefficient of $\mu$ is reduced in intensity obeying the absorption law,

$$I = I_0 \cdot e^{-\mu \cdot t}. \tag{4.9}$$

As already pointed out in chapter 2 (eq. 2.23), the absorption coefficient $\mu$ in the case of a magnetic material for circular polarized x-rays can be separated into a spin-independent part $\mu_0$ and a spin-dependent part $\mu_c$ and can be written

$$\mu = \mu_0 \pm P_c \cdot \mu_c \tag{4.10}$$

where $P_c$ is the degree of circular polarization of the incident x-rays. Depending if the helicity of the x-rays are parallel ($\uparrow\uparrow$) to the direction of the magnetization or antiparallel ($\uparrow\downarrow$) the transmitted intensity can be now formulated as

$$I_{\uparrow\uparrow \, (\uparrow\downarrow)} = I_0 \cdot e^{-(\mu_0 \pm P_c \mu_c) \cdot t}. \tag{4.11}$$

The asymmetry ratio is defined as the difference divided by the sum. By putting in (4.11) for the spin-dependent transmitted intensities leads to following equations

$$\begin{aligned} \frac{\Delta I}{I} &= \frac{I_{\uparrow\uparrow} - I_{\uparrow\downarrow}}{I_{\uparrow\uparrow} + I_{\uparrow\downarrow}} = \frac{I_0 \cdot e^{-(\mu_0 + P_c \mu_c) \cdot t} - I_0 \cdot e^{-(\mu_0 - P_c \mu_c) \cdot t}}{I_0 \cdot e^{-(\mu_0 + P_c \mu_c) \cdot t} + I_0 \cdot e^{-(\mu_0 - P_c \mu_c) \cdot t}} \\ &= \frac{e^{-P_c \mu_c \cdot t} - e^{P_c \mu_c \cdot t}}{e^{-P_c \mu_c \cdot t} + e^{P_c \mu_c \cdot t}} = \tanh\left(-P_c \cdot \mu_c \cdot t\right). \end{aligned} \tag{4.12}$$

This condition can be satisfied by choosing thin samples so that $t \cdot \mu_c \ll 1$. For small x, $\tanh(x) \cong x$, the expression can thus be simplified to

$$\frac{\Delta I}{I} \approx -P_c \cdot \mu_c \cdot t. \tag{4.13}$$

Often the transmitted thickness t of the material is unknown or hard to determine. Since $\mu_0 \gg \mu_c$ the thickness t can be substituted by

$$t = -\ln \frac{I}{I_0} \cdot \frac{1}{\mu} \approx -\ln \frac{I}{I_0} \cdot \frac{1}{\mu_0}, \tag{4.14}$$

where $I_0$ is the incident and I the averaged, transmitted intensity. This leads to the following expression for the ratio of spin-dependent and spin-independent absorption coefficient:

$$\frac{\mu_c}{\mu_0} = \frac{\frac{\Delta I}{I}}{\ln \frac{I}{I_0}} \cdot P_c \tag{4.15}$$

Figure 4.17 shows a MCD-absorption experiment on a 8μm thick iron foil, carried out at the X-13B beamline. While the energy is tuned through the K-absorption edge of iron the transmitted intensity I (upper solid line) get strongly absorbed, and the asymmetry ratio signal $\Delta I/I$ (lower solid and dashed line) exhibits clear oscillations. Both MCD signals were taken by switching the applied magnetic field on the foil from parallel to antiparallel beam direction, but measured with left (dashed) and right (solid) circular polarization.

The sample was mounted at an angle of $\alpha = 40°$ to the beam direction. Therefore the aligned iron spins also have the same angle, but only the projected component parallel or antiparallel to the beam direction contributed to the MCD signal. Comparing these measurements with the results of other groups gives the degree of circular polarization.

Maruyama et al. measured the MCD-effect on a iron foil of the thickness 5 μm and received an asymmetry ratio $\Delta I/I$ of 0.221% [93], which is in very good agreement with earlier measurements and evaluations [34]. In order to compare this with the result in figure 4.17 the
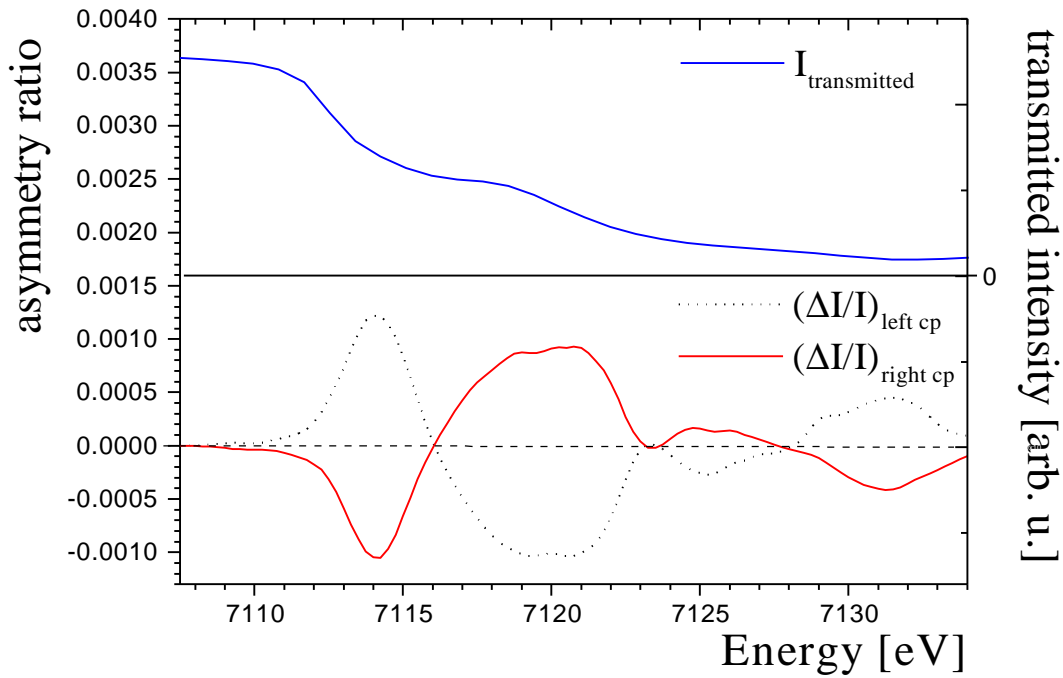
**Figure 4.17** *The transmitted intensity I and MCD asymmetry ratio $\Delta I/I$ of an 8µm thick iron foil by tuning the x-ray energy through the K-absorption edge. Full and dashed MCD-spectrum are taken by switching magnetic field on iron foil and for left and right circularly polarized x-rays, respectively.*

angle $\alpha$ of the tilted iron foil and the thickness difference have to be included and lead to the following formula

$$ P_c = \frac{\frac{(\Delta I / I)_{X13B}}{\sin \alpha}}{(\Delta I / I)_{Maruyama}} \cdot \frac{5\mu m}{8\mu m} \, . \tag{4.16}$$

With an maximal MCD effect of 0.118% at the X-13B beamline the degree of circular polarization of the X-13B beamline was determined to be about 52% at 7 keV

Taking into consideration the monochromator angle of about $\theta = 17°$ and therefore a scattering angle of $2\theta = 34°$ , which decrease the polarization by factor of $(1 - \cos 2\theta) = 17\%$, the original degree of circular polarization of EPW can be estimated to 63% which is in very good agreement with the calculated value in figure 4.6.
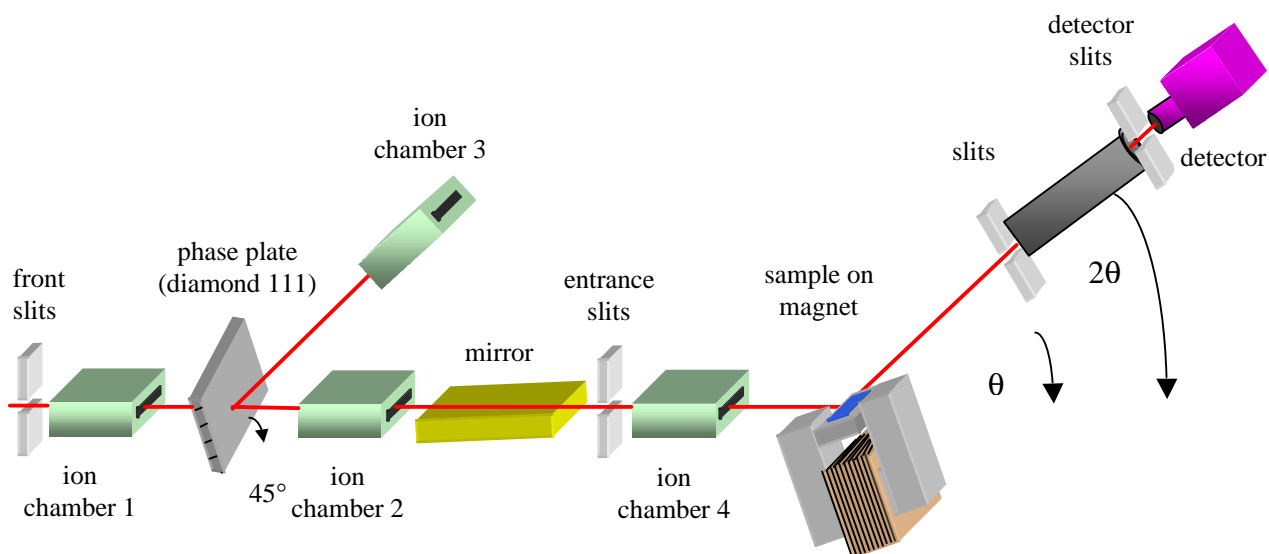
## 4.3 CMC-CAT beamline at the APS, ANL

### 4.3.1 CMC-CAT beamline layout

In the last section of this chapter the CMC-CAT beamline located at the Advanced Photon Source (APS) will be described. This storage ring with a circumference of 1104 m operates at an energy of 7 GeV. 40 BM are installed along the path with a bending radius of 39 m each, and thus has a high critical energy $E_c$ of about 19.5 keV, which allows the use of high photon energies for experiments. But as a synchrotron of the third generation it is mainly designed for the use of IDs. CMC-CAT is an undulator beamline. The undulator consists of 72 magnet periods with a period length of 3.3 cm and effective K-parameter of 2.78 at a minimum gap of 10.5 mm. The undulator has a source size of $\sigma_x = 359$ µm horizontal and $\sigma_y = 21$ µm vertical and a corresponding divergence of $\sigma_{x'} = 24$ µrad $\sigma_{y'} = 6.9$ µrad. The gap of the undulator can be adjusted in order to vary the energy of the intense, first harmonic in an energy range from 4.0 keV to 22.0 keV. By using other harmonics the energy range can be extended to 45.0 keV. 30.5 m from the source, a cryogenically cooled double crystal silicon (111) monochromator selects an energy between 3.1 keV and 22.5 keV with an energy resolution of $\Delta E/E = 10^{-4}$.

The setup of the experimental station is schematically shown in figure 4.18. The front slits define the beam size which were set in the experiments to 1 mm vertically and 2 mm horizontally. The first ion chamber shortly after the slits detects the incoming intensity. A diamond phase plate transforms the intense linear polarized x-rays into circularly polarized x-rays. Two ion chambers measure the transmitted and reflected intensity in order to determine the optimal angle for the phase plate. It should be noted that the x-ray beam gets attenuated through absorption by passing through the diamond plate by roughly a factor of 10. The principle of a phase plate and the performance of the particular diamond (111) phase plate used here in this setup is an essential point of this experiment and is discussed in more detail in the next section. In order to reduce the third and higher harmonics still contributing to the now circularly polarized x-ray intensity a subsequent aluminium mirror is used. The angle of the mirror has to be adjusted if the energy is changed over a larger range. Calculations show that at the iron edge (E = 7112 eV) the angle has to be set to 0.14° to reduce the contribution of the intense third harmonics at 21.34 keV to less than 2%. A conventional reflectivity experiment

setup followed this optic section. After some entrance slits defining the accepted beam, the ion chamber 4 serves as a monitor counter to normalize the measured reflectivity data. For the sample magnet the same experimental setup was used as for the hard x-ray beamline at X-13B at the NSLS in Brookhaven (see section 4.2.3). The reflected beam from the sample passes through an evacuated beam pipe between sample and detector. Two slits at the beginning and end of the pipe define the collimation path for the measured reflected beam. The distance between detector and sample is 0.776 m. For a typical detector slit opening of 0.5 mm vertically, a resolution of 0.037° can be achieved in specular reflectivity experiments.

The measured intensity of circularly polarized light at ion chamber 4 corresponds to a flux of $0.9 \cdot 10^{12}$ elliptically polarized photons per second for a direct beam spot size of 1 mm (vertical) x 2 mm (horizontal).



**Figure 4.18** *Experimental setup for magnetic reflectivity measurements at the CMC-CAT beamline at the APS, ANL. More details in text.*

## 4.3.2 Phase Plate Retarder

As discussed before, there are two different ways to produce circularly polarized x-rays from synchrotron radiation: first by increasing the degree of circular polarization of the x-ray radiation at a bending magnet when the beam was taken above or below the orbit plane of the synchrotron ring or by the implementation of elliptically polarized wigglers or undulators, which tilt the beam with crossed magnetic structures in the orbit plane as described in the example of the EPW in section 4.2. Another possibility to produce circularly polarized x-rays is the use of polarization conversion optics, which was applied at the CMC-CAT beamline at the APS.

From classical optics it is known that monochromatic linearly polarized light can be transformed into circularly polarized light if its electric field vector hits the neutral lines of a birefringent crystal at an angle $\psi$ of 45°, in which a phase shift $\phi$ between the two split components of 90° occurs. The polarization rate $\tau$ can be written as [94]

$$ t = \frac{I_r - I_l}{I_r + I_l} = \sin 2y \ \sin f , \tag{4.17} $$

with $I_r$ and $I_l$ are the intensities of the right and left circularly polarized waves.

In the hard x-ray case, one can take advantage of the birefringence of a perfect crystal near the Bragg diffraction condition, where the x-ray dynamical theory predicts a shift between the perpendicular and parallel components of $n_\sigma$ and $n_\pi$ , respectively. This phenomena can be observed either for the reflected and transmitted waves in Laue or Bragg geometry and within (high birefringence) or far away (low birefringence) from the Darwin width. Generally, the latter is preferred, since its small birefringence enables one to better control the shift between $n_\sigma$ and $n_\pi$ and moreover does not require a highly collimated beam. Far from the Bragg condition the phase shift $\phi$ can be calculated by [94, 95]

$$ f = \frac{2p}{l}(n_s - n_p) \cdot t = \frac{p}{2} \frac{r_0^2 \, l^3 \ \mathrm{Re}\!\left(F_h F_h^-\right) \sin 2q}{\left(pV\right)^2 \Delta\Theta} , \tag{4.18} $$

where $r_0$ is the classical electron radius, $\lambda$ the wavelength in vacuum, t the path of the x-rays through the crystal, $\theta$ the Bragg angle, V the volume of the unit cell, $F_h$ and $F_h^-$ the structure factors of the $hkl$ and $\overline{h}\,\overline{k}\,\overline{l}$ reflections, respectively, and $\Delta\Theta$ the angular offset between the incident angle and the center of the diffraction profile. At a fixed wavelength the phase shift can be experimentally controlled by the angular offset $\Delta\Theta$ and ideally set to 90°.

Figure 4.19 shows the schematic quarter wave plate setup in Bragg transmission geometry at the CMC-CAT beamline at the APS. The diamond crystal was tilted by $\psi = 45°$ perpendicular to the incident beam direction in order to split the linear polarized beam equally in $\sigma$ and $\pi$ polarized components. In order to fulfill the Bragg condition for the (111) reflection at $\theta_B = 25.0632°$ the crystal had to be rotated by $\vartheta = -10.2464°$. The right figure shows the intensity distribution for the reflected and transmitted beam as a function of the deviation from the Bragg condition of the (111) reflection at the iron K-edge of 7112 eV. The width of the rocking curve fitted with a Gaussian profile is 0.00582°.
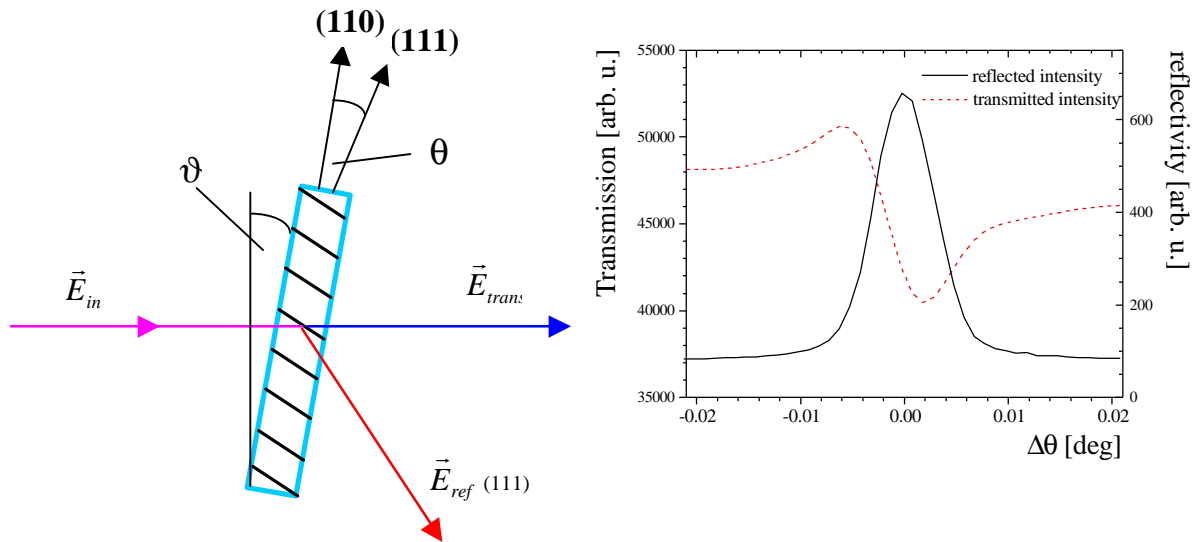


**Figure 4.19** *Left: incident beam gets Bragg-reflected on diamond quarter phase plate, which is rotated by $\psi = 45°$ towards the paper plane (not seen). By rotating slightly out of the Bragg condition $\sigma$ and $\pi$ components of transmitted beam get phase shifted, right: reflected and transmitted intensity in dependence of the deviation $\Delta\theta$ from the Bragg angle $\theta_B$.*

Figure 4.20 shows the MCD-spectrum energy on a 8 μm thick iron foil (full line) and the corresponding transmitted intensity (dashed line) with an offset parameter of $\Delta\theta$ = -0.016°. The measurement was done with the same setup used for the reflectivity experiment shown in Figure 4.18 (see section 4.3.1) with an ion chamber as a detector directly behind the sample magnet and entrance slits of 2 mm horizontal x 1 mm vertical. It shows the expected energy distribution with two distinct maxima in the asymmetry ratio while scanning the energy through the K-absorption edge of iron. At the first maximum at 7112 eV an asymmetry ratio of 0.16% can be found, which corresponds to a degree of circular polarization of about 65% (see eq. 4.16).
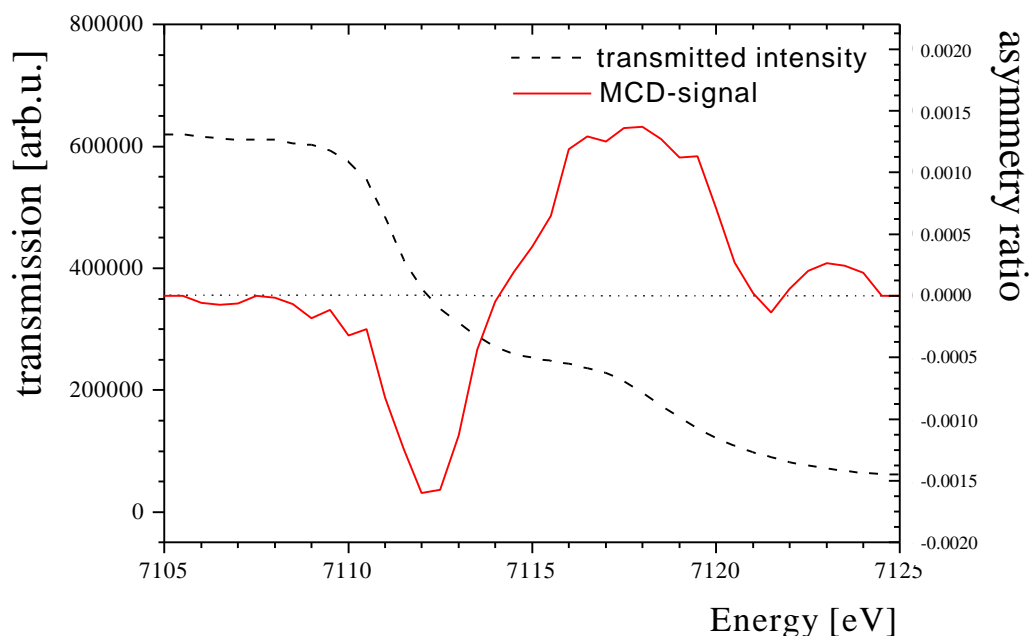


**Figure 4.20** *MCD-absorption measurement (solid line) on an 8**m**m thick iron foil with* ***Dq*** *=-0.16°. Maximum of MCD-effect found at 7112 eV. Dashed line shows the transmission intensity.*

Keeping the x-ray energy fixed at 7112 eV, the energy where the maximum of the MCD effect is expected independent of the other parameters, asymmetry ratios were measured as a function of the offset angle $\Delta\theta$ from the Bragg condition for the (111) reflection of the diamond phase plate. The result is shown in figure 4.21. Far from the Bragg reflection ($\Delta\theta$ > 0.01°) the variation of the asymmetry ratio of the MCD-signal and therefore the degree of polarization is very slow as expected. Furthermore, in this region both sides show a symmetric contribution and within the error bars the same degree of polarization but with opposite sign is observed by
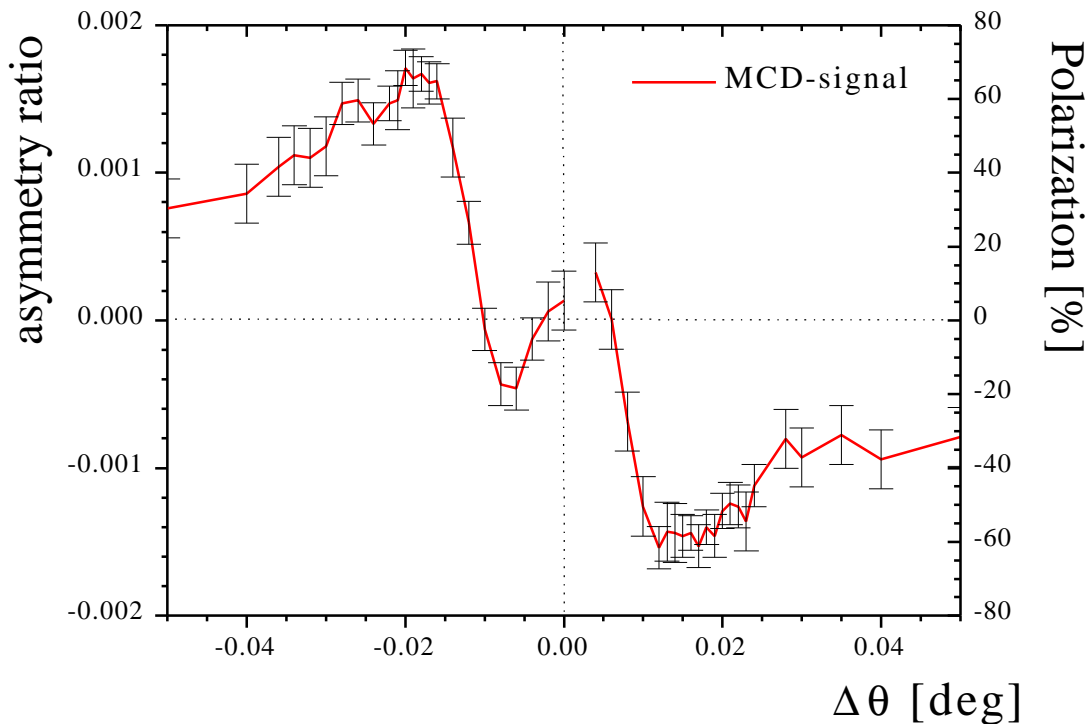
**Figure 4.21** *MCD-measurement on a 8 mm thick iron foil at 7112 keV in dependence of the deviation from the angle of the (111) reflection of the diamond phase plate.*

switching from $\Delta\theta$ to $-\Delta\theta$. For smaller $\Delta\theta$ the contribution gets less and less symmetric. As already mentioned before, within the dynamical theory frequent and rapid oscillations are expected within the reflection width [144], but could not be resolved in this experimental setup. For the magnetic reflectivity experiments performed at this beamline an offset angle, $\Delta\theta$, of $\pm$ 0.017 was chosen for both helicities with circular polarization of about 65%. The degree of circular polarization is less than observed by others [93, 95]. Different sources can lead to the reduced circular polarization, depending on the quality of the x-ray beam divergence and degree of linear polarization as well as on the quality of the diamond crystal. The Darwin width of a perfect diamond crystal for the (111) reflection is 0.00158° for the incident photon energy used [145]. This is nearly four times smaller than the measured one, which can be caused by the divergence of the x-ray beam that were vertically nearly perfect but could have some horizontal components or the mosaic spread of diamond crystal. This deviation from a perfect crystal does not allow the collimation of all incident beam the same way leading to slightly different phase shifts for individual beams and therefore a reduced averaged circularly polarization.

# 5. Magnetic X-ray Reflectivity on a Fe/Cr Double Multilayer

In the previous chapters the tool of specular magnetic reflectivity was developed. Chapter 2 described the principles of resonant magnetic x-ray reflectivity using a simple atomic picture. The method of magnetic reflectivity combines the MCD effect, which enhance the magnetic sensitivity of the x-rays, with the geometry of reflectivity to probe magnetic spin configurations. In chapter 3, the algorithm to calculate magnetic reflectivity spectra was explained, which can be used to simulate the experimental data and extract quantitative information from the measurements. Finally in the previous chapter, the experimental setups were described, which provide circularly polarized x-rays and the experimental reflectivity setup to carry out magnetic reflectivity experiment. In this chapter all the tools will be combined to extensively examine a Fe/Cr double multilayer via magnetic specular reflectivity and to demonstrate the feasibility of magnetic reflectivity. Furthermore, it will be shown how qualitative and quantitative information about the magnetic structures can be extracted from the measurements.

The sample itself consists of two multilayer structures, which are deposited one on top of the other. It exhibits an interesting magnetic behavior, which involves two magnetic phenomena: *interlayer coupling* and *exchange bias*. Both effects are important to understand the magnetic behavior of the whole system, and will be briefly discussed in a general context. The basic magnetic and structural properties of the Fe/Cr sample are characterized by SMOKE and conventional x-ray reflectivity measurements, respectively.

The magnetic reflectivity studies are taken at energies near the iron and chromium absorption edges in the soft and hard x-ray region. First, the L-edges in the soft x-ray regime will be discussed. The experimental procedure to extract magnetic reflectivity curves will be introduced followed by qualitative and quantitative analysis of the measured reflectivity spetra. Simulations are applied to model the observed features. In the second part the magnetic reflectivity is examined at the K-edge of iron in the hard x-ray region, where the effect is expected to be about 100 times smaller than that in the soft x-ray region. Again, calculations simulate the measurements to explain the observed magnetic hard x-ray spectra. In the last

section of the chapter, the results of both measurements at the hard and soft x-ray absorption edges will be summarized and compared with results from polarized neutron reflectivity experiments carried out on the same sample.

# 5.1 Properties of the Fe/Cr double multilayer sample

Interlayer coupling and the exchange bias effect are phenomena which have attracted a lot of attention in the last ten years. Both effects play an important role for the properties of the Fe/Cr double multilayer, which is considered in this chapter. A brief discussion of the fundamental ideas of both phenomena will be given here, before the principle setup and properties of the sample are illustrated. Magneto optical Kerr measurements and conventional x-ray reflectivity provide magnetic and structural information, which are important for the magnetic reflectivity studies following in the next section.

## 5.1.1 Interlayer exchange coupling and exchange bias

When magnetic films are separated by a non magnetic spacer, the magnetization of the layers are coupled to each other by exchange interactions through the spacer layer. This was discovered 1986 in transition metals Fe/Cr/Fe-trilayers [96] and in rare earth materials [97, 98]. Shortly after, the effect of giant magnetoresistance (GMR) was observed in these multilayer systems [99], where the electrical resistance changes by large amounts depending on whether the layers are ferromagnetically or antiferromagnetically coupled to each other, respectively. Systematic studies of the GMR effect in several transition metal multilayers unveiled that the coupling oscillates as a function of the spacer thickness [100]. Since then many efforts have been made to theoretically and experimentally understand the origin of these oscillatory interlayer coupling. The most common description is given by adopting the Rudermann-Kittel-Kasuya-Yosida (RKKY) interaction, originally developed to explain the coupling properties of magnetic impurities in a non magnetic material [101]. Here, in the case of single interfaces, it can be thought of two dimensional sheets of impurities embedded in a non-magnetic host. Unfortunately, the local moment approximation used in this model to describe the magnetic material is only valid for rare earth materials, but not for the magnetism in transition metals.

Their d-bands, responsible for the 3d transition metal magnetism, are itinerant with a bandwidth of several eV. An alternative approach postulates that the exchange coupling is due to quantum well states [102]. The strength of the interlayer coupling depends on the spin dependence of the reflection amplitudes for electrons in the spacer layer reflecting from the interfaces with the magnetic material. This spin dependent reflection from the interfaces creates the spin dependent quantum-well states (QWS) in the spacer layer [102]. By changing the thickness of the spacer layer the QWS move up or down in energy, depending on the band structure properties of the spacer layer. This energy dependence, associated with the filling and emptying of these QWS as they cross the Fermi level, is responsible for the oscillatory interlayer exchange.

In both models the exchange is strongly related to the topology of the Fermi surface. The periods of the oscillatory coupling are determined by the critical spanning vectors of the Fermi surface of the spacer material, which are vectors pointing in the direction of the interface normal and connect two sheets of the Fermi surfaces that are parallel to each other [103].

In a simple picture, the total coupling energy per unit area, can be written as

$$
\begin{aligned}
E_c &= -J_1\, \hat{m}_1 \cdot \hat{m}_2 - J_2 \left( \hat{m}_1 \cdot \hat{m}_2 \right)^2 \\
&= -J_1 \cos\theta - J_2 \cos^2\theta
\end{aligned}
, \tag{5.1}
$$

where $J_1$ and $J_2$ are exchange coupling terms, $\hat{m}_1$ and $\hat{m}_2$ indicating the unit vector of the magnetization direction of the two magnetic layers, and $\theta$ the angle between $\hat{m}_1$ and $\hat{m}_2$. The dot product of the magnetization unit vectors allows to distinguish between the first and the second part of bilinear (first term) and biquadratic coupling (second term), respectively. Thus, the actual coupling behavior depends on the sign and magnitude of the exchange coupling terms $J_1$ and $J_2$, respectively, and is determined by minimizing the coupling energy $E_c$. Two extreme cases can be considered. First, when the bilinear coupling is much stronger than the biquadratic term, if $|J_1| \gg |J_2|$, the coupling energy is minimized when the two magnetic layers are parallel or antiparallel coupled depending on the sign of $J_1$. Second, if $|J_1|$ is comparable $|J_2|$, the angle between the two magnetic layers can be calculated with $\cos\theta = -J_1/2J_2$ and results in a 90° coupling in the case of a vanishing $J_1$. In most cases the bilinear term is dominant and leads to parallel and antiparallel coupling, oscillating with the thickness of the spacer layer. However, it should be noted that the biquadratic contribution can become large in the presence

of strong interface roughness [103] or for antiferromagnetic spacers [104] and in such circumstances could even dominate the bilinear coupling term.

Among the different exchange coupled systems, Fe/Cr multilayers are some of the most heavily studied systems and have been the source of many new discoveries in the field of exchange coupling. It was the first system which showed exchange coupling [96] and oscillatory coupling as the thickness of chromium was varied [100]. Also the existence of short and long period oscillation was discovered in Fe/Cr/Fe trilayers [105]. The choice of chromium as the spacer material was certainly influenced by the fact that it is the only transition metal which lattice constant fits well with that of iron and thus, allows the growth of well-defined interfaces. In Fe/Cr systems, the bilinear term usually dominates the coupling process and possesses both a short and long coupling period, in which often the short-period coupling is averaged out due to thickness fluctuations of the spacer layers and only the long-period coupling is observable [105 - 107]. It should be mentioned that chromium, unlike most other spacer layers, exists in various state of magnetic order itself, which has a strong influence on the interlayer exchange coupling. Besides the paramagnetic phase, chromium can possess antiferromagnetic order, displaying both incommensurate and commensurate spin density waves. A detailed summary of the theoretical and experimental results concerning spin density waves in bulk and thin films of chromium, particular when in contact with ferromagnetic iron, can be found in [108, 109]. Besides the antiferromagnetic order in the chromium, also the roughness of the interfaces, as mentioned above, can have a significant impact on the magnetic coupling.

Even though it is still controversial which part of the Fermi surface is responsible for the long period coupling, it has been shown experimentally that multilayers of both Fe/Cr (001) and Fe/Cr (211) growth orientation exhibit a long-period oscillation of 12 monolayer [110, 111], which corresponds to about 18Å for chromium in the bcc structure.

An extensive review of interlayer coupling and the influence of roughness and antiferromagnetic order of chromium on the magnetic coupling properties in Fe/Cr multilayer is given by [112] and [113], respectively.

Another phenomenon attracting a lot of interest is the *exchange bias effect*. A system of a ferromagnet (FM) interfacing an antiferromagnet (AFM), where the AFM is cooled through the Néel temperature $T_N$ in the presence of a magnetic field, induces a magnetic anisotropy in the

FM. The exchange bias effect was discovered 1956 by Meiklejohn and Bean in a Co-CoO-system, where ferromagnetic cobalt particles were imbedded in antiferromagnetic CoO [114]. This effect has been observed in a wide variety of magnetic system containing FM - AFM interfaces [115, 116] and has made a large impact on the technological sector through the development of noval magnetic devices, especially in the last decade. Particularly interesting for technological applications are artificial layered systems consisting of thin films with FM and AFM magnetization, which is also the point of interest in the present work.
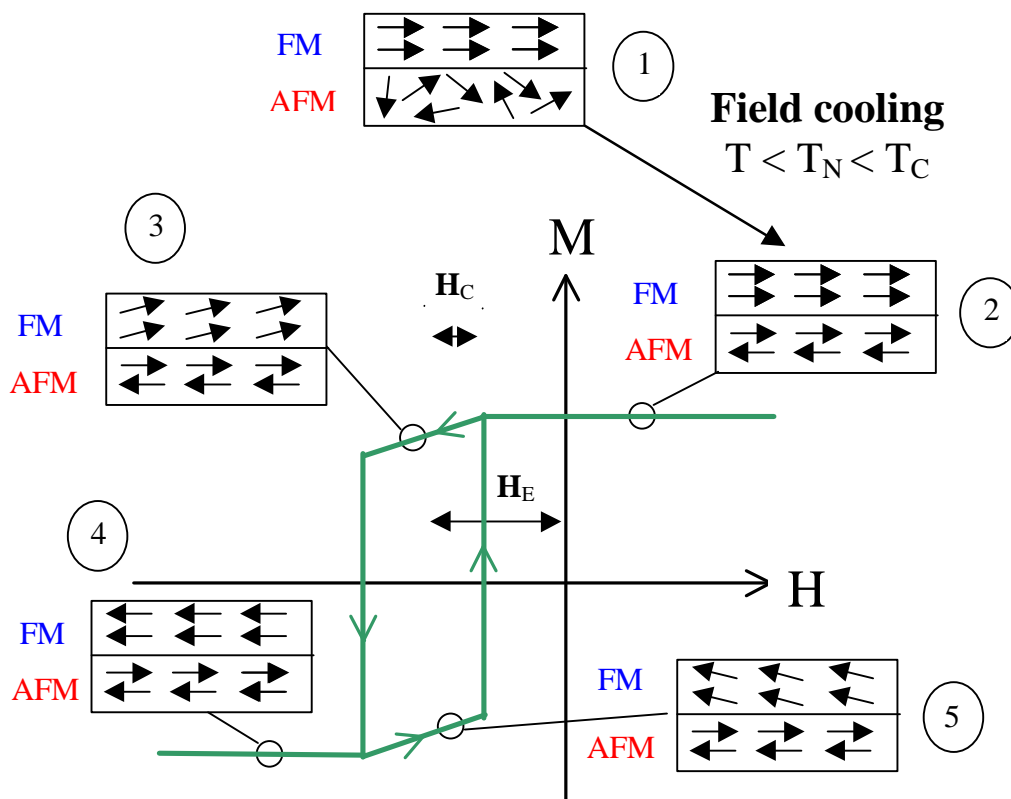


**Figure 5.1** *Schematic of a hysteresis loop of the ferromagnetic component and the according ferromagnetic and antiferromagnetic alignment in an ideal exchange bias system. The hysteresis loop is shifted by the exchange bias field of $H_E$. The spin configuration are illustrated as little cartoons for the different stage (1 to 5) while driving the magnetization through the hysteresis loop (detailed explanation see text).*

An intuitive picture of exchange bias is shown in figure 5.1. Phenomenologically, exchange bias exhibits a shift of the hysteresis loop (looking at the FM) as it is pictured in figure 5.1. First the temperature is taken below the Neél temperature $T_N$ of the AFM, which is in general also below the Curie temperature $T_C$ of the FM. At the same time a magnetic field is applied,

which orders the ferromagnetic spins and also aligns the interface spins of the AFM antiferromagnetically during the *field cooling* process (1 → 2) and determines the shift of the hysteresis loop in the opposite direction to the cooling field. If the magnetic field is now decreased, the ferromagnetic spins remain still aligned in the original direction and are only slightly tilted when the magnetic field switched the sign and even exceed the original switching field of the single FM (2→ 3). The ferromagnetic spins are influenced by the AFM spin alignment, which remain rigid at low fields. Qualitatively the shift can be pictured as a microscopic torque on the FM spins exerted by the AFM spin configuration on the interface. After applying an extra field to overcome the microscopic torque, the ferromagnetic spins finally become orientated in the opposite direction (3 → 4). This extra field, which is equal to the shift of the center of the hysteresis loop from zero field, is called the exchange bias field $H_E$. By reversing the magnetization process, the spins in the FM experience again the interfacial interaction to the AFM spins and are tilted (4 → 5), allowing the FM spins to switch back earlier into the state with their original alignment (5 → 2). This phenomenological model gives a very good intuitive picture of the exchange bias process. However, for the understanding of exchange bias on a more quantitative basis, it is necessary to include parameters like anisotropy, roughness, spin configuration and magnetic domains, which play an important role.

The first attempts to calculate the magnitude of the exchange bias field, taking into account the interfacial coupling energy $J_{INT}$ , the anisotropy terms for the FM and AFM and the saturation magnetization $M_{FM}$ of the FM, lead to [115, 117]

$$H_E = \frac{J_{INT}}{M_{FM} \cdot t_{FM}} ,$$ (5.1)

where $t_{FM}$ is the thickness of the FM layer. The FM and AFM spin structures were assumed to be rigid and the interface perfectly flat and uncompensated. Comparison with the experimental results revealed that the simple theoretical model predicted an exchange bias field which were two magnitudes too high and had to be modified. In order to solve this discrepancy several models has been proposed. Mauri [118] suggested a domain wall model. Here, AFM domain walls are formed during the magnetization reversal, which reduces the interfacial exchange energy and therefore also results in a lower exchange bias field. Another approach is proposed

from Malozemoff [119] suggested that interfacial disorder, such as roughness, can lead to in-plane AFM domains, which again reduce the interfacial energy. Other models including perpendicular coupling or spin flop transitions were also proposed recently [120 - 122]. These models clearly improved the understanding of the exchange bias mechanism, but still were not able to explain the microscopic origin of this phenomenon completely [115].

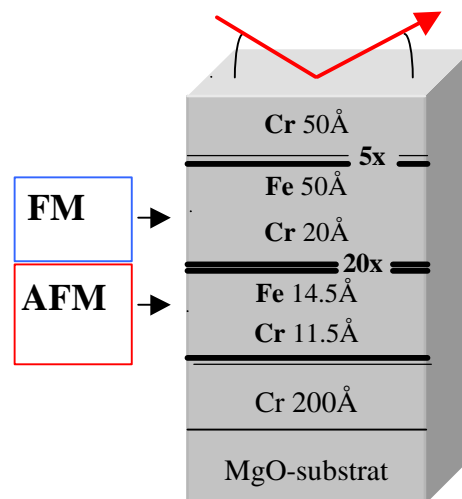## 5.1.2 Basic characterization of the Fe/Cr double multilayer

The Fe/Cr double multilayer sample was provided from S. D. Bader's group from Argonne National Laboratory, who designed and grew the system. In this section, information about the growing conditions and characterization of the sample will be summarized which includes results of G. Felcher's group also at Argonne National Laboratory. A more detailed description of their work on this sample can be found in other publications [123 - 124].

The sample was grown via magnetron sputtering onto a single crystal MgO (110) substrate. A 200 Å Cr buffer layer is deposited at 400°C to help establishing epitaxy with the substrate. Then the double lattice structure of Fe/Cr in (211) orientation was grown at 100°C and capped by a 50 Å chromium cover layer to avoid oxidation. The nominal setup is presented in figure 5.2. The bottom multilayer consists of twenty periods of Fe/Cr bilayers with nominal layer thickness of 14 Å and 11 Å for the iron and chromium layer, respectively. The top superlattice structure possesses five bilayers of 50 Å and 20 Å of iron and chromium layer thickness, respectively. The crystal structure is bcc. The anisotropy constant $K_S = 0.06$ erg/cm$^2$



**Figure 5.2** *Nominal structural setup of the Fe/Cr double multilayer.*

with anisotropy fields of 1.6 kOe for the 14 Å iron layers and 450 Oe for the 50 Å iron layers. As discussed in paragraph 5.1.1, the iron layers are coupled through the chromium layer in each of the two multilayer structures due to interlayer exchange coupling. The bottom multilayer (11.5 Å Cr) shows antiferromagnetic (AFM), while the top multilayer (20 Å Cr)

ferromagnetic (FM) coupling. Also, previous experiments showed that (211) oriented Fe/Cr multilayers epitaxially grown on a MgO (110) substrates show uniaxial, inplane magnetic anisotropy with an easy axis in Fe/Cr $(0\bar{1}1)$ direction [126].

A ferromagnetic coupled system on top of an antiferromagnetic coupled system is the basic setup of an exchange bias system, as described in the previous section. The interface between the FM and AFM here consists of an 20 Å chromium layer, which gives rise to ferromagnetically inter-superlattice coupling between both superstructurs. As pointed before, the interface between the FM and AFM in an exchange bias system plays a crucial role for the understanding of exchange bias phenomena. The effects of interface defects like roughness and thickness fluctuation, have a big impact for the whole system and still cause many problems to quantitatively understanding the mechanism. These effects could never be excluded in conventional exchange bias systems, since every system possesses at least roughness on an atomic length scale. Here in this artificially constructed system, the interfacial coupling between FM and AFM multilayer is very insensitive to thickness fluctuation or roughness due to the large coupling period of 18 Å. This gives rise to the possibility to observe properties, which are expected from an ideal exchange bias system with atomic flat interfaces, and was confirmed by Jiang et al. [123].
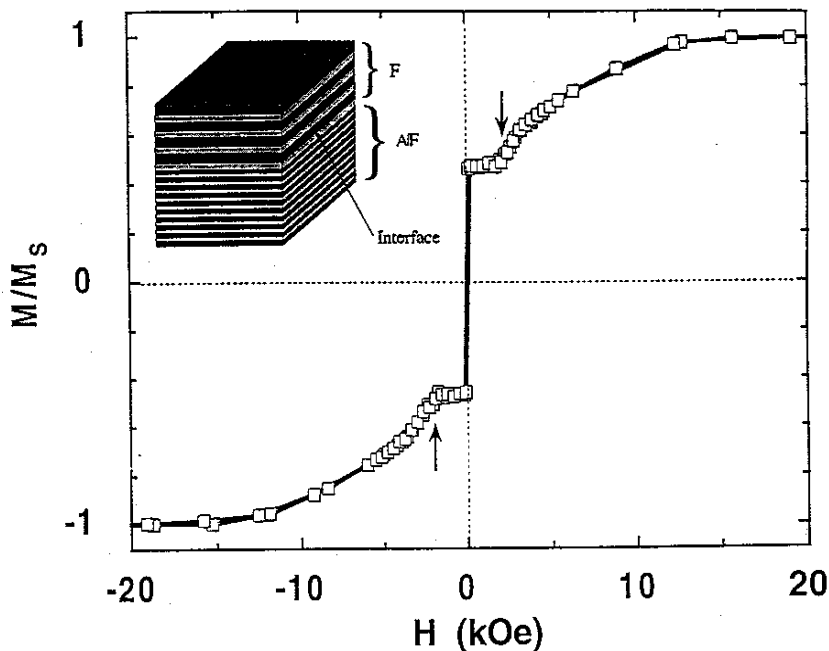


**Figure 5.3** *Magnetization curve of the Fe/Cr double multilayer system (schematic structure depicted in the left upper corner) measured per SQUID magnetometry along the easy direction at room temperature. The arrows mark the spin-flop transitions. Graph from Jiang et. al [123].*

In conventional exchange bias systems the AFM has to be cooled down below the Neél temperature $T_N$ in order to establish an unidirectional magnetic anisotropy. Here, it is sufficient to apply a large field of about 20 kOe to align all iron layers in both FM and AFM structure. Figure 5.3 shows the magnetization curve measured by Jiang et al. [123] on the same sample with a superconducting quantum interference device (SQUID). At low fields the FM switches and contribute about 47% to the total moment. At about 2 kOe the magnetization starts to increase again (indicated with the arrows) due to the occurrence of spin-flop transitions in the AFM superlattice. The more the field increases the more the iron layers in the AFM structure rotate towards parallel alignment and the magnetization slowly reaches its saturation at about 14 kOe. After aligning the AFM at a high magnetic field, sufficient to align all the spins of the FM and AFM coupled multilayer in the field direction, the symmetry is broken and the interfacial iron layer of the AFM ferromagnetically couples the interfacial iron layers of the FM in the direction of the alignment. Due to the exchange interaction between the iron layer at the FM/AFM interface and the other iron layers in the FM superlattice, the hysteresis loop
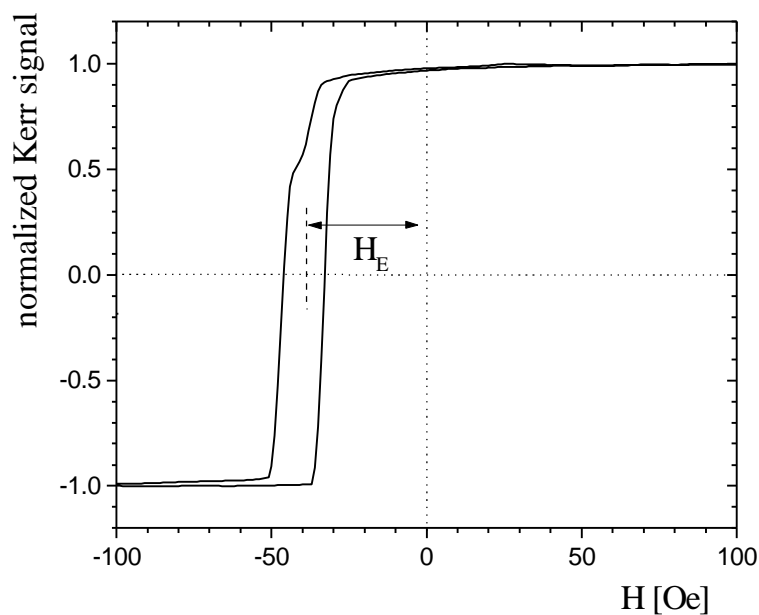


**Figure 5.4** *Minor hysteresis loop of Fe/Cr double multilayer after field cooling of +18 kOe.*

shifts in the opposite direction and establishes an unidirectional exchange, known as exchange bias. Figure 5.4 shows the magneto-optical Kerr signal of the minor hysteresis loop after the sample was aligned in a field of 18 kOe in positive field direction. The Kerr signal was

obtained by measuring the reflected intensity of a helium-neon laser on the Fe/Cr sample mounted on an electromagnet with adjustable field. Its penetration depth of about 300 Å makes it possible to examine the FM structure of the top multilayer. A shift in the hysteresis loop of an exchange bias field $H_E$ of 39 Oe with a coercive field of $H_C = 7$ Oe can be clearly observed. The width of the hysteresis loop is with 2 $H_C = 14$ Oe much smaller than the anisotropy field $H_E$, which indicates that the reversal of the FM superlattice probably does not occur by coherent rotation, but by nucleation and growth of reverse magnetic domains [123]. From negative to positive field values the switching is sharp and indicates pinning free domain wall motion while the opposite side has a little kink before the magnetization is reversed.

## Charge structure

Accurate determination of the structure is a crucial issue for the characterization of artificial thin film and multilayer systems. The analysis of the density profile is not only important to understand and characterize the coupling and interface properties of the system, but also has a major influence on the magnetic structure. As mentioned in Chapter 2, the interference term between the magnetic and charge scattering is the largest contribution to the resonant magnetic x-ray reflectivity with circularly polarized x-rays. Therefore a good determination of the charge profile is necessary to understand the magnetic reflectivity profile in more detail. The parameters needed for the magnetic simulations as presented in chapter 3 will be shown later in this chapter.

In order to determine the structural parameters of the multilayer system conventional x-ray specular charge reflectivity studies with linearly polarized light were carried out at the X-13B beamline at the NSLS in Brookhaven. The experimental setup is illustrated in chapter 4 (see figure 4.12). The photon energy was set here to 7105 eV, which is just below the iron K-edge. At this energy the absorption in the iron layers is still small. The entrance slits accepted a beam spot of 7 mm x 1 mm, horizontally and vertically, respectively, which illuminated the sample (size 10 mm x 7 mm) completely at angles higher than 5.74º. The detector slits were opened to 1 mm and the slits in front of the collimation pipe were set to 2 mm to reduce the scattering background. The collimation pipe was filled with helium to reduce the absorption of the
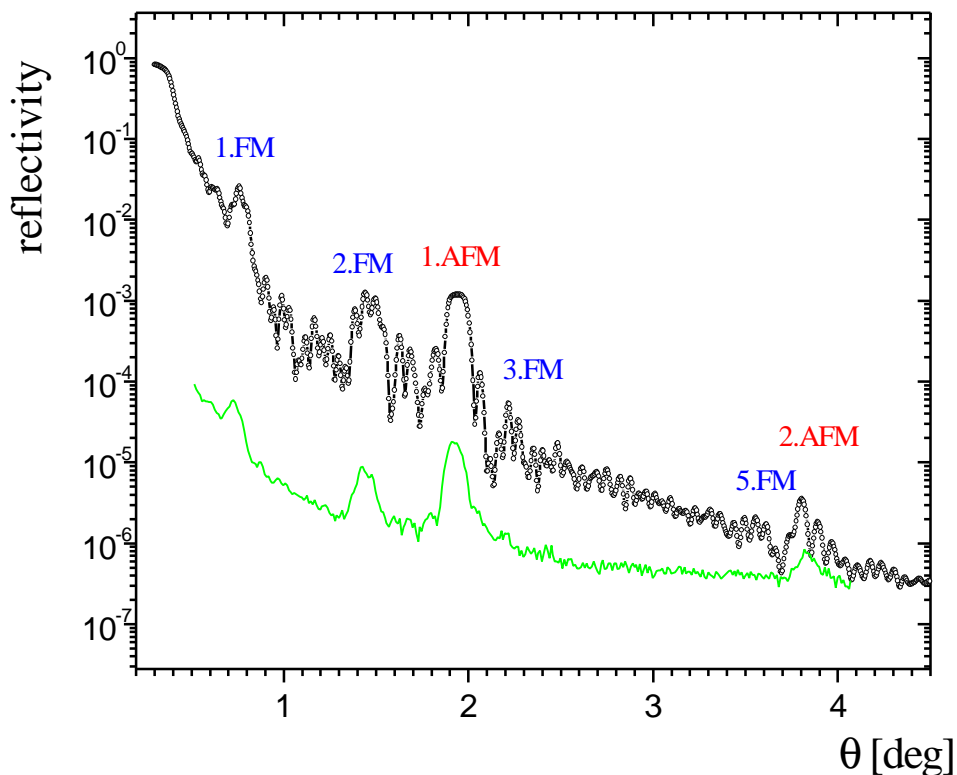
**Figure 5.5** *Specular charge reflectivity on the Fe/Cr double multilayer (line with circles) and offset scan (full line) with an offset angle of **Dq** = 0.15º.*

reflected x-rays by air. With these slit settings, the angular resolution can be calculated to be $\Delta\theta = 0.038º$. Figure 5.5 shows the specular reflectivity curve (line with circles). The diffuse background was measured via *offset scan* (full line). In this scan mode, the sample angular position is set slightly off the specular position by $\Delta\theta = 0.15º$, while the same reflectivity curve is recorded. The offset angle $\Delta\theta$ was determined by *rocking scans*, where the sample is scanned around the specular position while the detector remains at fixed angular position. For the specular reflectivity scan presented in figure 5.5, the diffuse background determined is already subtracted from the originally measured curve. The diffuse signal, received from the offset scan, is more than one order of magnitude lower than the corrected specular intensity even for higher angles, which indicates quite well-defined and smooth interfaces. The critical angle of $\theta_c = 0.375º$, which separates a region where the beam is totally reflected due to the index of refraction being slightly smaller than one from the higher angle region, is slightly below the critical angle which is expected from a thick chromium layer ($\theta_c = 0.415º$). This could be explained by the oxidation of the top chromium layer, which changes the density and therefore
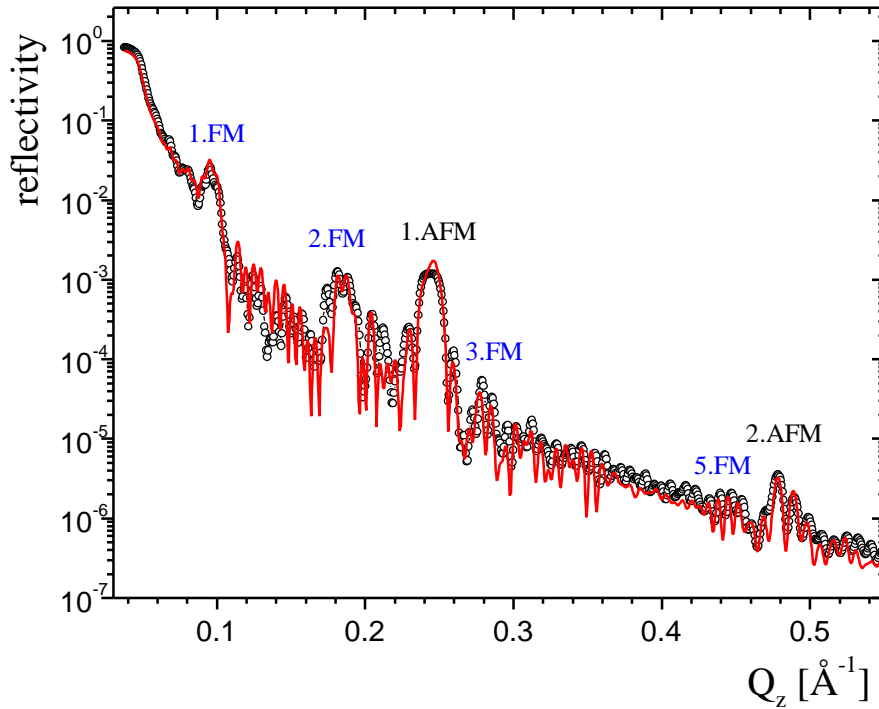
**Figure 5.6** *Specular reflectivity curve (circles) with simulation (solid curve). Parameters are listed in table 5.1.*

the critical angle. Or, more likely, this could be due to the contribution of the first iron layer since the penetration depth is about 70 Å at total reflection, and iron has a smaller critical angle of $\theta_c = 0.35°$. Furthermore, the specular reflectivity was corrected for the partial illumination of the sample at low angles, where only a small part of the beam hits the sample.

The reflectivity curve clearly exhibits structural peaks superlattice periods - which can be clearly assigned to antiferromagnetic (AFM) superlattice configuration. Str the first AFM Bragg peak, while the third and the fifth already very much damped. Furthermore, the fourth which is mainly due to the thickness ratio of the i multilayer structure, which leads to destructive interfere. The reflectivity picture yields important information, quantitative information about the structural setup of applying simulations. The calculations for the simulatio in chapter 3.1. Parameters of layer thickness, mass dens in order to obtain a reasonable agreement between the

|  |  | t [Å] | $\sigma_{rms}$ [Å] |
|---|---|---|---|
|  | **Cr** | 48.0 | 8.0 |
| 5x | **Fe** | 51.0 | 5.5 |
|  | **Cr** | 20.5 | 5.5 |
| 20x | **Fe** | 15.0 | 4.5 |
|  | **Cr** | 11.2 | 4.5 |
|  | **Cr** | 20.0 | 3.5 |
|  | **MgO** |  | 2.5 |

**Table 5.1** *Parameter list for specular reflectivity simulation on Fe/Cr double multilayer in Fig. 5.6*

parameters listed in table 5.1 and the fit shown in figure 5.6. It should be noted that instead of the incident angle the measured and simulated reflectivity is plotted along the momentum transfer $Q_z$.

 The thicknesses for the iron and chromium layer desired in this manner agree very well with the nominal thicknesses, originally aimed at in the growth process. The simulation suggests a cumulative interface roughness from the substrate to the cover layer, but for the sake of simplicity the interfacial roughness was assumed uniform for each superlattice and show values of 4.5 Å and 5.5 Å, respectively. This cumulative roughness is very common and observed in many epitaxially grown multilayer systems.

After the structural and basic magnetic properties of the Fe/Cr double multilayer are determined and connected to the occurrence of interlayer coupling and the exchange bias, everything is prepared for magnetic reflectivity studies. The following sections will show the magnetic reflectivity measurements on the Fe/Cr double multilayer and the qualitative and quantitative analysis at the soft and hard x-ray absorption edges.

# 5.2 Magnetic x-ray reflectivity with soft x-rays

In this section magnetic reflectivity near the L-edges of iron ($L_3$: 706.6 eV and $L_2$: 719.9 eV) and chromium ($L_3$: 574.1 eV and $L_2$: 583.8 eV) will be examined, which requires soft x-rays as a probe. As pointed out in chapter 2 discussing the MCD effect, it is known that the MCD effects at the 3d transition L-edges are about two orders of magnitudes larger compared to those at the K-edges, which makes the detection of the magnetic signal much easier. The first absorption edges for the examination via magnetic reflectivity are the iron L-edges. The strong effect will be used to illustrate the general procedure to measure the magnetic reflectivity curves. Different scan modes can be used to extract information and gain a qualitative picture of the magnetic spectra. In order to understand the magnetic reflectivity on a quantitative basis, simulation of the magnetic reflectivity has to be applied. The weak magnetic moment of chromium is then examined by tuning the x-ray energy to the L-edges of chromium and proceeding in the same way.

## Experimental details

Before a description of the measurements is presented, first some experimental details will be explained. The experiment in the soft x-ray region is carried out at the X13A beamline at the National Synchrotron Light Source, Brookhaven National Laboratory. The setup and features are extensively described in section 4.2.3. The sample was mounted on an electromagnet providing an adjustable magnetic field of ± 500 Oe on the sample along the sample surface. The vacuum at the sample chamber was on the order of $10^{-7}$ Torr to minimize the strong absorption of the soft x-rays in air. Systems of slits defined the incident beam size to 200 μm horizontally. The horizontal detector slits at a distance to the sample of about 23 cm were opened to 1.6 mm. A set of slits was mounted on the detector arm in 7.5 cm distance to the sample with also 1.6 mm opening horizontally to avoid scattering from other sources and therefore reduces the background. The resolution in this setup is given by 0.40° in the scattering plane. Due to the dimensions of the sample magnet, the incident angle could not exceed $\theta = 25°$ and therefore restricted the momentum transfer $Q_z$ of the measurements.

In order to make the terminology clear some additional comments will be made here. As explained in chapter 2 and 3, the reflectivity channels are recorded by combinations of left and right circularly polarized x-rays and opposite magnetic fields. The experiments performed in the soft x-ray region measure the charge and magnetic reflectivity by taking the sum and the difference of the intensities of left and right circularly polarized x-rays, respectively, while keeping the magnetic field on the sample constant. In the following sections, the *sum* is always referred to as the *charge reflectivity* and the *magnetic reflectivity* is represented by the *difference signal*.

Another way to present the magnetic data is as the *asymmetry ratio*, which is the difference divided by the sum, and is used to connect amplitudes of the charge and magnetic reflectivity. Furthermore it is important to note, that all measurements are taken in the *specular condition*: the detector position is always at twice as the angle at the sample and is called the $\theta/2\theta$ condition. Here, often only the incident angle $\theta$ is given, which always implies that the detector is at the specular condition $2\theta$.

## 5.2.1 Magnetic x-ray reflectivity at the iron $L_{2,3}$-edges

It is well known from soft x-ray MCD measurement that iron exhibits a large MCD effect when the energy is tuned near the iron L-edges. Experiments by Kao et al. demonstrated that the magnetic scattering signal can clearly be measured and is close in magnitude to the charge signal [31]. Here, first the procedure will be illustrated which is generally used in this work to determine magnetic reflectivity spectra. Then the observed features will be discussed and explained in a qualitative picture. Finally, simulations based on the calculation described in chapter 3, will be applied to also gain quantitative understanding of the reflectivity spectra.

### Procedure of magnetic reflectivity

The recording of magnetic reflectivity curves can be basically described as a three step process, provided that the magnetic field is known which is needed to magnetize the sample. In the case of the Fe/Cr multilayer, the field is already measured by the hysteresis loops shown in figure 5.3 and 5.4.

**Step 1** *Charge reflectivity of the Fe/Cr double multilayer with soft x-rays*

Basically, the charge structure is already known by the charge reflectivity measurement with hard x-rays in section 5.1.3 and the $Q_z$-positions of the individual Bragg peaks for both multilayer structures determined by simulation. Due to the longer wavelength of soft x-rays, the angular range of the measurement has to be changed in order to probe the same $Q_z$-range. By changing the incident x-ray energy from the hard x-rays (e.g. 7 keV) to the soft x-ray region (e.g. 0.7 keV) the required angular range has to be extended by an order of magnitude.

Even though the positions for the structures can be calculated from the hard x-ray measurements, the soft x-ray reflectivity shows obvious differences. Particularly the penetration depth is strongly influenced by the wavelength of the x-rays as it is illustrated in figure 5.7. While hard x-rays have a penetration depth of several thousands of Å even for incident angles just a little bit larger than the total reflection, soft x-rays experience a much stronger absorption, especially near the absorption edges. The presented curves in figure 5.7
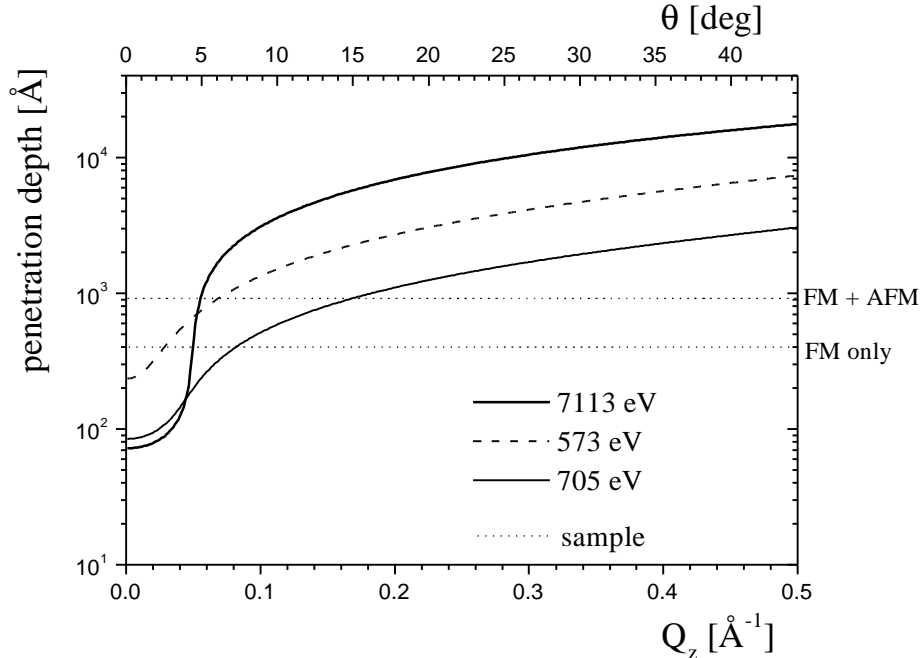


**Figure 5.7** *Penetration depth of x-rays for different energies in Fe/Cr double multilayer in dependence of $Q_z$. Dotted lines indicate the thicknesses of the FM and AFM coupled multilayer. Upper x-scale indicates angle range for E = 705 eV, near the iron L-edges. Curves are calculated by equation (3.11) (see chapter 3).*

are calculated for energies near the iron (705 eV, 7113 eV) and chromium edges (573 eV) for the Fe/Cr double multilayer. The dotted lines denote the thicknesses of only the FM and both the FM and AFM coupled multilayer, respectively. Especially for energies near the iron L-edges, at which the absorption for both chromium and iron are very strong, the whole multilayer structure is not probed until the incident angle $\theta$ exceeds 15°.

Figure 5.8 shows the charge reflectivity of the Fe/Cr multilayer, measured at a photon energy of 702.5 eV. The energy is chosen to be right before the L-edges of iron. The observed peaks can be clearly assigned to the structural superlattice peaks of the double multilayer structure. The first and the second FM and the first AFM Bragg peaks can be covered in the range of about 22°. It should be noted, that the structures and the Bragg peaks appear broader and more smeared out compared to the hard x-ray reflectivity measurements.

It is also important to keep in mind that the angular position of the Bragg peaks depends on the incident photon energy. Especially in the soft x-ray regime, changes of a few eV can shift the angular positions of one $Q_z$-position by small but significant amount. However, for reflectivity scans near the iron L-edges such as shown in figure 5.8 these shifts are small when the energy is tuned through the iron L-edges in comparison with the width of the individual Bragg peaks.
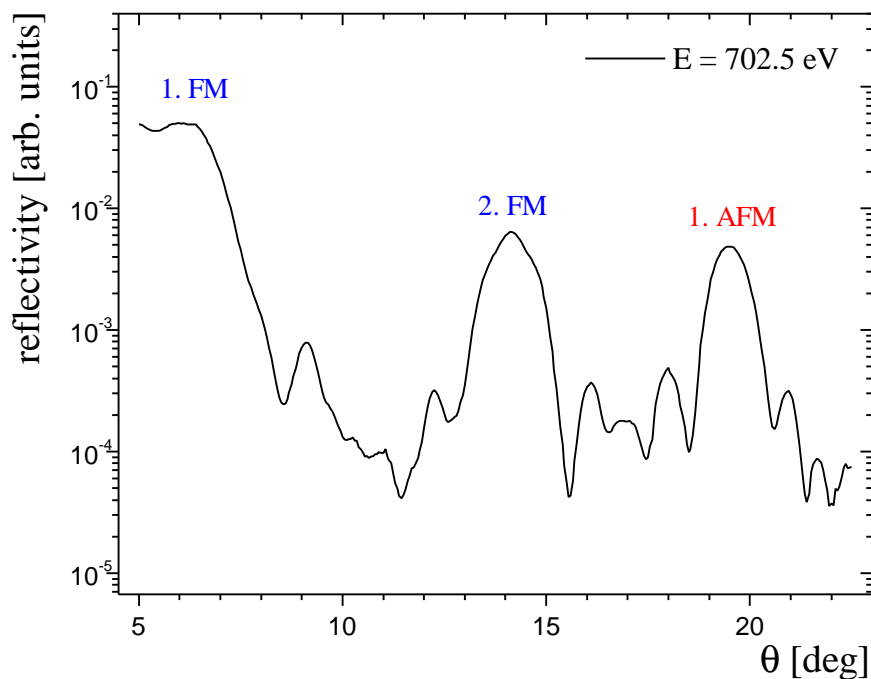


**Figure 5.8** *Charge reflectivity of the Fe/Cr double multilayer at a x-ray energy of 702.5 eV. The structural Bragg peaks are indicated for the ferromagnetic (FM) and antiferromagnetic (AFM) multilayer.*

**Step 2** *Energy scan in reflectivity at fixed $q/2q$-position*

When the angular positions of the Bragg peaks are determined, a $\theta/2\theta$-position in the reflectivity scan is selected to measure the energy dependence of the charge and magnetic reflectivity in order to find the energy, which shows the largest magnetic sensitivity. Since the magnetic peaks are expected to be at the same position as the charge peaks in ferromagnetic materials, a FM Bragg peak is usually chosen to scan the energy through the absorption edge of iron and find the largest magnetic effect. Figure 5.9 shows such an energy scan at the second FM Bragg peak at around $\theta = 14°$ incident angle. The charge reflectivity (upper plot) exhibits two distinct peaks while tuning the energy through the $L_3$ and $L_2$-edges of iron. The enhancements can be clearly assigned to each of the two L-edges. Similar behavior can be found in the difference signal of left and right circularly polarized x-rays, corresponding to the magnetic reflectivity and are plotted in the lower part of figure 5.9. The magnetic reflectivity curve was recorded for opposite magnetic field directions and can be seen as the dotted and the full line in bottom part of figure 5.9, respectively. The applied magnetic field of 150 Oe was more than sufficient to magnetized the iron layers in the FM multilayer on the sample as
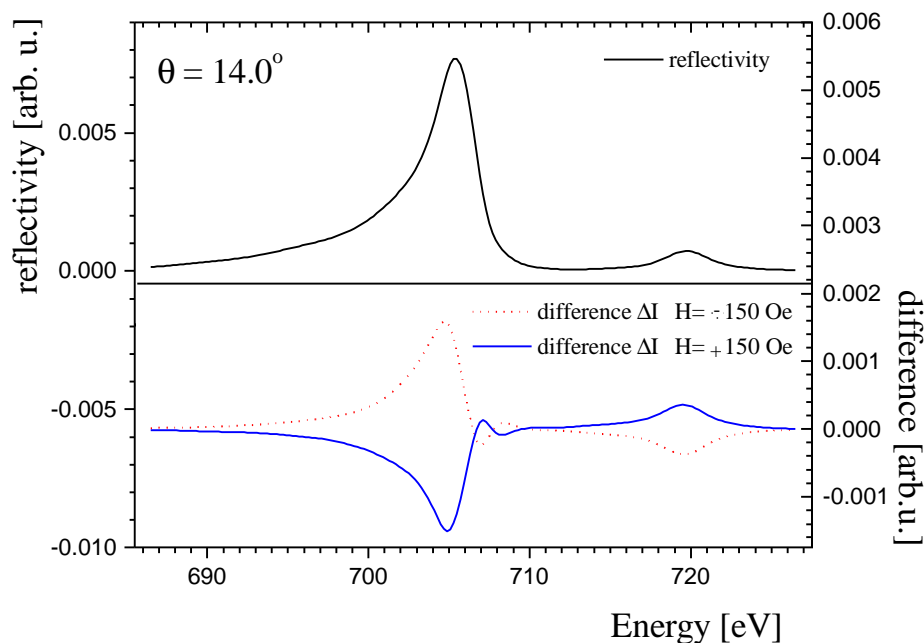


**Figure 5.9** *Energy scan in reflectivity on Fe/Cr double multilayer at $q = 14.0°$. Upper figure shows the charge reflectivity (sum), lower the magnetic signal (difference). Magnetic signal was recorded for negative (full line) and positive magnetic field direction (dashed line) of the sample magnet*

determined from the MOKE measurements described before. Similar to the charge profile, the magnetic signals also show enhancements when the energy is tuned near the L-edges of iron. The change in sign can be explained with the opposite spin-orbit coupling of the $L_3$ and $L_2$ transition. The nearly perfect symmetry between the two curves indicates that the iron spins, contributing to the magnetic signal at this angle and energy, completely flip their orientation when the magnetic field on the sample is switched. This ferromagnetic behavior is expected from the iron spins of the FM multilayer. The maximum of both curves is found at an energy of about 705 eV. As mentioned in the beginning of the section, the magnetic reflectivity signal is shown here as the difference signal. The asymmetry ratio, which is the difference divided by the sum, is about 17% at the maximum of the difference signal.

## Step 3 *Magnetic reflectivity*

In step 2 an energy of about 705 eV was determined, at which the measured magnetic effect at the 2.FM Bragg peak was strongest. At this energy and fixed applied magnetic field on the sample (H = -150 Oe), the reflectivity curve is recorded by scanning the incident angle θ.
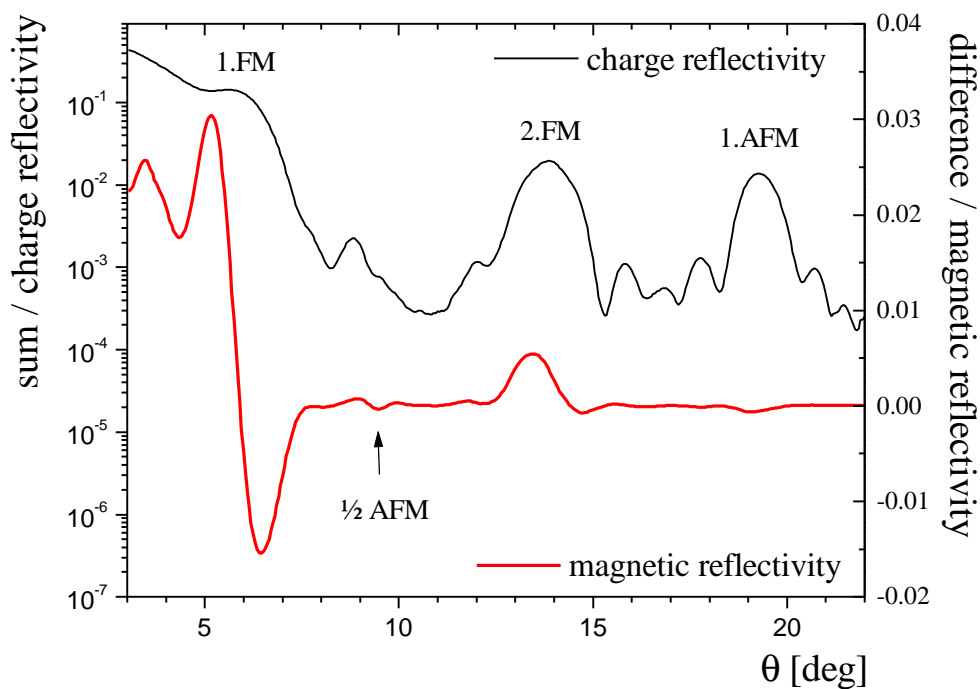


**Figure 5.10** *Charge (upper line) and magnetic reflectivity (lower line) of the Fe/Cr multilayer at 705 eV incident x-ray energy and an applied magnetic field of -150 Oe.*

Figure 5.10 shows the sum and the difference of the detected intensity of left and right circularly polarized x-rays, which represent the charge and the magnetic reflectivity curve, respectively. The magnetic reflectivity curve shows clear enhancements at the first and second FM Bragg peak position of the charge reflectivity and some at the AFM structural peak. At half of the AFM peak position an oscillation appears in the difference signal, which indicates that the reflectivity is also sensitive to the AFM spin contribution of the lower multilayer. The spins of the iron layers with parallel alignment in the AFM multilayer structure have twice the distance of the next iron layer. In reciprocal space, which is probed in the x-ray reflectivity, it results in magnetic intensities at half AFM peak position. It is important to note that the absorption of the x-rays in the material plays an important role in the difference signal putting different weights on the parallel and antiparallel aligned layers. Without or only very weak absorption, the magnetic contribution of both opposite aligned layers would cancel each other and no difference signal would be detected. Independent of the difference signal, a magnetic enhancement would be still observable in the sum signal due to the differences in the index of refraction of the iron layers with opposite magnetic orientations, but is superimposed by the strong signal of the charge scattering.
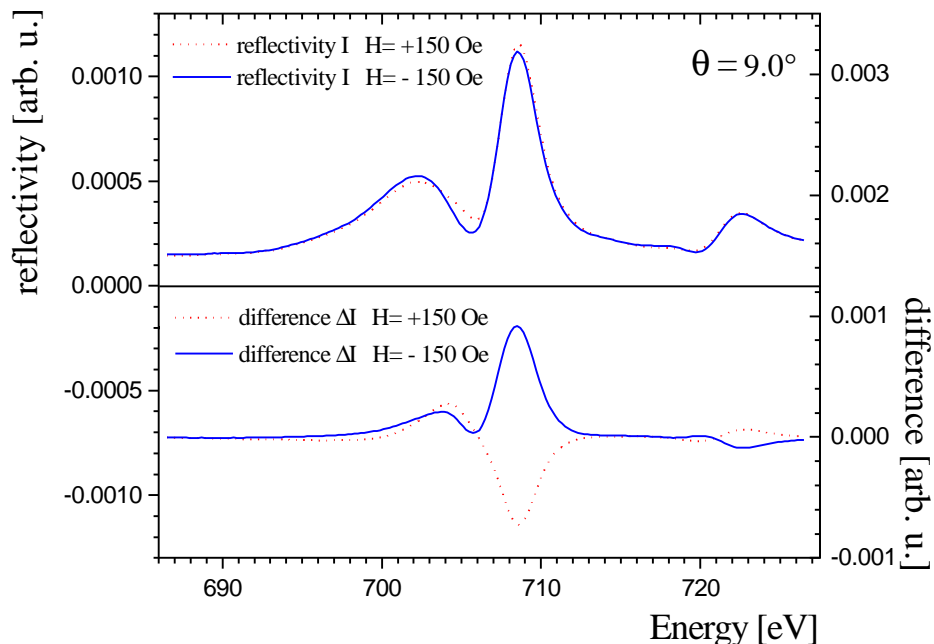


**Figure 5.11** *Energy scan at* $q = 9.0°$ *for both magnetization directions*

It should be also noted that according to the calculated penetration depth in figure 5.7 the strong absorption of soft x-rays at the iron $L_3$-edge only about half of the bilayers in the AFM coupled multilayer contribute to the AFM magnetic signal, leading to a weaker signal.

That this feature is originated from the rigid spin configuration of the AFM multilayer can be clearly confirmed by scanning the energy at the angular position. Such an energy scan at the incident angle of 9.0° is shown in figure 5.11. As for the determination of the largest magnetic signal at the FM Bragg peak in figure 5.9, two energy scans were carried out with reversed magnetic field directions (doted and full line). In the charge part an additional peak appears at around 702 eV caused by scattering interference due to the structural configuration of the sample. Similar behavior can be observed in the difference signal. It is clearly seen that the magnetic signal does not change sign, when the magnetic field is switched. This can be understood by assuming that the antiferromagnetic spin configuration is rigid at low magnetic fields, as it is indicated in the SQUID measurements by Jiang et al. [123], and cannot be flipped by reversing the low magnetic field on the sample. By increasing the energy, absorption becomes stronger and the incident soft x-rays do not penetrate in the AFM multilayer any more. Figure 5.12 shows the penetration depth for $\theta = 9.0°$ (middle curve) which confirms how
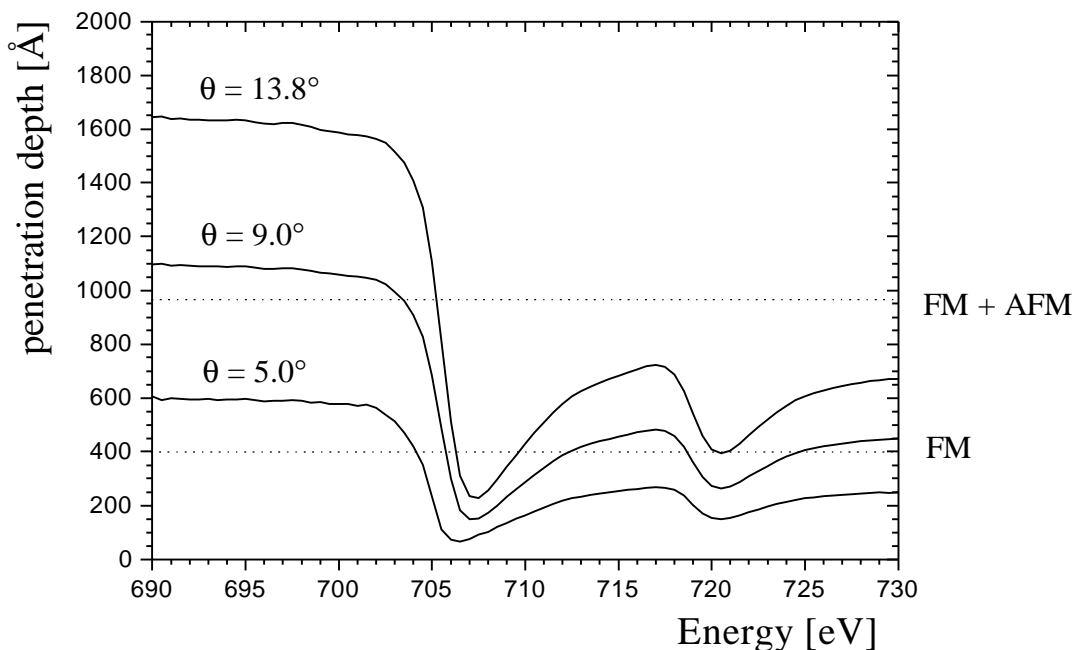


**Figure 5.12** *Penetration depth in the Fe/Cr double multilayer for different incident angles in dependence of the incident energy. Dotted line indicate the thickness of the FM and both, FM and AFM coupled multilayer.*

strong the energy dependence of penetration depth is near the iron edge. At E = 706eV the x-rays do not reach the AFM coupled multilayer any more and therefore the FM contribution dominates the difference signal showing two magnetic signals with reversed magnetization fields split in opposite directions. To represent the FM and AFM contribution in this energy scan clearer, the symmetric and asymmetric contributions between the two difference signals are plotted in figure 5.13. The full line represents the symmetric part, calculated by taking the difference of the two difference signals in figure 5.11. As pointed out before, the symmetric contribution presents the scattering from the iron spins which reverse their direction and align with the magnetic field, and is therefore an indication for the ferromagnetic contributions in the FM coupled multilayer. The dotted line, calculated by adding up the two difference signals in figure 5.11, shows the asymmetric contribution and contains all signals which are not reversed in the difference signal by reversing the magnetic field. There is a strong contribution at about 704 eV, which can be assigned to the AFM spin configuration and weaker one at about 708 eV, which is already strongly superimposed by the symmetric, ferromagnetic signal from the FM coupled multilayer.
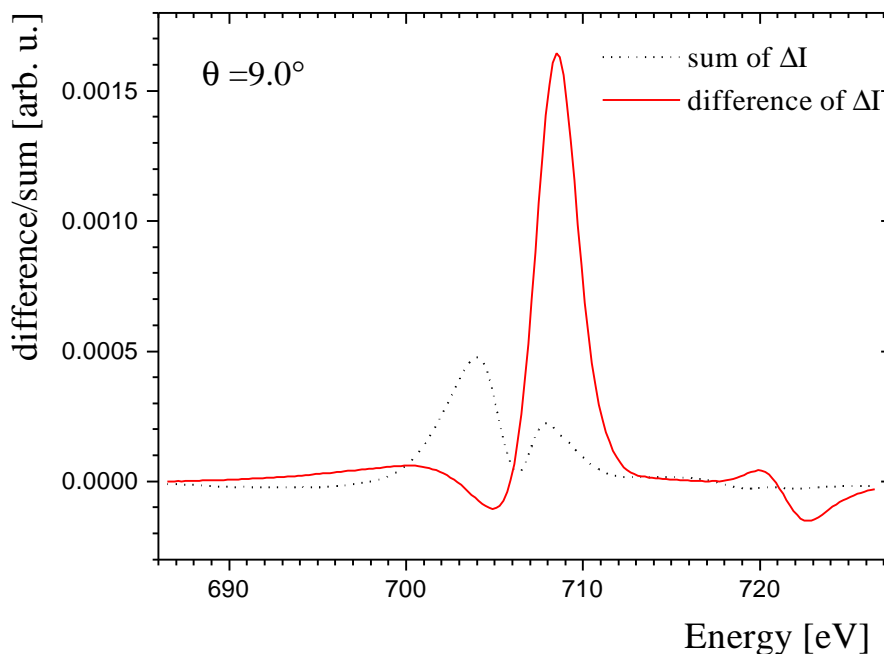


**Figure 5.13** *Symmetric (full line) and asymmetric contribution (dotted line) of the difference signal in figure 5.14.*

## Hysteresis loops

Besides angular and energy scan, the magnetic field dependence of the sample magnetization can also be examined by magnetic reflectivity. Here, the incident angles and the photon energy are fixed at certain values while the magnetic field on the sample is varied. As in the energy and reflectivity scans, the magnetic information is recorded as the difference signal between left and right circularly polarized intensity. The magnetic field on the sample is changed in a magnetization cycle, thus a hysteresis curve is measured. Figure 5.14 shows two hysteresis loops taken at a photon energy of 705 eV. The solid line represents the magnetic intensity at an incident angle of 13.8°, which is about the angular position of the second FM Bragg peak (see figure 5.10). The hysteresis loops is shifted by 39 Oe from the zero field with a coercive field of about $H_c$ = 7 Oe, which agrees perfectly with the results of the MOKE measurements discussed in section 5.3. The very symmetric contribution around zero signal confirms the FM character of the iron spins probed at the second FM peak. Moreover, the hysteresis loop indicates, that the FM spins are already saturated at very low fields.
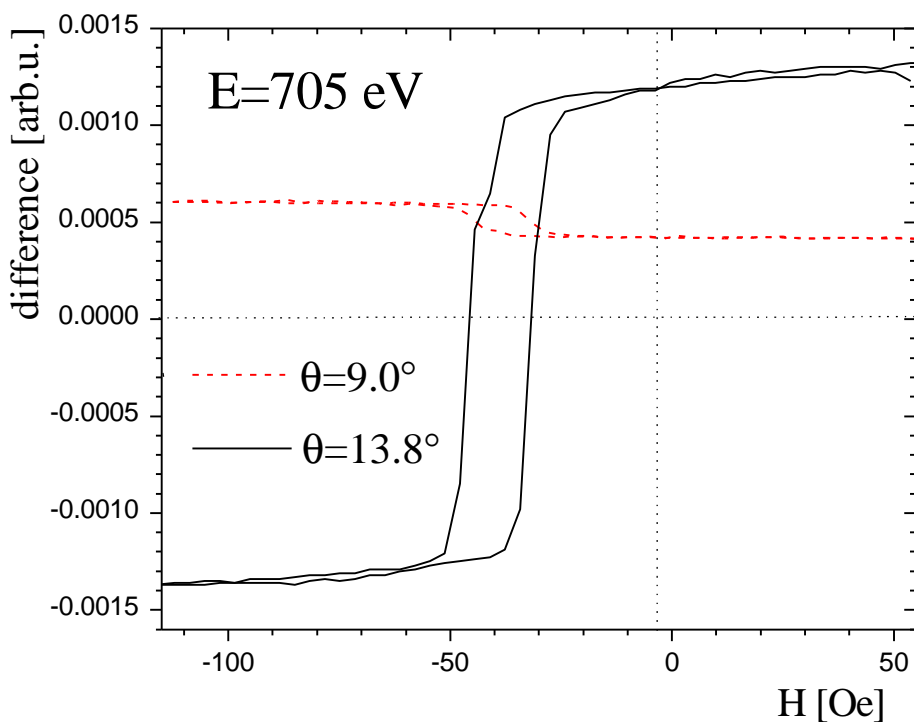


**Figure 5.14** *Hysteresis loop at E=705 eV for two different incident angles $q$ = 9.0° and $q$ =13.8°*

A different behavior is seen in the measurement shown by the dotted curve in figure 5.14. Here, the incident angle was fixed at 9.0°, which is, at the energy of 705 eV, an angular position where the rigid AFM spin configuration contribute dominantly to the magnetic signal (see magnetic reflectivity scan in figure 5.10). The magnetic difference signal does not change its sign, but exhibits a small hysteresis loop, which is also shifted and of the same coercive field as the hysteresis loop at 13.8°. This indicates that besides the constant AFM spin configuration, a small ferromagnetic contribution exists which is superimposed. Such small FM contribution exists through the whole reflectivity spectrum as long as the penetration depth of the x-rays reach the FM Bragg peak structure.

## 2D mapping of the magnetic reflectivity

In the previous section the procedure is described to extract information about the magnetization profile by using magnetic x-ray reflectivity. Basically three parameters can be varied: the incident photon energy, E, the angular position in reflectivity, $\theta$, and the magnetic field on the sample, H. In all scans presented so far, two parameters are kept constant and only one is scanned resulting in energy scans, reflectivity scans and hysteresis loops when the energy, angular position or the magnetization is the varied parameter, respectively. As seen in the section before, all scans are needed to optimize the magnetic measurement. First the specular charge reflectivity scan provides information about the structural distribution of the multilayer. Then the energy scan allows one to find the energy at which the magnetic signal is largest - which is usually not the position of the maximum in the MCD absorption spectra - and the hysteresis loops probe the general magnetic behavior of the sample, e.g. the saturation magnetic field, the shifts of the hysteresis loop due to exchange bias effect and the coercive fields in ferromagnetic materials. Of special interest here are energy and reflectivity scans. When the sample is magnetized in one or the other direction, both spectra carry information of the magnetization profile. It is also important to notice that energy and angular position are not independent parameters in the charge and magnetic reflectivity experiment. The momentum transfer $Q_z$, which is indirectly proportional to the correlation length probed in the reflectivity scans, depends on the photon energy and the angular position at the same time. Moreover, the effects in the magnetic reflectivity depends strongly on the selected energy. By choosing a different energy the charge and magnetic reflectivity curve can change drastically. The same is true for the energy scan, where the incident angle influences the shape of the curve due to structural changes in the reflectivity position.

In order to receive a complete picture of the magnetic behavior, both parameters have to be varied independently. Figure 5.15 shows the two dimensional plot from a series of energy scan with increasing reflectivity angles. The axis are the reflectivity angle and the photon energy, respectively, as indicated in the figure. Angular reflectivity from $\theta = 5°$ to $\theta = 16°$ and an energy range from 686 eV - 726 eV were covered in the measurements, where the magnetic field was fixed at H = -150 Oe. The upper plot shows the charge reflectivity plotted on a logarithmic scale. The two first FM structural peaks are clearly visible as well as oscillation between the two peaks.

126

Sum:
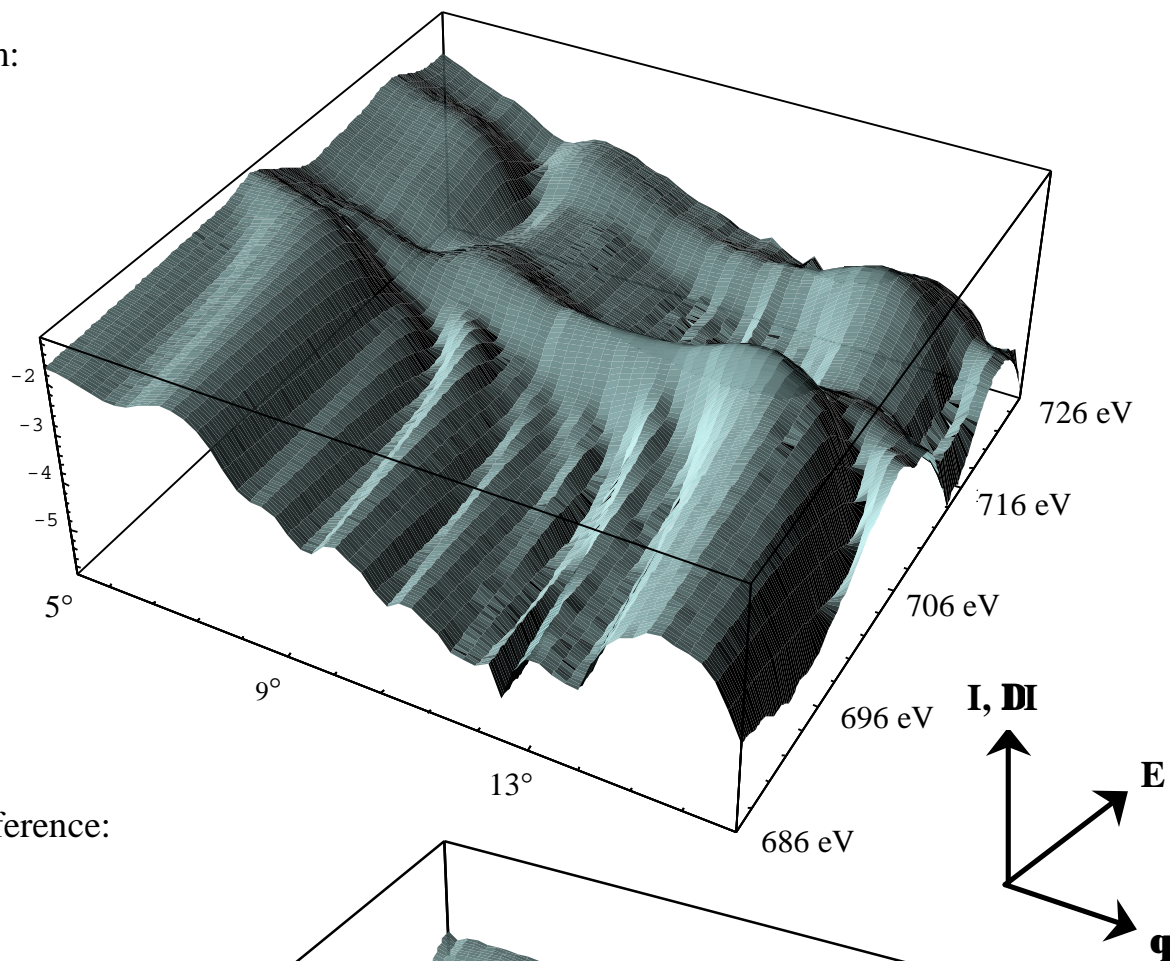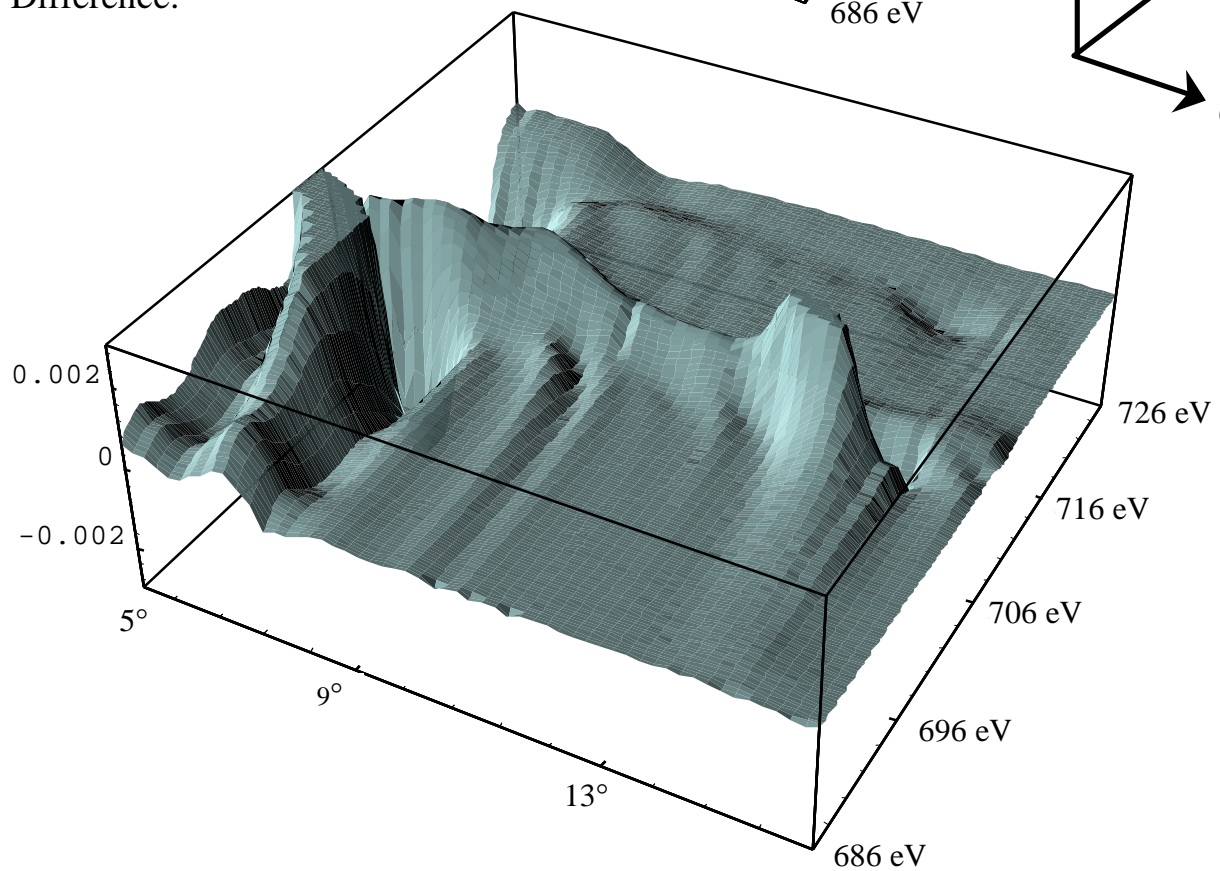


Difference:



**Figure 5.15** *2D Plot of the sum and difference signal in dependence of the angular reflectivity position and incident energy. Detailed description in text. Peaks in difference signal are partly cut.*

Following the FM peaks and interpeak oscillation along the energy range, an increase in intensity up to the $L_3$ edge at about 707 eV is observed. There is also the tendency of the structures to move to smaller angular positions due to the energy dependence of the momentum transfer $Q_z$. After a large drop in intensity after the $L_3$ edge, the intensity starts to increase again and reaches another maximum at the $L_2$ edge. Along the angular reflectivity direction, one can observe that the maximum of the detected signal is not always exactly at the energies of the $L_3$ and $L_2$-edges. It also exhibits some deviations around these positions as the angular position is changed, which shows the dependence of the reflectivity curve on the structural parameters of the sample.

The lower curve presents the difference signal between the right and left circularly polarized x-ray intensity, representing the magnetic reflectivity. The magnetic intensity is plotted on a linear scale. Similar to the charge part, the magnetic reflectivity is also enhanced near the two L-edges. Especially close to the $L_3$-edge the magnetic reflectivity is increased by a large amount, while at the $L_2$-edge the intensity change is less dramatic. At low angles around the first FM Bragg peak of the charge structure large difference signals can be detected, which exhibit also a large oscillatory behavior. Depending on energy and angle, negative or positive magnetic signals are detected. A similar behavior is observed in the region of the second FM Bragg peak at around $\theta = 13.5°$. At the half angular position of the AFM structural Bragg peak, additional oscillations can be observed. As already seen in the energy scan at $\theta = 9.0°$, these oscillations are due to the spin structure of the AFM Bragg peak and indicate the sensitivity of the method to the AFM spin configuration over a wide energy range. Exactly as detected in the charge reflectivity, all features tend to move to lower angular positions as the energy increases, which indicates that the dependence of the magnetic signal on angle and energy is similar to the behavior in the charge structures.

# Simulations of the magnetic x-ray reflectivity at the iron L-edges

The last section demonstrated how magnetic reflectivity is measured in various scans. Qualitatively, the features observed in magnetic reflectivity measurements are quite well understood and, similar to the charge reflectivity, can be assigned to structural properties of the sample. At the FM structural and half AFM peak positions magnetic Bragg peaks appear in the magnetic reflectivity data and the mapping of the energy and angular distribution provides a complete picture of the dependence of the magnetic reflectivity in energy and angle. Missing so far but important is a more quantitative understanding of the magnetic measurements, allowing one to specify the magnetic spin configuration and therefore make it possible to compare the magnetic spin configuration of different samples.

Similar to the charge reflectivity measurements, simulations are applied in the magnetic case based on model calculations including the magnetic spin configuration. The algorithm for the magnetic calculations has been extensively described in chapter 3.2.
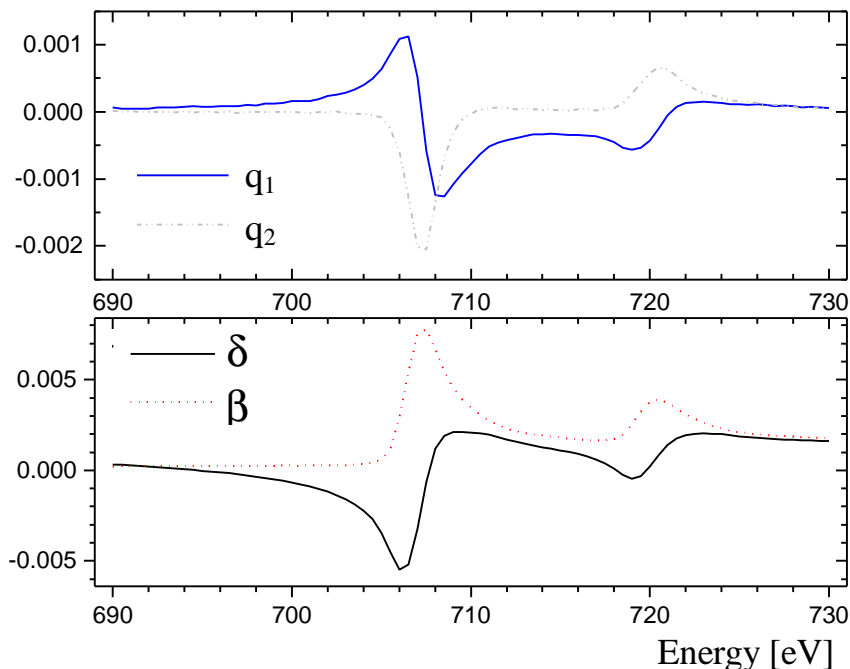


**Figure 5.16** *Optical constants for iron at the $L_3$ and $L_2$-edges. Upper figure shows the magnetic optical constant $Q = q_1 + i \times q_2$ and lower the corrections for the index of refraction $N = 1 - d + i \times b$.*

Basically, there are three ingredients needed for the simulation of the magnetic reflectivity: the charge distribution of the sample, the optical constants N and Q for each element and the magnetic spin configuration throughout the sample. The charge distribution is already well examined by the conventional reflectivity study in section 5.3. The layer thicknesses and structural setup are accurately determined by simulations of the charge reflectivity and can be used in the magnetic calculations as fixed parameters.

The second ingredient, the optical constants, are determined via the procedure described in section 3.3 for the specific element. Figure 5.16 shows the optical constants of iron at the L-edges and were derived from MCD measurements by C.T. Chen on a thin iron foil [30] as demonstrated in chapter 3.3. For all other elements, which are not close to an absorption edge, tabulated values for N are accurate enough and the magnetic optical constant Q can be assumed to be zero.

The last ingredient, the spin configuration of the magnetic layers throughout the sample, is the parameter to be extracted from the simulation. The magnetic reflectivity is calculated by assuming a certain magnetization profile and is then compared with the measurement. How different spin configuration influence the magnetic reflectivity spectra is shown in various examples in chapter 3.4.

Here, at the Fe/Cr double multilayer, it is known from the measured hysteresis loops that the iron spins of the FM multilayer can be easily saturated at low fields. Neutron reflectivity studies by Jiang et al. on a sample with the same structural and magnetic properties suggest collinear alignment for the spin configuration of the sample [123]. Thus, it can be assumed here that the iron spins are magnetized completely along the surface plane in one or the other direction.

It should be remembered that the spin structure of the iron layers in the AFM multilayer are antiferromagnetic aligned and are not influenced by the reversal of a low magnetic field.

With all ingredients derived it is now possible to calculate the magnetic reflectivity spectra. In figure 5.17, the difference signal for a series of energy scans in three different angular regions of reflectivity have been calculated and are compared to the experimental data seen on the left side. The experimental data shown here is part of the two dimensional magnetic reflectivity representation in figure 5.15. The angular positions are indicated in between experimental and simulated data.
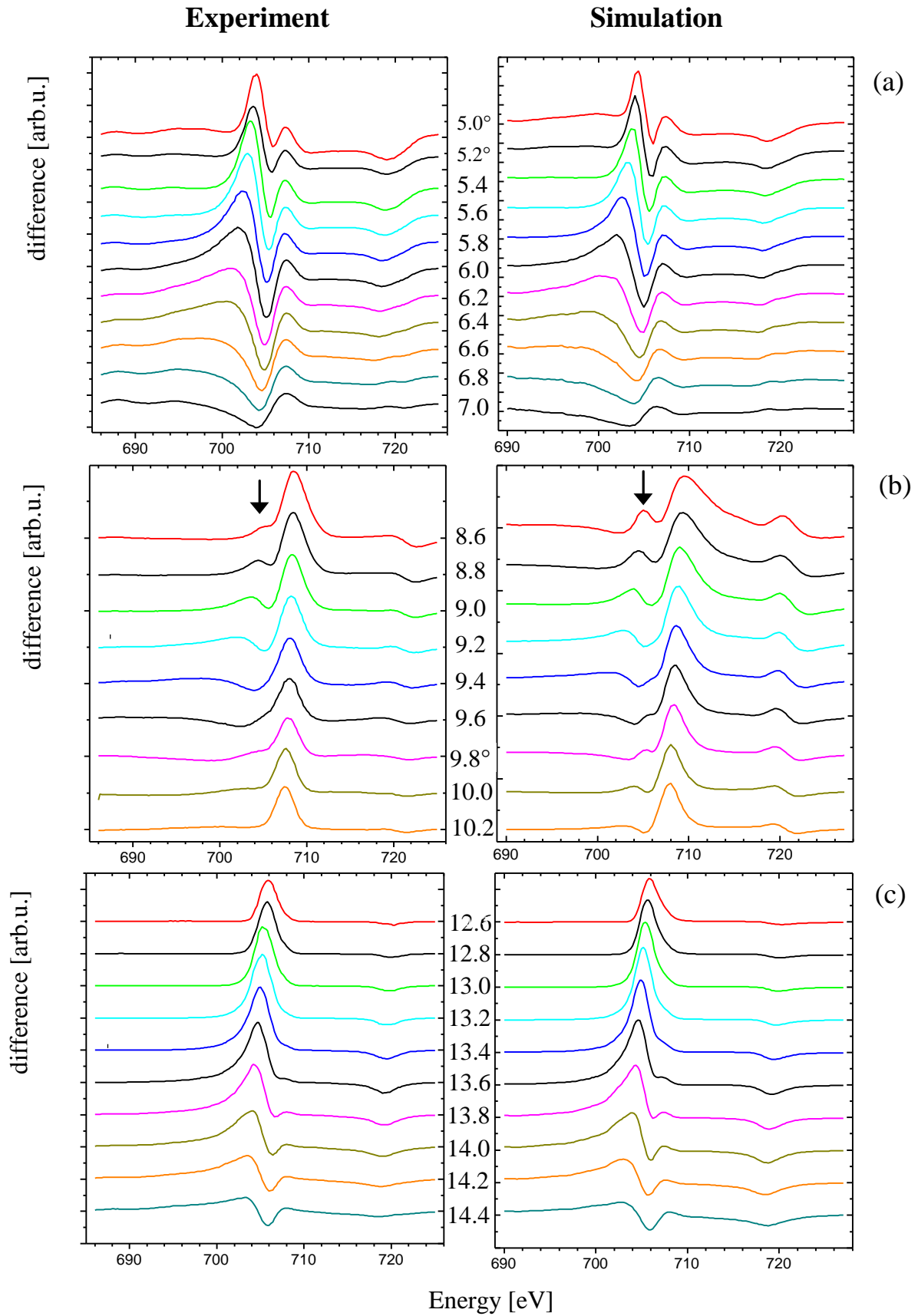
**Figure 5.17** *Difference signal for experimental (left) and simulated (right) energy scans for three different angle regions. Incident angle is indicated between both figures. For a detailed explanation see text.*

The first series (a) from $\theta = 5.0°$ - $7.0°$ covers the region around the first FM Bragg peak, which exhibits a strong energy dependence near the $L_3$-edge. At an energy of 705 eV the first FM Bragg peak can be found at about $\theta = 6.2°$ pointing in the negative direction. Both simulation and experimental curves show very similar energy dependence for all angular positions in this series. The second series (b) from $\theta = 8.6°$-$10.4°$ is in the region where magnetic peaks can be observed in the experimental data, which are caused by the AFM structure. They are indicated by an arrow in the figures. The energy dependence due to the AFM structure moves to lower energies while the incident angle is increased and vanishes finally around $\theta = 10.2°$. The simulation shows similar behavior. Here, the oscillation also moves from higher to lower energies, but shows much stronger signal at $\theta = 8.6°$ already. Moreover, the oscillation can be observed even at angles higher than $\theta = 10.2°$, which cannot be observed in the experimental data.

The third series (c) includes the second FM Bragg peak. Similar to series (a), oscillations near the $L_3$-edge can be observed for incident angles higher than $\theta = 13.6°$, but less dramatic and with opposite sign. Here again, there is nearly perfect agreement between the experiment and simulation in shape and in the development of the magnitude.

All three series show that the simulations reproduce the shape of the in the experiment observed features very well. There are deviations, most obviously seen in series (b) with the appearance of a much stronger side peak and additional small oscillation which were not seen in the experimental curves. Furthermore, comparing the experimental and simulated spectra in the first series, one can see that the magnitude of the oscillations in the energy scans develop differently with increasing incident angle for both experimental and simulated spectra. To understand the discrepancy between the simulated and experimental, one has to keep in mind that the simulations use simplifications. When the calculated curves are fitted to the experimental data, two assumptions are made in the calculations which limit the level of agreement between the calculated and experimental data. In simulations in general, it is desired to keep the number of variables as low as possible and reduce them to a few significant parameters. Especially for complicated structured samples like the double multilayer studied here, it is reasonable to make simplifications according to the structural setup, e.g. assuming that the layer thicknesses for the iron and chromium layers are uniform for every bilayer in each multilayer structure. Besides the structural simplifications, it has to be noted that the

interface roughness, which damps the intensity and smears out the features in the experimental specular reflectivity curves, could not been implemented in the simulation yet. The different scaling factors between experimental and simulated data as well as broadened features are likely to be caused by interfacial disorder. As is known from the charge reflectivity simulation, this roughness is not negligible.

Nevertheless, the simulations show very good agreement with the experimental data and qualitatively confirm the model used in the simulation. In order to gain more quantitative information from the simulation, the simulated magnetic reflectivity has to be directly fitted to the experimental data. Figure 5.18 shows the measured and simulated energy scans at an incident reflection angle of $\theta = 13.8°$ for three different scans. The top figure shows both the experimental (open circles) and simulated (full line) difference signal. The simulation was
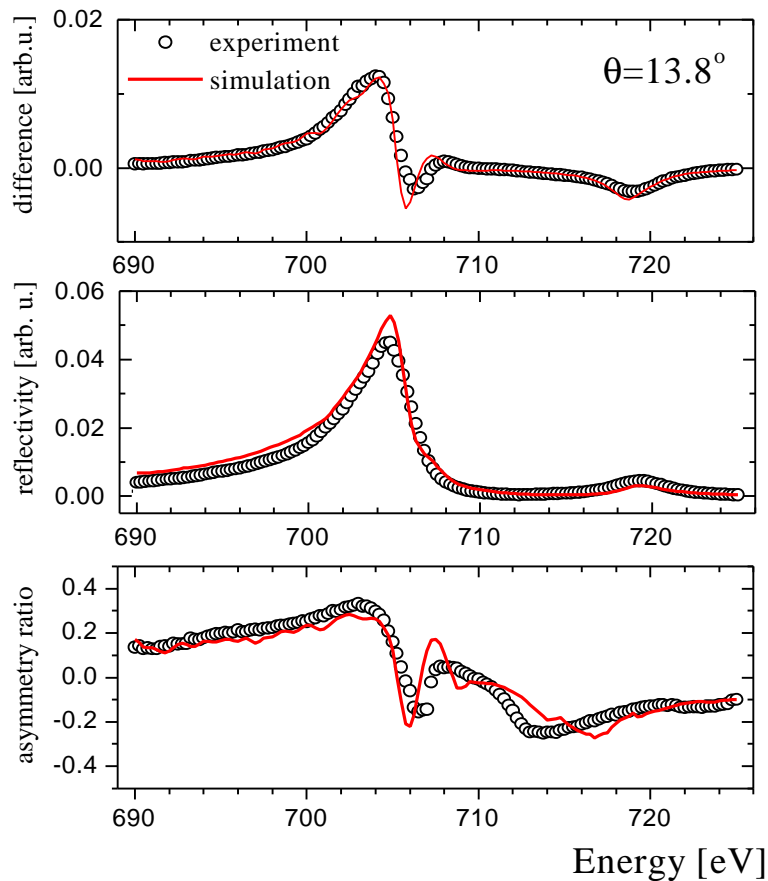


**Figure 5.18** *Measurement (circles) and simulation (line) of energy scan at $q = 13.8°$ and $H = -150$ Oe. Upper and middle plot shows the magnetic (difference signal) and charge (sum signal) reflectivity, respectively. Last figure plots the asymmetry ratio.*

scaled in order to fit the experimental data and is in good agreement as already seen qualitatively in the energy series (c) of figure 5.15. The middle figure shows the charge reflectivity spectra, which is represented by the sum of the intensity of left and right circularly polarized x-rays divided by two. Again, the simulated reflectivity was scaled in order to show best agreement with the measured curve. Here, the scaling factors of difference and sum factors are kept the same, only corrected for the assumed 60% degree of circular polarization in the difference signal (see chapter 4). This indicates that the relative magnitude of the magnetic reflectivity signal is identical for both experimental and simulated curves. The asymmetry ratio between magnetic and charge curves is shown in the last plot in figure 5.18. As mentioned before, the asymmetry ratio presents the magnetic reflectivity relative to the measured charge intensity and can be used to measure quantitatively the size of the detected magnetic intensity. As for the difference signal, it is also important for the fitting of asymmetry ratio to take into account the degree of circular polarization. The simulated asymmetry ratio reproduces most of the features observed in the experimental data, but also shows disagreement in the shape in the region just after the $L_3$-edge. It  should be noted, that peaks and features in the asymmetry ratio usually appear at other positions than in the magnetic reflectivity signal. Often minima in the charge reflectivity lead to huge signals, even though the total magnetic intensity seen in the difference curve is low. Therefore differences in both the charge and magnetic signal are very much enhanced and can lead to large variations seen between experimental and simulated curves. Therefore it is important for the simulation and understanding of the magnetic reflectivity to consider both spectra at the same time. An important result is the very similar asymmetry ratios for the experimental and simulated energy scan at $\theta = 13.8°$, which shows a large value of up to 32%. Thus, the relative magnetic intensity in the simulation is very close to the experimental measured data and confirms the collinear spin arrangement of the iron spins assumed in the simulation.

 Two further simulations of energy scans are shown in figure 5.19. They are selected at two different angular positions of the reflectivity curve, at $\theta = 5.0°$ and $\theta = 9.0°$, respectively, representing two examples from the energy scan series (a) and (b) of figure 5.17. At $\theta = 5.0°$ the momentum transfer $Q_z$ is low and therefore the penetration depth of the probing x-ray into the sample is very shallow. The energy scan at $\theta = 9.0°$ is the angular position where the magnetic peak from the AFM multilayer occurs near the resonance energy of the $L_3$-edge with

its maximum around 704 eV. At both angular positions the simulations are again scaled in the difference and sum spectra to visually fit both curves best. Here again, the scaling factors for the difference and the sum signal for each angular position differ only of the factor due to the degree of circular polarization of 60%. Both, the magnetic and charge reflectivity could be fit very well by using the same model with collinear aligned iron spins for the simulation as for the energy scan at $\theta = 13.8°$. The asymmetry ratio reproduces the observed relative magnetic intensities. The deviations are similar to these observed in the first case and can be again assigned to simplification made in the simulation for the structural configurations.

It is important to mention that the scaling factors for the three different angular positions are all different. As discussed before, there is no interface roughness included in the calculations, which modifies both the magnetic and the charge reflectivity curve and leads to reduced and damped intensities. Since the simulations do not include this effect, it has to be compensated by the individual scaling amplitudes. Furthermore, the damping factors due to interface roughness as they have been applied in the calculation of the specular charge reflectivity (see
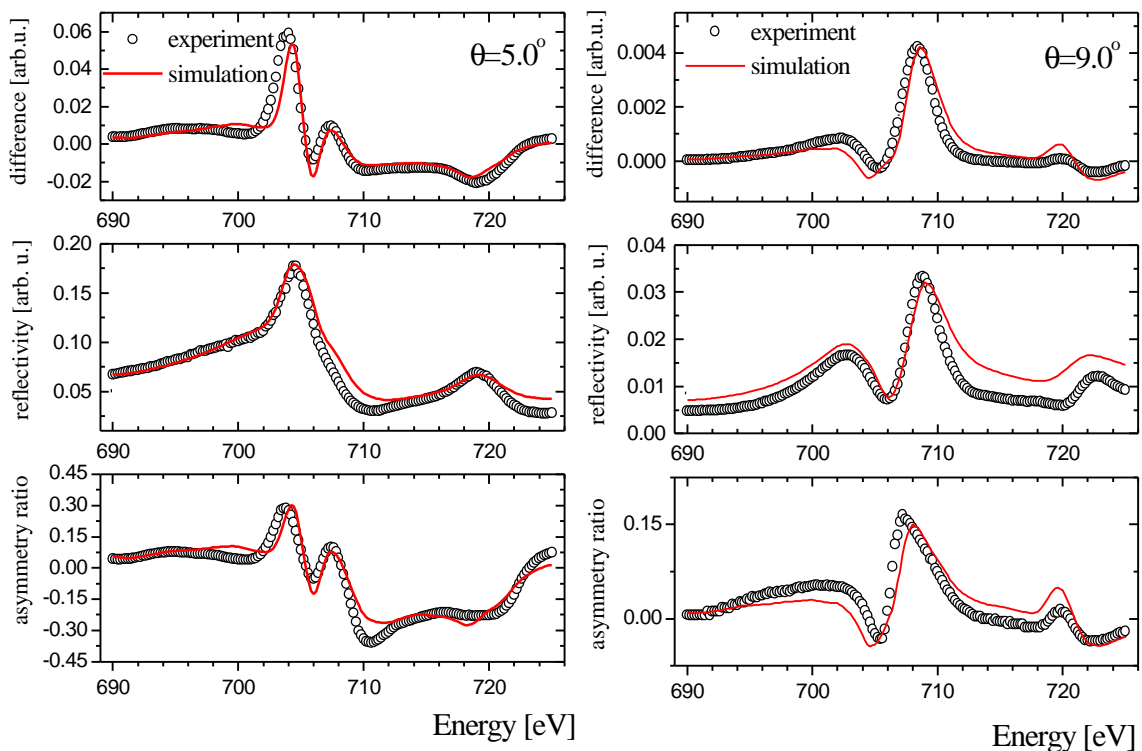


**Figure 5.19** *Measured (circles) and simulated (line) energy scans at $q = 5.0°$ and $q = 9.0°$ showing the difference (top) and sum (middle) signal and the asymmetry ratio (bottom panel). The magnetic field was fixed at H = -150 Oe. Figure setup see figure 5.18.*

chapter 3.1) depend on the wave vector $\vec{k}$, which is defined in equation (3.2) in chapter 3. The angular changes from a few degrees alters the value of $\vec{k}$ much stronger than changes of a few eV in energy, provided that the energy is in the range of several hundred eV or more. Therefore the energy scans are much less affected than angular reflectivity scans.

Besides the simulation of the energy scans, it is also possible to calculate charge and magnetic angular reflectivity at constant energy. Figure 5.20 shows the angular scans at an energy of E = 705 eV. Similar to the energy scans, three different plots are shown: The first plot shows the sum signal (charge reflectivity), the second the difference signal (magnetic reflectivity) and the third the asymmetry ratio. It should be noted that the charge reflectivity is presented on a logarithmic scale. In the first two plots the simulations are again scaled to the experimental
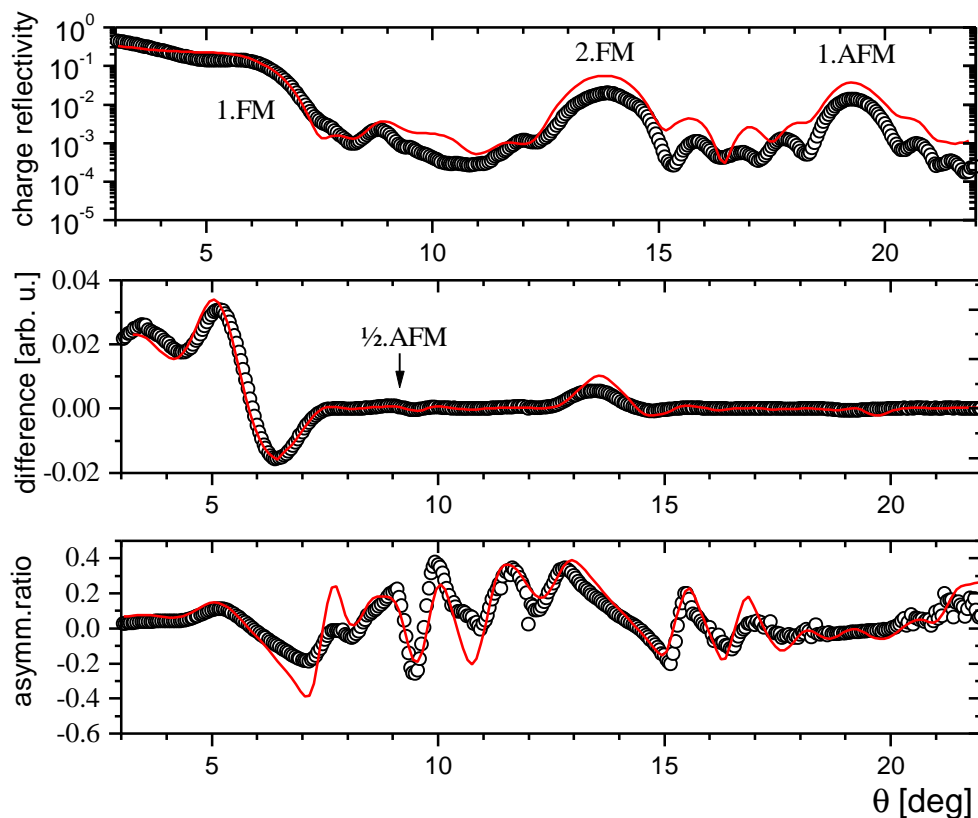


**Figure 5.20** *Experimental (circles) and simulated (line) angular reflectivity curve at E = 705 eV and H = -150 Oe. Left upper and middle plot show the sum and the difference reflectivity representing the magnetic and charge reflectivity. Lower plot shows the asymmetry ratio.*

curve as a guide to the eye. It can be clearly seen that the positions of the charge and magnetic Bragg peaks could be well reproduced, but, as discussed above, the interface roughness has a much larger affects in the angular scans. The intensity in the experimental curves drop significantly faster and are more smeared out compared to the simulation, where the interface roughness is not considered. However, despite the disagreements in the amplitude in the sum and difference signal, the asymmetry ratios in the last plot show again good agreement between simulation and experiment in shape as well in the magnitude over most of the recorded spectra. Only in the lower regions around $\theta = 7.5°$ the magnitude of the oscillations in the simulation deviates strongly from the observed experimental spectrum, which is mainly influenced by the disagreement in the charge structure. Especially at the first and second FM and the AFM Bragg peak position simulation and experiment show very good agreement. As already mentioned for the energy scans, the peaks seen in the asymmetry ratios are often caused by minima in the charge reflectivity and are not at the positions of the strongest FM contributions observed in the difference signal.

Particular interesting is the oscillation at the half $Q_z$-position of the structural AFM Bragg peak where the angular reflectivity curve is sensitive to the antiparallel coupled iron layers of the
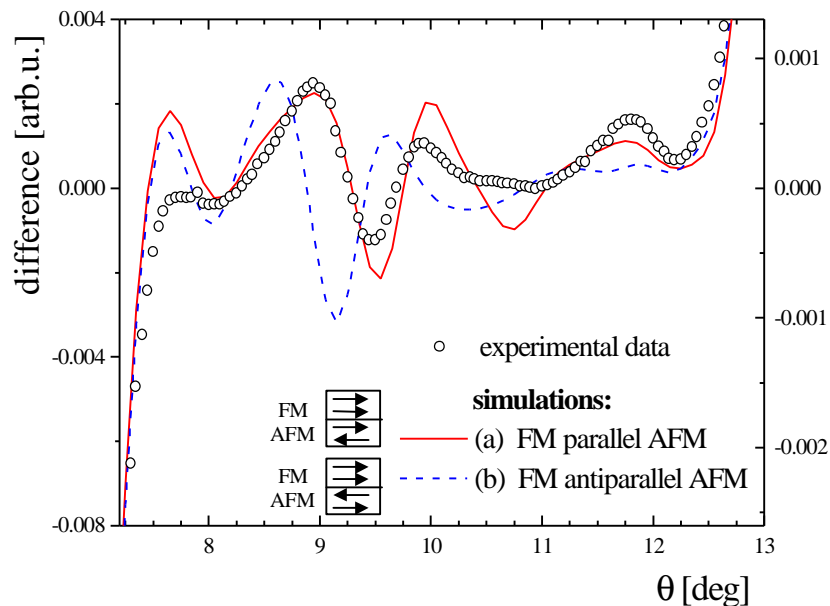


**Figure 5.21** *Region of half $Q_z$-position of the structural AFM Bragg peak showing the experimental and simulated difference signals. The two simulations assume parallel (full line) and antiparallel (dashed line) coupling at the FM-AFM interface of both multilayers.*

AFM multilayer. Figure 5.21 presents a magnified view of the difference signal in that angular region. Two simulations are plotted, where the coupling between the FM and the AFM multilayer is assumed to be parallel and antiparallel, determining the sequence of the antiferromagnetic coupled iron layers in the AFM multilayer. As it can be clearly seen, the simulation of the AFM oscillation can only be reproduced if the coupling is assumed to be ferromagnetic, while in the antiferromagnetic case the oscillation is shifted. Therefore, the magnetic x-ray reflectivity also allows to probe the layer sequence of the AFM coupled iron layers and therefore makes it possible to determine the coupling mechanism of this double multilayer system. It is important to note as already mentioned before that the magnetic signal and thus the oscillatory behavior is only detectable due to the absorption of the x-rays. Without significant absorption parallel and antiparallel coupling could not be distinguished via the magnetic reflectivity method.

In summary, the simulations at the L-edges of iron reproduce the experimental features very well and allow quantitative evaluation. Both scan modes, energy and angular reflectivity scans, are simulated and could be fitted to the experimental data. The simulated difference and the sum signal, representing the magnetic and charge reflectivity were scaled to experimental curves and provided qualitative understanding of the observed shape of the magnetic reflectivity spectra while the asymmetry ratios allow to quantify the observed magnetic intensity. Despite neglecting interface roughness in the calculations, the simulation with collinear aligned iron spins reproduces the experimental data very well. Thus, possible other spin configuration as shown in chapter 3.4 leading to different shapes and reduced magnetic amplitudes can be here excluded.

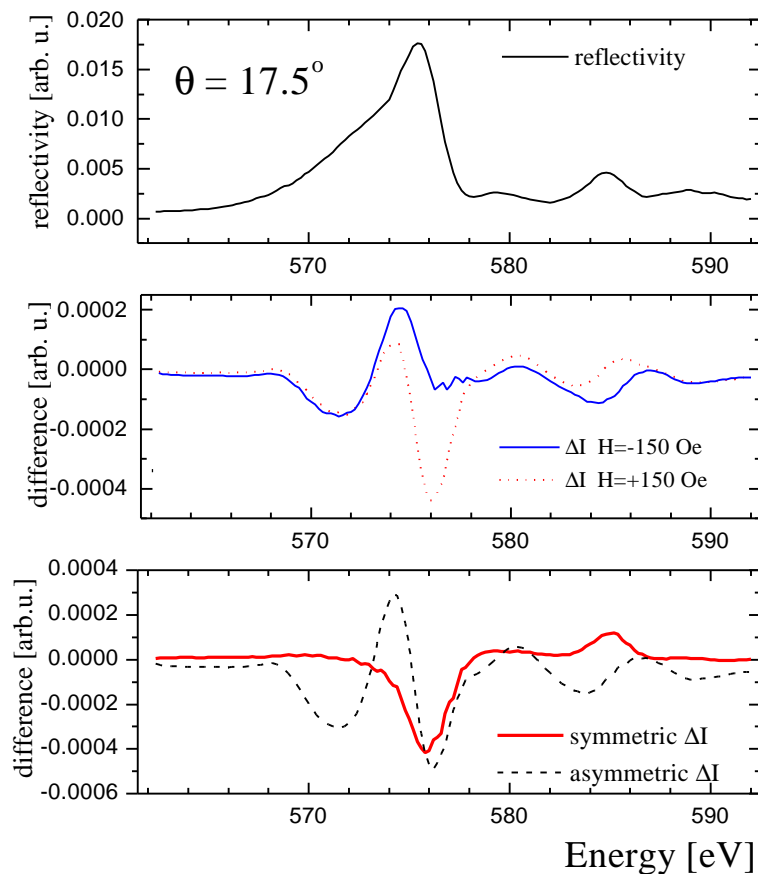## 5.2.2 Magnetic x-ray reflectivity at the chromium L$_{2,3}$-edges

In the last section the relatively large magnetic effect at the L-edges of iron caused by the collinear aligned iron spins could be easily detected. On the other side it is also known that chromium exhibits an enhanced magnetic moment on surfaces and interfaces [108, 128]. Moreover, the proximity of the magnetic iron layers have an additional big impact on the magnetic order in the chromium through the iron-chromium interface. Since magnetic x-ray reflectivity is an element specific tool, it enables one to examine magnetic contributions due to chromium separately by tuning the x-ray energy to the chromium absorption edges. Here in particular, measurements on the chromium L-edges are accessible in the soft x-ray range. Similar to the iron case, the spin-orbit splitting of the initial state lead to a larger polarization dependence for the excited photoelectron as has been discussed in chapter 2. In order to detect the chromium magnetic reflectivity the same procedure will be applied as for at the iron L-edges.

First a charge reflectivity scan allows one to verify the angular positions of the FM and AFM Bragg peaks. The energy was tuned to 573 eV, just before the chromium L$_3$-edge (574 eV). The specular reflectivity scan is shown in figure 5.22. Compared with the specular reflectivity curve near the iron edge, the Bragg peaks are shifted to higher angles due to the lower x-ray energy.
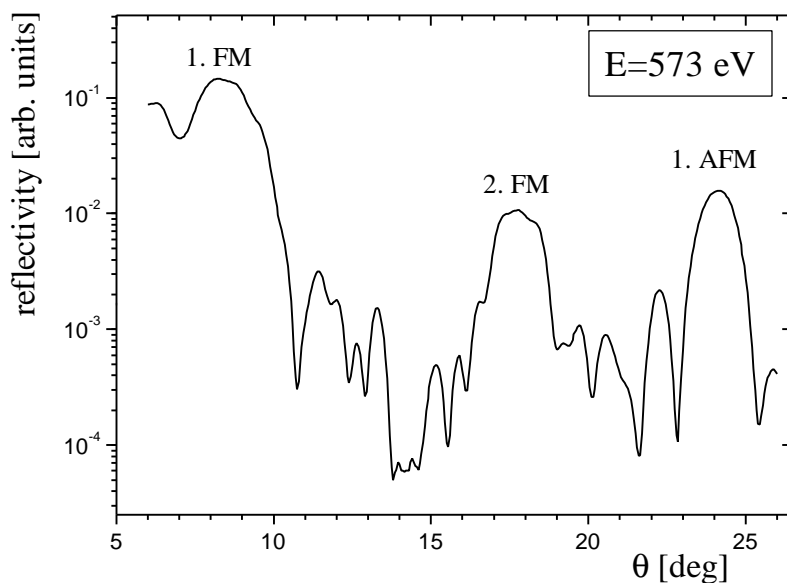


**Figure 5.22** *Specular charge reflectivity on the Fe/Cr double multilayer at a photon energy of 573 eV. Bragg peaks of the FM and AFM multilayer are indicated.*

Furthermore the peaks and oscillations are more sharply defined since the absorption from both chromium and iron layers is still weak at this photon energy. With the knowledge of the angular positions in the charge reflectivity, the energy can be now selected for which the magnetic reflectivity shows significant magnetic signal. For this purpose an energy scan at the angular position of the second FM Bragg peak is measured, as has been done for the iron layers. The energy scan is shown in figure 5.23. In the upper panal the charge reflectivity exhibits two distinct peaks at about $E = 575.5$ eV and $E = 584.8$ eV, which are due to the $L_3$ and $L_2$ edge of chromium, respectively. The difference signal between left and right circularly polarized light was measured for magnetic fields in opposite directions and are shown in the full and dotted line in the middle panel of figure 5.23. Even though the signal is much weaker



**Figure 5.23** *Energy scan at the chromium L-edges. The upper panel shows the charge reflectivity. The middle panel shows the difference signal between left and right circularly polarized intensity for opposite magnetic field. In lower panel the difference and sum of the difference signal for both magnetization directions are plotted, which show the symmetric and asymmetric contributions.*

than at the iron L-edges, it can be clearly seen how both signals split up in opposite directions when they approach energies near both L-edges and therefore confirms the magnetic nature of the effect. Besides the splitting for both signals, a variations in intensity along the energy scale is visible for both signal. Moreover, the peak positions for both magnetization channels seem to be shifted to each other. The lower plot shows the symmetric (full line) and asymmetric contribution (dashed line) of the difference signals for both magnetization states. The symmetric contribution shows clearly the shape expected from a ferromagnetic material with the distinct peaks near the $L_3$ and $L_2$-edge and opposite signs due the spin orbit coupling. But there is also a large asymmetric contribution which is on the same order as the symmetric part which exhibits a periodic oscillation. It turned out, that this oscillation are not of magnetic origin but produced by the elliptically polarized wiggler itself and superimpose a background to the recorded difference signal [127]. Therefore, if the signal gets weak, this background deforms the detected signal, as it is seen in figure 5.23. Here, it should be noted that the magnetic signal detected at the chromium edges is about twenty times smaller than the signal detected at the iron edge. Nevertheless, the energies where the splitting between the two difference signals is maximized can be taken as the photon energy where the sensitivity to the FM contribution is maximized. For the angular reflectivity scan, an energy of 575.0 eV is chosen, which is slightly lower than the maximum effect at E = 575.5 eV. At this energy, the magnitude for both magnetization direction is symmetric to zero, which minimize the background from the wiggler device.

Figure 5.24 shows the recorded charge and magnetic reflectivity curve at the selected photon energy. The difference signals can be clearly measured for both magnetic field directions and show opposite signs at the FM Bragg peaks as expected for ferromagnetic contributions. Also at the first AFM peak a comparable FM contribution can be detected. It should be noted that the ferromagnetic contributions at all of these peaks are weak and only on the order of one percent or less compared to the charge signal. They are very much enhanced in the difference signal due to the high intensities measured at the charge reflectivity.

At the half AFM position both difference signals exhibit a clear oscillation in the same direction, indicating their sensitivity to the magnetic contribution of the AFM structure in the second multilayer, as it has been already detected at the iron L-edges. Here, the peak is significant strong. Even though the reflected intensity at the charge curve is much lower, the difference signal of the AFM contribution is not only on the order of the FM part at the second
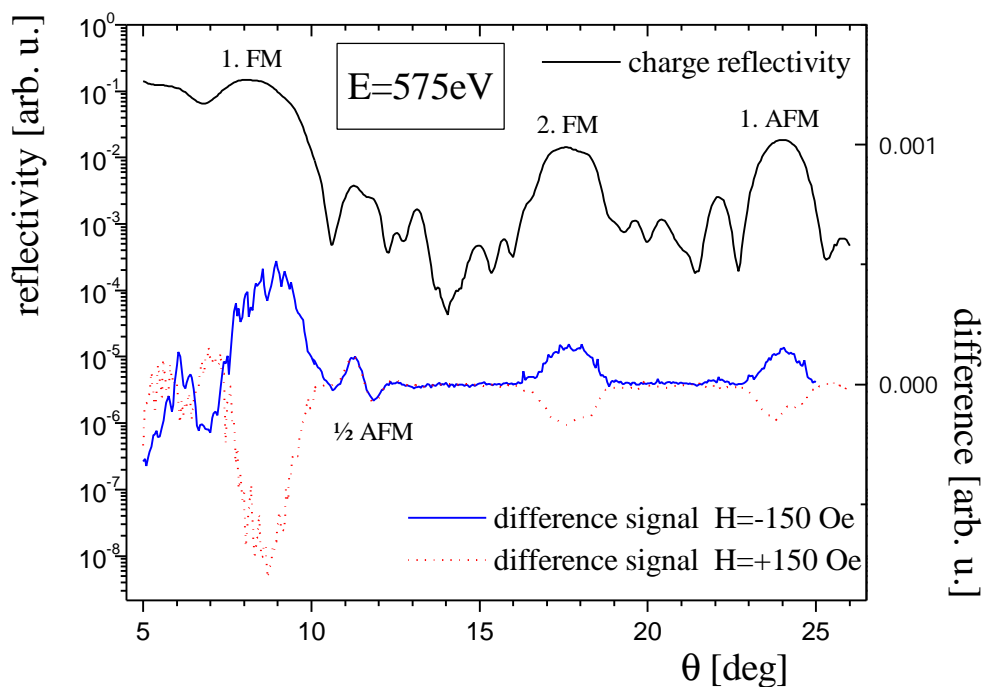
**Figure 5.24** *Charge (upper graph) and magnetic reflectivity (lower graph) near the chromium L-edges (E = 575 eV). The difference signal is recorded for opposite magnetic fields (full and doted line, respectively). Structural peaks are indicated in the figures.*

Bragg peak, but also appears to be much smoother. Since the FM multilayer possesses only five, and the AFM multilayer twenty bilayers, the magnetic signal due to the AFM is expected to be stronger and smoother as it is observed here. The soft x-rays at an energy of 575 eV also penetrate through the whole double multilayer system and therefore all twenty bilayers of the AFM coupled multilayer contribute as it can be seen in figure 5.7 shown earlier in the previous section. The absorption for the soft x-rays before the chromium L-edges is much less than in the iron L-edges.

Figure 5.25 shows an energy scan recorded at an incident angle of $\theta = 11.3°$, right at the AFM peak, which is detected in the magnetic reflectivity in figure 5.24. In the charge reflectivity curve an additional peak can be observed at about E = 580 eV. The difference signal in the middle plot shows a clear oscillation but nearly no splitting between the two magnetic field directions. The artificial oscillation due to the wiggler output can be still observed, but are much smaller with respect to the main features as for the energy scan at the second FM Bragg peak. Here, the asymmetric contribution depicted in the lower figure is much stronger than the symmetric part. Contrary to the energy scan at the second FM Bragg peak position it clearly

shows the magnetic contribution from the AFM aligned multilayer and therefore confirms the rigid antiferromagnetic coupling of the induced magnetic moments of these chromium layers.
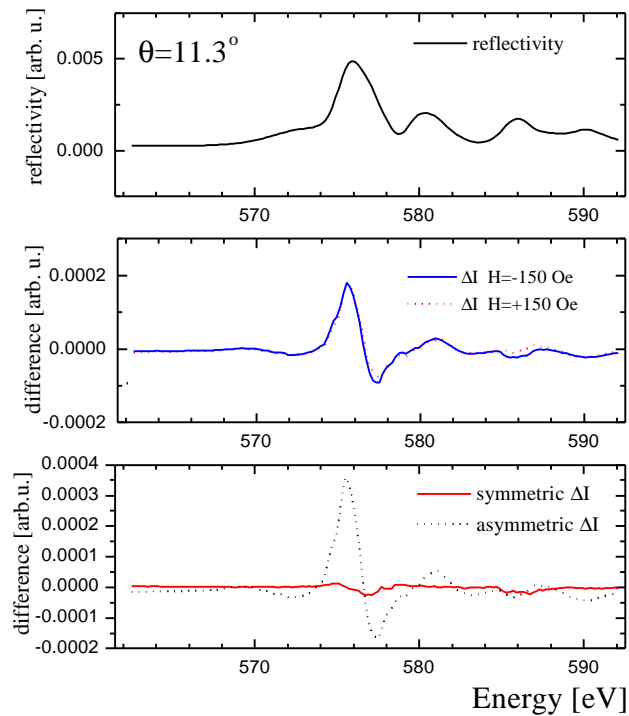


**Figure 5.25** *Energy scan at $q=11.3°$, description see figure 5.23.*

In order to check the switching behavior of the chromium moments compared to the iron moments, it is important to measure the hysteresis loop also near the L-edges of chromium, where the signal is only sensitive to the magnetized chromium site. Figure 5.26 shows the hysteresis curve at an energy of 575 eV at the second FM Bragg peak position at $\theta = 17.5°$. The hysteresis curve is shifted of an exchange bias field of about $H_E = 39$ Oe and possesses a coercive field $H_E = 7$ Oe, which are the same values observed in the hysteresis curve at the second FM peak measured near the $L_3$-edge of iron (see figure 5.14). The individual features for the chromium and iron hysteresis loops are identical. This implies that the chromium spins must follow the iron spins in their switching behavior, therefore supports the assumption that the chromium moment is strongly influenced by magnetic behavior of the iron layers.
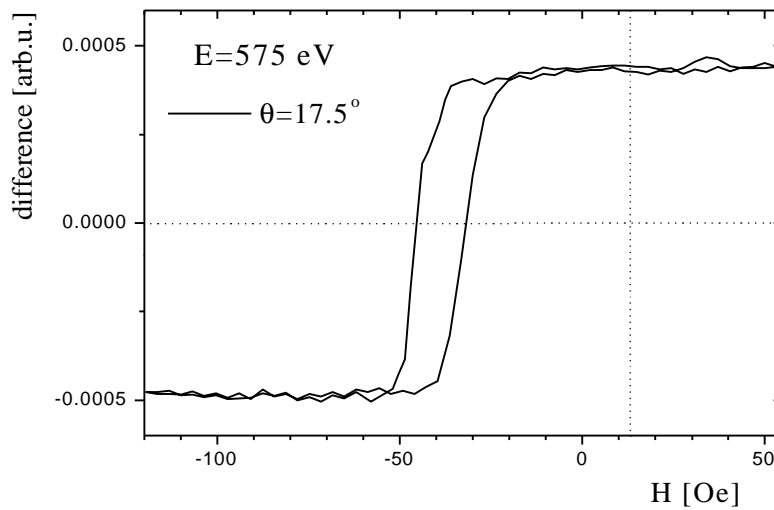
**Figure 5.26** *Hysteresis loop at E=575 eV and incident angle of* ***q*** *= 11.3°.*

Comparing the hysteresis loops from chromium and the iron layers at the second FM Bragg peak at the $L_3$-edges of chromium and iron, respectively, shows identical orientation of the hysteresis loops for both elements. However, it is important to note that in reflectivity experiments this observation does not allow one to determine the coupling of the adjacent chromium and iron layers as it can be done in a MCD absorption experiment, where ferromagnetic and antiferromagnetic can be distinguished by comparing the sign of magnetic contribution at the individual L-edges for each element [128]. While the imaginary part of the magnetic scattering amplitude is the main contribution in an MCD absorption experiment, the real part plays an important role in the evaluation of magnetic reflectivity data and usually exhibits a very different behavior.

It is also important to note that in a reflectivity experiment the contributions of real and imaginary part depend not only on energy, but also on the angular position. Particular at Bragg peak positions the contribution from the real part is stronger. For the discussion, simulations are the appropriate tool to distinguish between the different scenarios as already discussed for the magnetic data at the iron L edges. In the next section the magnetic reflectivity at the chromium edges will be simulated. A comparison of the sets of parameter for the simulation at the iron and chromium L-edges will allow one to determine the  actual coupling at the Fe/Cr interfaces.

# Simulations of magnetic x-ray reflectivity at the chromium L-edges

For the simulation at the chromium L-edges the three ingredients have to be found which are necessary to fit the experimental data. The first ingredient, the structural setup of the sample, is obviously identical to the numbers used for the simulations at the iron L-edges and will be considered again as fixed parameters. Next, it is important to determine the optical constants of chromium at the chromium L-edges, charge and magnetically. In contrast to iron, which can be magnetized easily by applying a magnetic field, the magnetic moment of chromium is strongly influenced by the magnetized iron layers which also enhance the magnetic moment of chromium layer at the interface. Idzerda et al. measured the MCD signal of 0.25 monolayer chromium deposited on a 150 Å thick iron layer, which was completely magnetized parallel to the interface [128]. The moment of the thin chromium layer is then assumed to be
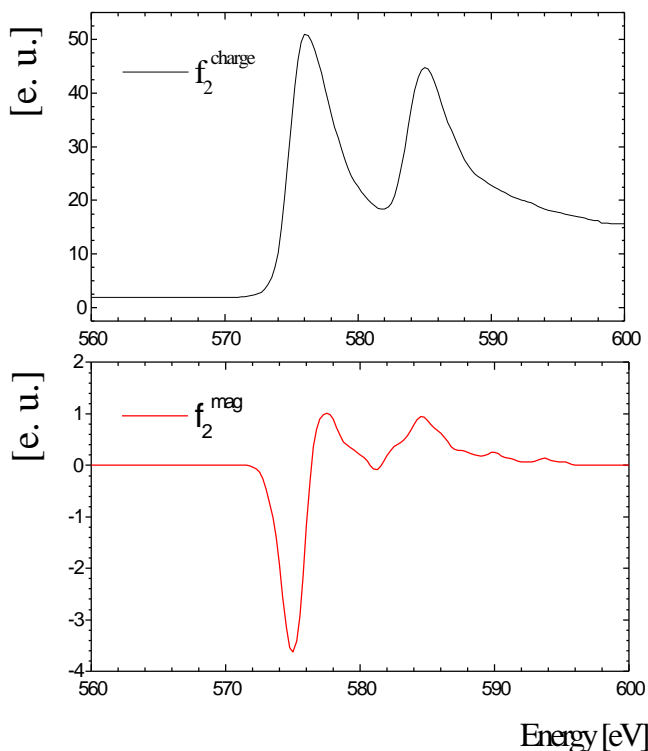


**Figure 5.27** *XAS and XMCD measurement of 0.25 ML chromium deposited on 150 Å iron at the chromium L-edges*
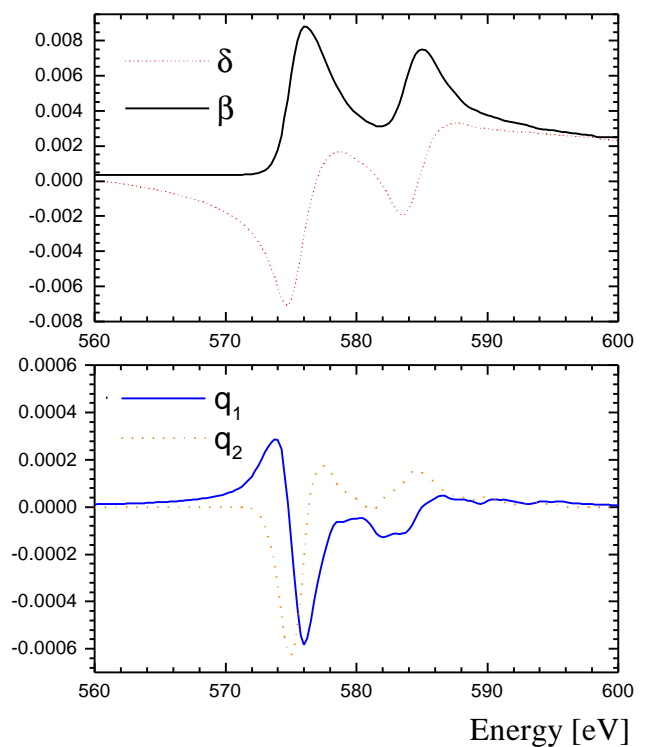
**Figure 5.28** *Upper plot: dispersive ($\delta$) and absorptive ($\beta$) correction factors for the index of refraction; lower plot: real ($q_1$) and imaginary ($q_2$) part of the magnetic optical constant for chromium.*

homogeneous and in-plane ferromagnetically coupled, while the coupling between the iron the chromium moments at the interface is antiferromagnetically. Figure 5.27 shows the absorption and magnetic circular dichroism spectra from the measurements by Idzerda et al. [128]. The peak height ratios between the MCD and the absorption at the $L_2$ and $L_3$ white lines are -3.5% and 7.2%, while the peak area ratios are -3.6% and 2.6%. The average magnetic moment in chromium can be therefore estimated to about $(0.6 \pm 0.2)$ $\mu_B$ per atom via sum rules, which is in good agreement with the theoretical bulk value of 0.59 $\mu_B$ per atom [129]. It should be noted that the magnetic moment of a monolayer of chromium on top of iron has been examined by many groups using different experimental techniques, e.g. spin resolved core level photoemission (SPPS) [130, 131], spin polarized electron-energy loss spectroscopy (SPEELS) [132, 133], energy resolved spin polarization secondary-electron emission [134] or in situ alternating gradient magnetometry technique [135]. The corresponding results show large variations from 0.5 - 1 $\mu_B$ up to 4 $\mu_B$ per atom. The disagreement in the experimental results are supposedly due to the quality of the chromium layers, since magnetism is highly sensitive to the structure of the interface and interfacial roughness. In this study the results of Idzerda et al. are used for the simulation, which enables one to extract the magnetic optical constant from the MCD measurement. Changes in the magnetic moment of chromium at the actual interface result in a linear scalar factor as it will be discussed later.

Figure 5.28 shows the dispersive $\delta$ and absorptive correction factor $\beta$ for the index of refraction in the upper figure and the real $q_1$ and imaginary part $q_2$ of the magnetic optical constant in lower figure, derived via Kramers-Kronnig Transformation. It should be noted that the sign of the MCD signal was chosen such that the $L_3$ peak is negative in order to be consistent with the MCD data used for the simulation at the iron L-edges. These values are now used to calculate the index of refraction and the magnetic optical constant for chromium near the chromium L-edges.

After defining the optical constants for the induced moment in chromium, a model for the spin configuration for the chromium has to be chosen in the next step. Since the magnetic moment is strongly influenced by the Fe/Cr interface it is likely to assume that the magnetic moment of chromium is strongest close at the interface and decreases with increasing distance from the iron layer. In the extensive study of the magnetic structure of chromium in (001) and (100) orientation  sandwiched between two iron layers, chromium is expected to possess a spin

density wave with alternating magnetic moments from sublayer to sublayer with ferromagnetic coupling in plane of each sublayer and an antiferromagnetic coupling at the interface to iron [108, 109]. Such a model is e.g. proposed by Stoeffler and Gautier using tight binding calculations for Fe/Cr trilayers [136]. Figure 5.29 shows a schematic of such a possible model. The magnetization can be thought of an oscillatory damped wave with alternative magnetic directions due to the AFM order in chromium itself. However, the magnetic moment of chromium layer can be further simplified by a single magnetic layer with a constant magnetic moment over an effective thickness $t_{eff}$ at the Fe/Cr interface, which results in a measure of an effective magnetic moment of the chromium layer. For this constant magnetic moment in the chromium layer, the values calculated in Fig. 5.28 are used in the following calculations.
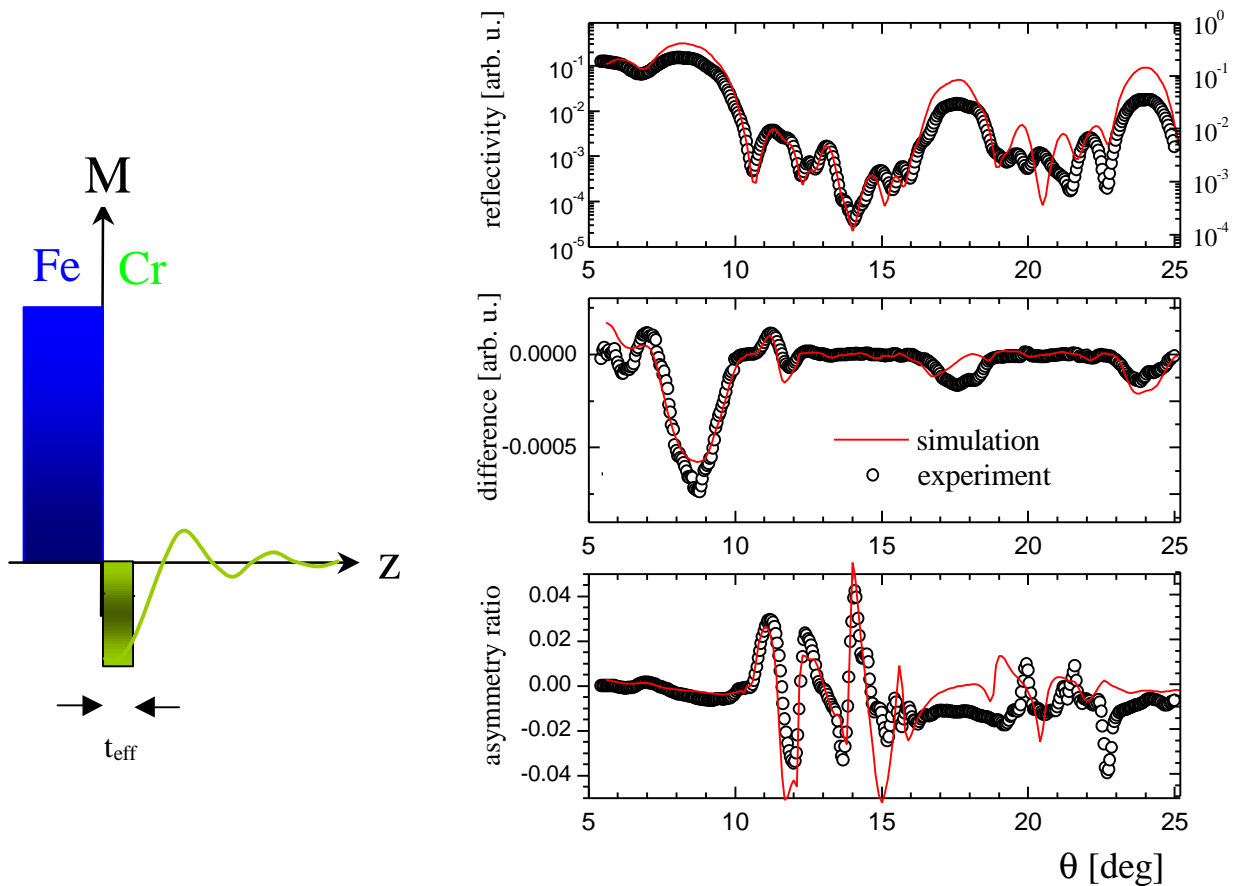


**Figure 5.29** *Magnetic simulation on the Fe/Cr double multilayer at the chromium L-edges (E = 573 eV). Left figure shows schematically the model at the Fe/Cr interface used for the calculation (explanation in text). On the right side, the experimental data (circles) and the simulation (line) with an effective thickness of $t_{eff} = 0.5$ Å for the magnetized part in chromium shown for the difference (upper panel) and sum signal (middle panel) and the asymmetry ratio (lower panel)*

The right plots in figure 5.29 show the experimental and simulated data for the angular reflectivity scan at an incident photon energy of 575 eV and an applied magnetic field H = +150 Oe as depicted in figure 5.24. An effective thickness of the chromium layers $t_{eff}$ of 0.5 Å is assumed in the simulation. The calculated curves for the charge reflectivity and the difference signal were scaled in order to fit them to the experimental data. For the first part of the charge reflectivity, the simulation fits very well with the experimental curve and shows only larger discrepancy after the second FM Bragg peak. In the difference signal most features could be also very well reproduced, except for the region around the second FM Bragg peak, where the assumed model could not fit the experimental curve. The bottom panel shows the asymmetry ratio. As already mentioned for the simulation of the iron layers in the previous section, it is important to note that for this representation no scaling factors were implied except the assumed 60% degree of circularly polarization of the soft x-ray beam. Here, it can be clearly seen that the magnetic signal from the AFM coupled chromium layer exhibits a much larger effect than the chromium layer from the FM multilayer. Around the AFM half position oscillations on the order of four percent in the asymmetry ratio were detected stemming from the AFM coupled chromium layers, while at the FM positions the magnetic effect is only about one percent. As already mentioned before, this difference in the magnetic asymmetry ratio can be understood, since in the case of the AFM coupled multilayer twenty bilayers contribute and in the FM coupled multilayer only five bilayers. The simulation of the asymmetry ratio fits very well for the first part of the reflectivity curve, especially at the position of the oscillation from the AFM coupled multilayer. For higher angles the simulation and measurement show large discrepancies, caused mainly by the disagreement between experimental and simulated charge reflectivity curve, but is also due to the shift of the second FM Bragg peak in the difference simulations, which could not be explained yet.

To determine the effective thickness $t_{eff}$ we take advantage of the larger signal at the AFM half peak. Figure 5.30 shows the changes in the difference signal and asymmetry ratio when the thickness of the enhanced magnetic moment at the interface, approximated as a step function presented in figure 5.29, is varied. The charge reflectivity curve and the difference signal are scaled to fit the experimental curve as it has been done in the previous figures. The simulations are in qualitative good agreement with the experimental data. They especially show how the effective thickness $t_{eff}$ influences the amplitude of the difference signal in the middle plot. By reducing $t_{eff}$ to half of its value, the amplitude of the oscillation decreases by about a factor

two, and scales therefore roughly linear with $t_{eff}$. The effect on charge reflectivity curve is negligible due the very small magnetic effect as seen in the upper plot of figure 5.30. In order to approximate the effective thickness $t_{eff}$, the asymmetry ratio has to be considered, giving a quantitative measure for the magnetic effect. It clearly shows that a $t_{eff}$ of 1 Å and larger
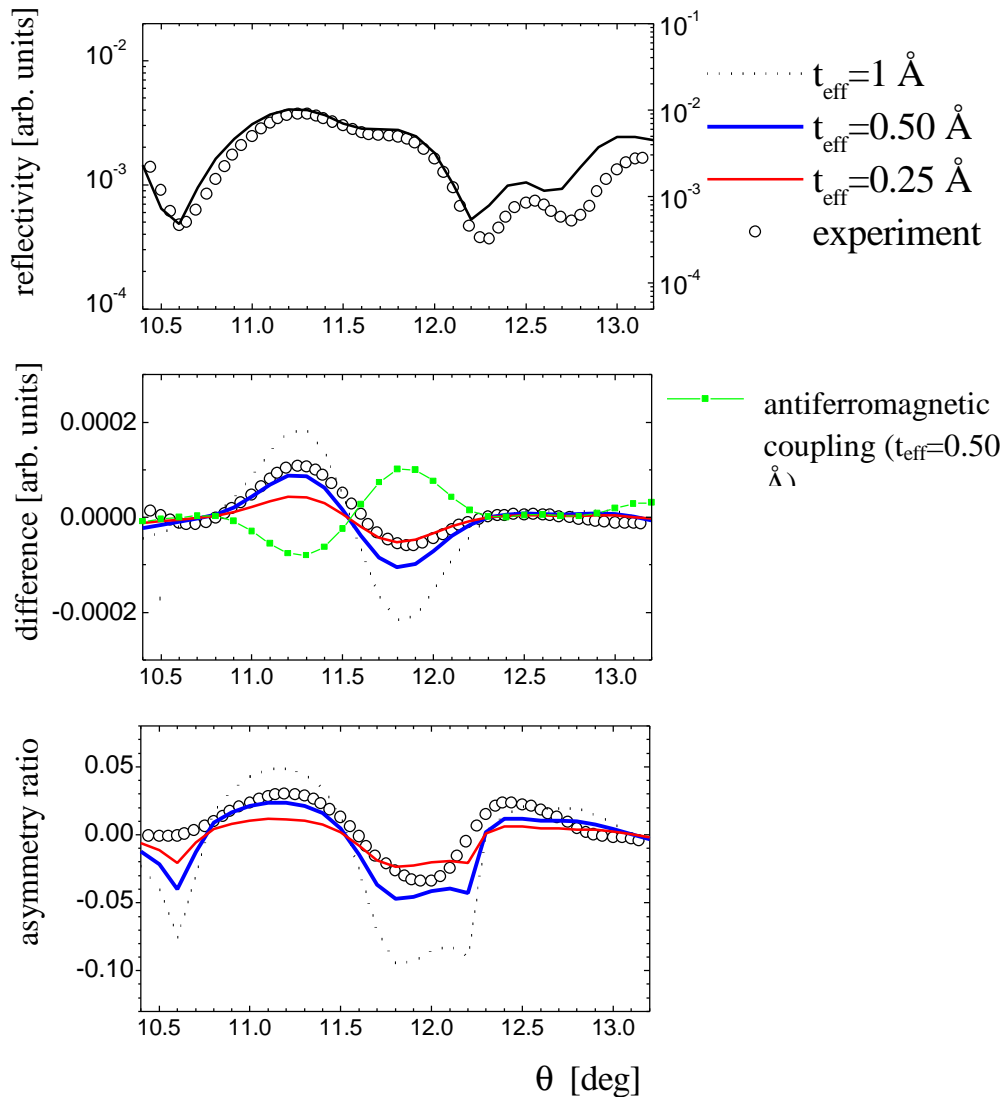


**Figure 5.30** *Charge reflectivity (upper panel), difference signal (middle panel) and asymmetry ratio (lower panel) for experimental (open circles) and simulated (lines) curves for the AFM half peak at E=575 eV assuming model depicted in figure 5.26. Simulations with effective thicknesses $t_{eff}$ of the magnetic active chromium layer at the iron-chromium interface of 1 Å (dashed line), 0.5 Å (full thick line) and 0.25 Å (thin full line) are shown with ferromagnetic coupling between the interfacial spins of the FM and AFM multilayer.In the middle plot for the difference signal an additional simulation for $t_{eff}$ = 0.5 Å with antiferromagnetic coupling (line with closed squared symbols) at the FM-AFM interface is*

produce oscillations in the asymmetry ratios which are too large to fit the experimental data. By reducing to 0.5 Å the agreement is good, even though the second half of the oscillation is a little too large. Further reducing of the effective thickness $t_{eff}$ to e.g. 0.25 Å improves the second part, but is too small for the first part. From this fit it can be concluded that by assuming a step function magnetization profile for the chromium layer, an effective thickness $t_{eff}$ of about 0.5 Å reproduces the data best.

Moreover, the simulations presented in figure 5.29 and 5.30 allow one to draw further conclusions. Only by assuming a ferromagnetic coupling between the interfacial iron layers at the FM and AFM multilayer and the thus induced moments of the chromium spins reproduce the experimental features, especially at the half AFM peak position in the difference signal and asymmetry ratio. In the case of antiferromagnetic coupling between the two multilayer structures, the oscillation in the difference signal and asymmetry ratio would change sign as it is depicted in a simulation presented in the middle plot of figure 5.30 for antiferromagnetic coupling and an effective thickness $t_{eff}$ of 0.5 Å. It should be noted that the effective thickness determined by this approach depends on the MCD measurement used to extract the magnetic optical constants. In case of variations e.g. due to interface quality the effective thickness has to be adjusted. Simulations show that the magnetic moment in chromium and the effective thickness scale linearly.

Furthermore, the relative orientation of the iron and chromium spins can be now determined from the simulations. Both parameter sets used in the simulation at the iron and chromium L-edges indicate clearly that the effective magnetic moment of chromium is antiferromagnetically coupled to the adjacent iron layers. As mentioned before, this result shows that by measuring hysteresis curves in reflectivity, the sign and orientation of the hysteresis curve does not by all means deliver the interfacial coupling behavior between two different magnetic sites. Even though the hysteresis curve show identical orientation at the second magnetic Bragg peak near the $L_3$-edges of both elements, the coupling turns out to be still antiferromagnetic as it is predicted and measured in a range of other experimental techniques [130 - 135].

Further modeling, e.g. assuming a spin structure following the antiferromagnetic order as depicted in figure 5.29, seems to bring no further advantage. Nevertheless, certain scenarios can be excluded, as for example a commensurate AFM order in the chromium. Only an enhanced moment at the interface to the iron layers is necessary to reproduce the measured

magnetic reflectivity profiles. In order to extract more accurate information of the magnetization profile of the induced chromium layer, more orders of the AFM peak oscillation would be required to be measured. Unfortunately, at this point, the next AFM peak oscillation would be superimposed with a charge Bragg peak of the FM structure. The simulations showed that even under perfect conditions, e.g. absolute smooth interfaces, both magnetic signals from the FM and AFM coupled multilayer would be very difficult to be separate from each other. The third order would be already at such large angles of about 55° that the reflectivity is much too low in order to measure even the charge signal. Furthermore the limited angle range imposed by the sample magnet restricts the feasibility of this approach here in this experimental setup.

In summary, it could be shown here that even the low magnetic signal from the enhanced magnetic moment of chromium at the Fe/Cr interface could be measured and evaluated in a quantitative way. By assuming a step function for the magnetic moment of chromium an effective thickness $t_{eff}$ of about 0.5 Å fits the experimental data best. Similar to the evaluation at the iron L-edges the simulations at the chromium L-edges show also sensitivity to the interfacial magnetic coupling behavior, especially at the half AFM Bragg position, and confirm the results obtained at the iron L-edges. Furthermore by taking the parameters for the simulated fits for both, iron and chromium L-edges into account, the antiferromagnetic coupling between the magnetic moment of the iron and the interfacial enhanced magnetic moment of chromium can be confirmed.

# 5.3 Magnetic x-ray reflectivity with hard x-rays

In the previous section the magnetic reflectivity on the Fe/Cr multilayer was examined and discussed at the iron and chromium L-edges. It showed large magnetic enhancements of the magnetic scattering amplitude for the 3d transition metals by tuning the energy to the L-absorption edges in the soft x-ray regime and clearly demonstrated the feasibility of extracting qualitative and quantitative information from the measured magnetic reflectivity spectra.

But reflectivity experiments in soft x-rays suffer from several drawbacks. Due to the long wavelength, the accessible reciprocal space ($Q_z$) is restricted. Therefore the number of structural Bragg peaks of thin multilayer films which can be measured are limited and thus reduce the accuracy of the qualitative and quantitative determination of the charge and magnetic structure. The biggest problem is the strong absorption of the soft x-rays in matter, which limit the probing depth to a few hundred Å. Often structures are inaccessible with soft x-rays, which are thicker than several hundred Å or buried under a large cover layer which is necessary to protect the magnetic layer from oxidation and other destructive processes. By using hard x-rays - *hard* means here a photon energy of more than 3keV - these problems could be avoided. Hard x-rays are much less absorbed and can penetrate matter by several thousand Å, which is usually more than the thickness of most multilayer system of interest here. Additionally, as known from conventional charge reflectivity experiments with hard x-rays, the combination of the wavelength and angle region also allows to cover a wide range of the reciprocal space, i. e. to detect structural Bragg peaks of thin multilayer films to several orders, best suitable to determine structures in the order from 10 Å to several 1000 Å. It should also be noted, that since soft x-ray operations requires vacuum due to its strong absorption through air, it is also much more demanding from an experimental point of view. The whole beam path and therefore the sample has to be under vacuum, where the experimental setup is usually more restricted. Using hard x-rays does not only simplify the experimental setup but also makes the preparation and changes of samples easier. From this point of view, hard x-ray offers various advantages compared to the experiments carried out in soft x-rays, which would in principle make this wavelength region also a useful tool for the accurate determination of magnetization profiles of thin films and multilayer systems.

The 3d transition metals possess also absorption edges in the hard x-ray regime, which can be used to apply the magnetic reflectivity technique, as explicitly illustrated in the last section in the soft x-ray region. Unfortunately, the magnetic enhancement by tuning to the K-absorption edges of 3d transition metals is much smaller compared to the effect yielded from the L-absorption edges. Taking the MCD measurements as an indicator, the MCD effect of an iron foil is about 100 times weaker at the K-edge than at the $L_3$ edge of iron. A maximum effect on the order of only $10^{-3}$ compared to the charge scattering is expected in the measurements. Due to the small MCD effect at the K-edge, most experimental efforts for magnetic structure determination of 3d transition metals were concentrated on the soft x-ray region so far (e.g. [138 - 141]). But, nevertheless, the development and ongoing improvements of synchrotron radiation, especially of high intensity insertion device beamlines, have increased the possibility to examine smaller and smaller effects.

Here in this section the results of magnetic hard x-ray reflectivity measurements on the Fe/Cr double multilayer at the iron K-edges will be presented and discussed in detail. Since the magnetic enhancement at the K-edges is expected to be very small, the demand of intensity is high in order to detect the weak signal within the statistical errors. Other than the measurements in the soft x-ray region, where lock-in amplifiers modulate the difference and sum signal of the detected intensity with a frequency to retrieve the magnetic signal via lock-in technique, a photon counting detection was used for the hard x-ray measurements. In consideration of pure Poisson statistic for single photon detection, $10^8$ photons need to be counted to reduce the statistical error in the order of $10^{-4}$ compared to the total detected intensity, including both charge and magnetic signal. Therefore the use of a high flux beamline is essential in order to detect the magnetic reflectivity at higher angles where the reflected intensity is reduced by several orders of magnitude due to Fresnel reflectivity and interfacial roughness or other structural disorders.

The experiment was carried out at the CMC-CAT beamline at the Advance Photon Source at Argonne National Laboratory. The beamline and the experimental setup is described in chapter 4.3 in detail. The linear polarized beam was converted to circular polarization by a phase retarder consisting of a diamond crystal, delivering close to $10^{12}$ photons/sec with a circular polarization of about 67%.

As already discussed in Chapter 2, the difference signal and asymmetry ratio, both representing magnetic reflectivity signal, can be measured by reversing the magnetic field at fixed helicity of the incoming circularly polarized photons or by flipping the helicity at constant magnetic field, respectively. Both methods deliver basically the same information about the magnetic configuration as long as the magnetic field is sufficient to reverse the magnetization. As already discussed before, the Fe/Cr double multilayer sample consists of two artificial magnetic multilayer structures which requires different magnetic fields to switch their magnetization. The top FM coupled multilayer structure only needs low fields on the order of 50 Oe to be reversed (see figure 5.3), and the bottom AFM coupled multilayer needs nearly two Tesla.

## 5.3.1 Ferromagnetic structure

In the first part of the magnetic reflectivity experiment the magnetic field on the sample was flipped while holding the helicity of the x-rays constant. Since only a small magnetic field of about ± 200 Oe could be applied, only the iron spins of FM multilayer were switched while the spin configuration of the AFM multilayer remained in their original state, as already mentioned
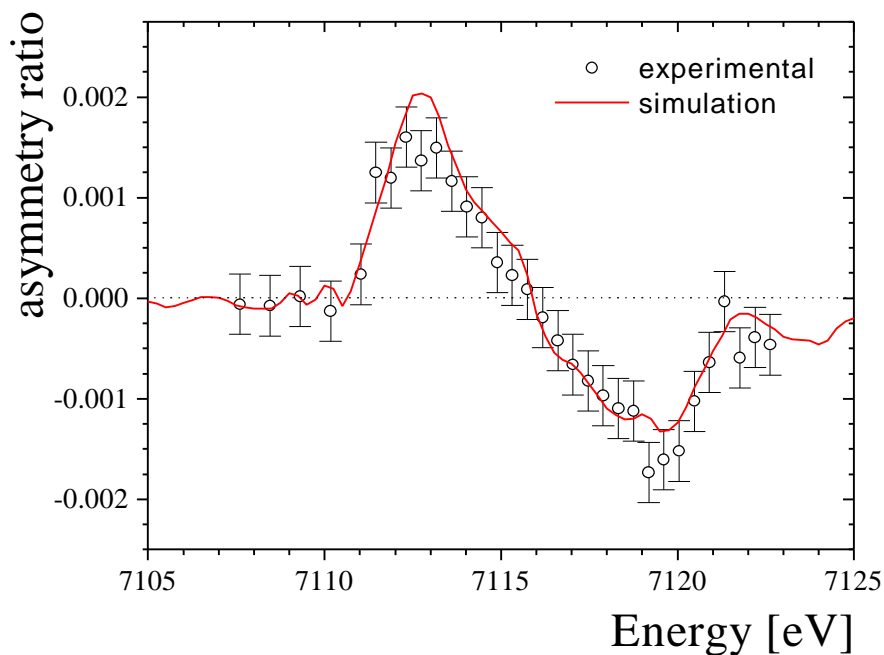


**Figure 5.31** *Energy scan at the 1.FM Bragg peak position by flipping the magnetic field at the sample at constant helicity of the x-ray beam. Symbols and line show the asymmetry ratio (difference divided by the sum) for magnetic reflectivity measurement and simulation, respectively. The error is estimated per Poisson statistic to $3.0 \cdot 10^{-4}$.*

above. Therefore, the measurements were only sensitive to the magnetic spin configuration of the FM multilayer. Any magnetic contribution of the AFM superstructure with its AFM aligned iron layers can be ignored.

In order to measure the magnetic reflectivity, the same procedure is applied as it was described in 5.2.1 at the $L_3$-edge of iron. First, the charge reflectivity curve close to the iron K-edge, including the angular position of FM structural peaks, is determined. In the next step the energies corresponding to the maximum magnetic effect has to be determined, which exhibits large magnetic signal. For this purpose the first Bragg peak of the FM coupled multilayer was chosen and the energy was scanned through the K-absorption edge of iron. The magnetic measurement (open circles) is plotted in figure 5.31. It should be noted that in the hard x-ray region the magnetic signal is in general presented as the asymmetry ratio, where the difference is dived by its sum. The experimental curve shows two distinct peaks at about 7113 eV and 7119.5 eV, which indicates the maximum of the magnetic sensitivity. The magnitude of the magnetic effect of about 0.15% is in the same order as the MCD-absorption experiment with the iron foil, which is sufficient to be clearly detected within the statistical error. For the following experiments the first maximum at 7113 eV was chosen while the magnetic reflectivity signal is recorded. In order to receive comparable statistics for the whole energy range, the total counts at the detector were held constant with $15 \cdot 10^6$ counts for every energy point, and the measured curve were extracted from the monitor counts. Assuming Poisson distribution the magnetic effect was measured with an accuracy of about $\pm\ 2.5 \cdot 10^{-4}$ normalized to the charge reflectivity. The line in figure 5.31 presents a simulated fit to the measured energy scan, using the algorithm described in chapter 3 and the optical constants for iron extracted from magnetic (MCD) and nonmagnetic absorption measurement on a thin iron foil (see chapter 3.2). By taking into account the degree of polarization and structural parameters determined from the charge reflectivity data in chapter 5.1, the calculated curve is in very good agreement with the experimental data. Before the magnetic reflectivity curve is recorded, the magnetic effect at the first FM Bragg peak can be used to measure a hysteresis loop in order to verify the shifted hysteresis loop due to the exchange bias effect. The hysteresis loop was measured by monitoring the magnetic reflectivity signal at the first Bragg peak and at a photon energy of 7113 eV. Since the magnetic signal was measured by taking the difference of the detected intensities at two magnetic applied fields, both branches of the hysteresis loop have to be
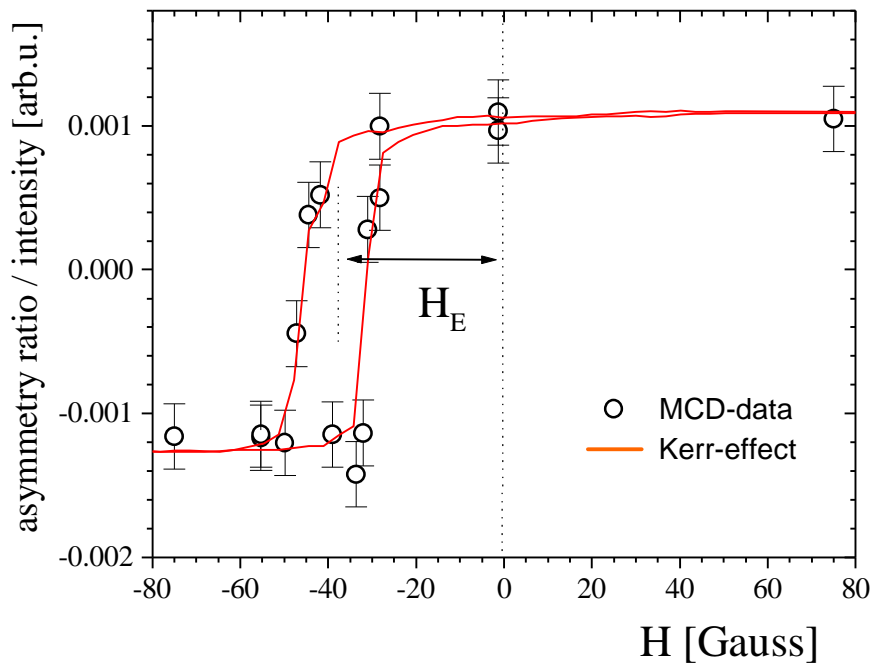
**Figure 5.32** *Magnetic hysteresis curve measured with the asymmetry ratio (circles) at the 1.FM Bragg peak, compared with laser Kerr measurements (line)*

recorded separately. Therefore the magnetic reference point was chosen successively at H = -100 Oe and +100 Oe while the magnetic field was driven gradually to H = +100 Oe and -100 Oe, respectively. At the field of H = ± 100 Oe the magnetization of the iron layers in the FM coupled multilayer are saturated. Figure 5.32 shows the measurements (open circles). The shift from the zero magnetic field due to exchange bias can be clearly detected. Furthermore, comparison with the hysteresis loop measured via optical Kerr effect in chapter 5.1 (full line) shows very good agreement. It should be noted that latter curve is scaled in height to fit the x-ray data.

After choosing the appropriate energy and verification of the shifted hysteresis loop and therefore the magnetic fields, which are necessary to reverse the magnetization at the sample, everything is prepared to measure the magnetic x-ray reflectivity curve. Similar to the energy scan shown above, the total count was again fixed constant at the detector and the reflectivity calculated from the monitor counts. Here, for each point of the reflectivity curve $30 \cdot 10^6$ photons were counted, which led to a statistical error of about $1.8 \cdot 10^{-4}$ normalized to the charge reflectivity. The recorded magnetic specular reflectivity curve (circles) - plotted as the asymmetry ratio $(I_{\uparrow\uparrow} - I_{\uparrow\downarrow}) / (I_{\uparrow\uparrow} + I_{\uparrow\downarrow})$ - is shown in figure 5.33 and compared with the charge
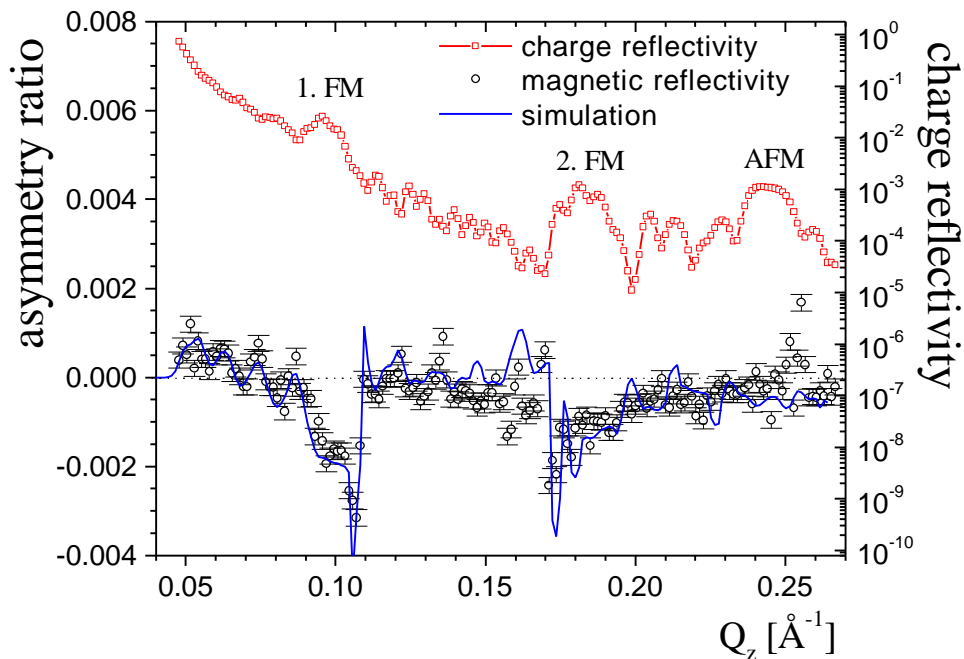
**Figure 5.33** *Magnetic x-ray reflectivity on Fe/Cr double multilayer with hard x-rays at 7113 eV by flipping the magnetic field at the sample between -100 Oe and 100 Oe. Squares show the measured charge reflectivity (sum of both reflectivity channels divided by two) and circles the asymmetry ratio (difference divided by the sum), representing the magnetic data. The full line presents the simulated curve assuming collinear alignment and fully magnetized iron spins.*

reflectivity curve $(I_{\uparrow\uparrow} + I_{\uparrow\downarrow}) / 2$ (straight line). It should be noted, that the reflectivity is recorded along the reciprocal space vector $Q_z$, which is connected to the incident angle (see equation 3.51). It can be seen that the magnetic reflectivity signal exhibits clear maxima at the same $Q_z$ position as the FM-Bragg peaks appear in the charge reflectivity curve, which indicates that the magnetic periodicity - the alignment of the iron spins along one direction - follows very much the chemical thickness of the iron layers. Further, distinct oscillations can be found in the front part and in between the FM-Bragg peaks, which originate from the total thickness of the ferromagnetic layer configuration of the FM superlattice structure. In order to retrieve information from the magnetic reflectivity curve the measured curve has been simulated as has been done for the energy scan at the first FM Bragg peak, but now at fixed energy and along the incident angle. The simulation (solid line) shows good agreement in the first part as well as for the magnetic Bragg reflections. Some features are too sharp and exaggerated in the simulation which is due to the fact that the calculation considers only flat interfaces. Further, as already pointed out for the fitting of the soft x-ray data, the simulation of such a double multilayer

structure is quite complicated that even the charge reflectivity could not be fitted perfectly. In order to keep the numbers of fitting parameters reasonable low, it seems quite impossible to achieve much better agreement with the data and further improvement was not attempted. Also, it is important to mention that by plotting the difference divided by the sum, minima in the charge reflectivity can lead to large spikes in the magnetic data, which are not physical. This can be seen in the spikes after the first and before the second FM Bragg peak, which are more enhanced in the simulation. The $Q_z$ resolution was implemented in the simulation to smooth the calculated curves and enables better fitting. However, important information can be extracted from the simulation. By fitting the size and shape of the FM Bragg peaks as well as the total thickness oscillations simultaneously, a magnetic optical constant can be derived, which is in very good agreement with the value of the magnetic optical constant calculated from the fully magnetized iron foil at the MCD-measurement. This indicates that the iron spins in the FM structure are also completely collinear aligned with the field direction and excludes the occurrence of magnetic dead layer. The oscillations especially in the $Q_z$ region before and after the first Bragg peak also agree very well with the simulation, which shows that the total thickness of the magnetization profile of the FM-lattice structure can be very well reproduced with the assumed model calculation.

## 5.3.2 Antiferromagnetic structure

The FM-structure has been magnetically and chemically well understood by magnetic hard x-ray studies, but so far no information about the AFM coupled multilayer could be extracted by the hard x-ray measurements. Even though the iron layers of the AFM coupled multilayer contribute to the each magnetic reflectivity spectrum, the measurement method by reversing the applied magnetic field in order to extract the very weak magnetic signal would require also a change in the magnetic configuration of the AFM superstructure. For that, the applied fields are much too low as already known from the SQUID measurements shown in 5.1. But even higher magnetic fields of about two Tesla applied on the sample would align all iron layers in the second multilayer ferromagnetically and destroy the AFM ordering. This renders the
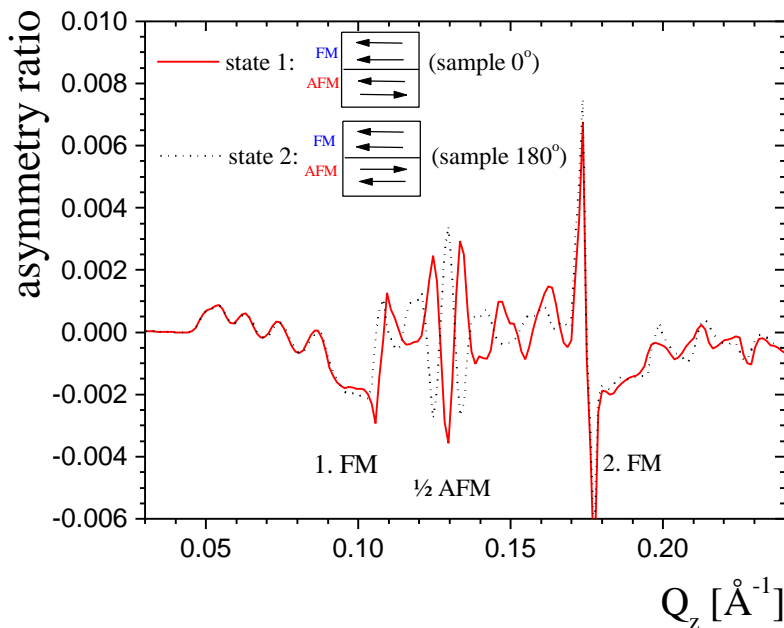
**Figure 5.34** *Simulation of the magnetic x-ray reflectivity obtained by flipping the helicity of the x-rays at constant magnetization for two scenarios: first iron layer of the AFM multilayer is parallel coupled (state 1) or antiparallel (state 2) to the orientation of the magnetization of the top FM multilayer. Both scenarios can be reproduced by turning the sample 180° at constant magnetic field.*

method in which the applied magnetic field is used for the magnetic contrast not useful in retrieving information about the AFM coupling. Therefore, in order to become sensitive to the antiferromagnetic structure, the helicity of the x-rays has to been flipped instead of the magnetic field as has been done in the soft x-ray region in the previous section. The magnetic field was now kept constant at H = -100 Oe. Figure 5.34 shows a simulation of the asymmetry ratio by switching the helicity of the photon beam, using the structural and magnetic parameters obtained from the charge and magnetic reflectivity data above. Besides the known ferromagnetic structure additional oscillation occur between the first and the second FM Bragg peak exactly, as expected, at half $Q_z$-position of the AFM Bragg peak, as it already has been seen in the soft x-ray data in 5.2. As already discussed for the magnetic reflectivity scans in the soft x-ray region the sign of the oscillation depends exclusively on the alignment between the ferromagnetic spins and the first magnetic layer of the AFM structure after the FM-AFM interface. Depending whether the interfacial spins of the two multilayer are ferromagnetically or antiferromagnetically coupled, the oscillations exhibits opposite sign and allow to distinguish both cases easily. It should be noted that experimentally this two scenarios can be

also realized by turning the sample of 180° but keeping the magnetic field applied in the same direction to keep the FM spin structure still aligned in the same direction as before.

In the experimental setup the helicity of the photon beam is reversed by moving the diamond phase plate from one side of 111-Bragg reflection to the other in order to shift the phase between $\sigma$ and $\pi$ polarization 180°. This is detailed described in chapter 4.3. Since the
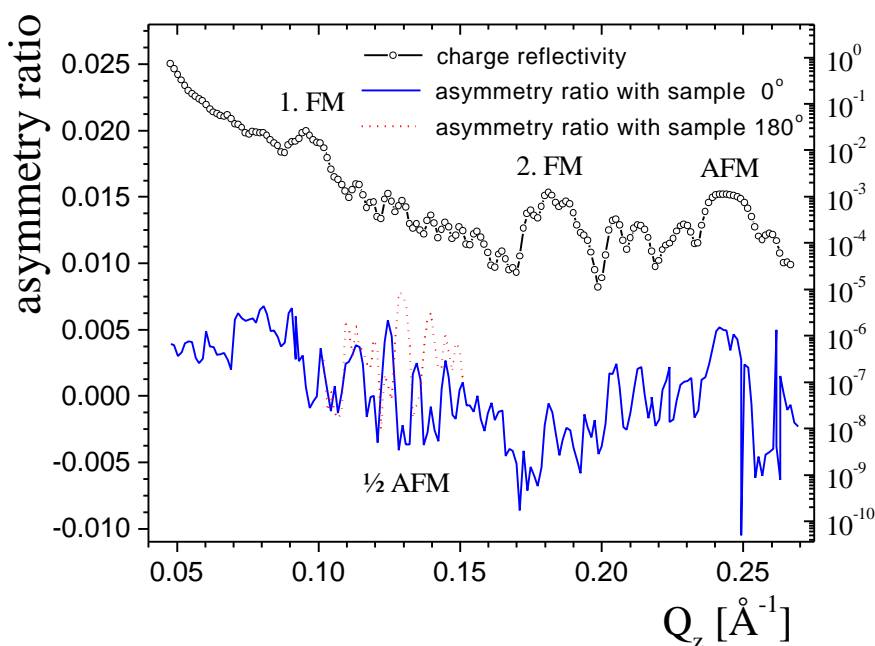


**Figure 5.35** *Experimental magnetic reflectivity data by flipping the helicity of the x-rays at constant magnetization. Symbols show charge reflectivity. Full and dashed line present the asymmetry ratio for the sample at 0° and 180° orientation to the magnetic field. More detailed explanation and discussion is given in text.*

transmitted beam is used, the intensity difference due to the change of the thickness of the phase retarder, which the beam has to go through, has to be corrected.

Figure 5.35 shows the experimental asymmetry data (full line) obtained by switching the helicity of the x-rays while holding the magnetization of the sample constant. Unfortunately it exhibits extra structures superposed on the magnetic signal. The ion chamber which served as the monitor counter was obviously not able to correct for the intensity change leading to additional modulations of the data. Such additional residual effects have been also reported by other groups [137].

In spite of this artificial effects, the examination of the structure at the $Q_z$ position where the AFM oscillation is expected reveals features which are probably due to the AFM alignment. In order to verify the observation the sample was turned by 180° and the experiment repeated around the half $Q_z$ position of the AFM peak (dashed line). Assuming that this residual effect shows the same behavior for both magnetic asymmetry curves and is only shifted to each other, the following way to evaluate is used: In order to neglect the shift the derivative of both curves is considered. By taking their difference all residual effects can be eliminated which are common to both measurements as well as the ferromagnetic contribution. The remaining signal is then only due to the arrangement of antiferromagnetic aligned iron layers in the second multilayer of the Fe/Cr double multilayer sample. Figure 5.36 shows the data (circles) treated as described above. It clearly exhibits oscillation at the half $Q_z$ position of AFM structure, which are due to the AFM aligned multilayer. The same treatment is applied to the simulated curves in figure 5.34 and is also presented in figure 5.36. In this case, a ferromagnetic coupling between the FM aligned iron spins and the first iron layer at the FM / AFM interface was assumed. It is important to notice that without applying any corrections for position or
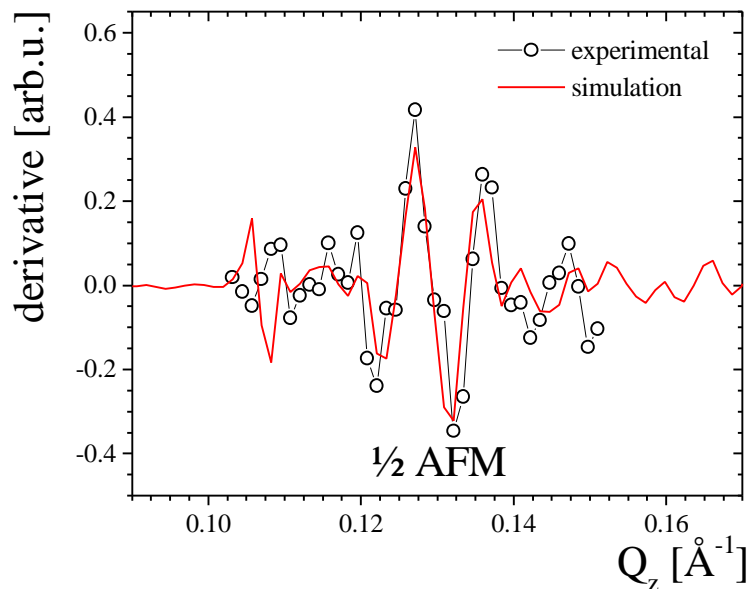


**Figure 5.36** D*erivatives of the difference of the asymmetry ratios between 180° turned sample at the half position of the 1. Bragg peak of the AFM multilalyer structure: symbols and line show the result yielded from experimental and simulated curves, respectively.*

magnitude the experimental data is very well reproduced and confirms the sensitivity to the alignment of the AFM coupled multilayer structure independently from the FM contribution.

This section showed the difficulties associated with the use of phase plates to measure the magnetic signal by changing the helicity of the incident x-ray beam. The intensity changes due to the different path length through the diamond crystal for left and right circularly polarized x-rays could not be corrected completely by using the ion chambers as a monitor, thus resulted in a residual effect superposing the whole magnetic reflectivity signal. In order to improve, other methods for intensity normalization are required. Nevertheless, the whole setup still enables one to extract the orientation of the relative magnetic spin orientation between the ferromagnetically and antiferromagnetically coupled iron layers at their interface, therefore demonstrating the ability of this technique to answer questions about the relative orientation of magnetic layers, even in complicated sample configurations with weak magnetic signals.

## 5.4 Summary of soft and hard magnetic x-ray reflectivity on Fe/Cr double multilayer

In the previous two sections 5.2 and 5.3 magnetic x-ray reflectivity measurements performed on a Fe/Cr double multilayer were described and discussed in detail. The experiments demonstrated that magnetic x-ray reflectivity on 3d transition metal is feasible in both x-ray regimes - at the L-edges in the soft x-ray regime and the K-edges in the hard x-ray regime. The technique enables one to extract qualitative and quantitative information about the magnetization profile from the measurements, especially in combination with the algorithm for the calculation of magnetic reflectivity curves described in Chapter 3.

The FM coupled iron layers could be studied in both wavelength region and were confirmed to be collinear aligned without the occurrence of magnetic dead layers. In both cases, at the L- and K-absorption edges, respectively, the extracted value for the magnetic optical constant agreed very well with the calculated value from MCD measurements on bulk fully magnetized iron samples. While the effect at the L-edges of iron was large and easily measured, the magnetic sensitivity at the iron K-edge is about 100 times smaller, on the order of $10^{-3}$. Nevertheless, the magnetic reflectivity curve could be observed at the iron K-edge. Moreover, a sensitivity to effects smaller than $10^{-3}$ has been demonstrated.

The AFM Bragg peak at half position of the structural Bragg peak could also be observed when the helicity of the photon beam was flipped instead of the magnetization in both x-ray regimes. Due to the absorption effects the order of the antiparallel aligned iron layers in the AFM structure becomes important in the x-ray case and leads to a magnetic contrast in the magnetic x-ray reflectivity spectrum. In the soft x-ray region, only the first few periods of the AFM structure could be detected due to the strong absorption, but the magnitude of the enhancement and the smoother interfaces of the AFM coupled superlattice led to clearly observable oscillations. In the hard x-ray region the detection was masked by large residual systematic effects which stem from the non-linearity of the incident intensity. Nevertheless, by measuring the flipping ratio for both magnetizations, the residual effect could be eliminated to a great

extent and the orientation between FM and AFM coupled multilayer was determined. In both cases, soft and hard x-ray measurements, the coupling between the FM and AFM multilayer could be clearly identified. The interfacial iron layers of the FM and AFM multilayers couple ferromagnetically.

It is important to mention that without absorption no signal at the half AFM Bragg peak would be measured in the difference or asymmetry channel which are used here to represent the magnetic reflectivity. Nevertheless, even in the absorption free case, a magnetic signal could be detected in the sum signal due to the slight change in the index of refraction whether the sample is magnetized in the one or other direction. The same is true for left and right circularly polarized light.

Furthermore, it should also be noted, that with hard x-rays the whole sample was probed, which confirmed that the whole AFM coupled multilayer stays rigid while the magnetic field was flipped at low fields.


Due to the element selectivity by tuning to element specific absorption edges, it was also possible to study the weak moment of chromium by tuning the energy to the chromium L-edges. Effects 20 times smaller than those observed at the L-edges of iron could be measured and evaluated. Especially the chromium layers in the AFM coupled multilayer exhibit a clear signal and could be used for quantitative analysis. The thickness of the magnetic moment into the chromium was approximated to about an effective thickness of 0.5 Å assuming a step function in the magnetization profile and could be clearly assigned to the Fe/Cr interface. Even though a detailed analysis of the magnetization profile in the chromium layers was not feasible, the value of the effective thickness allows one in principle to compare the enhanced magnetic moment at Fe/Cr interfaces on a quantitative basis.

Furthermore, comparison of the simulation parameter for the reflectivity curves at both iron and chromium L-edges suggests antiferromagnetic coupling at the Fe/Cr interface, which confirms former experimental and theoretical work done on Fe/Cr interfaces.

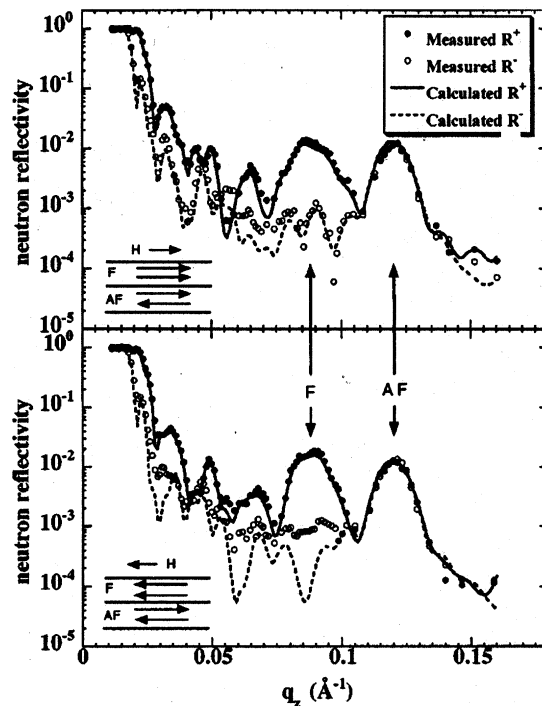# 5.5 Comparison with Polarized Neutron reflectivity

In order to evaluate magnetic x-ray reflectivity as a tool to determine the magnetization profile of thin films and multilayer, the results discussed in the previous subchapters will be compared with Polarized Neutron Reflectivity (PNR) studies on the same Fe/Cr double multilayer. The measurements and evaluation were carried out at Felcher's group at the Argonne's Intense Pulsed Neutron Source and are published in [123, 124].

In this section, the method of PNR will be briefly explained, followed by a presentation of the measurements and results on the Fe/Cr double multilayer by Felcher's group. These will be then compared with the result obtained by x-ray magnetic reflectivity.

Polarized Neutron Reflectivity is the standard tool for the examination of magnetic depth profiles. PNR measures the reflected intensities $R^+$ and $R^-$ of neutrons which are polarized parallel and antiparallel to the applied magnetic field H, respectively. $R^+$ and $R^-$ are basically the optical transform of $n(z) + m(z)$ and $n(z) - m(z)$, respectively, where n is the nuclear scattering amplitude and m the depth-dependent magnetization. By alternatively measuring the reflectivity with neutrons of both spin states, the magnetization profile can be determined. Furthermore, by analyzing the polarization state of the reflected neutron, further information about the magnetic spin configuration can be gained. More details about polarized neutron reflectometry can be found in several review articles [142, 143].

Figure 5.37 shows two neutron reflectivity measurements, in which the FM multilayer was switched in opposite direction by applying a low magnetic field of H = 166 Oe (top panel) and H = -72 Oe (bottom panel), respectively, while the AFM multilayer structure stays rigid. The range in reciprocal space of 0.16 $\text{Å}^{-1}$ covers the first Bragg peak stemming from the FM multilayer structure at about 0.09 $\text{Å}^{-1}$ and the first AFM magnetic Bragg reflection at half of the AFM Bragg peak position of 0.12 $\text{Å}^{-1}$. The measurements were carried out for both parallel (full circles) and antiparallel (open circles) polarization to the magnetic field direction H, and denoted $R^+$ and $R^-$, respectively. In both figures a clear difference between the two reflectivity curves for both polarization states can be observed, which shows the high sensitivity of polarized neutrons to the magnetization of the sample. At the first Bragg peak of the FM

**Figure 5.37** *The measured and calculated polarized neutron reflectivity (PNR) study on the Fe/Cr double multilayer in H = 166 Oe (top panel) and H = -72 Oe (bottom panel). Neutrons with spin parallel to H are indicated by filled symbols and full line ($R^+$), those antiparallel to H by open symbols and dashed line ($R^-$). Graph from te Velthius et al. [27]*

multilayer at 0.09 $\text{Å}^{-1}$ the difference is large and indicates that there must be a significant magnetization parallel to the neutron spin as denoted in the insets in both figures. At the AFM reflection at 0.12 $\text{Å}^{-1}$, the difference vanishes completely since the number of iron layers magnetized parallel and antiparallel to the applied magnetic field is equal. The low absorption of neutrons makes it extremely hard to distinguish the order at the AFM reflection (constructive interference). All measured scans were also calculated assuming a model with collinear magnetization and structural parameter extracted from conventional x-ray reflectivity measurements. The simulated curves are plotted in the figures as full and dashed lines for neutrons polarized parallel and antiparallel to the applied field, respectively, reproducing the large differences observed experimentally. In order to verify the collinear alignment at the low field, the polarization state of measured neutron reflectivity has to be analyzed. The reflectivity $R^+$, representing the reflected intensity of neutrons which are parallel polarized to the applied field, can be separated into $R^{++}$ and $R^{+-}$ parts. The second index denotes the final polarization of the scattered neutron. As long as the magnetization of the sample is aligned parallel or antiparallel to the neutron polarization, no transformation of the neutron spin appears. But in

case of non-collinear magnetization, spin flip transitions occur and the spin flip reflectivity $R^{+-}$ is non zero. Figure 5.38 shows the ratio of $R^{+-}$ to $R^{++}$ measured over the whole $Q_z$-space for two magnetic fields, H = -68 Oe and H = -3.6 kOe, respectively. At the low field, which is identical to the magnetization state in figure 5.37 and in the x-ray measurements, the ratio is close to zero and therefore confirms the assumption of collinear alignment. A different scenario can be observed at the second, higher field. A huge spike at the AFM Bragg reflection can be detected, which indicates clearly the occurrence of spin flip transitions and thus non-collinear spin configuration. It can be assumed that the AFM superlattice is still antiferromagnetically ordered, but now perpendicular to the applied field H. This is further supported by the SQUID measurements of the hysteresis loop in figure 5.3 (see chapter 5.1), in which the magnetization starts to rise again with increasing magnetic field.
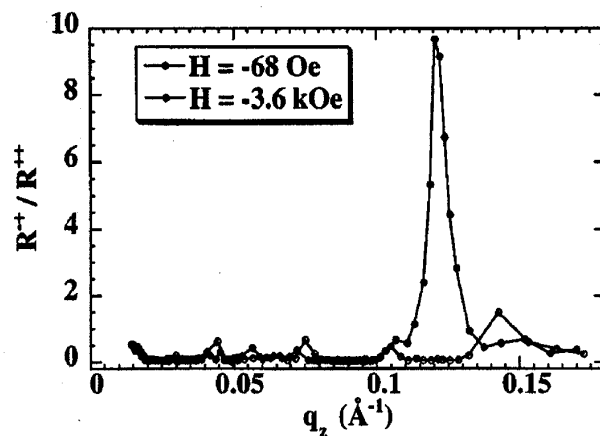


**Figure 5.38** *Ratio between the reflectivity measured for neutrons with the incident spin antiparallel and reflected spin parallel to the field ($R^{-+}$), and with the incident and reflected spin parallel to the field ($R^{++}$), in H = -68 Oe (open circles) and H = -3.6 kOe (filled circles). Graph from te Velthius et al. [124].*

In summary, Polarized Neutron Reflectivity is a very sensitive tool to examine magnetic spin configuration. It exhibits very large differences in the reflectivity profile whether the magnetization of the sample is parallel or antiparallel to the neutron spin. The FM and AFM Bragg peaks from the magnetic structures are clearly observable and allow the determination of depth dependent analysis of magnetic superstructures via model calculations. Moreover, by analyzing the final spin polarization of the reflected neutron, even parallel or perpendicular magnetization configurations of the sample can be distinguished.

In comparison, the magnetic x-ray reflectivity measurement presented and discussed before in the hard and soft x-ray region, also demonstrates the possibility to extract important magnetic information with x-rays, in spite of the weak interaction between photon beam and the magnetization state of matter. Both, hard and soft x-ray measurements showed the sensitivity of x-rays to the magnetization of the iron layers in both FM and AFM multilayer. Especially in the soft x-ray region magnetic effects can be achieved, which are similar to PNR. At the L-edges, here for the 3d transition metal iron, magnetic contrast of more than 30% of the charge intensity can be observed. By assuming a depth dependent magnetic spin configuration, it is possible to calculate the magnetic x-ray reflectivity in good agreement with the experimental curves. Therefore it enables one to determine magnetization profiles in a qualitative and quantitative way similar to neutron reflectivity.

Moreover, there are features which are unique to the x-ray technique and can be exploited for an advanced study of magnetic thin films and multilayer.

A property of x-rays which can lead to additional information for the x-ray case is the fact that the absorption for x-ray is not negligible, while neutrons practically do not experience any absorption in the thin films or multilayer systems considered here (up to 1000Å), unless they contain strong neutron absorbing material like gadolinium. X-rays allow more detailed depth information of the sample to be obtained. By using x-rays, it was possible to distinguish the orientation of the FM multilayer to the AFM multilayer at the Fe/Cr double multilayer. The first layer is "more seen" by the x-rays than the following layer due to increased absorption of the x-rays the deeper they penetrate. The modulation observed at half $Q_z$-position of the AFM structural peak depends therefore strictly on the orientation of the first iron layer in the AFM structure to the direction of the FM aligned iron layers of the FM multilayer. This effect could be observed in the soft as well as in the hard x-ray measurements. In the neutron case, the distinction between the relative orientation is much more difficult. At the AFM reflection the parallel and antiparallel polarized neutrons basically see the same number of parallel and antiparallel aligned iron layers. Due to the very weak absorption none of the iron layers scatter more or less of the neutron beam and therefore identical intensities are measured.

In order to determine the charge structure of the multilayer system, conventional hard x-ray measurements have been carried out. The determination is accurate for two major reasons. First, the technique of hard x-ray reflectivity probes a larger $Q_z$ -range due to the available high

x-ray intensities at synchrotrons and provides therefore more accurate information about the real space. As a rule of thumb, the smallest dimension in real space which is probed can be estimated by the reciprocal value of the maximal $Q_z$. Second, the resolution in reciprocal space is in general about one order of magnitude above conventional neutron scattering. Synchrotron radiation sources, e.g. insertion device undulator beamlines, produce tiny x-ray beams with diameters in the millimeter region and nearly vanishing divergence, which helps to improve the $Q_z$ resolution, while neutron reflectometry deals with much larger beam sizes and divergences. Besides the better $Q_z$-resolution, the small beam size of x-rays also makes them favorable to examine small samples, which would not be possible with neutrons. Due to the minimization of most technological devices, small sample sizes and their physical behavior become also more and more the focus of  interest.

The most important additional feature offered by magnetic x-ray reflectivity compared to PNR is its element specificity. Many magnetic materials of technological and scientific interest contain two or more magnetic species, which all contribute to the magnetic moment. As an example, in conventional exchange bias or spin valves systems which consist of FM and AFM layer usually containing different magnetic materials, the magnetic x-ray technique enables one to examined the magnetic sites separately and help to distinguish the magnetic contributions from each layer. This is possible since the magnetic scattering amplitude is only very much enhanced at the absorption edges of the particular magnetic site and allows the measurement of the magnetic profile independently for every magnetic element in the sample. Here at the Fe/Cr double multilayer sample, it was therefore possible to extract the interfacial enhanced magnetic moment of the chromium separately from the large moment of the iron layers, which would otherwise overpower the weak magnetic effect of the chromium layers. Neutron scattering does not distinguish between the magnetic moments of the different sites. Therefore it was also possible to extract information about the coupling at the Fe/Cr interface by comparing the simulation parameters of the separately measured reflectivity curves at the iron and chromium L-edges.

Moreover, next to the element specificity it is possible to use the different absorption edges for one magnetic site to probe the magnetism for different transitions and therefore be sensitive to different final states which are responsible for the magnetism. Here in the case of iron, the L-edges, in which the transition from the 2p to the 3d states takes place, is probing the magnetic

sensitivity of the 3d states, while at the K-edges, in which basically the transition from the 1s to the 4p states occurs, one is more sensitive to the 4p states. In the case of iron, both dipole transitions can be assumed to be direct proportional to the magnetization of the sample and do not exhibit different behavior. But in elements like holmium or other rare earth, in which e.g. d and f orbitals contribute, the analysis of the magnetic reflectivity at different absorption edges would allow to characterize the preferred orbitals responsible for the complex magnetic structure.

In summary, neutron and x-ray magnetic reflectivity both allow the determination of magnetic structures. PNR is a long established tool for magnetic studies due to the large interaction between neutrons and magnetic matter, which enables one to easily measure magnetic contributions of magnetic thin films and multilayer systems. PNR can be complemented by using x-ray magnetic reflectivity. It allows in principle the extraction of more detailed information about the magnetization profile due to its better $Q_z$-resolution, absorption effects and particularly its element and site specificity, which is not provided by PNR. Combining all these techniques, neutron, soft and hard x-ray magnetic scattering, a better understanding of the magnetic properties and i.e. magnetization profile of magnetic thin films and multilayer systems can be gained.

# 6. Outlook

In this work the theoretical and experimental feasibility of using magnetic x-ray reflectivity as a probe to extract element specific information about the magnetization profile of thin magnetic films and multilayer systems was demonstrated and illustrated on a complex sample containing a FM and AFM coupled multilayer. Moreover it was pointed out how this method can complement polarized neutron reflectivity and helps to retrieve additional information about the magnetic configuration not available from neutron diffraction. Specifically, the element selectivity was used here to extract the effective magnetic thickness of the chromium layers.

The key demands for the magnetic x-ray reflectivity technique are high x-ray intensity and a high degree of circular polarization. At synchrotron sources of the second and third generation these requirements are met and allow reasonably fast data collection even for 3d transition metal K-edges, where the MCD effect is very weak. In the near future the development of new sources and the progress in the undulator technology will give even higher flux and will make it possible to measure magnetic reflectivity curves to even high $Q_z$-values.

In order to produce circular polarization the elliptically polarized wigglers and undulators are used in the soft x-ray region and, the relatively inexpensive phase plates are applied in the hard x-ray region. Both technologies are already well established for producing a high degree of polarization with relatively little loss in the incident intensity.

Several developments are needed to improve the sensitivity limit demonstrated in this work. In the case of phase plates another way for the intensity correction has to be found, which takes into account the necessary high demand on statistics to measure small effects by switching between left and right circularly polarized x-rays.

Another limiting factor for the experiment is the detector count rate. The scintillation detector used in the photon counting mode was limiting to about 200 000 counts per second in order to stay in their linear range. Therefore, the counting time for each point in the reflectivity curve was kept to at least two and an half minutes to receive a statistic of $1.8 \cdot 10^{-4}$ assuming Poisson statistics, allowing to detect signals of about $10^{-3}$ in their maximum effect. In order to even measure effects of $10^{-4}$ and smaller, counts of $10^{10}$ photons per point would be required leading to a counting time of nearly 14 hours per point. In the future it will be of great interest to

develop reliable photon counting detectors with shorter pulse length and even larger dynamic range. As an example, the use of avalanche photo diodes (APD) could improve the situation, which could deliver in principle pulse lengths on the order of 1ns. In consideration of all limiting factors like the electronic efficiency, which reduce the maximum count rate by about a factor of 100, a count rate of $10^7$ photons per second is possible and reduce the counting time by a factor of 50 compared to the scintillation counter used here. The development and testing of such detectors is already in progress.

In summary it should be noted that by using high intensity x-ray sources providing circularly polarized light and fast photon counting detectors with a large dynamical range will permit the use of the method of the magnetic x-ray reflectivity routinely for fast characterization of magnetic depth profiles of all kind of magnetic thin films and multilayer systems similar to the situation presently hold by the standard charge x-ray reflectivity established for the determination of chemical profiles.

Besides the development of magnetic x-ray reflectivity as a standard experiment for the determination of magnetization profiles, the magnetic enhancement of the MCD effect can be also exploited in many other scattering geometries than absorption or reflectivity experiments. As an example, by applying the magnetic sensitivity of circularly polarized x-rays in a small angle scattering experiment would allow to determine element specific magnetic particle sizes. Another example, x-ray microbeam technique can be used in combination with the MCD effect to resolve domain structure of all kinds of magnets. Nearly any x-ray technique can be adopted and by applying the magnetic sensitivity of the MCD technique would permit probing magnetic samples and learn more about their magnetic properties and behavior.

# References

[1] M.Gell-Mann and M.L. Goldberger, Physical Review **96**, 1433 (1954)

[2] P. Zeeman, Research in Magneto Optics, MacMillian and Co., London 1913

[3] P.M. Platzman and N.Tzoar, Phys. Rev. B **2**, 3536 (1970)

[4] F.de Bergevin and M. Brunel, Phys. Lett. **39A**, 141 (1972)

[5] F.de Bergevin and M. Brunel, Acta Cryst. A **37**, 314 (1981)

[6] M.Blume, J. Appl. Phys. **57**, 3615 (1985)

[7] M.Blume and D.Gibbs, Phys. Rev. B **37**, 1779 (1988)

[8] G.Schütz, W.Wagner, W.Wilhelm, P.Kienle, R.Zeller, R.Frahm and G.Materlik, Phys. Rev. Lett. **58**, 737 (1987)

[9] J.B. Goedkoop, J.C.Fuggle, B.T.Thole, G.van der Laan and G.A.Sawatsky, J. Appl. Phys. **64**, 5595 (1988)

[10]    K. Namikawa, M.Ando, T.Nakajima, H. Kawata, J. Phys. Soc. Japan, **54**, 4099 (1985)

[11]    D.Gibbs, D.R.Harshmann, E.D. Isaacs, D.B.McWhan, D.Mills and C.Vettier, Phys. Rev. Lett. **61**, 1241 (1988)

[12]    J.H.Hannon, G.T.Trammell, M.Blume and D.Gibbs, Phys. Rev. Lett. **61**, 1245 (1988)

[13]    M.Blume, *Resonant Anomalous Scattering*, edited by G.Materlik, C.J.Sparks, K.Fischer, (North-Holland 1994)

[14]    J.P.Hill, D.F.McMorrow, Acta Crystallogr. A **52**, 236 (1996)

[15]    G.Schütz, R.Wienke, W.Wilhelm, W.Wagner, P.Kienle, R.Zeller, R.Frahm, Z. Phys. B **75**, 495 (1989)

[16]    S.W.Lovesey, S.P.Collins, X-ray Scattering and Absorption by Magnetic Materials, Oxford Science Publications, Oxford, 1996.

[17]    B.T.Thole, P.Carra, F.Sette, G. van der Laan, Phys. Rev. Lett. **68**, 1943 (1992)

[18]    P.Carra, B.T.Thole, M. Altarelli, X.Wang, Phys. Rev. Lett. **70**, 694 (1993)

[19]    V. Chakarian, Y.U.Idzerda, C.T. Chen, G.Meigs, C.C.Kao, Synchrotron Radiation Techniques in Industrial, Chemical and Material Science, Plenum Press, New York, 1996 (187)

[20]    C.T.Chen, Y.U.Idzerda, C.C.Kao, L.H.Tjeng, H.-J.Lin, G.Meigs, Mat. Res. Soc. Symp. **375**, 59 (1995)

[21]   C.T.Chen, Y.U.Idzerda, H.-J.Lin, N.V.Smith, G.Meigs, E.Chaban, G.H.Ho, E.Pellegrin, F.Sette, Phys. Rev. Lett. **75**, 152 (1995)

[22]   S.Eisebitt in *Magnetische Schichtsysteme*, 30. IFF-Ferienkurs, Forschungszentrum Jülich 1999

[23]   R.Wu, D.Wang, A.J.Freeman, Phys. Rev. Lett. **71**, 3581 (1993)

[24]   R.Wu, A.J.Freeman, Phys. Rev. Lett. **73** , 1994 (1994)

[25]   J.Stöhr, H.König, Phys. Rev. Lett **75**, 3748 (1995)

[26]   J.Stöhr, R.Nakajima, IBM J.Research and Development **48**, No. 1 (1998)

[27]   J. Stöhr, J. Magn. Magn. Mater.  **200**, 470 (1999)

[28]   O.Eriksson, B.Johansson, R.C.Albers, A.M.Boring, M.S.S.Brooks, Phys. Rev. B **42**, 2707 (1990)

[29]   P.Söderlind, O.Eriksson, B.Johansson, R.C.Albers, A.M.Boring,  Phys. Rev. B **45**, 12911 (1992)

[30]   C.T.Chen, F.Sette, Y.Ma, S.Modesti, Phys. Rev. B **42**, 7262 (1990)

[31]   C.C.Kao, J.B.Hastings, E.D.Johnson, D.P.Siddons, G.C.Smith and G.A.Prinz, Phys. Rev. Lett. **65**, 373 (1990)

[32]   C.C.Kao, , C.T.Chen, E.D.Johnson, J.B.Hastings, H.-J.Lin, G.H.Ho, G.Meigs, J.-M.Brot, S.L.Hulbert, Y.U.Idzerda, C.Vettier, Phys. Rev. B **50**, 9599 [1994]

[33]   H.Ebert, P.Strange, B.L.Gyorffy, J. Appl. Phys.  **63**, 3055 (1988)

[34]   S.Stähler, G.Schütz, H.Ebert, Phys. Rev. B **47**, 818 (1993)

[35]   B.T.Thole, G.van der Laan, G.A.Sawatzky, Phys. Rev. B **55**, 2086 (1985)

[36]   G.van der Laan and B.T.Thole, Phys. Rev. B **43**, 13401 (1991)

[37]   G.van der Laan, Phys. Sci. **41**, 574 (1990)

[38]   P.Kuiper, B.G.Searle, P.Rudolf, L.H.Tjeng, C.T.Chen, Phys. Rev. Lett. **70**, 1549 (1993)

[39]   J.Stöhr, A.Scholl, T.J.Regan, S.Anders, J.Lüning, M.R.Scheinfein, H.A.Padmore, R.L.White, Phys. Rev. Lett. **83**, 1862 (1999)

[40]   J.Stöhr, H.A.Padmore, S.Anders, T.Stammler, and M.R.Scheinfein, Surf. Rev. Lett. **5**, 1297 (1998).

[41]   J.Stöhr, Y.Wu, B.D.Hermsmeier, M.G.Samant, G.R.Harp, S.Koranda, D.Dunham, and B.P.Tonner, Science **259**, 658 (1993).

[42]   D.P.Siddons, M.Hart, Y.Amemiya, J.B.Hastings, Phys. Rev. Lett.  **64**, 1967 (1990)

[43]   J.B.Kortright, M.Rice, R.Carr, Phys. Rev. B **51**, 10240 (1995)

[44]    C.Vettier, *Resonant Anomalous Scattering*, edited by G.Materlik, C.J.Sparks, K.Fischer, (North-Holland 1994)

[45]    E.D.Isaacs, D.B.McWhan, C.Peters, G.E.Ice, D.P.Siddons, J.B.Hastings, C.Vettier, O.Vogt, Phys. Rev. Lett. **62**, 1671 (1989)

[46]    H.Ebert, R.Zeller, Phys. Rev. B **42**, 2744 (1990)

[47]    M.Born, E.Wolf, Principles of Optics, Pergamon (1980)

[48]    L.G.Parratt, Phys. Rev. **95**, 359 (1954)

[49]    J.Als-Nielsen, F.Christensen, P.S.Pershan, Phys. Rev. Lett. **48**, 1107 (1982)

[50]    P.S.Pershan, J.Als-Nielsen, Phys. Rev. Lett. **52**, 759 (1984)

[51]    E.Spiller, Rev. Phys. Appl. **23**, 1687 (1988)

[52]    B.Lengeler in *Synchrotronstrahlung zur Erforschung kondensierter Materie*, 22. IFF-Ferienkurs, Forschungszentrum Jülich 1992

[53]    J.Als-Nielsen *in Topics in Current Physics*, Ed. W.Schlommers, P.van Blanckenhagen, *Handbook on Synchrotron Radiation,* Springer 1987

[54]    T.P.Russel, Mat.Sci.Rep. **5**, 171 (1990)

[55]    W.Spirkl, J. Appl. Phys. **74**, 1776 (1993)

[56]    B.Vidal, P.Vincent, Appl. Opt. **23** , 1794 (1984)

[57]    L.Névot, P.Croce, Rev. Phys. Appl. **15**, 761 (1980)

[58]    S.K.Sinha, E.B.Sirota, S.Garoff, H.B.Stanley, Phys. Rev. B **38**, 2297 (1988)

[59]    T.Salditt, *Diffuse Röntgenstreuung an rauhen Grenzflächen*, dissertation LMU Munich (1995)

[60]    M.Tolan, X-Ray Scattering from Soft-Matter Thin Films, Springer (1999)

[61]    M.Faraday, Trans. R. Soc. (London) **5**, 592 (1846)

[62]    J.Kerr, Philos. Mag..**3**, 339 (1877)

[63]    J.Zak, E.R.Moog, C.Liu, S.D.Bader, J. Magn. Magn. Mater..**89**, 107 (1990)

[64]    J.Zak, C.Liu, E.R.Moog, S.D.Bader, J. Appl. Phys. **68**,  4203 (1990)

[65]    J.Zak, E.R.Moog, C.Liu, S.D.Bader, Phys. Rev. B **43** 6423 (1991)

[66]    L.D.Landau and E.M.Lifshitz, *Electrodynamics of Continuous Media*, Pergamon (1960)

[67]    D.T.Cromer, D.Liberman, J. Chem. Phys. **35**, 1891 (1970)

[68]    D.T.Cromer, D.Liberman, Acta Cryst. A **37**, 267 (1981)

[69]    D.T.Cromer, J.Appl.Cryst. **16**, 437 (1983)

[70]    B.L. Henke, E.M. Gullikson, and J.C. Davis. *X-ray interactions: photoabsorption, scattering, transmission, and reflection at E=50-30000 eV, Z=1-92*, Atomic Data and Nuclear Data Tables, July 1993, **54**, (no.2):181-342

[71]    R. de L. Kronig, J. Opt. Soc. Am. **12**, 547 (1926)

[72]    S.S.P.Parkin, R.Sigsbee, R.Felici, G.P.Felcher, J. Appl. Phys. **57**, 3771, (1985)

[73]    J.F.Ankner, C.F.Majkrzak, H.Homma, J. Appl. Phys. **73**, 6436 (1993)

[74]    Q.Leng, H.Han, M.Mao, C.Hiner, F.Ryan, J. Appl. Phys. **87**, 6621 (2000)

[75]    W.Hahn, M.Loewenhaupt, G.P.Felcher, Y.Y.Huang, S.S.P.Parkin, J. Appl. Phys. **75**, 3564 (1994)

[76]    R.J.Melville, R.S.Eccleston, G.J.McIntyre, S.B.Palmer, J. Phys. Cond. Matt. **4**, 10045 (1992)

[77]    R.M.Osgood III, S.K.Sinha,J.W.Freeland,Y.U.Idzerda,S.D.Bader, J. Appl. Phys. **85**, 4619 (1999)

[78]    F.de Bergevin and M. Brunel, Phys. Lett. A **39**, 141 (1972)

[79]    V.Saile in *Synchrotronstrahlung  zur Erforschung kondensierter Materie*, 22. IFF-Ferienkurs, Forschungszentrum Jülich 1992

[80]    W. Brefeld and P. Gurtler, "Synchrotron Radiation Sources," *Handbook on Synchrotron Radiation*, S. Ebashi, M. Koch, and E. Rubenstein, Eds., Elsevier Science, Holland, 1991.

[81]    Encyclopedia of Physics, edited by R.G.Lerner and G.L.Trigg, 2nd edition, VCH Publisher, INC., New York (1990)

[82]    J.Sweet, IBM J. Research and Development, No. 4 (2000)

[83]    F.R.Elder, A.M.Gurewitsch, R.V.Langmuir and H.C.Pollock, Phys. Rev. **71**, 829 (1947)

[84]    S.Yamamoto and H.Kitamura, Japan Journal of Applied Phys. **26**, 1613 (1987)

[85]    R.Walker and B.Diviacco, Rev. Sci. Instrum., **63**, 332 (1992)

[86]    A.Friedman, S.Krinsky, E.Blum, BNL Informal Report 47317, March 1992

[87]    S.Krinsky, C.C.Kao, Synch. Rad. News **8**, 38 (1995)

[88]    O.Singh, S. Krinsky, P.M. Ivanov and E.A. Medvedko, 1996 (not published??)

[89]    J.Sutherland, K.Polewski, D.C.Monteleone, J.G.Trunk, C.Sanchez-Hanke, S.L.Hulbert, C.C.Kao, E.D.Johnson, submitted to Rev. Sci. Instrum.

[90]    private communication with Cecilia Hanke-Sanchez

176

[91]  K.J.Randall, Z.Xu, E.Gluskin, I.McNulty, R.Dejus, S.Krinsky, O.Singh, C.C.Kao, E.D.Johnson, C.T.Chen, G.Meigs, J. Electron Spectroscopy and Related Phenomena **80**, 433 (1996)

[92]  Code *Urgent*, ESRF generated, calculations by Steve Hulbert

[93]  H.Maruyama, M.Suzuki, N.Kawamura, M.Ito, E.Arakawa, J.Kokubun, K.Hirano, K.Horie, S.Uemura, K.Hagiwara, M.Mizumaki, S.Goto, H.Kitamura, K.Namikawa, T.Ishikawa, J. Synchrotron Rad. **6**, 1133 (1999)

[94]  C.Giles, C.Malgrange, J.Goulon, F.de Bergevin, C.Vettier, A.Fontaine, E.Dartyge, S.Pizzini, F.Baudelet, A.Freund, Rev. Sci. Instrum. **66**, 1549 (1995)

[95]  C.Giles, C.Vettier, F.de Bergevin, C.Malgrange, G.Grübel, F.Grossi, Rev. Sci. Instrum. **66**, 1518 (1995)

[96]  P.Grünberg, R.Schreiber, Y.Pang, M.B.Brodsky, H.Sowers, Phys. Rev. Lett. **57**, 2442 (1986)

[97]  C.F.Majkrzak, J.W.Cable, J.Kwo, M.Hong, D.B.McWhan, Y.Yafet, J.V.Waszak, C.Vettier, Phys. Rev. Lett. **56**, 2700 (1986)

[98]  M.B. Salamon, S.Sinha, J.J.Rhyne, J.E.Cunningham, R.W.Erwin, J.Borchers, C.P.Flynn, Phys. Rev. Lett. **56**, 259 (1986)

[99]  M.N.Baibich, J.M.Broto, A.Fert, F.Nguyen Van Dau, F.Petroff, P.Etienne, G.Creuzet, A.Friedrich, J.Chazelas, Phys. Rev. Lett. **61**, 2472 (1988)

[100]  S.S.P.Parkin, N.More, K.P.Roche, Phys. Rev. Lett. **64**, 2304 (1990)

[101]  P.Bruno and C.Chappert, Phys. Rev. B **46,** 261 (1992)

[102]  D.Edwards, J.Mathon, R.B.Muniz, M.S.Phan, Phys. Rev. Lett. **67**, 493 (1991)

[103]  U.Rücker, S.Demokritov, E.Tsymbal, P.Grünberg, W.Zinn, J. Appl. Phys. **78,** 387 (1995)

[104]  M.E.Filipkovsky, J.J.Krebs, G.A.Prinz, C.J.Gutierrez, Phys. Rev. Lett. **75**, 1847 (1995)

[105]  J.Unguris, R.J.Celotta, D.T.Pierce, Phys. Rev. Lett. **67**, 140 (1991)

[106]  D.T.Pierce, J.A.Stroscio, J.Unguris, R.J.Celotta, Phys. Rev. B **49**, 14564 (1994)

[107]  E.E.Fullerton, M.J.Conover, J.E.Mattson, C.H.Sowers, S.D.Bader, Phys. Rev. B **48**, 15755 (1994)

[108]  H.Zabel, J.Phys.:Condens.Matter **11**, 9303 (1999)

[109]  R.S.Fishman, J.Phys.:Condens.Matter **13**, R235 (2001)

[110]  S.Mirbt, A.M.N.Niklasson, H.L.Skriver, B.Johansson, Phys. Rev. B **54**, 6832 (1996)

[111] D.D.Koelling, Phys. Rev. B **50**, 273 (1994)

[112] M.D.Stiles, J. Magn. Magn. Mater. **200**, 322 (1999)

[113] D.T.Pierce, J.Unguris, R.J.Celotta, M.D.Stiles, , J. Magn. Magn. Mater. **200**, 290 (1999)

[114] W.H.Meiklejohn, C.P.Bean, Phys.Rev. **102**, 1413 (1956)

[115] J.Nogués, I.K.Schuller, J. Magn. Magn. Mater. **192**, 230 (1999)

[116] A.E.Berkowitz, K.Takano, J. Magn. Magn. Mater. **200**, 552 (1999)

[117] W.H.Meiklejohn, J. Appl. Phys. **33**, 1328 (1962)

[118] D.Mauri, H.C.Siegmann, P.S.Bagus, E.Kay, J. Appl. Phys. **62**, 3047 (1987)

[119] A.P.Malozemoff, Phys.Rev. B **35**, 3679 (1987)

[120] N.C.Koon, Phys. Rev. Lett. **78**, 4865 (1997)

[121] T.C.Schulthess, W.H.Bulter, Phys. Rev. Lett. **81**, 4516 (1998)

[122] K.Takano, R.H.Kodama, A.E. Berkowitz, W.Cao, G.Thomas, Phys. Rev. Lett. **79**, 1130 (1997)

[123] J.S.Jiang, G.P.Felcher, A.Inomata, R.Goyette, C.Nelson and S.D.Bader, Phys. Rev. B **61** (2000), 9653

[124] S.G.E. te Velthuis, G.P.Felcher, J.S.Jiang, A.Inomata, C.Nelson, A.Berger and S.D.Bader, J. Appl. Phys. **75**, 4174 (1999)

[125] S.G.E. te Velthuis,  J.S.Jiang, G.P.Felcher, will be published

[126] E.E.Fullerton, M.J.Conover, J.E. Mattson, C.H.Sowers and S.D.Bader, Phys. Rev. B **48**, 15755 (1993)

[127] private communication with Cecilia Hanke-Sanchez, beamline scientist X13A

[128] Y.U. Idzerda, L.H.Tjeng, H.J.Lin, C.J. Gutierrez, G.Meigs and C.T. Chen, Phys. Rev. B **48**, 4144 (1993)

[129] L.E.Klebanoff, R.H.Victora, L.M.Falicov, D.A.Shirley, Phys. Rev. B **32**, 1997 (1985)

[130] R.Jungblut, C.Roth, F.U.Hillebrecht, E.Kisker, J. Appl. Phys. **70**, 5923 (1991)

[131] F.U.Hillebrecht, C.Roth, R.Jungblut, E.Kisker, A.Bringer, Europhys.Lett. **19**, 711 (1992)

[132] T.G.Walker, A.W.Pang, H.Hopster, S.F.Alvarado, Phys. Rev. Lett. **69**, 1121 (1992)

[133] Z.Xu, Y.Liu, P.D.Johnson, B.S.Itchkawitz, Phys. Rev. B **52**, 15393  (1995)

[134] P.Fuchs, V.N.Petrov, K.Totland, M.Landolt, Phys. Rev. B **54**, 9304  (1996)

[135] C.Turtur, G.Bayreuther, Phys. Rev. Lett. **72**, 1557 (1994)

[136]   D. Stoeffler, F.Gautier, Phys. Rev. B **44**, 10389  (1991)

[137]   L.Varga, C.Giles, Y.L.Zheng, S.Pizzini, F.de Bergevin, A.Fontaine, C.Malgrange, J. Synchrotron Rad. **6**, 1125 (1999)

[138]   M.Sacchi, A.Mirone, C.F.Hague, J.M.Mariot, L.Pasquali, P.Isberg, E.M.Gullikson, J.H.Underwood, Phys. Rev. B **60**, 12569 (1999)

[139]   J.M.Tonnerre, L.Sève, D.Raoux, G.Soullié, B.Rodmacq, P.Wolfers, Phys. Rev. Lett. **75**, 740 (1995)

[140]   J.W.Freeland, V.Chakarian, Y.U.Idzerda, S.Doherty, J..Zhu, J.-H.Park, C.C.Kao, Appl. Phys. Lett. **71**, 276 (1997)

[141]   P.Srivastava, L.Lemke, H.Wende, R.Chauvistré, N.Haack, K.Baberschke, J.Hunter-Dunn, D.Arvanitis, N.Mårtensson, A.Ankudinov, J.J.Rehr, J. Appl. Phys. **83**, 7025 (1998)

[142]   J.F.Ankner, G.P.Felcher,  J. Magn. Magn. Mater. **200** (1999), 741

[143]   G.P.Felcher,  J. Appl. Phys. **87**, 5431 (2000)

[144]   J.C.Lang, G.Srajer, Rev. Sci. Instrum. **66**, 1540 (1995)

[145]   B. .W.Batterman, Phys. Rev. B **45**, 12677 (1992)

[146]   Calculations by L. Xu using the code UR. More about code UR in "Program UR: general purpose code for synchrotron radiation calculations", Nucl. Instr. and Meth. A **347**, 61 (1994)

# Danksagung / Acknowledgment

Ich möchte Herrn Prof. Dr. Peisl danken, der es mir durch seine sehr guten Kontakte in den USA ermöglicht hat, meine Promotion an der National Synchrotron Light Source durchzuführen. Seine unermüdliche Bereitschaft mich über eine Entfernung von 6000 km zu betreuen und sein grosses Interesse am Fortschreiten in meiner Arbeit gaben mir viel Motivation.

Tim Salditt und Uwe Klemradt bin ich sehr dankbar, die mir bei meinen regelmässigen Lehrstuhlbesuchen stets mit wertvollen Tips und Anregungen weiterhalfen und so bedeutenden Einfluss am Fortschritt meiner Arbeit hatten.

Die äusserst kollegale Hilfsbereitschaft aller in dieser Zeit anwesenden Doktoranden und Doktorandinnen trug zudem sehr zu dem sehr angenehmen Betriebsklima bei. Sie gaben mir auch als Aussenstellen-Doktorand immer das Gefühl auch zur Gruppe zu gehöhren. Auf ihre Hilfe und Diskussionsbereitschaft konnte ich immer zählen.

I want to thank Chi-Chang Kao and Jerome Hastings, who advised me in Brookhaven and who made this work possible. They introduced me into the method of magnetic scattering and taught me many interesting aspects of physics, related and unrelated. They also helped me to share their enthusiasm for science and the reasons why people are willing to spend so much time counting photons, even at midnight. In my work they gave me all the freedom to develop my own ideas and interest, but also helped me every time when discussions were necessary to find the right directions for my work. Working with them was a great pleasure.

I am also very grateful to Cecilia Hanke Sanchez, who joined the group two and a half years ago as a postdoc and supported me not only at exhausting beamtimes at Brookhaven and the APS in Chicago, but was also willing to discuss my work with me at any time. I learnt many things from her, especially how to work more efficient or to find the right paper among a monstrous pile of others. Also the lunch times should not be forgotten, where it was possible to relax and talk about *normal* everydays topics.